Design of High-Speed SerDes Transceiver for Chip-to-Chip Communications in CMOS Process

Xuqiang Zheng
Supervisor: Professor Shigang Yue

School of Computer Science
University of Lincoln

A thesis submitted in partial fulfilment of the requirements of the
University of Lincoln for the degree of Doctor of Philosophy

May 2018

Abstract

With the continuous increase of on-chip computation capacities and exponential growth of data-intensive applications, the high-speed data transmission through serial links has become the backbone for modern communication systems. To satisfy the massive data-exchanging requirement, the data rate of such serial links has been updated from several Gb/s to tens of Gb/s. Currently, the commercial standards such as Ethernet 400GbE, InfiniBand high data rate (HDR), and common electrical interface (CEI)-56G has been developing towards 40+ Gb/s. As the core component within these links, the transceiver chipset plays a fundamental role in balancing the operation speed, power consumption, area occupation, and operation range. Meanwhile, the CMOS process has become the dominant technology in modern transceiver chip fabrications due to its large-scale digital integration capability and aggressive pricing advantage. This research aims to explore advanced techniques that are capable of exploiting the maximum operation speed of the CMOS process, and hence provides potential solutions for 40+ Gb/s CMOS transceiver designs. The major contributions are summarized as follows.

A low jitter ring-oscillator-based injection-locked clock multiplier (RILCM) with a hybrid frequency tracking loop that consists of a traditional phase-locked loop (PLL), a timing-adjusted loop, and a loop selection state-machine is implemented in 65-nm CMOS process. In the ring voltage-controlled oscillator, a full-swing pseudo-differential delay cell is proposed to lower the device noise to phase noise conversion. To obtain high operation speed and high detection accuracy, a compact timing-adjusted phase detector tightly combined with a well-matched charge pump is designed. Meanwhile, a lock-loss detection and lock recovery is devised to endow the RILCM with a similar lock-acquisition ability as conventional PLL, thus excluding the initial frequency set-

up aid and preventing the potential lock-loss risk. The experimental results show that the figure-of-merit of the designed RILCM reaches -247.3 dB, which is better than previous RILCMs and even comparable to the large-area LC-ILCMs.

The transmitter (TX) and receiver (RX) chips are separately designed and fabricated in 65-nm CMOS process. The transmitter chip employs a quarter-rate multi-multiplexer (MUX)-based 4-tap feed-forward equalizer (FFE) to pre-distort the output. To increase the maximum operating speed, a bandwidth-enhanced 4:1 MUX with the capability of eliminating charge-sharing effect is proposed. To produce the quarter-rate parallel data streams with appropriate delays, a compact latch array associated with an interleaved-retiming technique is designed. The receiver chip employs a two-stage continuous-time linear equalizer (CTLE) as the analog front-end and integrates an improved clock data recovery to extract the sampling clocks and retime the incoming data. To automatically balance the jitter tracking and jitter suppression, passive low-pass filters with adaptively-adjusted bandwidth are introduced into the data-sampling path. To optimize the linearity of the phase interpolation, a time-averaging-based compensating phase interpolator is proposed. For equalization, a combined TX-FFE and RX-CTLE is applied to compensate for the channel loss, where a low-cost edge-data correlation-based sign zero-forcing adaptation algorithm is proposed to automatically adjust the TX-FFE's tap weights. Measurement results show that the fabricated transmitter/receiver chipset can deliver 40 Gb/s random data at a bit error rate of $< 10^{-12}$ over a channel with >16 dB loss at the half-baud frequency, while consuming a total power of 370 mW.

Declaration

I, Xuqiang Zheng, declare that this thesis describes an original study carried out on my own. It has not been previously submitted to any university for the award of any degree. Where I have quoted from the work of others, the source is always given.

Acknowledgements

First and foremost, I would like to thank my academic advisor, Professor Shigang Yue, for his tolerance and patience in letting me explore my interested fields. He encouraged me to think deeply and creatively. He also taught me how to effectively communicate my research in papers and presentations. I hope through the years I have been able to pick up a little of his ability to find and explain ideas and concepts with such clarity. He will always be a role model to me in my future academic career.

Professor Chun Zhang is my co-advisor, and I am grateful to him for his help and support when I was on secondment to Tsinghua University. I especially value his trust in giving me plenty of tapeout chances, regardless of consequences for him. I have learned a lot from him on how to communicate with people and how to address troublesome issues. I also want to thank my second co-advisor, Dr. Tryphon Lambrou, for his nice advice and kind discussions.

I would like to take this chance to thank my family for their selfless love and constant support. Especially, my parents-in-law who gave me great support on deciding to start my Ph.D. study and provided me generous help during my study. I am grateful to my wife who supported the whole home when I was studying abroad. I also want to say sorry to my son for the absence during my abroad study.

The environment at the University of Lincoln is full of brilliant and enthusiastic colleagues who have provided me valuable help and discussions. I wish to thank the previous and present members in Lincoln Centre for Autonomous Systems (L-CAS) research group who have brought me great convenience in daily life and academic research. In particularly, I want to thank Farshad Arvin, Yi Gao, Junxiong Jia, Feng

List of Main Publications

[1] **X. Zheng**, C. Zhang, and F. Lv *et al.*, "A 40-Gb/s quarter-rate SerDes transmitter and receiver chipset in 65-nm cmos," *IEEE J. Solid-State Circuits (JSSC)*, vol. 52, no. 11, pp. 2963–2978, Nov. 2017.

[2] **X. Zheng**, Z. Wang, and F. Li *et al.*, "A 14-bit 250 MS/s IF sampling pipelined ADC in 180 nm CMOS process," *IEEE Trans. Circuits Syst. I, Reg. Papers (TCAS-I)*, vol. 63, no. 9, pp. 1381–1392, Sep. 2016.

[3] **X. Zheng**, F. Lv, and F. Zhao *et al.*, "A 10 GHz 56 fsrms-integrated-jitter and -247 dB FOM ring-VCO based injection-locked clock multiplier with a continuous frequency-tracking loop in 65 nm CMOS," in *Proc. IEEE Custom Integrated Circuits Conf. (CICC)*, Jul. 2017, pp. 1–4.

[4] **X. Zheng**, C. Zhang, and S. Yuan *et al.*, "An improved 40 Gb/s CDR with jitter-suppression filters and phase-compensating interpolators," in *Proc. IEEE Asian Solid-State Circuits Conf. (ASSCC)*, Nov. 2016, pp. 85–88.

[5] **X. Zheng**, C. Zhang, and F. Lv *et al.*, "A 5-50 Gb/s quarter rate transmitter with a 4-tap multiple-MUX based FFE in 65 nm CMOS," in *Proc. IEEE European Solid-State Circuits Conf. (ESSCIRC)*, Sep. 2016, pp. 305–308.

[6] W. Cao, **X. Zheng**, Z. Wang, and D. Li *et al.*, "A 15Gb/s wireline repeater in 65nm CMOS technology," in *Proc. IEEE International Conference on Electron Devices and Solid-State Circuits (EDSSC)*, Oct. 2015, pp. 590–593.

List of Figures

List of Tables

List of Acronyms and Abbreviations

ADC   analog-to-digital converter
BBPD   bang-bang phase detector
BER   bit error rate
CAGR   compound annual growth rate
CCI   cross-coupled inverter
CDR   clock data recovery
CEI   common electrical interface
CFP   centum form-factor pluggable
CML   current-mode logic
CP   charge pump
CPU   central processing units
CTLE   continuous linear equalizer
DAC   digital-to-analog converter
DFE   decision feedback equalizer
DIV   divider
DJ   deterministic jitter
DLL   delay-locked loop
DNL   differential nonlinearity
DRC   Design rule check
DSP   digital signal processing
EDC-SZF   edge-data correlation based sign zero-forcing
EDR   enhanced data rate
ESD   electro-static discharge
FEC   forward error correction
FFE   feed-forward equalizer
FIR   finite impulse response
FOM   figure-of-merit
FS-PDDC   full-swing pseudo-differential delay cell
FTG   forward transmission gate
FTL   frequency tracking loop
GbE   gigabit ethernet
GBW   gain-bandwidth product

HDR	high data rate
HPF	high-pass filter
IBTA	InfiniBand trade association
IEEE	institute of electrical and electronics engineers
ILCM	injection-locked clock multiplier
ILO	injection locked oscillator
IL-RVCO	injection-locked ring voltage-controlled oscillator
INL	integral nonlinearity
ISI	inter-symbol interface
JGEN	jitter generation
JTOL	jitter tolerance
JTRAN	jitter transfer
LD	lock detector
LLD-LR	lock-loss detection and lock recovery
LMS	least mean square
LPF	low-pass filter
LR	long reach
LSSM	loop-selection state machine
LVS	layout versus schematics
MAC	media access control
MEO	maximum eye opening
MR	medium reach
MUX	multiplex
NRZ	non-return to zero
NTF	noise transfer function
OC	optical carrier
OSC	oscillator
PCB	printed circuit board
PD	phase detector
PEX	parasitic extraction
PFD	phase frequency detector
PG	pulse generator
PI	phase interpolator
PLL	phase-locked loop
POD	polarity detector
PSD	phase shift detection
PTL	phase tracking loop
QSFP	quad small form-factor pluggable
RILCM	ring-oscillator-based injection-locked clock multiplier
RJ	random jitter

RVCO	ring voltage-controlled oscillator
RX	receiver
S/H	sample-and-hold
SerDes	serializer/deserializer
SFP+	small form-factor pluggable plus
SNR	signal noise ratio
SONET	synchronous optical network
SS-LMS	sign-sign least mean square
SST	source-series terminated
SSTPD	sub-sampling timing-adjusted phase detector
TAL	timing-adjusted loop
TDC	time-to-digital converter
TPD	timing-adjusted phase detector
TX	transmitter
UI	unit interval
USR	ultra short reach
VCDL	voltage-controlled delay line
VCO	voltage-controlled oscillator
VCTLR	control voltage
VSR	very short reach
XSR	extra short reach
ZF	zero-forcing
f_{BW}	-3dB bandwidth
f_T	cutoff frequency of the transistor
f_c	corner frequency of the oscillator
f_{inj}	injection-locking bandwidth of the injection-locked oscillator
$1/f^2$	white noise of the oscillator
$1/f^3$	flick noise of the oscillator
$S_\theta(f)$	phase noise spectrum of the oscillator

Contents

Chapter 1

Introduction

1.1 Background

The exponential growth of cloud computing, social networking, and multimedia sharing has led to an explosive bandwidth demand on data communication. Cisco global IP traffic forecast estimates that the global IP traffic will grow at a compound annual growth rate (CAGR) of 22 percent from 2015 to 2020. By 2020, it is expected to see 50 billion connected devices generating more than two Zetta bytes (2^{30} Tera bytes) of data traffic annually (see Fig. 1.1). Moreover, 64 percent of all the Internet traffic will be delivered globally crossing the content delivery networks [1]. To accommodate this aggregated bandwidth requirement, the study group of Institute of Electrical and Electronics Engineers (IEEE) P802.3bs has approved a 400 Gigabit Ethernet (GbE) standard to quadruple the backbone bandwidth of the existing 100 GbE [17] and the InfiniBand® trade association (IBTA) has announced its 600 Gb/s computer networking communication standard high data rate (HDR) in the roadmap [18]. To support such high-speed data communications, multi-lane high-speed serial links are usually employed to extend the throughput bandwidth. As an example, the next-generation 400 GbE will be most possibly implemented by multiple serial links in forms of 16x25 Gb/s or 8x50 Gb/s, where the latter lane configuration is more in line with the trend because of its low cost, high capability, simplified cabling, high power efficiency, and less coherent optical devices.

Among a variety of components in these high-speed links, the physical Serializ-
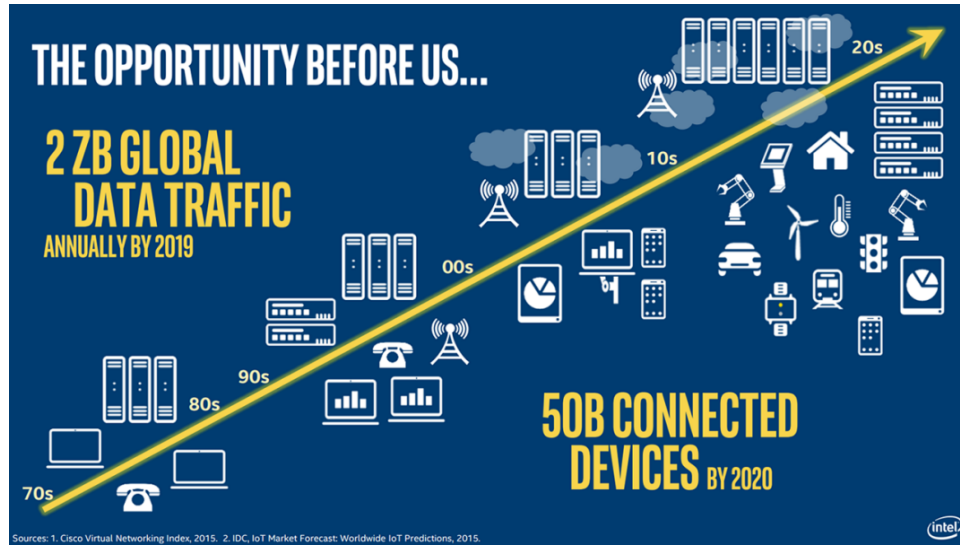
Figure 1.1: Diagram of the global data traffic trend [1]. By 2020, 50 billion devices will be connected generating more than two zetta bytes of data traffic annually.

er/Deserializer (SerDes) transceiver plays a critical role in making up the communication connections between the data link layer and the physical medium. Due to the development of the optical communication and post massive data-processing ability, the data-moving capability is mainly limited by the maximum speed of the SerDes transceivers. Over the past few decades, the transceiver data rate has constantly been increased from Mb/s to tens of Gb/s [19]. Fig. 1.2 shows the wired network roadmap since 2000 [2], where the small form-factor pluggable plus (SFP+) line describes the port speeds on servers, the quad small form-factor pluggable (QSFP) curve shows the speeds of switches above the servers, and the centum form-factor pluggable (CFP) line illustrates the data rates of routers. Similar to 10 Gb/s ports on servers that have driven the speed of switches to 40 Gb/s and 100 Gb/s, the development of 25 Gb/s networking has updated 100 Gb/s switching and 400 Gb/s routing. At present, the Ethernet Alliance is evaluating potential standards for 50 Gb/s on the server and 200 Gb/s on the switch. Looking forward to 2025, the data communication speed is tend to be renewed to 100 Gb/s on the server, 400 Gb/s on the switch, and 1 Tb/s on the router. So far, 25-28 Gb/s serial links approved by InfiniBand enhanced data rate (EDR), 32G fibre channel (32GFC), and common electrical interface (CEI)-28G have stepped into the period of industrial deployment [20, 21, 22]. Meanwhile, 38-64 Gb/s transceivers, which will play key roles in the next-generation data rates supported by Ethernet 400 GbE, InfiniBand HDR, and CEI-56G, have attracted increasing research attention in

Figure 1.2: Wired network roadmap [2]. The data rates in SFP+, QSFP, and CFP are updating towards 100Gb/s, 400Gb/s, and 1Tb/s, respectively.

both the industry and academia [17, 18, 23, 24, 25, 26]. This dissertation mainly focuses on the advanced techniques of high-speed SerDes transceivers for chip-to-chip communications operating at 40+ Gb/s in CMOS process.

1.2 Challenges in Cutting-Edge Transceivers

To accommodate the requirement of the continuously increasing data communications, cutting-edge transceivers operating at 38-64 Gb/s have become standard modules within the next-generation connections for data centers and backbone networks [17, 18, 27]. The main challenges in designing such high-speed transceivers originate from the ever decreased UI period [23, 24, 25], which not only poses high bandwidth requests on the blocks located at the critical path, but also makes the link timing budget extremely tight. The CMOS fabrication process, which is preferred due to its large-scale integration and aggressive pricing advantage, has made the designs even more challenging because of its limited cutoff frequency and poor noise performance [7, 28, 29]. Although an advanced process can provide a higher operation speed, it cannot completely solve these problems as the parasitic capacitances/resistances at the high-speed outputs usually do not scale well with the technology because of the bonding and/or electro-static discharge (ESD) protection requirements. Meanwhile, economic feasibility is another factor that must be considered when constructing multi-lane connections. It usually involves power consumption, area occupation, and heat

3

dissipation, where small area occupation and low power consumption could improve the port density and lower the requirement of heat dissipation, hence reducing the overall cost [28, 30, 31]. For implementations, the digital media access control (MAC) layer and the analog physical layer (SerDes transceiver) are developing at different stages. Specifically, the 200G MAC (4×50 Gb/s) has been implemented and validated in the industry [31], while the physical layer is still in the period of moving from the lab to the market [17, 18, 23, 24, 25, 26, 27, 32]. This is because the MAC mainly processes the parallel data streams, where the timing requirement can be relaxed by increasing the parallel bit width. In contrast, the SerDes transceiver has to provide accurate timing information, sufficient bandwidth, and appropriate equalization for the full-rate data communication.

1.3 Research Objectives

The next-generation SerDes transceivers that support 38-64 Gb/s have attracted great attentions from both the industry and the academia due to their broad market potential and significant academic value. Although the technical feasibility has been proved by several 40-56 Gbs transceiver designs [33, 34, 35, 36], plenty of research studies are still demanded to further optimize the power consumption, area occupation, and operation robustness, thus paving the path for the upcoming industrial deployment. This thesis mainly focuses on the enhancement techniques to explore the maximum process limit and hence provides potential solutions for the cutting-edge transceiver designs. The major research objectives are summarized as follow.

- Designing a robust ring-oscillator-based injection-locked clock multiplier (RIL-CM) with optimized figure-of-merit. RILCM has been proven to be one of the most promising solutions for high-speed low-jitter clock multiplications since it combines the good properties of small area occupation and low phase noise. However, there still exists two difficulties that hinder its wide spread in product applications. One is the limited accuracy of the frequency offset detection as the accumulated phase error can always be reset by the injection pulse. The other is the fragile robustness due to its limited lock-in range and weak lock-acquisition

ability. This thesis aims to overcome these two difficulties and hence provides a reliable, low-cost clock multiplier for wireline transceivers.

- Designing a wide-range transmitter that explores the maximum process limit. The direct 4:1 MUX multiplexing scheme has provided a promising solution to satisfy the stringent timing requirement at the final serialization stage. Nonetheless, the doubled self-drain capacitance has limited the maximum bandwidth and hence constrains the overall transmission data rate. Another difficulty in the transmitter design is how to generate the UI-spaced serial sequences for the FFE. This thesis targets to optimize the bandwidth of the 4:1 MUX and develop a quarter-rate transmitter with a multi-MUX-based 4-tap FFE.

- Designing a jitter-performance-improved receiver. Quarter-rate PI-based CDR has become the preferred choice for data rates over 20 Gb/s due to its robustness, portability, and compactness. Nevertheless, its jitter performance is limited by the nonlinearity-caused cycle-limited oscillation and the nonlinearity of the phase interpolation. This thesis seeks to improve the CDR architecture to suppress the deterministic jitter caused by the cycle-limited oscillation while maintaining the loop parameter unchanged to satisfy the JTOL specification. Meanwhile, we make an effort to optimize the linearity of the PI.

- Developing a low-cost adaptive equalization algorithm. Adaptive equalization has become a dominant option for data rates over 20 Gb/s. Previous adaptation algorithms such as sign-sign least mean square (SS-LMS), zero-forcing (ZF), and maximum eye opening (MEO) have manifested their validity. However, the auxiliary circuits associated with these methods have degraded their competitiveness in the cutting-edge transceiver design. This thesis aims to develop a low-cost adaptation algorithm that only uses the existing data/edge information to automatically adjust the tap weights of the TX-FFE.

1.4 Research Contributions

This dissertation explores several advanced techniques to make the data rates of the cutting-edge wireline transceivers approach the fundamental technology limit. It addresses some of the architecture-level and circuit-level challenges with appropriate compromises of power consumption, area occupation, performance margin, and operation robustness. The main contributions of this dissertation are summarized in the following.

- A low-jitter ring-oscillator-based injection-locked clock multiplier (RILCM) is designed in 65-nm CMOS process. It employs a hybrid frequency tracking loop that consists of a traditional phase-locked loop (PLL), a timing-adjusted loop, and a loop selection state-machine to automatically adjust the control voltage of the injection-locked voltage-controlled oscillator (VCO). In the ring-VCO, a full-swing pseudo-differential delay cell is proposed to lower the device noise to phase noise conversion. To satisfy the requirements of high operation speed, high detection accuracy, and low output disturbance, a compact timing-adjusted phase detector tightly combined with a well-matched charge pump is designed. Meanwhile, a lock-loss detection and lock recovery is devised to endow the RILCM with a similar lock-acquisition ability as conventional PLLs, thus excluding the initial frequency setup aid and preventing the potential lock-loss risk. The measurement results show that the implemented RILCM achieves a good balance among jitter performance, area occupation, operation speed, and power efficiency.

- A 5-50 Gb/s quarter-rate transmitter (TX) with a 4-tap feed-forward equalization (FFE) based on multiple-multiplexer (multi-MUX) is designed in 65-nm CMOS technology. To increase the maximum operating speed, a bandwidth enhanced 4:1 MUX with the capability of eliminating charge-sharing effect is proposed. To produce the quarter-rate parallel data streams with appropriate delays, a compact latch array associated with an interleaved-retiming technique is designed. The measurement results indicate that the fabricated transmitter achieves better jitter

performance and power efficiency, even in comparison to the LC-delay-based FFE, mainly because of the proposed high-speed 4:1 MUX and the compact interleaved-latching scheme.

- A 40 Gb/s receiver (RX) with excellent performance on both jitter suppression and jitter tracking is implemented in 65-nm CMOS process. Passive low-pass filters with adaptively adjusted bandwidth are introduced into the data-sampling path to automatically balance jitter tracking and jitter suppression for data decisions. Additionally, a time-averaging-based compensating phase interpolator is proposed to not only improve the phase-step uniformity but also reduce the phase-spacing drift between edge and data sampling clocks. The measurement results show that the maximum tolerable amplitude of sinusoidal jitter at high frequency outperforms previous receivers, which is mainly because of the introduced LPFs and the developed compensating PI.

- A chip-to-chip connection over a 12-cm printed circuit board (PCB) channel using the designed transmitter and receiver chips is constructed. The channel loss is compensated by a combination of TX-FFE and RX-CTLE. To obtain the optimal equalization coefficients and track the channel-loss variations with respect to operation environment, a low-cost edge-data correlation-based sign zero-forcing (EDC-SZF) adaptation algorithm is proposed to automatically adjust the TX-FFE's tap weights. The measurement results indicate that the equalization scheme of the combination of TX-FFE and RX-CTLE is a good choice for the equalization of the 16-dB loss channel at 40 Gb/s, and the proposed EDC-SZF adaptation can effectively tune the TX-FFE to its optimal tap weights for a given control voltage applied to the RX-CTLE.

1.5 Organization of the Thesis

This thesis is composed of seven chapters. Chapter 1 outlines the research background, objectives, contributions, and organization of the dissertation. Chapter 2 summarizes the mainstream techniques developed on the high-speed serial links. The main

contributions of this thesis are detailed in Chapters 3, 4, 5 and 6, which present the designed clock multiplier, transmitter chip, receiver chip, and chip-to-chip link, respectively. In each of these four chapters, we discuss the design motivation, describe the prototype implementation, and present the experimental results. Finally, Chapter 7 concludes this thesis and outlooks the possible future work. The details in each chapter are summarized as follows.

Chapter 2 reviews the mainstream techniques that have been developed within the wireline transceiver designs. It begins with a brief discussion on the general design considerations when constructing a serial communication link, including technology selection, link space choice, and on-chip wire modeling. Then, we summarize the major metrics that are used to characterize the overall performance of a serial communication link. Following that, the mainstream techniques of the crucial components within a serial link are discussed in detail, including clock multiplier, transmitter, receiver, and equalizers.

Chapter 3 presents the design of the RILCM. It firstly summarizes the challenges in previous RILCM and then describes the proposed RILCM architecture. Following that, we demonstrate the details of the ring-based voltage-controlled oscillator, the phase-shift detection scheme, and the introduced lock-loss detection and lock recovery. Finally, the experimental results are presented and discussed. This chapter is extended based on the publications [3] on page VI.

Chapter 4 presents the designed transmitter chip. It firstly discusses the two main challenges (i.e., timing constrains and bandwidth limitations) in high-speed transmitter designs, and then presents our transmitter architecture. Following that, the enhancement on the 4:1 multiplex and the clocking techniques are separately illustrated. Finally, the experimental results are demonstrated and discussed. This chapter is an enriched version of the contents published in [1] and [5] on page VI.

Chapter 5 presents the implemented receiver chip, which mainly focuses on the improvement on the clock data recovery (CDR) design. It firstly summarizes the design considerations of the receiver, and then displays the receiver architecture. Following that, we separately describe the improved digital CDR and the linearity-optimized

compensating PI. Finally, the experimental results are presented and discussed. This chapter is extended based on the contents published in [1] and [4] on page VI.

Chapter 6 constructs an overall chip-to-chip communication link utilizing the chips designed in Chapters 4 and 5. It firstly describes the link connection and equalization scheme, and then demonstrates the developed low-cost EDC-SZF adaptation algorithm. After that, we present the experimental setup and the measurement results. The condensed contents of this chapter has been published in [1] on page VI.

Chapter 7 summarizes this dissertation in conclusions and discusses the potential optimization work that can be further done in the future.

Chapter 2

Literature Review

High-speed serial links are commonly adopted in chip-to-chip communication applications ranging from handheld electronics to supercomputers. Driven by the exponential growth of the computation ability and storage-volume capability, the throughput bandwidths within the connections among memories, graphics, processors, chassis, racks, and routers [37, 38, 39] have been continuously increased. In practical designs, these bandwidth increases are achieved by either raising the number of data lanes or increasing the data rate per lane [40]. As one of the most important component in such links, serial transceiver needs to provide precise timing information, sufficient bandwidth, and appropriate equalization for the data transmission. These requirements have posed significant challenges in the implementation of wireline transceivers and hence made the design of the wireline transceivers a hot research field [41, 42, 36].

This chapter will review the related works for the wireline transceiver designs. It begins by introducing the general design considerations when constructing a serial chip-to-chip connection in Section 2.1. Section 2.2 then presents the crucial metrics that are usually employed to characterize the performance of a serial link. Following that, the pros and cons of the mainstream techniques within a serial link including clocking techniques, transmitter techniques, receiver techniques, and channel equalizers are detailedly discussed in Section 2.3.
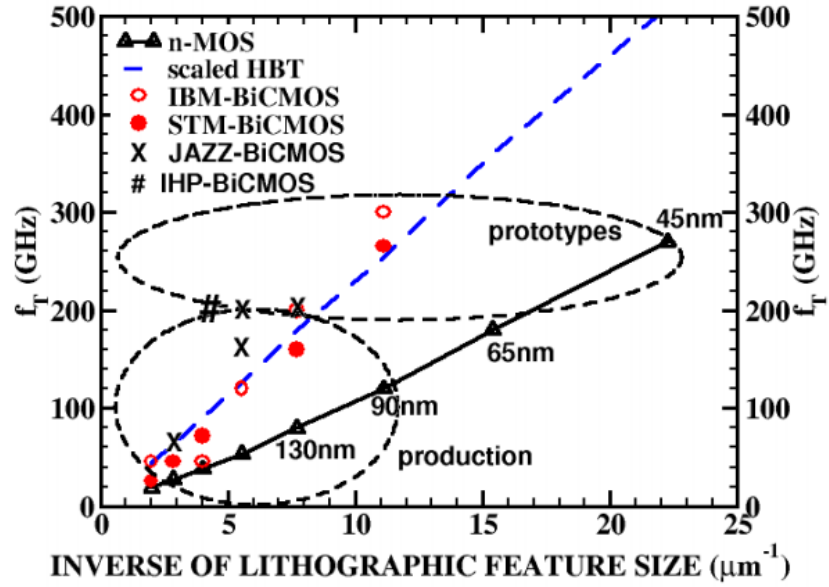
Figure 2.1: Cutoff frequency (f_T) scaling comparison among different processes in terms of the inverse of the lithographic feature size [3].

2.1 General Design Considerations

2.1.1 Technology Choices

High-speed links over 10 Gb/s have traditionally been implemented in SiGe BiCMOS technology due to its integration of high-speed SiGe bipolar and low-cost CMOS transistor, where the former is suitable for the high-speed, low-noise blocks such as transmitter (TX) driver and receiver (RX) pre-amplifier, while the latter is appropriate for the control-logic implementation [43, 44]. However, for more complex applications where SerDes function is combined with complicated digital functions, CMOS process is preferred because of its fast shrinking that makes it feasible to keep the die size, power consumption, and fabrication cost as low as possible [43]. These area, power, and cost savings over equivalent SiGe circuits mainly come from the simple and compact transistor implementation in CMOS process that makes the designs easily scaled downward as semiconductor processes improve. Line card and optical module manufacturers utilizing CMOS products will benefit from the large community of competing foundries, which engages in aggressive pricing strategies and rapid adoption of ever-smaller process nodes that deliver successively lower cost per chip, reduced operating voltages, and decreased power consumption [28]. Fig. 2.1 shows the scaling trend

of CMOS process versus SiGe BiCMOS technology in terms of the cutoff frequency (f_T). Although the SiGe BiCMOS technology always remains a speed advantage over CMOS process, the f_T of 45 nm CMOS already reaches 270 GHz, which makes it feasible to implement high-speed transceivers around tens of Gb/s.

Note that the potential advantages of using low-cost CMOS process come with several significant challenges. The primary challenge is that mainstream CMOS transistors are slightly slower than exotic SiGe devices (see Fig. 2.1). Therefore, more innovative designs for crucial blocks such as voltage-controlled oscillator (VCO), transmitter driver, receiver analog front-end, and channel equalizer are required to overcome the slower, noisier characteristics of CMOS transistors. Driven by the large-scale market requirements, Moore's law curve is developing towards ever-better power, performance and price. Meanwhile, process nodes are constantly scaled down under the aggressive investment of the foundries. The resulting processes have provided platforms for the development of several tens of serial transceivers with high efficiencies in both cost and power. So far, 25-28 Gb/s serial transceivers in CMOS processes supporting InfiniBand enhanced data rate (EDR), 32G fiber channel (32GFC), and common electrical interface (CEI)-28G have stepped into the period of industrial deployment [20, 21, 22]. Meanwhile, 38-64 Gb/s transceivers, which will play a key role in the next-generation data rate supported by 400 Gigabit Ethernet (GbE), InfiniBand high data rate (HDR), and CEI-56G, have been successfully demonstrated in lab and been under the period of moving from the lab to the market [17, 18, 23, 24, 25, 26, 27, 32].

2.1.2 Spaces of Electrical Links

Fig. 2.2 shows the main SerDes application spaces in electrical links, including rack-to-rack link, chassis-to-chassis connection, and intra-chassis interconnect. This thesis mainly focuses on the chip-to-chip connections described in Fig. 2.2(c). According to the communication distance, these serial links can be classified into ultra short reach (USR), extra short reach (XSR), very short reach (VSR), medium reach (MR), and long reach (LR). Fig. 2.3 summarizes the connection details of each application space defined in CEI-56G.

(a)

(b)   (c)
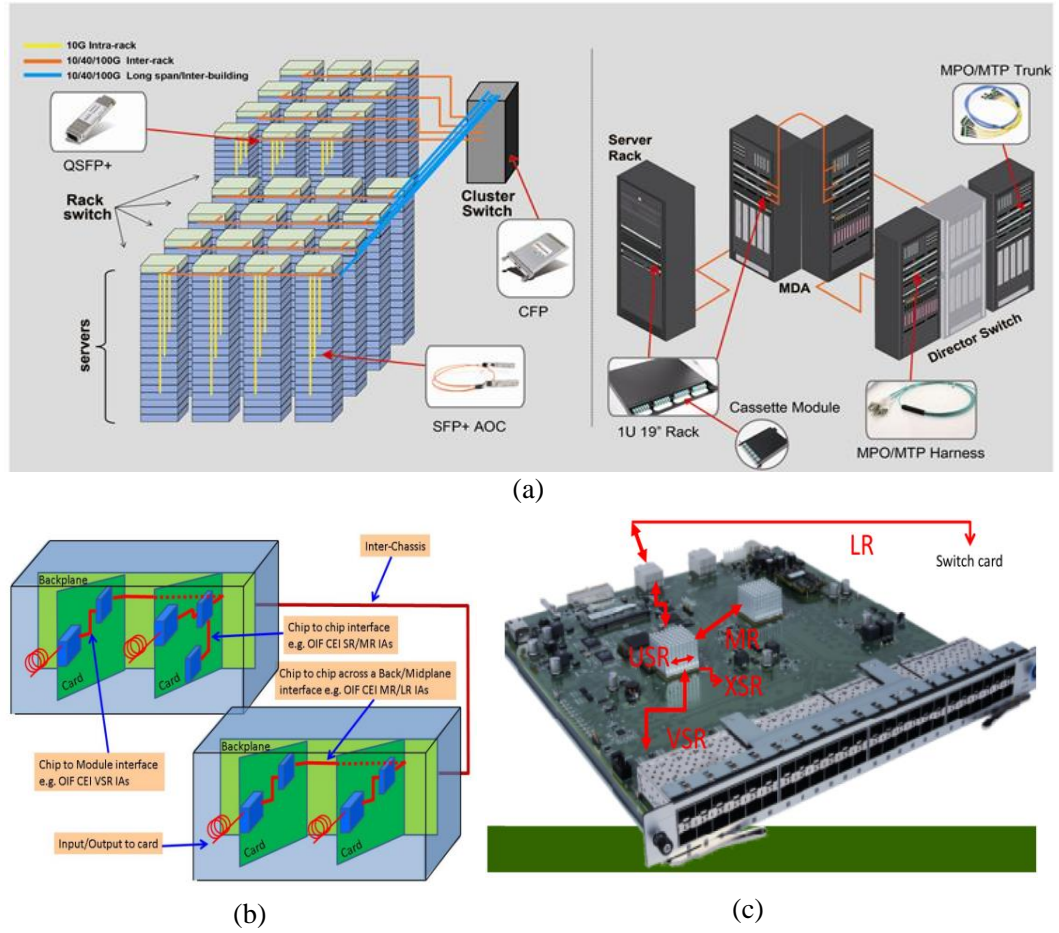
Figure 2.2: Typical SerDes application spaces. (a) rack-to-rack link, (b) chassis-to-chassis connection, and (c) intra-chassis interconnect [4].
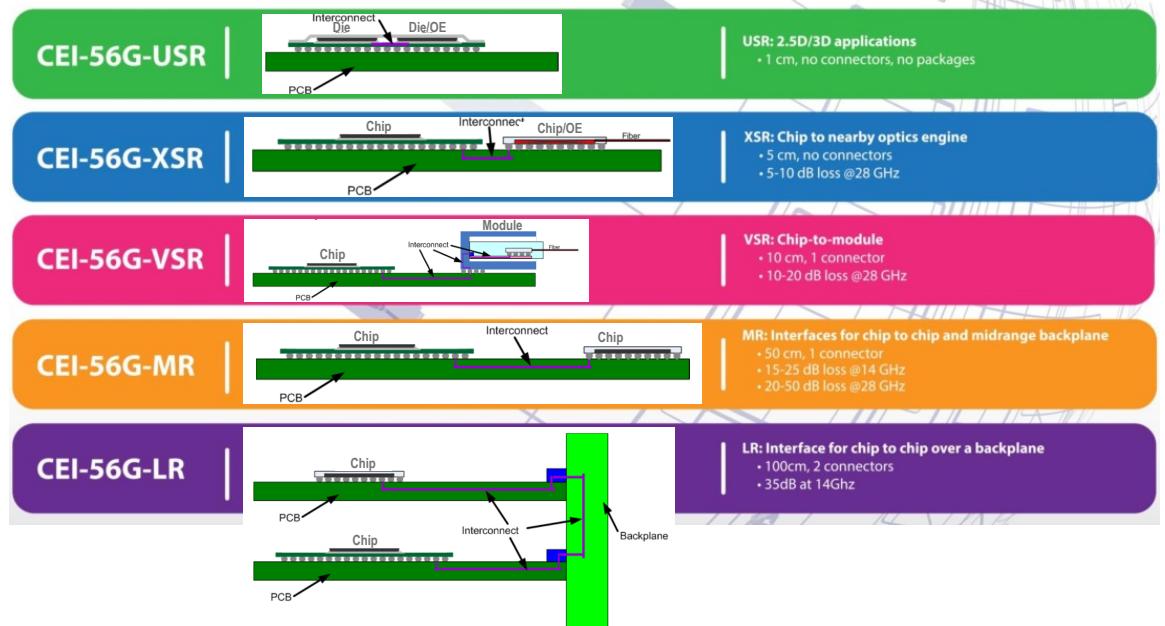
Figure 2.3: Reach details of each application space defined in CEI-56G [4].

13

The USR link is usually used to connect multiple dies and optical engines within a multi-chip module to achieve the power and signal integrity objectives. This 2.5/3-dimension packaging solution can save substantial power since the communication distance is typically less than 10 mm. This short channel length allows for a much simple physical layer implementation since it can be treated as a synchronous link. Meanwhile, the low-cost communication channel makes it possible to rule out equalizations.

The XSR link is often employed to realize the data communication between electrical chips and optical devices, where the link distance is usually less than 50 mm. Meanwhile, central processing units (CPUs) and digital signal processings (DSPs) can also be connected via such a short connection to satisfy the latency requirements. This XSR link is used to connect CPUs with memory stacks to optimize the responding time of memory access as well.

The VSR link mainly refers to the connection between electrical chips and pluggable modules. Its typical communication distance is around 10 cm, where the channel loss could reach 10-20 dB at the Nyquist frequency.

The MR link is usually used to implement the connection between two chips on the same printed circuit board (PCB) or one on the main card and the other on a daughter card [4]. Its communication distance ranges up to 50 cm and the channel loss is in the range of 15-25 dB at the half frequency of the symbol rate.

The LR interface is usually applied to realize the connection between two daughter cards across a legacy backplane with an up to 35 dB channel loss at the Nyquist frequency. The total channel length is limited less than 100 cm, and two connectors are allowed.

The channel loss in VSR, MR, and LR links has posed significant challenges in transceiver designs as they need to compensate for the high-frequency loss within the power budget. This problem becomes extremely severe for the large switch chips where heat dissipation also plays a performance-limiting factor. To address these issues, complex equalization scheme, high-order modulation, and forward error correction (FEC) have been developed [4]. To accommodate difference channel loss, a proper

combination of these techniques is usually employed to correct the signal distortion. For example, a solely TX-side feed-forward equalizer (FFE) is usually sufficient for VSR links to compensate for the small channel loss (<10 dB) while a sophisticated combination of complex equalization scheme, advanced modulation, and FEC is required in the LR links to cope with the signal integrity problem associated with the legacy communication channel, including severe signal attenuation caused by dielectric loss (> 30 dB), signal reflection resulting from impedance discontinuity, and mutual crosstalk among different transmission channels.

2.1.3 On-Chip Wire Modeling

With the rapid development of the manufacturing technologies, the channel length and the transistor delay are respectively shrinking down to nanometer scale and sub-tens of ps. These miniaturization trend for CMOS integrated circuits has led to a tremendous cost advantage and performance improvement. However, the narrowed cross-section and wire spacings have dramatically increased the parasitic effects of the connection wires, thus degrading their high-speed performance. Previous studies have demonstrated that when the signal's rise/fall time roughly matches the propagation time through the line, the connection wire actually isolates the receiver from the driver and plays the role of output/input impedance of the driver/receiver [45, 46, 47]. Consequently, how to model on-chip connection wires has become a tricky problem for high-speed circuit designers. If it is not handled appropriately, the interconnect effects including voltage ring, signal delay, distortion, reflection, and crosstalk could degrade the system robustness or even lead to undesired errors. Considering the fact that a simple model may ignore some important effects to result in a design failure while a sophisticated model could complicate the simulation to extend the design cycle or even make the simulation unapplicable. Hence, it becomes extremely important for designers to properly simulate the entire designs as efficiently as possible while maintaining the simulation accuracy [48].

The concept of "high-speed interconnect" is a relative concept. It refers to the interconnect where the propagation time to travel between the two connection points cannot

be neglected. As discussed in [48, 47], the "*electrical length*" of an interconnect can be considered as a criterion for classifying interconnects. If the wire length is shorter than one-tenth of the corresponding wavelength (e.g., for a 10 GHz signal, λ=3 cm), the interconnect can be considered as electrically short and hence can be modeled by the lumped model. Otherwise, the interconnect can be referred as electrically long (i.e. "high-speed interconnect"), which should be treated as a distributed or full-wave model [45, 49]. In high-speed serial links, the highest frequency of interest is determined by the rise/fall time of the transmission signal since most of the trapezoidal pulse energy is concentrated inside the first lobe. Correspondingly, f_{max} can be defined as the -3 dB bandwidth of this major lobe [46, 47],

$$f_{max} = \frac{0.35}{t_r},$$ (2.1)

where t_r is the rise/fall time of the signal. This implies that for a 0.1 ns rise time, the maximum interest frequency is around 3 GHz and the minimum wavelength is 10 cm. In some special cases, a more conservative bandwidth can be set as [50],

$$f_{max} = \frac{1}{t_r}.$$ (2.2)

2.2 SerDes Design Metrics

2.2.1 Data Rate and Power Efficiency

The data-rate of a high-speed serial link is the number of data bits transferred per second from the transmitter to the receiver, while the power efficiency refers to the normalized power consumption when transferring every Gigabit data in one second . The former is usually measured in Gb/s and the latter is frequently characterized by mW/Gb/s. Previous studies [51, 52, 53] have demonstrated that there exists an optimal data rate to exploit the maximum potential of a given process to achieve the best power efficiency. The analyses in [52] and [53] suggest that the power efficiency reaches the optimal value when the bit time (the reciprocal of the data rate) is around (4$\sim$6) $\times$

FO4 (the inverter delay of the target technology with a fan-out-of-4). At this speed, it is relatively easy to drive the half-rate clock and build critical high-speed blocks (e.g., TX-side half-rate 2:1 multiplexers and RX-side edge/data samplers) in power-efficient CMOS logic [51]. The FO4 delays can be roughly approximated as 500 ps per μm of minimum drawn gate length in CMOS technologies [54]. On one hand, if the data rate is too low, the overhead of the stationary currents will become dominant, thus deteriorating the power efficiency. On the other hand, when the bit period is too short, power-hungry current-mode logic (CML) circuits and complicated equalization techniques are usually employed to satisfy the stringent timing requirement and compensate for the severe channel attenuation. This is also the reason why the cutting-edge transceivers running at tens of Gb/s usually show an increasing trend in power efficiency values. Previous research has demonstrated 2 mW/Gb/s transceivers in 65 nm CMOS operating around 10 Gb/s [55, 56]. Meanwhile, the commercial 28 Gb/s transceivers with sophisticated equalizers using 28 nm CMOS is around 7 mW/Gb/s [30]. Recently published non-return to zero (NRZ) transceivers operating from 40 to 60 Gb/s with an equalization ability of <20 dB in 28-65 nm CMOS processes have shown energy efficiencies ranging from 4.4 to 16.4 mW/Gb/s [25, 34, 57, 35, 36].

2.2.2 Bit Error Rate

Bit error rate (BER) is the ratio of the error bit number to the total transmitted bit number in a specific period. It is a measure of the correctness of the link operation, which is expected to be lower than 10^{-12} for most serial connections. In serial communication systems, the BER could be affected by the distribution of the random jitter (RJ) and the deterministic jitter (DJ) in the link. Fig. 2.4 gives the jitter decomposition components and their corresponding jitter sources [58], where the jitter generation and amplification mechanisms can be found in [54] and [59, 60, 61], respectively. Combining the jitter generated by each source, the total RJ and DJ can be respectively computed by the following two equations,

$$T_{rj} = \sqrt{t_{rj1}^2 + \cdots + t_{rjn}^2,} \tag{2.3}$$
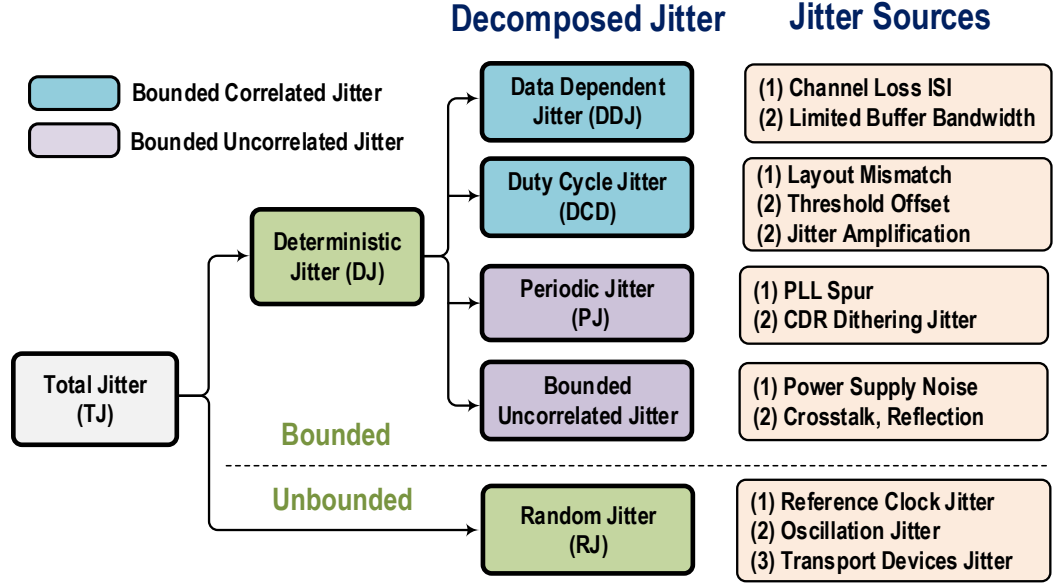
Figure 2.4: Jitter decomposition and jitter sources.

$$T_{dj} = t_{dj1} + \cdots + t_{djn}, \tag{2.4}$$

where T_{rj} denotes the total RJ, $t_{rjn}, (n = 1, 2, ...)$ refers to the independent RJ generated by different sources, T_{dj} represents the total DJ, and $t_{djn}, (n = 1, 2, ...)$ stands for the separate DJ produced by different blocks. Assuming the samplings that happen outside the bit period produce bit errors, the horizontal Q-factor of the BER can be represented by,

$$Q_{BER} = \frac{T_{bit} - T_{dj}}{2T_{rj}}, \tag{2.5}$$

where T_{bit} is the bit period. Referring to the analysis in [62], the BER can be roughly evaluated by,

$$BER = \frac{1}{2} erfc(\frac{Q_{BER}}{\sqrt{2}}), \tag{2.6}$$

where $erfc()$ is the complementary error function, which is defined as,

$$erfc(x) = \frac{2}{\sqrt{\pi}} \int_x^{\infty} e^{-x^2} dx. \tag{2.7}$$

According to Eq. (2.6), the horizontal Q-factor should be 7.0 to satisfy the commonly required BER of 10^{-12}. It is worth noting that the BER can be further degraded by the non-ideal impairments such as asymmetric jitter distribution [63], non-optimal

sampling position [64], phase-spacing error, sampler input-offset [65], and sampler metastability [65].

The vertical amplitude dimension is another factor that could affect the BER. It usually involves the TX-side output swing, channel equalization, and RX-side input sensitivity. The receiver sensitivity is defined as the lowest signal amplitude that the receiver can correctly extract the transmitted data. It is a function of equivalent input noise, input offset, and minimum latch resolution. When the received signal has a sufficient large swing, the vertical amplitude shows negligible effect on the BER. If the received signal swing is reduced close to the receiver sensitivity, the BER of the whole link could be determined by the signal noise ratio (SNR) of the received signal even though there is adequate horizontal timing margin. Similar to the relationship between the BER and horizontal Q-factor in Eq. (2.6), the BER is related to the SNR through the following equation [66],

$$BER = \frac{1}{2}erfc(\frac{\sqrt{SNR}}{2\sqrt{2}}).$$ (2.8)

Note that Eq. (2.8) takes place under the condition that there is a sufficient horizontal timing margin. It seems that a vertical eye opening at the RX-side can always be obtained by increasing the output swing at the TX-side. However, the enhanced inter-symbol interface (ISI), reflection, and crosstalk associated with the increased swing could overwhelm the RX-side amplitude increment and hence deteriorate the overall performance of the link. The enlarged swing also needs a higher capacitor-charging current and thus increases the power consumption. In practical designs, signal swing and equalizer scheme are often sophisticatedly selected and designed to achieve both low BER and power consumption. Offset cancellation techniques are often employed in the receiver to lower its sensitivity to reduce the minimum swing requirement as well, and hence optimize the power efficiency of the link.

2.2.3 Clock Data Recovery (CDR) Specifications

The CDR used to extract the sampling clocks and retime the transmitted data must satisfy stringent jitter specifications. Its performance is usually evaluated by "jitter
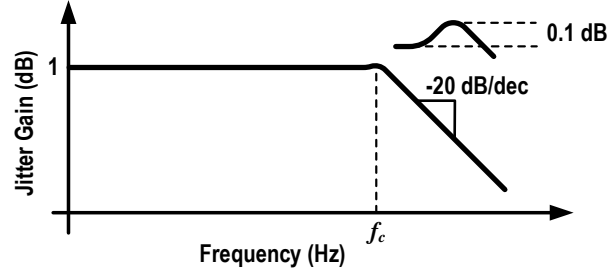
OC Level	Rate	f_c	P
1	51.84 Mb/s	40 kHz	0.1 dB
3	155.52 Mb/s	130 kHz	0.1 dB
12	622.08 Mb/s	500 kHz	0.1 dB
48	2.48832 Gb/s	2 MHz	0.1 dB
192	9.95328 Gb/s	120 kHz	0.1 dB

(a)
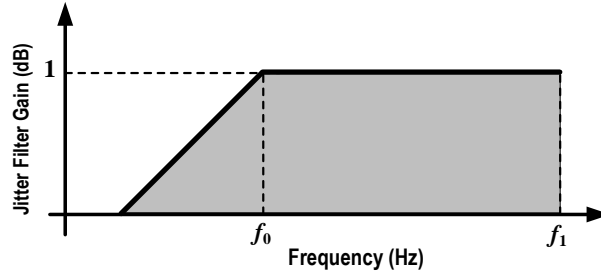
OC Level	Rate	f_0	f_1	Total Jitter
1	51.84 Mb/s	12 kHz	400 kHz	10 mUI RMS
3	155.52 Mb/s	12 kHz	1.3 MHz	10 mUI RMS
12	622.08 Mb/s	12 kHz	5 MHz	10 mUI RMS
48	2.48832 Gb/s	12 kHz	20 MHz	10 mUI RMS
192	9.95328 Gb/s	50 kHz	80 MHz	10 mUI RMS

(b)
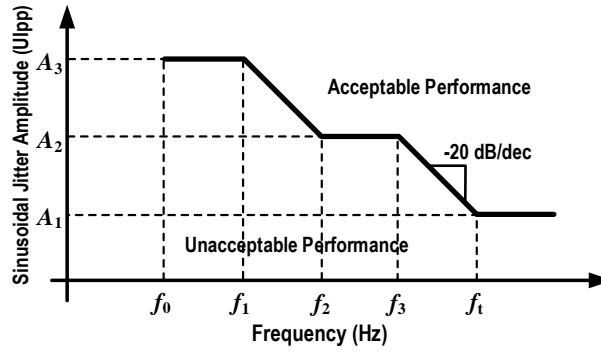
OC Level	Rate (Mb/s)	f_0 (Hz)	f_1 (Hz)	f_2 (Hz)	f_3 (Hz)	f_t (Hz)	A_1 (UIpp)	A_2 (UIpp)	A_3 (UIpp)
1	51.84	10	30	300	2k	20k	0.15	1.5	15
3	155.52	10	30	300	6.5k	65k	0.15	1.5	15
12	622.08	10	30	300	25k	250k	0.15	1.5	15
48	2488.3	10	600	6k	100k	1M	0.15	1.5	15
192	9953.3	10	2k	20k	400k	4M	0.15	1.5	15

(c)

Figure 2.5: CDR specifications of (a) JTRAN, (b) JGEN, and (c) JTOL in SONET [5].

transfer (JTRAN)", "jitter generation (JGEN)", and "jitter tolerance (JTOL)" [67, 68]. Fig. 2.5 summarizes these three metric definitions in synchronous optical network (SONET) [5].

- The JTRAN is characterized by calculating the ratio of output jitter to input jitter as a function of frequency. This metric is often used in long-haul networks employing many data regenerators. To implement reliable data communications in such cascaded systems, the JTRAN peaking of each regenerator must be sufficiently small to ensure that the output jitter after tens of successive amplifications is still acceptable. As depicted in Fig. 2.5(a), the maximum jitter peaking of the retiming regenerator in SONET must be less than 0.1 dB [5].

- The JGEN is a measure of the intrinsic jitter produced by the CDR itself when there is no jitter in the input data. It can be measured at the output of the CDR using a high-pass filter with a specific cut-off frequency. Fig. 2.5(b) gives the corner frequencies at different data rates for SONET and the maximum allowable integration rms-jitter. For different OC levels, the rms-jitter is always demanded to keep lower than 10 mUI.

- The JTOL is used to characterize the CDR jitter tacking ability, and it is defined as the maximum amplitude of the injected sinusoidal jitter that the link can tolerate without dropping below a specific BER. Fig. 2.5(c) displays the JTOL mask for SONET, which defines the minimum jitter amplitude that can be tolerated while not exceeding a specific BER at different frequencies [68].

In summary, the JTRAN, JGEN, and JTOL separately answer the following three questions: (i) how much jitter passes through the CDR from the input to the output, (ii) how much jitter is created by the CDR itself, and (iii) how much jitter can be there at the input of the CDR [68].

2.3 Basics of Electrical Serial Links

Fig. 2.6 describes a typical serial link for chip-to-chip communications. It is composed of three primary components: a transmitter, a receiver, and a channel. The main
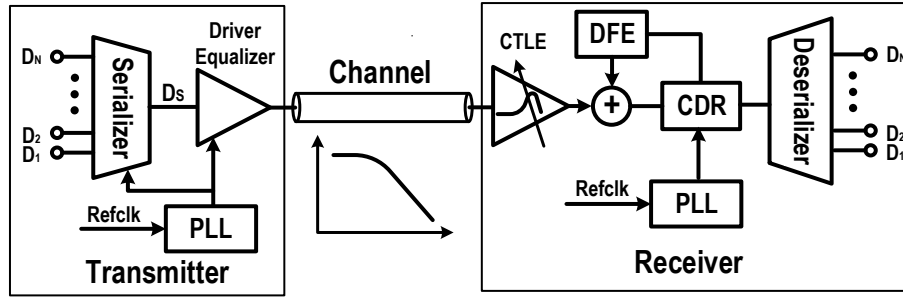
Figure 2.6: Typical serial link for wireline communications.

function of the transmitter is to convert the parallel digital data into an electrical signal and launch it on the transmission channel with a proper waveform shape such that the received signal after the lossy channel can be correctly recovered. A general transmitter (see Fig. 2.6) usually consists of a phase-locked loop (PLL), a serializer, and a combined driver-equalizer. Driven by the clocks with appropriate frequency and phase, the parallel data D_1-D_N are successfully multiplexed into a full-rate data stream D_S using the multiplexing stages in the serializer. To guarantee a robust serialization, the bandwidth and timing margin of each multiplexing stage must be sufficient. After the full-rate data streams are generated, they are applied to the combined driver-equalizer to pre-distort the output waveform and launch it into the transmission channel. The main task of the receiver located at the other end of the transmission channel is to extract the originally transmitted data from the received signal using appropriate e-qualization and clock data recovery (CDR) techniques [69, 61, 70]. A general receiver (see Fig. 2.6) usually contains a front-end equalizer, a CDR, and a deserializer. The incoming signal is firstly equalized by the front-end equalizer to obtain a sufficient vertical eye opening and an adequate horizontal-sampling margin. This equalized output is then sliced by the samplers, where the sampling position is continuously adjusted by the CDR loop. These sliced data sequences are further demultiplexed by the dese-rializer to attain the originally transmitted data D_1-D_N. The communication channel is adopted to move the serial data from the TX side to the RX side. The main problem associated with the transmission channel is the channel loss. To overcome this diffi-culty, a combination of TX-side feed forward equalization (FFE) along with RX-side continuous linear equalizer (CTLE) and decision feedback equalizer (DFE) is usually

employed, as shown in Fig. 2.6.

In the remainder of this chapter, we firstly present the clocking techniques which mainly focus on clock synthesis and distribution in Section 2.3.1. Then, the general architectures and crucial blocks of the transmitter and receiver are respectively discussed in Sections 2.3.2 and 2.3.3. Finally, Section 2.3.4 illustrates the equalization techniques for ISI cancellation.

2.3.1 Clocking Techniques

Clocking circuitry plays a critical role in modern high-speed wireline communication systems since the clock signals not only establish the flow-of-time for the downstream data processing but also provide accurate timing information for the upstream data serialization/deserialization and data transmission. The timing accuracy of the retiming clocks at the TX-side and the sampling clocks at the RX-side can directly affect the timing margin of the serial link. According to the operation functions, the clock circuitry in a serial link can be classified as clock synthesis, distribution, and recovery. This section mainly focuses on the clock synthesis and distribution while the clock recovery will be discussed in Section 2.3.3.1 together with the receiver basics.

2.3.1.1 Clock Synthesis

Clock synthesis is usually accomplished by a PLL- or delay-locked loop (DLL)-based frequency multiplier, which takes a low reference clock with low jitter to synthesize high-frequency clocks. As the source of the high-frequency clocks, any jitter at the output of the clock multiplier can be directly converted into timing uncertainty in the serial link and hence compresses the jitter budget of the whole link. Given that the numerous theoretical analyses and circuit implementations are already available for integrated PLLs and DLLs [29, 71, 72, 73, 74, 75, 76], this section does not review the design principles and implementation details. Instead, we summarize the main features and design points of these two clock synthesis schemes. Additionally, injection locking-based clock multiplier has been developed in recent years to improve the clock jitter performance. The features and challenges of this technique are also briefly intro-
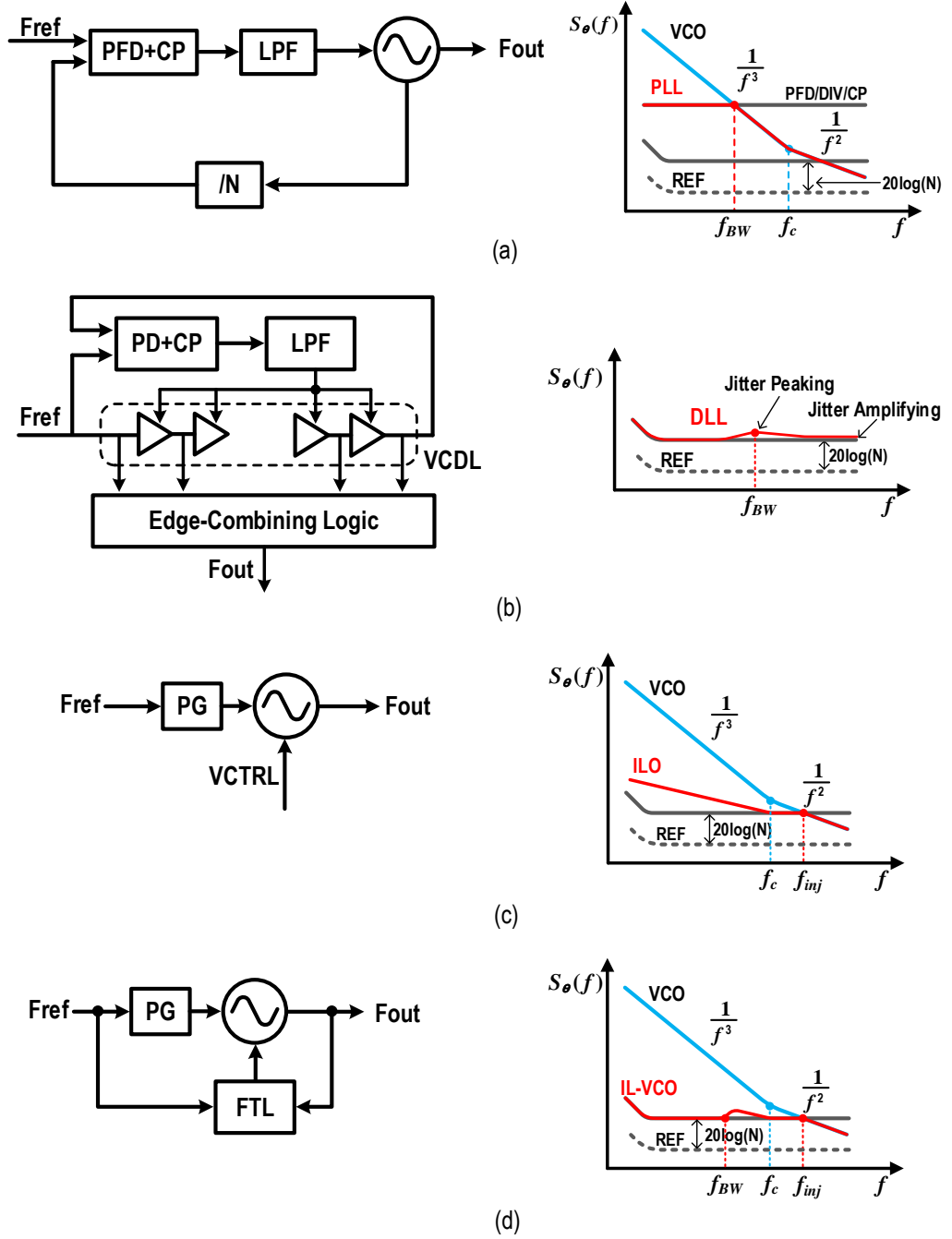
Figure 2.7: Clock synthesis implementations and phase noise performances for (a) PLL, (b) DLL, (c) ILO, and (d) IL-VCO. Here, f is the frequency of the noise, $S_\theta(f)$ stands for the phase noise spectrum, f_{BW} refers to the -3dB bandwidth of the loop, f_c denotes the corner frequency of the VCO, and f_{inj} represents the injection-locking bandwidth of the ILO.

duced in this section to give an overview of the common clock generation schemes for serial links. The details of this injection locking technique will be discussed together with the designed ring-oscillator-based injection locked clock multiplier (RILCM) in

Chapter 3. Fig. 2.7 presents the widely used clock generation techniques and their corresponding phase noise performance.

The most general method to produce high-frequency clocks from a low-frequency input is the traditional PLL [see the left diagram in Fig. 2.7(a)], due to its compact implementation, robust operation, and convenient rate configuration. It consists of a phase frequency detector (PFD), a charge pump (CP), a low-pass filter (LPF), a voltage-controlled oscillator (VCO), and a divider (DIV). The PFD is utilized to detect the phase errors between the input reference clock and the feedback divided clock, the CP is used to convert the phase errors into current pulses, the LPF is adopted to suppress the ripples on the control voltage, the VCO generates high-frequency clocks, and the divider is introduced to set the clock multiplication factor. Theoretical analyses show that the PLL acts as an LPF for the reference noise, DIV noise as well as PD noise, a band-pass filter for the CP noise, and a high-pass filter (HPF) for the VCO noise [29, 71, 72]. X. Gao *et al.* [77] proposed two useful designing criteria to minimize the PLL output jitter for a given power budget. One is spending equal power on the loop (including PFD, DIV, and CP) and the VCO. The other is setting the PLL bandwidth at an optimal value that makes the loop components and the VCO equally contribute to the total jitter. As shown in the right diagram in Fig 2.7(a), the optimal bandwidth can be approximated by the phase-noise intersects of the loop components and the VCO. The jitter performance of the PLL heavily relies on the oscillator (OSC). Different types of OSCs provide different advantages and drawbacks with respect to power efficiency, area occupation, phase noise, tuning range, and multi-phase generation. The Ring-OSC holds the advantages over the LC-OSC in terms of small area occupation, wide tuning range, and convenience of multi-phase generation, while the LC-OSC possesses the good properties of low phase noise and high power efficiency. Neither of them can satisfy all the clock synthesis requirements of small area, low power, low phase noise, and multi-phase generation. The poor phase noise of the Ring-OSC is mainly because of the device noise accumulation, while the large area of the LC-OSC is due to the involvement of the large inductor. Additionally, the phase noise of both these two OSCs degrades rapidly when the operation frequency exceeds 10

GHz. Therefore, a wide PLL bandwidth is desirable to suppress the phase noise of the VCO. However, the maximum loop bandwidth is often limited by the input reference frequency for loop stability consideration.

DLL-based clock synthesizer is one of the possible solutions to satisfy the afore-mentioned requirements [76, 78, 75, 79]. The left diagram in Fig. 2.7(b) presents its conceptional implementation, which consists of a conventional DLL and an edge com-biner. Driven by the phase detection loop, the voltage-controlled delay line (VCDL) is forced to produce equally spaced phases within a specific duration (e.g., a period of the input clock). These evenly spaced low-frequency phases are then fed into the edge combiner to produce the desired high-frequency clocks. The main advantage of this DLL-based clock synthesizer is its high jitter performance, which can be mainly attributed to that the jitter accumulation in the open-loop VCDL only lasts within a single-line delay [78]. In addition, the phase noise transferred from the the PD and CP is negligible due to the small gain of the VCDL. The right diagram in Fig. 2.7(b) presents the phase noise characteristics of the DLL-based clock synthesizer, where the accumulated phase noise associated with the VCDL and the phase noise introduced by the PD/CP are so small that can be neglected. Note that there does exist jitter amplification for the out-band frequencies although they are usually very small. Com-pared to the phase noise in traditional PLL [see the right diagram in Fig. 2.7(a)], the DLL-based synthesizer exhibits excellent jitter performance. It can be roughly ap-proximated by the reference clock jitter [75]. Another benefit of the DLL-based clock synthesizer comes from its natural stability, which manifests itself as a single-pole sys-tem. However, this architecture has three major drawbacks. Firstly , its performance is sensitive to static nonlinearities. Any phase inaccuracy of the evenly spaced clocks translates directly into duty cycle error and/or phase spacing error. This phase inaccu-racy could be either caused by the mismatches in the PD, CP, and VCDL or induced by the waveform-shape inconsistency due to an improper input waveform. These fac-tors make the DLL-based clock synthesizer fragile to fabrication mismatch and power, voltage, and temperature (PVT) variations, thus exhibiting weak robustness. Second-ly, the clock multiplication factor is difficult to program due to limited VCDL stages.

Thirdly, the additional high-speed edge combiner could significantly degrade its power efficiency. Constrained by the fragile robustness, huge power consumption, and inconvenient combining-timing control, the DLL-based clock synthesizer is difficult to reach frequencies higher than 10 GHz [80].

Injection-locked clock multiplier (ILCM) is another promising scheme to produce high-frequency multi-phase clocks with small area occupation, low power consumption, and high jitter performance [81, 82, 83, 84, 85]. It has shown great potential in serial link communications [86, 87, 88]. Fig. 2.7(c) depicts the functional diagram of the injection locked oscillator (ILO) and its phase noise suppression effect. The injection locking actually acts as a single-pole HPF system that achieves 20 dB/dec of in-band noise shaping against the intrinsic phase noise of the OSC [82, 89]. Nonetheless, this simple ILO suffers from the following three issues. Firstly, the jitter suppression is sensitive to the frequency offset between the target frequency and the free-running frequency of the OSC [81]. As the frequency deviation increases, the phase noise tracking ability will be significantly degraded while the spur increases dramatically. Therefore, the ILO should be tuned to be close to the center of the locking range for best jitter performance. Secondly, this injection locking technique cannot completely suppress the $1/f^3$ noise. This problem becomes particularly prominent for ring-OSC implemented in deep sub-micron CMOS processes because their flicker-noise corner frequencies usually reach tens of MHz [82]. Consequently, phase calibration mechanisms are needed to assist in suppressing the $1/f^3$ noise of the OSC. Thirdly, the small locking range of the ILO reduces its robustness and reliability against PVT variations. To address these issues, frequency tracking loop (FTL) is introduced to provide a proper control voltage such that the natural oscillation frequency of the VCO can always stay around the desired multiple of the injection frequency [see the left diagram in Fig. 2.7(d)]. This FTL brings in the following two benefits [83, 84]. One is that the frequency deviation between the target frequency and the natural frequency of the VCO can be optimized. This not only enhances the jitter suppression effect of the injection locking [see the right diagram in Fig. 2.7(d)], but also improves the robustness of the system since the frequency deviation can always be controlled within the locking range of the

IL-VCO. The other is the noise shaping ability which helps to suppress the in-band noise of the VCO. Combining with the 20 dB/dec low-frequency noise suppression of the injection lock, the $1/f^3$ noise of the VCO can be effectively attenuated.

2.3.1.2   Clock Distribution

Clock distribution plays an important role in modern high-speed volume-lane transceiver applications. The clock frequency can range from a few GHz to tens of GHz, and the distribution distance is able to reach several millimeters when a common clock lane is amortized across multiple data lanes [61]. Moving such high-frequency clocks over such long distances has posed significant challenges for the on-chip clock distribution [90]. Firstly, the ever-increased clock frequency has compressed the absolute jitter budget for the timing uncertainty and duty-cycle error. Secondly, the increas-
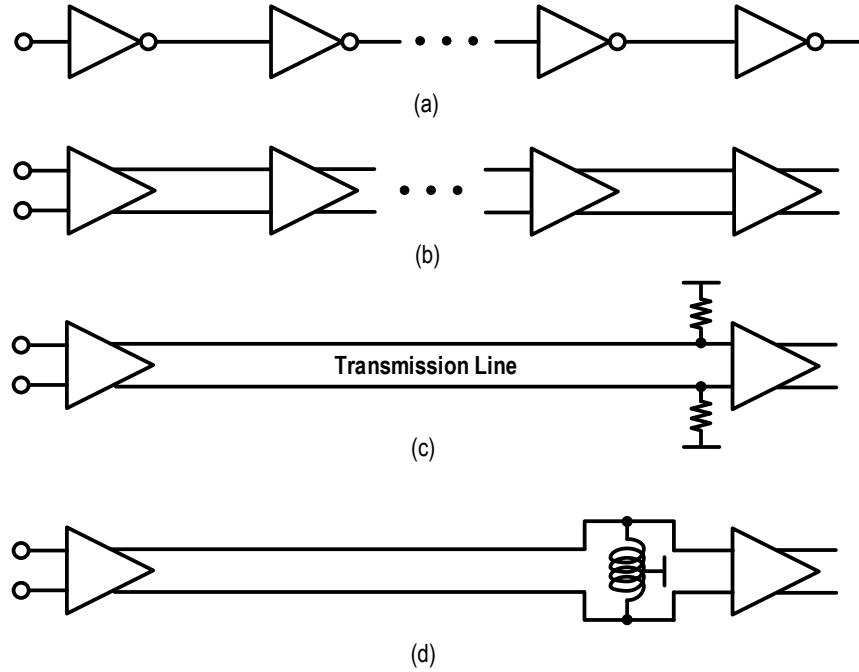
Figure 2.8: Clock distribution structures based on (a) inverter chain, (b) CML chain, (c) transmission line, and (d) inductive load.

ing distribution distance is approaching to one tenth of the "*electrical length*" of the transmission clock, thus making the connection wires exhibit transmission line characteristics. Thirdly, the parasitic resistance and capacitance have limited the bandwidth of the interconnect wires. This problem becomes even more severe when the feature

size scales downwards. The reason is that the scaled geometry could significantly increase the parasitic effects, hence degrading the bandwidth of the connection wires.

Fig. 2.8 shows the four widely used clock distribution techniques. The most traditional method is to employ a buffer chain that can be implemented by either simple inverters [see Fig. 2.8(a)] or compact CMLs [see Fig. 2.8(b)]. In these two approaches, the transmission wire is divided into several segments to optimize the desired metrics, e.g., delay time, jitter performance, and power consumption. The analysis in [91] shows that there exist optimal segment number and wire geometry for a specific distribution distance and a distinct optimization metric (delay, jitter or power). Compared to the full-swing digital inverter, the CML buffer is more suitable for high-frequency cock distribution due to the following reasons. Firstly, the propagation delay of the CML is much shorter than that of the logical inverter, since the CML can use a small swing to reduce the edge-transition time. Secondly, the CML buffer can fully exploit the process potentials as its compact NMOS driving topology naturally features fast current switching speed and small parasitic capacitance. Thirdly, the CML buffer with resistor loads has much less delay sensitivity to supply noise than inverters [92], due to its excellent power supply rejection ratio (e.g., $5\times$ in Intel 90 nm 1.2 V CMOS process). The main disadvantage of the CML is the high power consumption because it always draws a current from the supply even when the clock is not switching [61]. Considering the fact that the delay variation with respect to the supply fluctuation is mainly caused by the clock buffers rather than the transmission wires [91], minimizing the delay through the clock buffers is helpful to reduce the delay susceptibility of the clock network to the power-supply noise.

Fig. 2.8(c) shows a repeaterless clock distribution network, which usually employs an open-drain CML buffer to drive the terminated on-chip transmission lines [see Fig. 2.8(c)]. The measurement results in reference [92] demonstrate that a 10 GHz global clock can be transmitted nearly 3 mm using an open-drain buffer to drive a pair of differential transmission lines with on-chip terminations. The delay of the transmission line is the smallest due to its speed-of-light propagation velocity. For the characteristic impedance, it is not necessary to design exactly 100 Ω as long as it matches with the

far-end terminations. In practice, large characteristic impedance is preferred, because it not only improves the ratio of the impedance to the metal resistance, but also saves the power of the driving CML buffer by reducing the driving current. Nonetheless, the characteristic impedance is limited by the parasitic capacitance per wire length. The design in [91] shows that a 120 Ω differential characteristic impedance can be achieved by adjusting the metal geometry parameters such as metal layer, width, and spacing. Due to nonnegligible resistance of the transmission line, it exhibits a limited bandwidth and hence causes random jitter and duty-cycle distortion amplifications during clock transmission. The analysis in [61] indicates that these amplification effects increase very rapidly while the clock frequency exceeds the effective bandwidth of the transmission line. Note that the main issue associated with the clock distribution line is its large capacitive loading, many researchers have proposed to adopt an LC resonance-based clock distribution to neutralize this capacitor [93, 94, 95]. As shown in Fig. 2.8(d), the introduced differential spiral inductor and the parasitic wire capacitance actually constitute an LC tank. Owing to the characteristics of energy cycling and impedance peaking within the LC resonance [93], this clock distribution scheme exhibits great potential on power reduction and clock jitter suppression [94, 95]. It is worth noting that the quality factor Q of the on-die inductor does not play a key role in this clocking network, since the resistance of the long wire has dominated the Q of the LC tank [91]. Consequently, a compact multi-layer inductor can be used to save die area. Since the impedance of the LC tank shows a frequency selection characteristic, it is not suitable for the applications that need to support a wide operation range.

2.3.2 Transmitter Techniques

2.3.2.1 Driving Mode

According to driving mode, the output stage of the transmitter can be mainly divided into current-mode logic (CML) and source-series terminated (SST) drivers. Fig. 2.9(a) shows the implementation details of a typical CML driver, which consists of a differential pair, a pair of resistive loads, and a tail current. Compared to the SST driver described in Fig. 2.9(b), it poses the good properties of high-speed switch-
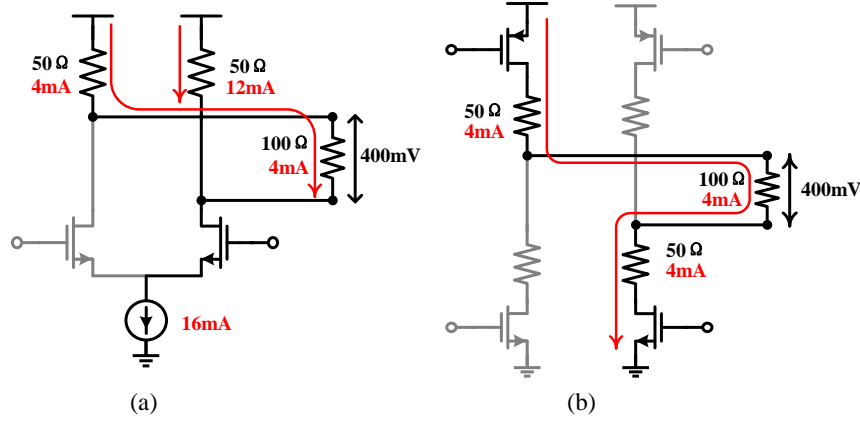
Figure 2.9: Typical transmitter driver modes. (a) CML mode and (b) SST mode.

ing, adjustable output swing, good impedance matching, and convenience to integrate peaking inductors [96, 97]. These features endow it with the capability of exploiting the maximum process potential, thus making it more suitable for cutting-edge drivers that operate at tens of Gb/s. Recently, 50-64 Gb/s transmitters using CML drivers have been implemented in 65 nm CMOS process [24, 25, 26]. The SST driver evolves from traditional CMOS inverter, where 50 ohm resistors are inserted in each branch to reduce the impedance discontinuities and thus optimize the reflections. The SST driver demonstrates a high power efficiency, which only consumes one fourth of that of the CML driver (see Fig. 2.9). The symmetrical topology makes it compatible with all of the low, high, and mid common-mode terminations. Nonetheless, the large self-load capacitances, slow PMOS transistors, and incompatibility with bandwidth-extension inductors have limited its maximum operation speed. These factors of the SST driver make it popular in power-sensitive high-volume designs using advanced process with adequate speed margins. For examples, a 28 Gb/s SST transmitter has been fabricated in a 32 nm CMOS [98] and a 16-40 Gb/s NRZ/PAM4 dual-mode transmitter utilizing SST driver has been implemented in a 14 nm CMOS [99].

2.3.2.2 Multiplexing Scheme

The serializer usually utilizes a multiplexing tree to combine the low-speed parallel data into a high-speed stream. Each multiplexing stage is composed of a multiplexer (MUX) and several latches, where the latches are placed before the MUX to guarantee
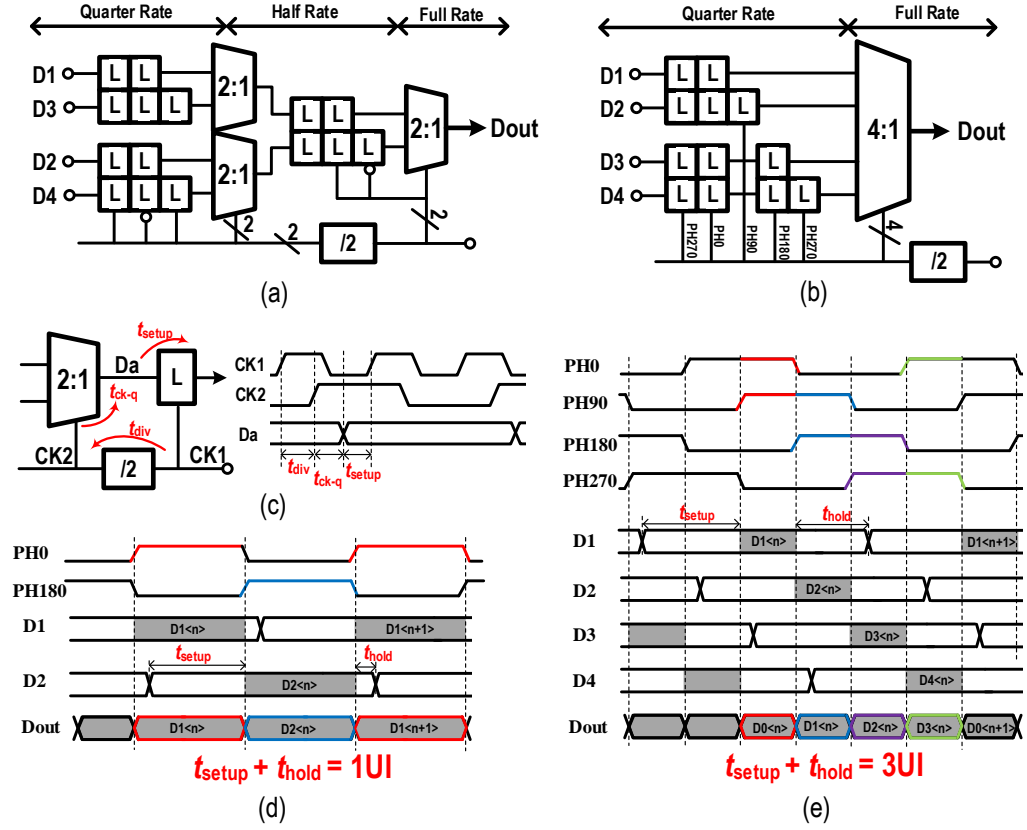
Figure 2.10: Schemes of the final 4:1 multiplexing. (a) Half-rate topology based on two-stage 2:1 MUXs, (b) quarter-rate structure based on direct 4:1 MUX, (c) critical path and timing diagram of the 2:1 MUX, (d) timing margin of the 2:1 MUX, and (e) timing margin of the 4:1 MUX.

sufficient timing margin for the following data selection and/or data sampling. These timing constraints have posed significant challenges for the high-speed serialization in the last few stages. According to the ratio of the data rate to the maximum clock frequency, the transmitters can be partitioned into half-rate architecture and quarter-rate architecture. Fig. 2.10 describes the conceptional implementations and timing requirements of the two typical multiplexing schemes.

For the half-rate architecture, the final 4:1 multiplexing is implemented by three 2:1 MUXs, where two of them work in quarter rate and the final one operates at half rate [see Fig. 2.10 (a)]. This serialization topology is ubiquitously used mainly owing to its simple clocking scheme, which only requires a pair of complementary clocks to alternatively select the input data. The pulse width of the MUX output is subject to the duty cycle of the driving clocks, thus a 50% duty cycle is required. In practical designs, a duty cycle correction circuit is usually employed to guarantee the desired duty cy-

cle. The main drawbacks of this architecture are the tight timing constraints and large number of latches (15 for the 4:1 serialization). Fig. 2.10 (c) and (d) displays the two possible critical paths. One is located at the first latch in the final 2:1 MUX, where the summation of the delay of the divider (by 2), the ck-to-q of the previous 2:1 MUX, and the setup time of the latch must be smaller than 1 unit interval (UI). The other occurs at the final 2:1 MUX, where the data selection margin [i.e., $t_{setup} + t_{hold}$ in Fig. 2.10(d)] is only 1 UI. When the data rate reaches several tens of Gb/s, it becomes a nontrivial task to satisfy these timing requirements. The delay variations along with different PVT corners make this problem even more challenging. To overcome this difficulty, traditional half-rate transmitters often insert extra delay matching buffers [27, 24] or phase calibration loops [100, 33, 26] between CK1 and the latch [see Fig. 2.10(a)]. For the former method, the delay fluctuation between the multiplexing path and the matching buffer may beyond 1 UI and thereby causes bit errors. For the latter approach, the automatic phase adjusting suffers from the accuracy of phase detection, which could reduce the stability, reliability, and robustness of the serializer. Additionally, both of these two techniques involve substantial power and area overheads.

For the quarter-rate architecture, the final 4:1 multiplexing is performed by a single 4:1 MUX, where the input data operate at the quarter rate [see Fig. 2.10 (b)]. This serialization structure has attracted increasing attentions to the applications beyond 10 Gb/s. This is because it not only addresses the timing issues in traditional 2: 1 MUX by removing the critical path in Fig. 2.10(c) and relaxing the data-selection margin from 1UI [see 2.10(d)] to 3 UI [see Fig. 2.10(e)], but also saves substantial power by halving the maximum clock speed and removing the half-rate latches [see Fig. 2.10(e)]. However, these benefits come with the penalty of a doubled self-drain capacitance, which dramatically degrades the bandwidth of the 4:1 MUX, hence limiting its maximum operation speed. Another difficulty associated with this 4:1 MUX is how to generate the evenly 90°-spaced multi-phase clocks and produce the UI-spaced input sequences for the data selection. Both of these issues are addressed in this thesis, which will be detailed in Chapter 4.
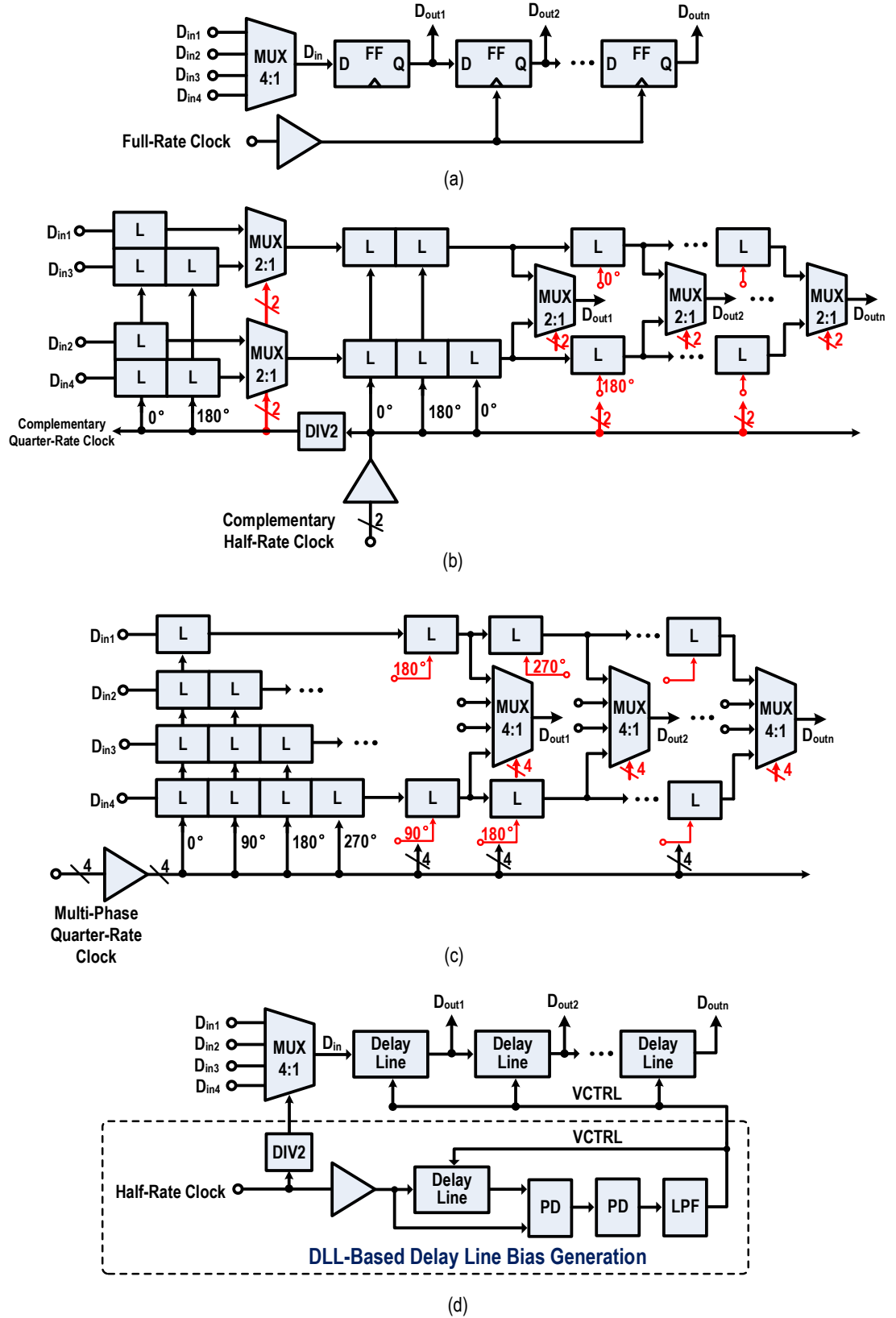
Figure 2.11: Techniques of 1-UI delay generation based on (a) full-rate FF, (b) half-rate 2:1 MUX, (c) quarter rate 4:1 MUX, and (d) analog delay line.

2.3.2.3 1-UI Delay Generation

TX-FFE, which performs as a finite impulse response (FIR) filter and pre-distorts

the transmitted signal, is one of the most common techniques that is employed in high-

34

speed serial links to alleviate the ISI caused by the frequency-dependent channel loss. In practical designs, the FIR taps are usually driven by full-rate 1 UI-spaced sequences. To accommodate the exponentially growing data rate, the 1 UI delay generation techniques have also evolved. Fig. 2.11 summarizes the mainstream 1 UI delay generation techniques utilized in previous FFE implementations.

The most general method is to utilize flip-flops (FFs) driven by a full-rate clock to sequentially retime the serial data stream [see Fig. 2.11 (a)]. The main advantage of this approach is its compactness, which only requires one FF for each tap sequence generation. As the data rate exceeds the maximum reliable operation rate (e.g., 10 Gb/s for 65 nm CMOS [101]) of the FFE, the full-rate structure inevitably consumes substantial power because every single block in it has to be realized in power-hungry CML. Constrained by the ck-to-q delay, this FF-based 1 UI delay generator even with CML topology fails to operate beyond 24 Gb/s in 65 nm CMOS process [34]. Another drawback of this structure is that it needs a sophisticated full-rate clock tree to drive the heavy loads of these retiming FFs, which results in considerable power consumption and area occupation. The stringent full-rate timing requirement can be relaxed by half-rate structure based on 2:1 MUX or quarter-rate architecture based on 4:1 MUX [see Fig. 2.11(b) and (c)]. As discussed in [101], the half-rate structure in 65 nm CMOS running at 20 Gb/s saves 12 mW (50%) of power in contrast to its FF-based counterpart. Compared to the half-rate structure, the quarter-rate architecture further relaxes the critical path timing margin from 1 UI to 3 UI and halves the maximum clock speed, thus showing more potentials in cutting-edge transceiver designs.

As the data rate approaches to the delay of a single buffer, the desired 1 UI delay can also be produced by analogy delay line [see Fig. 2.11(d)], where a DLL-based bias generator is often integrated to adaptively tune the control voltage of the delay line [102]. The delay cell can be implemented in LC-cells [24] or CML-buffers [103]. Nonetheless, these techniques suffer from either a penalty of large area occupation (LC cells) or a cost of huge power consumption (CML buffers). Additionally, the delay produced by the analog delay line is susceptible to PVT variations, power fluctuation, and substrate noise. Moreover, the limited adjusting range makes this technique only
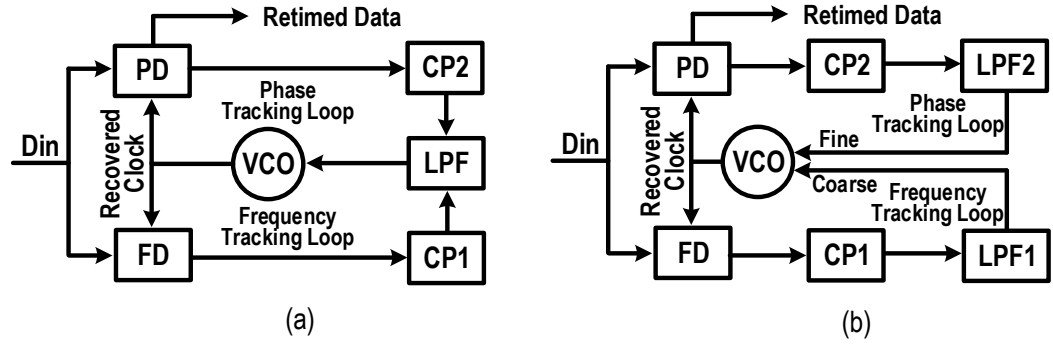
Figure 2.12: CDR topologies without a reference. (a) Single control of VCO frequency tuning and (b) coarse and fine control of VCO frequency tuning.

suitable for narrow range applications [104]. As an example, the design in [16] demonstrates that the power consumption for each tap in the LC-cell delay line-based FFE is about 12 mW, which is much lower than that (48 mW) implemented in multi-MUX-based FFE. On the other hand, it cannot support the speed below 50 Gb/s and occupies a whole area of 1.2 mm^2 which is one time larger than that based on multiple MUXs in [104, 105].

2.3.3 Receiver Techniques

2.3.3.1 CDR Architectures

Nowadays, modern CDR design mainly uses a dual-loop architecture consisting of a frequency tracking loop (FTL) and a phase tracking loop (PTL), where the FTL is in charge of frequency capture, and the PTL is responsible for phase position adjustment [106]. According to whether or not an external reference clock is needed, CDRs can be categorized into reference-less CDR and reference CDR. The frequency information in the former one is extracted from the received random data through a frequency detector (FD), while the latter one utilizes a traditional PLL to pull the VCO oscillation frequency to the target value. The common feature of these two topologies is to integrate a similar PTL with a dedicated phase detector (PD) to finely adjust the sampling position of the recovered clock to the mid-point of the incoming data.

Reference-less CDR- Reference-less CDRs arise from the applications where the use of an external crystal is not feasible [107]. One example is a repeater for either optical

or copper media in which the space and number of pins are severely limited to include an external crystal oscillator. Additionally, adding a low-noise, rate-adjustable crystal could increase the overall cost and complexity of these receivers [108].

Fig. 2.12(a) depicts a CDR without a reference clock, where the currents generated by both the FTL/CP1 and PTL/CP2 are applied to a common LFP to produce the control voltage of the VCO [109]. During either CDR startup or loss of phase lock, the FD plays a key role to generate a control voltage through the CP1 and LPF to coarsely tune the VCO oscillation frequency towards the input data rate. When the frequency difference between the VCO and the input data falls into the capture range of the PTL, the PD takes over to finely adjust the control voltage through the CP2 and LPF, thus making the VCO output clock coincide with the input data phase [110]. There are two possible issues associated with this CDR architecture. Firstly, the FTL and the PTL may potentially interfere with each other when the voltage control is transferred from the FD to the PD, resulting in prominent ripples on the VCO control line that could even lead to a phase-lock failure [111]. Secondly, the FD could become momentarily confused about the actual input data rate if the received input data contains random consecutive identical digits or if the received rising and falling edges are corrupted by the channel loss or electromagnetic crosstalk. To mitigate the effects of these two issues, the loop bandwidth of the FTL is often chosen to be much smaller than that of the PTL so as to reduce the noise contribution from the FD for ensuring the clock quality of the VCO [111]. Meanwhile, a CDR bandwidth proportional to the data rate is required to satisfy the protocol specification. To independently optimize the bandwidths of the FTL and the PTL, separate LPFs are adopted in the two loops [see Fig. 2.12(b)], where the line voltages generated by the FTL and PTL respectively drive the coarse control and fine control of the VCO [110]. The main drawback of this architecture is it requires a larger area due to the presence of the two LPFs. To alleviate this area overhead, a hybrid analog/digital loop filter is developed in [112].

Reference CDR- Fig. 2.13 summarizes the main CDR topologies with a reference in which a traditional PLL is embedded to initially adjust the VCO oscillation frequency. Fig. 2.13(a) displays the dual-VCO architecture, which uses the conventional PLL
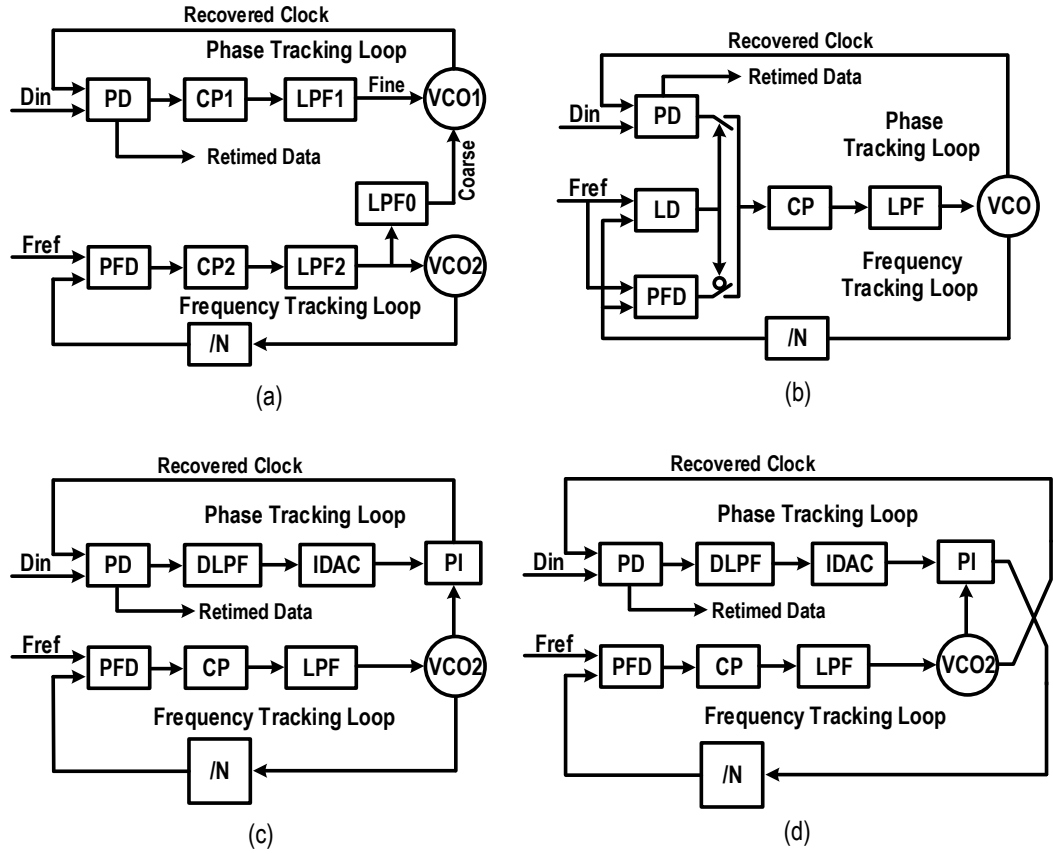
Figure 2.13: CDR topologies with a reference. (a) Dual VCO architecture, (b) sequential locking topology, (c) PI-based structure, and (d) variant of PI-based structure.

to lock the output clock phase of the VCO2 to that of the input frequency [113]. By applying the control voltage of the VCO2 in the PLL to the replica VCO1 through an additional LPF0, the oscillation frequency of the VCO1 should be very close to or equal to the target value. The remaining frequency offset as well as the output clock phase error with respect to the input data is finely tuned by the PTL. To accomplish a fast lock acquisition and maintain a fine control of the VCO1, the slew rate of the FTL should be higher than that of the PTL while the bandwidth of the FTL must be lower than that of the PTL. On one hand, the physical separation of the FTL and the PTL makes it easier to meet the lock-acquisition, loop stability, and tracking bandwidth requirements. On the other side, there are two possible problems associated with this CDR architecture. One is the mismatch between VCO1 and VCO2, which may lead to a difference in oscillation frequency even though the two VCOs share one coarse control voltage. The other is the frequency pulling between the two VCOs in asyn-

chronous systems. Specifically, the data rate in an asynchronous system often allows certain frequency offset between the transmitted data and the local clock frequency. The frequency pulling could make the output frequency of VCO1 shift away from the incoming data rate and towards N×Fref. This could be especially problematic when a spread spectrum clock is required since the pulling phenomena may make the output frequency of VCO1 unchange with its fine control input. Another issue associated with this CDR is the area overhead, especially in case of adopting an LC-VCO. To address the pulling issue and reduce the area overhead, a sequential locking scheme is proposed in [102, 114] to remove the needs of the dual CPs, LPFs, and VCOs. This CDR is presented in Fig. 2.13(b), which utilizes a lock detector (LD) to rotationally enable the FTL and the PTL by continuously monitoring the frequency locking state. During the CDR startup, the FTL is firstly selected to tune the control line of the VCO to pull the oscillation frequency towards the target frequency N×Fref. If the LD detects that the divided clock of the VCO output is locked to the Fref, it disables the FTL loop and enables the PTL. When there is a loss of frequency locking, the LD will swap the PTL to FTL to engage a lock recovery. One potential problem in this topology is that the transition from the FTL to the PTL may disturb the VCO control voltage and therefore causes a VCO frequency shift. Once the frequency shift is beyond the capture range of the PTL, a failure of phase lock could happen [111].

Fig. 2.13(c) presents another typical reference CDR based on phase interpolator (PI) [14, 115]. The conventional PLL is adopted to provide multi-phase clocks with a frequency of N×Fref that is very close or equal to the incoming data rate. These clocks are further rotated by a PI driven by the PTL to make the phase of the recovered clock lock to that of the input data. The availability of high-frequency clocks endows that this architecture possesses the good properties of faster phase acquisition, increased system stability, and less jitter peaking. It is worthy to note that jitter peaking in PI-based CDR is absence only when the PTL is a first-order loop and the loop latency is not significantly larger than the phase update period. This is because the fast changing jitter may have already reversed its direction by the time the updating phase code reaches the PI [116]. Additionally, the physical separation of the FTL and the PTL makes it easier
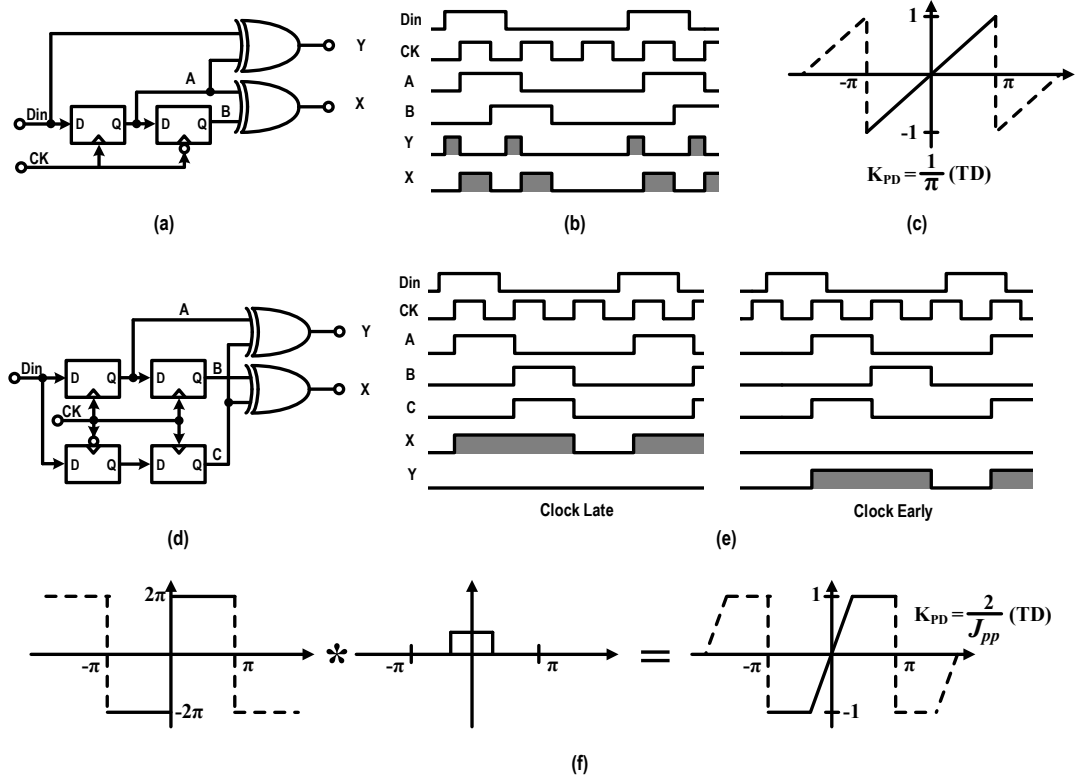
Figure 2.14: Two typical CDR PDs. (a) Hogge PD implementation, (b) Hogge PD detection mechanism, (c) Hogge PD gain, (d) Alexander PD implementation, (e) Alexander PD detection mechanism, and (e) Alexander PD gain.

to satisfy the loop bandwidth and stability requirements. This separation also allows the clock lane consisting of PLL and bias generator to be shared by multiple data lanes, thus making it a popular architecture in parallel-lane applications. Another advantage of the PI-based CDR is the complete digital implementation of the loop filter, which leads to smaller area occupation and fewer effects from PVT variations. The primary problem along with this CDR is the discrete updating phase steps, which may result in prominent cycle-to-cycle jitter. The steady-state oscillation existing in the digital PTL could make this impact even more severe, especially when the loop latency is large. To smooth out the discrete phase steps, the PI-based CDR evolves into the structure shown in Fig. 2.13(d), where the feedback clock and recovered clock respectively applied to the divider and the sampler in the PD are swapped. The primary advantage of this evolved CDR is that the discrete phase shift in the PI can be smoothed out by the LPF in the FTL, which provides a smooth phase shift in the PTL. However, it requires an FTL in each receiver lane, thus making it not suitable for multilane applications.

2.3.3.2 CDR Phase Detector

The main functions of the PD in CDR systems are to compare the phase difference between the input data and the recovered clock, provide information to adjust the sampling position, and simultaneously retime the incoming serial signal. Fig. 2.14 summarizes the implementations and behaviors of the widely used liner Hogge PD and non-linear Alexander PD [i.e., bang-bang PD (BBPD)].

Fig. 2.14(a) and (b) describes the implementation and operation waveforms of the Hogge PD. The phase differences between the input data and the recovered sequence are converted to high pulses [see signal X in Fig. 2.14(b)] by the top XOR. Meanwhile, the reference pulses [see signal Y in Fig. 2.14(b)] that equals a half of the clock cycle is produced by XORing the recovered sequence and its half-clock-cycle delayed version. Taking the width difference of X and Y as the PD output, the phase error between the optimal sampling position (i.e., lagging the data transition a half of a clock cycle) and the rising edge of the recovered clock can be obtained. Fig. 2.14(c) gives the phase transfer characteristics, and its PD gain can be given by,

$$K_{PD} = \frac{1}{\pi}(TD)\ (unit\ of\ radian^{-1}), \tag{2.9}$$

where TD is the transition density. The main advantage of the Hogge PD is that it provides both sign and magnitude information of the sampling phase error, which allows to construct a linear feedback loop. On the other hand, there also exist several imperfections in the Hogge PD. Firstly, the ck-to-q delay of the first data-sampling FF widens the pulse width of signal Y, but doesn't impact that of signal X, thus causing a skew of ΔT (i.e., the ck-to-q delay of the FF) when the CDR loop is locked. This skew effect becomes a serious issue at high speeds since ΔT can occupy a significant fraction of the clock period. The resulting phase offset may exceed several tens of degrees, thus degrading the sampling phase margin and finally deteriorating the jitter tolerance. This phase shift can be compensated by either narrowing the proportional pulses or widening the reference pulses through inserting proper dummy delay element [67]. Nonetheless, the delay introduced by the dummy element may not track the FF

delay well against PVT variations. Another drawback of the Hogge PD stems from the half-cycle shift between the two XOR outputs [see Fig. 2.14 (b)], where the reference pulse is after the proportional pulse. This phase shift makes the CP driven by the Hogge PD create tri-wave currents and hence generate ripples on the VCO control line, which could severely disturb the VCO output phase. This tri-wave issue can be ameliorated by introducing two additional reference pulses at a cost of one more full-rate latch and two more power-hungry XOR gates [117]. Finally, the output pulses of the Hogge PD are approximate to a half of the bit period, which demands extremely high-speed XOR gates to generate these narrow pulses. Combining with the complex implementation of the XOR, the Hogge PD could become the speed bottleneck of the whole CDR. As a consequence, the Hogge PD is suitable for CDR designs with a low to moderate data rate, where a sufficient margin can be guaranteed for the narrow pulse generation.

Fig. 2.14(d) describes the implementation of the BBPD. It utilizes three data samplers driven by three consecutive 180°-shifted clocks along with two XOR gates to determine whether the clock leads or lags the data when there is a data transition. In case that there is no data transition, the outputs of the three samplers are identical and hence the outputs of the two XORs remain at "0s". In presence of a data transition, the BBPD produces the signals of early Y and late X by XORing the edge sample with its previous data and following data, respectively. Fig. 2.14(e) illustrates the waveforms under the two possible locking conditions, namely, clock Late and clock Early. The BBPD only outputs the sign information of the phase error in the form of an early or late pulse with a fixed width, thereby its gain is ideally infinite at zero phase error [see the left diagram in Fig. 2.14(f)]. However, this gain can be linearized by the metastability of the samplers, the time uncertainty of the input data, and the jitter of the edge-sampling clocks. Previous studies [118, 119, 120] have demonstrated that the overall phase transfer function of the BBPD in practical CDRs can be obtained by convoluting the ideal PD transfer function with the probability density function (PDF) of the total jitter [see Fig. 2.14(f)] and its gain can be approximated as,

$$K_{PD} \approx \frac{2}{J_{PP}}(TD) \; (unit \; of \; radian^{-1}), \tag{2.10}$$

where TD is the transition density, and J_{PP} denotes the peak-to-peak jitter (including the sampler metastability, input data jitter, and edge-sampling clock jitter). The binary quantization of the BBPD has simplified the phase comparison, which utilizes the recovered data and quantized edge sequences to extract the early/late signals. Compared to the linear Hogge PD that needs to process pulses no wider than a half of the bit period, the minimum pulse width involved in this nonlinear BBPD equals the bit period. Hence, it is able to support an even higher data rate. By replacing the XORs following the full-rate samplers with a group of parallel XORs after the demultiplexer, the operation speed of the BBPDs can be further reduced to normal digital logic speed. Unlike the traditional liner PD whose outputs gently toggle around zero, the outputs of the BBPD exhibit abrupt toggling between the two states of '1' and '0'. On one hand, the abrupt toggling may introduce larger disturbances on the control voltage line of the VCO-based CDRs. On the other hand, the complete digital operation renders it more convenience to implement digital CDRs.

2.3.3.3   Clocked Compactor

The basic function of the clocked compactor is to sample and resolve the input signal to binary '0' or '1' at each rising edge of the driving clock. The output is determined by the polarity of the sampled instantaneous value compared to a specific reference (e.g., zero for the NRZ modulation). Unlike the digital latches which can be described by the setup time, hold time, and latch delay, the sampling latches in analog application are usually characterized by their sensitivity and bandwidth [121, 6]. To obtain correct bit streams from the attenuated noisy analog input, samplers with high timing precision and high input sensitivity are badly demanded.

Fig. 2.15 summarizes the two most popular samplers, which are based on CML-type latch and Strong-Arm latch, respectively. To convert the analog input to logic output, the CML-latch-based clocked compactor requires two CML latches and one CML2CMOS converter [see Fig. 2.15(a)] while the Strong-Arm-based counterpart only needs one Strong-Arm latch and one RS latch [see Fig. 2.15(b)]. Fig. 2.15(c) and (d) respectively displays the latch sensitivity function and latch transfer function for
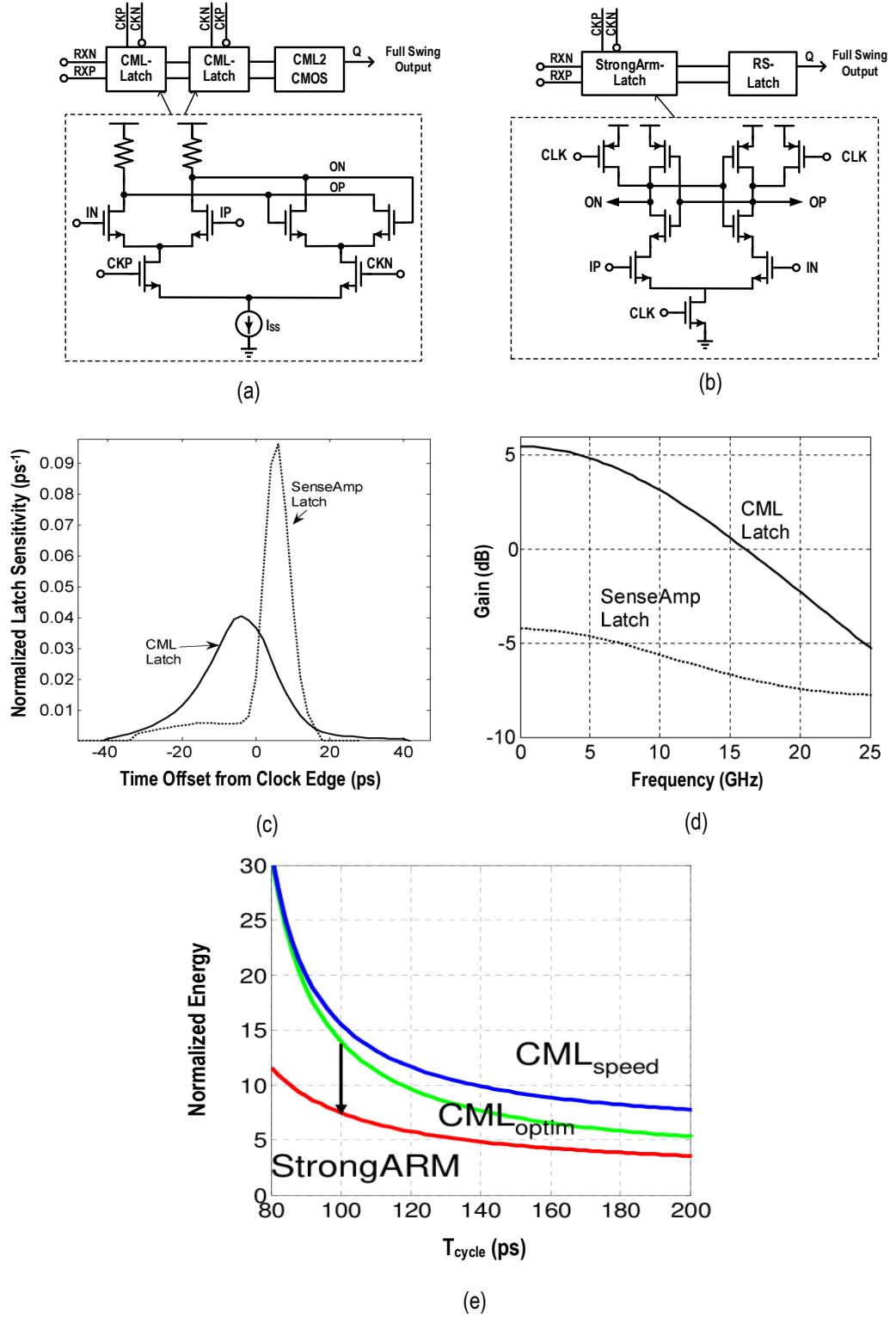
Figure 2.15: Clocked compactors. (a) CML-type latch-based compactor, (b) Strong-Arm latch-based compactor, (c) latch sensitivity function comparison [6], (d) latch transfer function comparison [6], and (e) energy consumption comparison [7].

the two clocked compactors in Fig. 2.15(a) and (b) [6]. Referring to the discussion in

[6], the following conclusions can be made: (i) the sensitivity window of the Strong-

Arm latch is smaller than that of the CML-type latch, meaning that the Strong-Arm latch shows better time resolution ability, (ii) the DC gain of the CML-type latch exhibits 10 dB more than that of the Strong-Arm latch, implying that the CML-type latch exhibits a high sensitivity, (iii) the gain-bandwidth product (GBW) of the CML-type latch is higher than that of the Strong-Arm one, indicating that the CML-type latch is more suitable for high-speed design. Fig. 2.15(e) describes the normalized energy comparison between the aforementioned two compactors, where the Strong-Arm latch always demonstrates a better power efficiency [7]. In practical designs, although Strong-Arm latches provide narrow sensitivity window and dissipate less power, CML latches are usually used in ultra high-speed receivers because of their large GBW, superior sensitivity (high gain), and high immunity to power fluctuation. Additionally, the CML-type latch possesses a superior convenience to integrate on-chip inductors to further extend its bandwidth.

2.3.3.4 Phase Interpolator

Phase interpolation can be performed by either a direct multiple-input PI [see Fig. 2.16(a)] or two coarse phase Muxes followed by a two-input phase mixer [see Fig. 2.16(b)]. Fig. 2.16(c) and (d) presents the two typical PI implementations based on inverters [12, 13] and CML buffers [14, 15], respectively. As shown in Fig. 2.16(b), by introducing a phase-selection Mux before the phase mixer, the input devices of the phase mixer can be reduced, thus optimizing the output bandwidth. However, the forward coupling through the overlap capacitances of the input devices could cause discrete phase jumps when the selected phase is updated in the Mux [11]. In contrast, the direct phase mixer [i.e., PI in Fig. 2.16(a)] can effectively avoid these discrete phase jumps since the forward coupling paths are always present between the input phases and the output regardless of the phase swapping [61]. Previous work has demonstrated that the direct PI [see Fig. 2.16(a)] is reasonable for four-phase mixing [8, 115, 9] while the Mux-based two-stage PI [see Fig. 2.16(b)] is more suitable for six/eight-phase interpolation. [10, 11, 61].

To keep the common voltage of the interpolated clock to be constant, linearly ad-
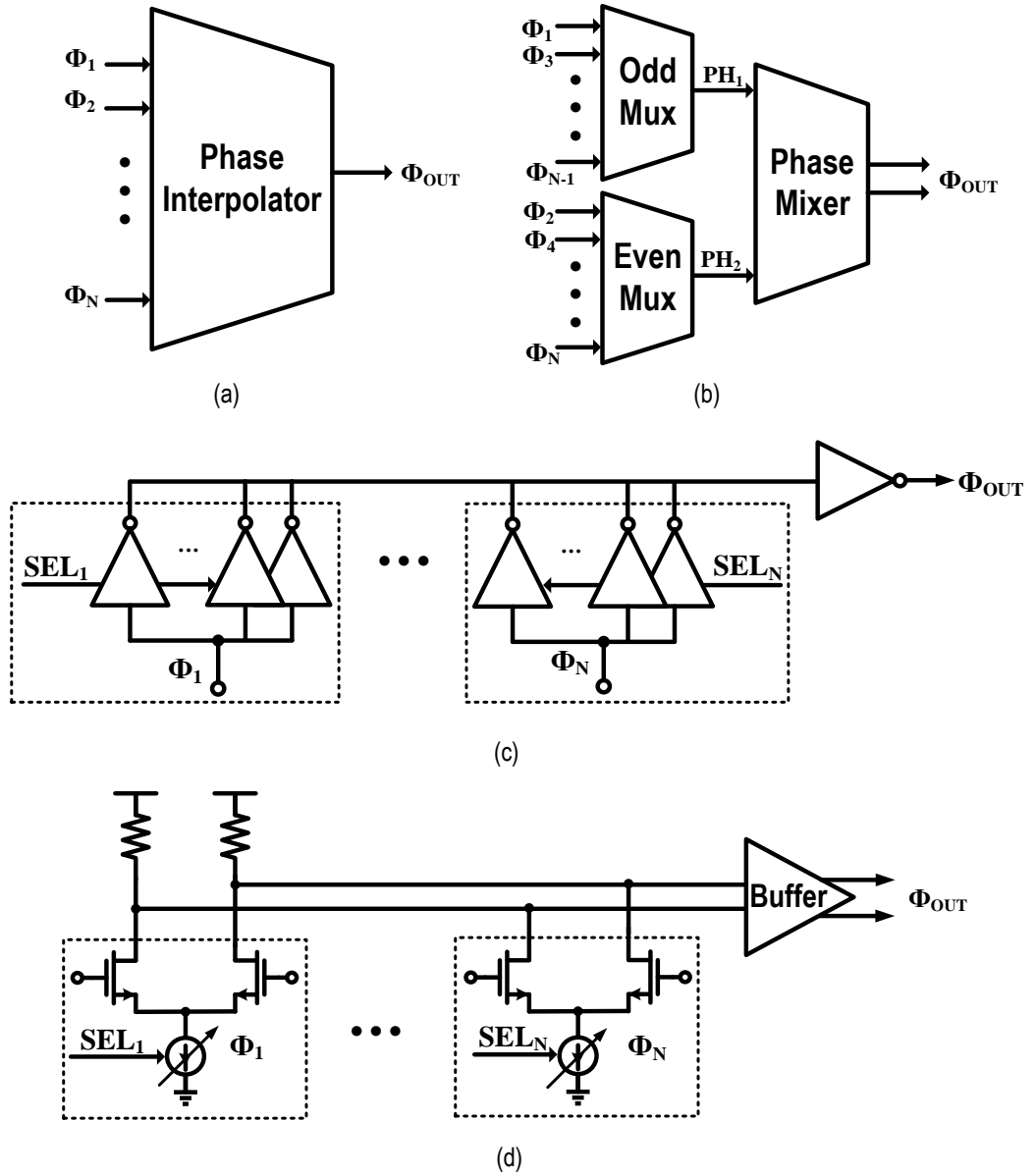
Figure 2.16: PI structures and implementations. (a) Structure with direct multiple-input phases [8, 9], (b) structure with coarse phase selection followed by a phase mixer [10, 11], (c) inverter-based implementation [12, 13], and (d) CML-based implementation [14, 15].

justing the weights of the two adjacent phases is usually employed in practical designs. For an ideal multiple-input PI, the input clocks should share an equal phase spacing between any two adjacent phases. Correspondingly, the interpolated output clock can be represented by,

$$CK_{PI}^{ideal} = A_{PI}e^{j\varphi_{PI}^{ideal}} = A_{PI}e^{j(\psi_{i+1}-\psi_i)\cdot m/K}, \psi_{i+1} - \psi_i = \frac{2\pi}{N}, \qquad (2.11)$$
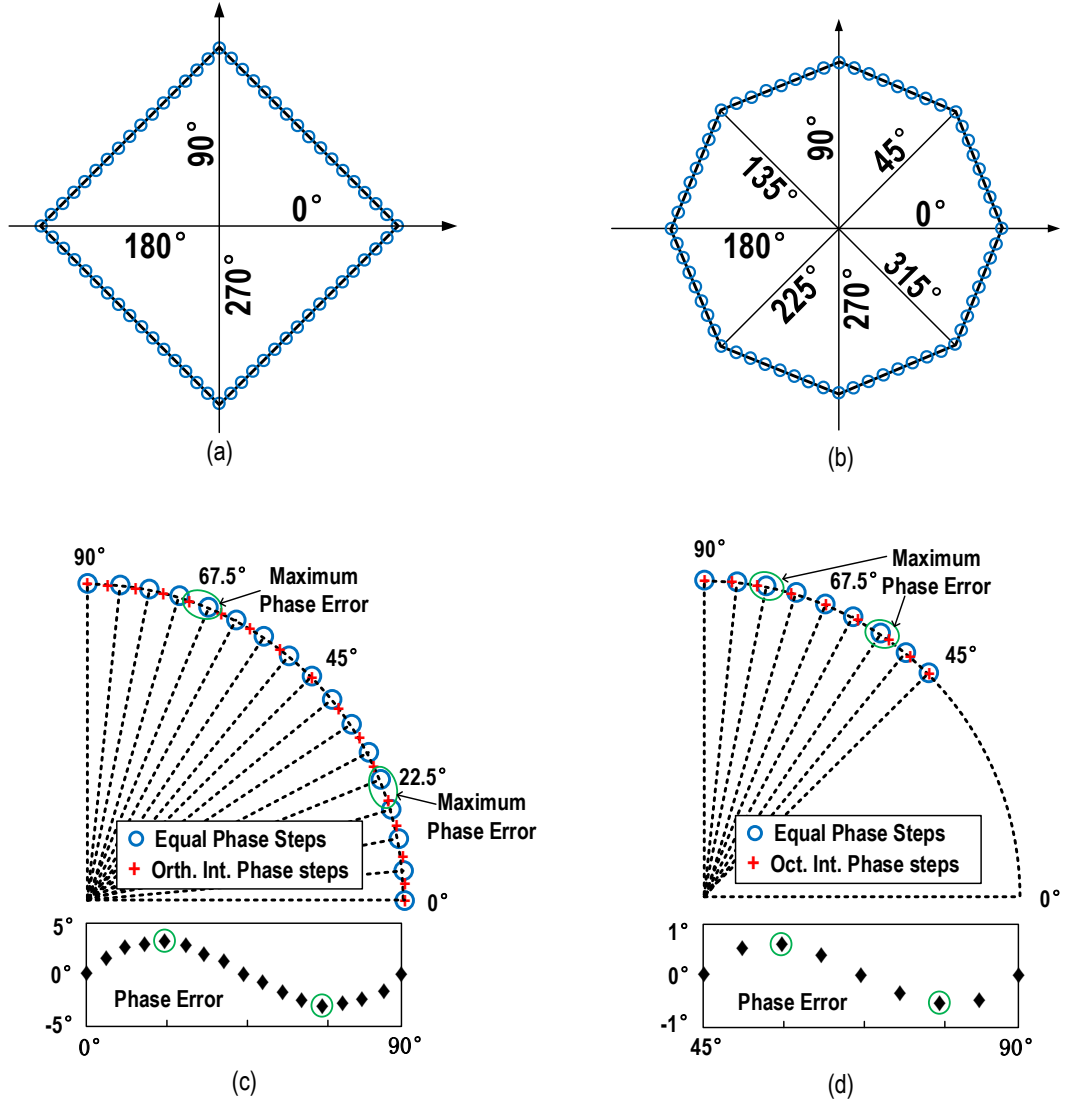
Figure 2.17: (a) Phase constellation for quadrature PI, (b) phase constellation for octagonal PI, (c) interpolated phase steps for quadrature PI in one quadrant, and (d) interpolated phase steps for octagonal PI in one octant.

$$\varphi_{PI}^{ideal} = \frac{(\psi_{i+1} - \psi_i) \cdot m}{K} = \frac{2\pi \cdot m}{KN}, \tag{2.12}$$

where N is the input phase number, A_{PI} denotes the interpolated clock amplitude, K stands for the total steps between ψ_{i+1} and ψ_i, and φ_{PI}^{ideal} represents the ideal output phase when the phase code m ranges from 0 to K. Considering the fact that the phase interpolation is achieved by mixing two input phases with different weights, the actual interpolated output signal can be calculated by,

$$CK_{pi} = A_{pi} \cdot e^{j\varphi_{pi}} = \frac{m}{N} \cdot A_0 e^{j\psi_i} + \frac{N-m}{N} \cdot A_0 e^{j\psi_{i+1}}, \tag{2.13}$$

where A_{pi} and φ_{pi} denote the instant amplitude and phase of the interpolated clock signal, respectively. Taking quadrature and octagonal PIs as examples, Fig. 2.17 describes the phase mixing constellations and the interpolated phase step allocations [8, 10, 122, 9]. It can be found that the maximum interpolation phase error for the quadrature PI reaches $4°$ and the maximum interpolation phase error for the octagonal PI is around $0.5°$, where the maximum deviation happens at the same positions for both the quadrature and octagonal PIs, which are located at the $1/4$ and $3/4$ of the total steps between the two mixing input phases. These phase errors stem from the linearly sweeping as the phase transfer characteristics of the PIs are in proportion to the anti-trigonometric function of the input-phase weight ratio rather than the input-phase weight ratio itself. It is worthy to note that the phase error of the octagonal PI is smaller than that of the quadrature PI. This makes the octagonal PI a superior choice for high-linearity phase interpolators, but the cost is the doubled input phases, complex phase-weight coding, and complicated circuit implementation.

The amplitude of the interpolated clock (A_{pi}) is also modulated by the phase code. When the phase code is 0, the PI actually performs as a buffer with a minimum mixing factor, hence a maximum amplitude can be obtained. As the phase code increases, the amplitude will decrease with the increasing mixing factor. Once the phase codes of the two input phases are adjusted to be equal to each other, the mixing factor reaches its maximum value and the amplitude decreases to its minimum value. If the phase code continues to rise, the amplitude will increase with the decreasing mixing factor and finally rise up to its maximum value. According to the discussion in [67], these amplitude fluctuations can be potentially converted into delay variations through amplitude modulation (AM) to phase modulation (PM) conversion, and the delay variation is approximately proportional to the square of the input-signal swing. Theoretically, the maximum amplitude reduction of a quadrature PI can reach 29.3%, occurring at the half of the total steps for each quadrant. It is also under the same condition that the phase deviation runs up to its maximum value, thus any extra delay caused by the AM-PM conversion can further aggravate the maximum DNL directly. The linearity of the phase interpolator can also be deteriorated by the I, Q mismatch, clock duty distortion,

and inadequate edge overlap of the input clocks [122, 123, 115]. To mitigate these effects, a variety of techniques including local duty cycle correction, I, Q phase correction, and slew rate calibration using slew buffers or harmonic rejection poly phase filters are usually utilized to optimize the quality of the I, Q clocks [14, 123, 115].

2.3.4 Channel Equalization

When transmitting data pass through electrical mediums, the insertion loss caused by frequency-dependent skin effect and dielectric absorption could result in prominent ISI. This ISI can be directly converted into the deterministic jitter to compress the link jitter margin and hence reduces the maximum support rate or deteriorates the BER of the serial link. For instance, for a -12 dB loss channel, the far-end eye-diagram after this channel can be completely closed. It seems that this issue can be solved by simply increasing the signal strength to go against the attenuation. In practical designs, there does exist an optimal swing for a specific channel loss. This is the reason why many transmitters have integrated the function of swing adjustment, and therefore allows the users to adjust the driving strength to the optimal values to accommodate to different applications. If the signal swing is too small, the received signal could be buried by the noise, thus exhibiting a low SNR. Theoretically, a high swing can effectively improve the SNR of the system. However, this does not mean a higher swing is always better for the link communication. Firstly, the increased signal swing does not solve the ISI problem. This is because the increased symbol swing also improves the energy spread to the other symbols, thus exhibiting no optimization on the ISI. Secondly, the increased swing also improves the strength of some proportional noises such as reflection, crosstalk, which could deteriorate the performance of the link. Thirdly, the increased swing always means substantial power consumption as the driver needs to draw more currents. To overcome this frequency-dependent signal dispersion, many equalization techniques have been developed to compensate for the channel loss by either attenuating the low-frequency components or boosting the high-frequency components [124]. This section will summarize the mainstream equalizers utilized in high-speed links, including the FFE, CTLE, and DFE. These equalizers are usually
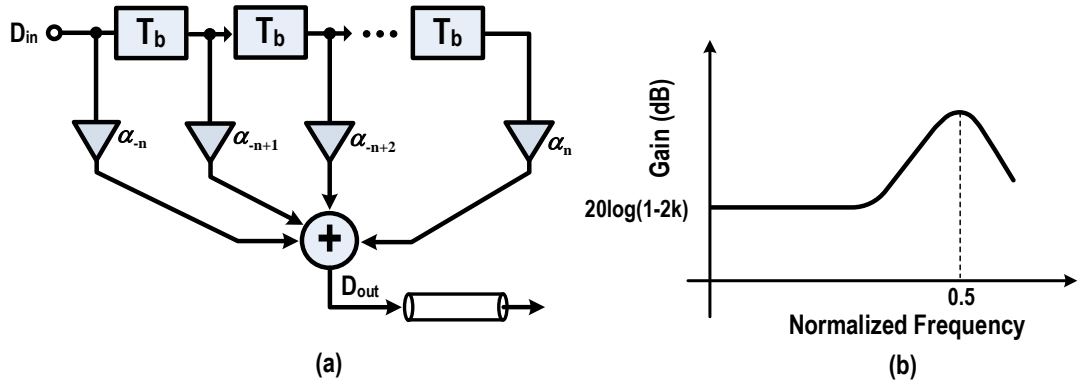
Figure 2.18: The FFE. (a) Functional block diagram, where T_b is the bit period and α_n is the weight of the nth tap. (b) Typical frequency response, where k is the summation of the absolute tap weights.

combined together to cover a broad range of channel spectrums, especially for high-loss legacy channels. The FFE is usually employed to cancel the pre-cursor ISI and partial nearby post-cursor ISI. The CTLE is often adopted to neutralize the long-tail ISI. The DFE is frequently utilized to remove the nearby post-cursor ISI.

2.3.4.1 Feed Forward Equalizer

The FFE, which is usually implemented using a finite impulse response (FIR) filter, is one of the most common techniques in high-speed serial links. It pre-distorts the output waveform shape over several symbols to pre-attenuate the low-frequency portion of the transmitted signal, thus making the signal spectrum after the lossy channel maintain a proper balance between various frequency components. Fig. 2.18(a) describes the functional block diagram of the FFE, where T_b is the bit period and $\alpha(l)$ is the normalized tap weight. Clearly, the waveform pre-distortion is actually performed by summing the symbol-spaced streams with different tap weights. Fig. 2.18(b) displays a typical frequency response of the FFE, which demonstrates prominent low-frequency attenuation. The maximum de-emphasis amount is $20log(1 - 2k)$, where $k = \sum_{l \neq 0} |\alpha(l)|$. Note that k must be within 0 and 1/2 to perform high-frequency boosting. For $k > 1/2$, the frequency response actually exhibits attenuation rather than boosting for high frequencies. The specific response shape is subject to the tap number as well as the tap-weight distribution. The discussion in [101] shows that more taps help to fit desired response. Meanwhile, the increased tap number implies

an almost linear increase of parasitic capacitance at the output node, thus limiting the output bandwidth. To keep sufficient bandwidth and maintain an adequate eye opening, a tap number of three or four is usually adopted for the data rate below 30 Gb/s [101, 9, 125, 13]. For the cutting-edge transmitters operating around 40-60 Gb/s, two-tap FFEs are usually adopted [23, 36, 57].

The FFE exhibits several unique advantages over its counterparts. Firstly, the FFE is able to cancel pre-cursor ISI by introducing pre-cursor taps. Secondly, the FFE shows negligible noise amplification due to its digital implementation. Thirdly, the tap weights of the FFE can be accurately controlled by employing a high-resolution digital-to-analog converter (DAC) For example, 5-6 bit resolution can be achieved conveniently, which is usually accurate enough for the FFE tap-weight adjustment. The main disadvantage of the FFE is that it is implemented by attenuating the low-frequency portion rather than boosting high-frequency ones. This equalization mode can significantly reduce the eye-height in the RX-side. Another drawback is its complex circuit implementation which involves multiple symbol-spaced full-rate data generations. It not only decreases the maximum allowable data-rate by introducing parasitic capacitance on the output nodes, but also increases the area occupation and power consumption. These penalties become even more severe in ultra-high-speed transceivers operating around the cutting-edge speed of the technology. The FFE equalization can be located either at the TX-side or the RX-side. In the following two paragraphs, we will separately discuss the pros/cons of the TX-FFE and RX-FFE.

Most designs put the FFE on the TX-side due to the following two reasons. One is the 1 UI delay can be accurately generated by simply relatching. The other is the coefficient multiplication can be simply performed on binary values by changing the current-controlling codes to adjust the tap weight. Nonetheless, TX-FFE has several prominent disadvantages. Firstly, it is difficult to perform automatic tap-weight adaptation since the quality of the received signal can only be known at the RX-side. Although a back channel can be employed to transfer the continuously adjusted tap weights [126], this extra back channel increases the system complexity in terms of extra chip pins, complicated chip packaging, and additional PCB routing. Moreover, this RX-side adaptation

scheme may not even be available due to the problems in interoperability, especially when the transmitter and receiver are from different vendors [13]. Secondly, the compensation ability is limited by the allowable minimum signal swing after de-emphasis, this is because the TX-FFE compensates for the high-frequency channel loss by attenuating low-frequency components rather than increasing high-frequency components in the signal.

By placing the FFE at the RX-side, the tap weights can be adapted locally at the RX-side, thus eliminating the need for a back channel and removing the issue of TX-RX interoperability. This also makes the driver at the TX-side simpler by removing the combining taps, thus reducing the output capacitances and improving the driving bandwidth. However, there also exist several drawbacks in the RX-FFE. The primary challenge is how to generate the symbol-spaced versions of the received signal [13]. Passive delay cells using inductors and capacitors need a large area, and their tunable delays are not wide enough to handle a wide operation range. Active delay cells such as CML buffers are power-hungry and distort the signal waveform due to their delay-dependent bandwidth. Another challenge in the RX-FFE is how to carry out the product of the coefficients and the analog signals [13]. In bipolar technology, a traditional Gilbert multiplier can be utilized to perform this multiplication. However, the limited linearity performance of the CMOS transistors makes the Gilbert multiplier far less accurate and its resulting distortion significantly degrades the FFE performance. Unlike the TX-FFE that only sums the weighted digital streams, the RX-FFE processes the received signal containing both the useful signal information and useless noise disturbance. Therefore, the high-frequency components of the noise are also boosted, which is not desired in high-speed communication systems.

2.3.4.2 Continuous-Time Linear Equalizer

The CTLE is a simple continuous-time circuit with a high-frequency boosting transfer function that effectively overcomes the high-frequency losses through a transmission channel. It usually acts as a front-end amplification stage at the RX-side to provide gain and high-frequency peaking with acceptable power and area overhead-
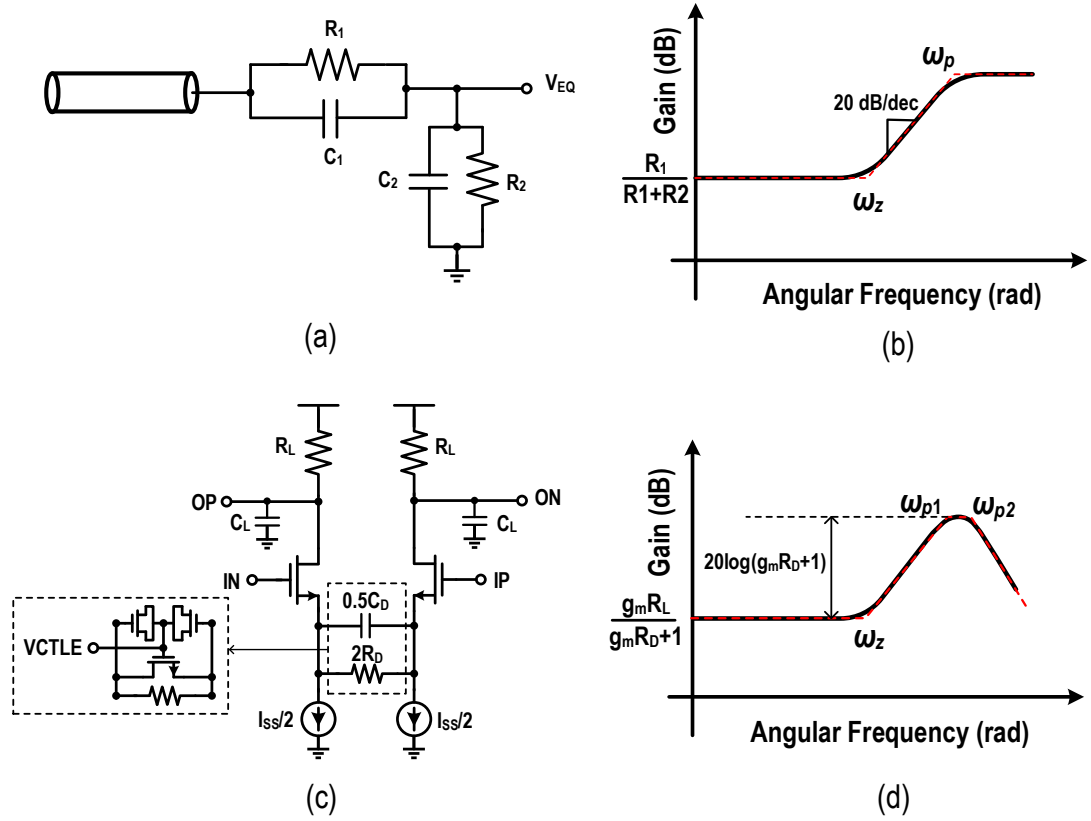
Figure 2.19: The CTLE. (a) Passive implementation, (c) frequency response of the passive CTLE, (c) active implementation, and (d) frequency response of the active CTLE. Here, ω_z is the angular frequency of the zero and ω_p is the angular frequency of the pole.

s. As the CTLE sharpens both the rising and falling edges of the received signal, it shows a capability of canceling both the long tail ISI caused by the pre-cursor and post-cursor taps. Similar to the RX-FFE, there are also some drawbacks associated with the CTLE. Firstly, the equalization ability of the CTLE is limited to first-order compensation. Secondly, it also amplifies the noise and crosstalk in the boosting band. Thirdly, its gain boosting is sensitive to PVT variations, and the tuning range is small. Finally, its operation speed is limited by the GBW product of the amplifier.

The CTLE can be realized in both passive components and active devices [124]. Fig. 2.19 displays both passive and active implementations of the CTLE and their frequency responses. For the passive CTLE shown in Fig. 2.19(a), the frequency shaping is achieved by a simple RC network, where low-frequency components are attenuated by the resistor and the high-frequency components are allowed to pass through the capacitor, thus leading to high-frequency gain boosting. According to the signal pro-

cessing theorems, the transfer function and the associated pole-zero positions can be calculated by,

$$H(s) = \frac{R_2}{R_1 + R_2} \cdot \frac{1 + R_1 C_1 s}{1 + \frac{R_1 R_2}{R_1 + R_2}(C_1 + C_2)s}, \tag{2.14}$$

$$\omega_z = \frac{1}{R_1 C_1}, \tag{2.15}$$

$$\omega_p = \frac{1}{\frac{R_1 R_2}{R_1 + R_1}(C_1 + C_2)}, \tag{2.16}$$

$$DC - Gain = \frac{R_2}{R_1 + R_2}, \tag{2.17}$$

$$Gain - Boost = 20log\left(\frac{\omega_p}{\omega_z}\right). \tag{2.18}$$

Fig. 2.19(b) displays a typical frequency response of the passive CTLE. The boosting frequency components are determined by the locations of the zero and the pole while the boosting factor can be approximated by the ratio of the pole to the zero, since the frequency response shows a 20 dB/dec rolling up [see Eq. (2.18)]. By appropriately choosing the resistor/capacitor values that determine the positions of the zero and the pole, reasonable gain boosting including both frequency components and boosting amounts can be achieved. The main feature of this equalizer is its compact implementation and zero power consumption since it only contains passive components of resistors and capacitors. However, there are three prominent disadvantages in this simple RC equalizer. Firstly, the RC network introduces large impedance discontinuity at the interface between the channel and the equalizer, which could cause significant reflection. Secondly, this approach cannot improve the SNR since the equalization is performed by attenuating low-frequency components. Thirdly, it is not convenient to adjust the boosting parameters since the configuration of the RC values could introduce additional overheads to the most high-speed critical path. Therefore, this technique has seldom been utilized in high-speed serial links.

Fig. 2.19(c) presents the widely used active CTLE implementation. It utilizes an RC source degradation to provide different gains for different frequencies in order to realize high-frequency boosting. By analyzing the linear equivalent half circuits, the

transfer function and the zero-pole positions can be given by,

$$H(s) = \frac{g_m}{C_L} \cdot \frac{s + \frac{1}{R_D C_D}}{s + \frac{g_m R_D + 1}{R_D C_D}} \cdot \frac{1}{s + \frac{1}{R_L C_L}}, \tag{2.19}$$

$$\omega_z = \frac{1}{R_D C_D}, \tag{2.20}$$

$$\omega_{p1} = \frac{g_m R_D + 1}{R_D C_D}, \tag{2.21}$$

$$\omega_{p2} = \frac{1}{R_L C_L}, \tag{2.22}$$

$$DC - Gain = \frac{g_m R_L}{g_m R_D + 1}, \tag{2.23}$$

$$Gain - Boost = 20 log \left(\frac{\omega_{p1}}{\omega_z} \right). \tag{2.24}$$

Fig. 2.19(d) presents a typical frequency response of the active CTLE. The response shape is mainly constrained by ω_z, ω_{p1} and $DC - Gain$ since the second pole is usually determined by the load resistor and output capacitor. The boosting ability of the active CTLE is usually changed by adjusting the source degradation RC network [see Fig. 2.19(c)]. As the control voltage VCTLE is tuned from high to low, both the equivalent resistor R_D and equivalent capacitor C_D become larger. The resulting zero (ω_z) can be reduced while the ratio of the dominant pole to zero (ω_{p1}/ω_z) will increase, thus the boosting frequency band and the boosting gain can be both improved. Inductive peaking [127] or forward-coupling capacitance neutralization [124] can be used to further increase the bandwidth of the CTLE and hence enhances the gain-boost ability. Compared to the passive CTLE, the main feature of the active CTLE is its ability to achieve higher gains (over 0 dB) for both low and high frequency components, which helps to improve the SNR to optimize the BER of the link.

2.3.4.3 Decision Feedback Equalizer

The DFE is another effective signal conditioning technique to cancel the ISI caused by frequency-dependent channel loss, which is commonly implemented at the RX-side in serial links. Fig. 2.20 gives the conceptional diagram and typical frequency response of the DFE. It works by directly subtracting (or adding) the previous decisions in multiplication with corresponding tap weights. This previous-decision-based
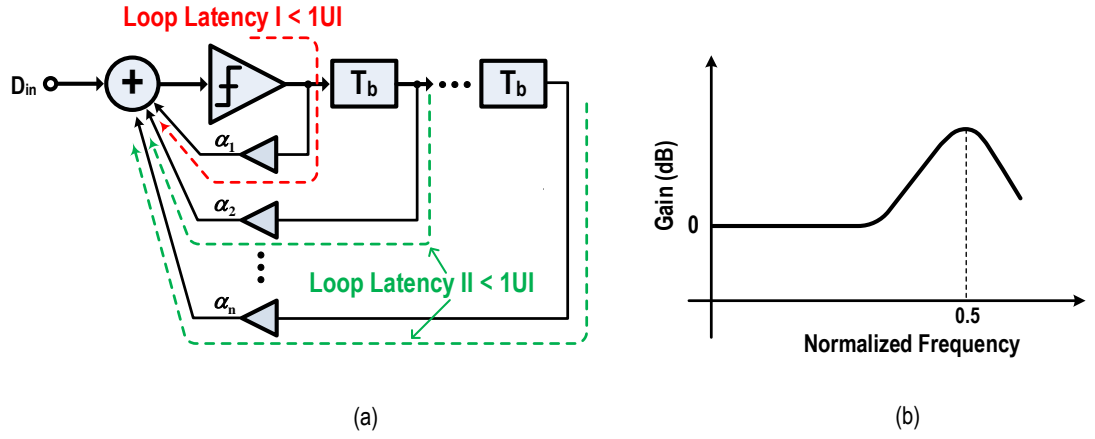
Figure 2.20: The DFE. (a) Functional diagram, where T_b is the bit period and α_n is the tap weight of the nth tap. (b) Typical frequency response, where the frequency is normalized to the value of the data rate.

ISI cancellation not only increases the boosting factor of the DFE, but also makes it immune to noise amplification since the feedback signal is the scaled version of well-recovered digital streams. Similar to the FFE, for a fixed tap-weight summation k, where $k = \sum_{l=1}^{n} |\alpha(l)|, (0 < k < 1)$, the maximum boost factor is a constant $[20log((1+k)/(1-k))]$, while the tap number and tap weight distribution only affect the shape of the response.

There are three issues in the DFE design [128]. Firstly, there exists error propagation problem in the DFE because the ISI cancellation is based on the assumption that all the previous decisions are correct. When there are bit errors, the subtraction or addition of the scaled decisions will rather exacerbate the ISI than cancel it. Fortunately, this error propagation can be neglected for a robust serial link since its BER is usually lower than 10^{-12}. Secondly, the DFE can only remove post-cursor ISI as the feedback sequences can only be the previously received data. This is the reason why the DFE is usually combined with the TX-FFE and/or RX-CTLE to cancel the ISI caused by both the pre-cursors and post-cursors. Finally, the DFE implementation suffers from a stringent timing problem. As described in Fig. 2.20(a), there are two possible critical paths. One is the feedback loop of the first tap, whose timing requirement can be expressed by,

$$t_{cq}^{slicer} + t_{setup}^{slicer} + t_{fb} < 1UI, \tag{2.25}$$

56

where t_{cq}^{slicer} is the ck-to-q delay of the slicer, t_{setup}^{slicer} denotes the setup time of the slicer, and t_{fb} stands for the feedback path delay. The other is the feedback loop on other taps, whose loop delay also must be lower than 1 UI,

$$t_{cq}^{ff} + t_{setup}^{slicer} + t_{fb} < 1UI, \tag{2.26}$$

where t_{cq}^{ff} represents the ck-to-q delay of the retiming FF. The main difference between these two loops is that their ck-to-q delays come from different components. Compare to the FF which retimes the sliced full-swing data sequence, the slicer needs to regenerate the digital output from a small input. Consequently, the t_{cq}^{slicer} should be larger than t_{cq}^{ff}, which makes the timing budget for the first tap [see Eq. (2.25)] tighter than that for other taps [see Eq. (2.26)]. This is the reason why various techniques are developed to relax the first tap timing requirement.

2.3.4.4 Equalization Adaptation

In practical transmission systems, the connection channels usually have the following features. Firstly, the exact channel profiles in practical serial links are usually unknown in advance. Secondly, the channel length can vary from one application to another. Thirdly, the channel profile may change due to the fabrication variation. Finally, the channel profile will vary in real time with its operation environment, which becomes particularly severe for data rates beyond 10 Gb/s. To accommodate to the different channel losses and track the real-time channel variations, many adaptive equalization techniques like least mean square (LMS) [129, 34, 130, 131], zero-forcing (ZF) [105, 132], maximum eye opening (MEO) [133], and spectrum matching [134] have been developed. Fig. 2.21 summarizes the conceptional diagrams of these adaptation methods.

Algorithm-Based Adaptation- Fig. 2.21(a) describes the conceptional diagram of the most widely used algorithm-based adaptation, which can be applied to any type of equalizers including the FFE, CTLE, and DFE. There are many algorithms that can be used to adjust the equalizer coefficients, but only a few of them are suitable for on-chip integrations. The most popular ones for compact hardware implementation are
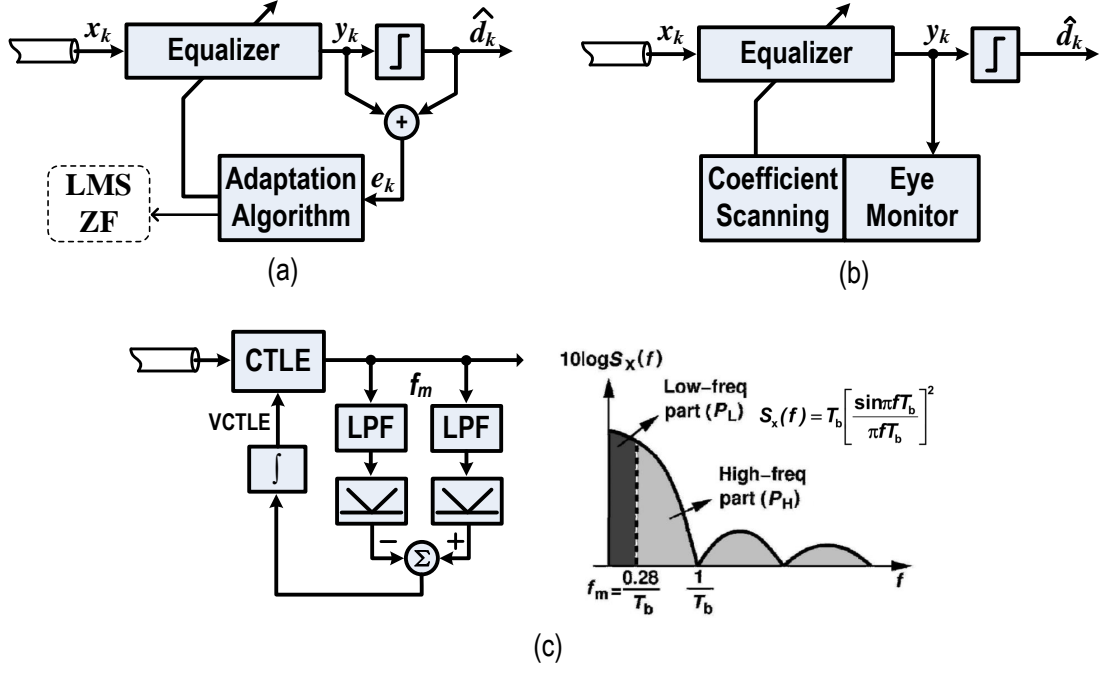
Figure 2.21: Equalization adaptations. (a) Algorithm-based adjustment, (b) eye monitor-based coefficient update, and (c) spectrum matching-based calibration.

the LMS, ZF, and their variants.

1. The LMS algorithm optimizes the equalization coefficients based on minimizing the mean squared error. The coefficient update equation can be express by,

$$\alpha_{(k+1,l)} = \alpha_{(k,l)} - \lambda \cdot e_k \cdot x_{k-l}, (l = 1, 2 \cdots, n), \quad (2.27)$$

where $\alpha_{(k,l)}$ denotes the lth tap weight at the kth iteration, λ is the update step size, x_k stands for the samplers at the channel output, $\widehat{d_k}$ is the estimate of the transmitted data, and $e_k = \widehat{d_k} - y_k$ represents the equalization error. The requirement of the analog multiplications (x_k and e_k are naturally analog signals) in Eq. (2.27) makes it difficult to be implemented in hardware, thus reducing its competitiveness in equalization coefficient adaptations. To reduce the complexity of the traditional LMS, the sign-sign LMS (SS-LMS) algorithm has been developed, which utilizes the binary quantized $sign(e_k)$ and $sign(x_{k-l})$ to replace the analogue e_k and x_{k-l} in Eq. (2.27). The update iteration is then changed to,

$$\alpha_{(k+1,l)} = \alpha_{(k,l)} - \lambda \cdot sign(e_k) \cdot sign(x_{k-l}), (l = 1, 2 \cdots, n). \quad (2.28)$$

Considering the fact that the binary quantized $sign(e_k)$ and $sign(x_{k-n})$ can be directly mapped from the sliced error sequence and recovered data stream, the SS-LMS obviates the need for analog operations, hence making it more feasible for on-chip integrations. Since the binary quantization significantly reduces the iterative accuracy, the convergence time of the SS-LMS is generally worsen than that of the traditional LMS. Fortunately, this increased convergence time is not a problem in most serial links.

2. The ZF solution is obtained by forcing residual ISI in the decision instant to zero [135], which can be theoretically achieved by completely inverting the channel response $H_C(s)$ [136],

$$H_E(s) = \frac{1}{H_C(s)}, \qquad (2.29)$$

where $H_E(s)$ is the frequency response of the equalizer. The resulting total transfer function of the convolution of the equalizer and the channel should be flat. Optimal ZF equalization requires equalization filters with infinite taps to fit the long-tail impulse response. In practical implementations, suitable truncation is usually applied to construct a finite impulse response (FIR) to approximate the infinite impulse response (IIR). This method is suitable for the time-invariant channel, which is well known in advance. To adaptively adjust the equalizer coefficients and track the slow channel changing, the equalizer coefficients can be updated by the following iteration [137],

$$\boldsymbol{\alpha}_{k+1} = \boldsymbol{\alpha}_k - \lambda \cdot \boldsymbol{e}_k \cdot \boldsymbol{x}_k,$$
$$\boldsymbol{e}_k = \widehat{\boldsymbol{s}}_k - \boldsymbol{s}_k, \widehat{\boldsymbol{s}}_k = \boldsymbol{x}_k^T \boldsymbol{\alpha}_k, \qquad (2.30)$$

where $\boldsymbol{\alpha}_k$ is the equalizer coefficient vector, λ denotes the update step that controls the adaptation rate, $\boldsymbol{e}_k$ stands for the error vector, $\widehat{\boldsymbol{s}}_k$ represents the estimate vector of the transmitted data, $\boldsymbol{x}_k$ is a vector being composed of the input signal applied to the equalizer, and $\boldsymbol{s}_k$ denotes a vector consisting of the training symbols. Note that the subscript k or $k+1$ refers to the kth or $(k+1)^{th}$ itera-

tion. Comparing Eq. (2.30) to Eq. (2.27), we can find that the ZF algorithm is equivalent to the LMS for FIR equalizers.

The errors utilized in the aforementioned LMS and ZF algorithms are extracted by measuring the amplitude differences between the equalized and desired outputs that are sampled at the data-sampling positions. This level-based error extraction method involves both data recovery and peak detection [138]. Moreover, this configuration often requires additional slicers or even an analog-to-digital converter (ADC) to extract the amplitude errors between the equalized and expected eye heights, which makes it less competitive for high-speed applications due to the following reasons. Firstly, these auxiliary circuits (slicers or ADC) degrade the maximum bandwidth because their input capacitances are directly connected to the maximum-speed signal path. Secondly, the additional high-speed circuits will inevitably introduce more connections, which not only makes the layout routing more complicated but also increases the parasitic capacitances. Thirdly, the additional circuits consume considerable power since they need to operate at the maximum speed. Meanwhile, the residual ISI can also be minimized using the errors at the crossing points since the ISI at the crossing points is heavily correlated to the transmitted data for bandwidth-limited systems [138]. Leveraging this characteristic, Xilinx [138, 139, 42] has developed an edge-based algorithm, where the the error in Eq. (2.29) is replaced with the error at the crossing points. These errors can be directly mapped from the quantized edge sequence that is indispensable for the CDR. Consequently, the additional samplers can be obviated to optimize the critical path capacitances and improve the power efficiency. Note that the indirect nature of the edge-based algorithm shows a relatively lower effectiveness when compared with its level-based counterpart. Fortunately, simulation results indicate that for low-loss applications, the edge-based adaptation is sufficient to guarantee an acceptable eye opening at the data-sampling point [138].

Eye Monitor-Based Adaptation- Fig. 2.21(b) describes the eye monitor-based adaptation, which is also applicable to any type of equalizer structures. The optimal equalization coefficients are attained based on maximizing the eye opening. The two-dimensional mask of the eye opening can be obtained by monitoring the BER while

adjusting the sampling position and slicing levels of the error-detection slicer [140]. As for the adaptive equalization process, the eye masks with different equalization coefficients are first measured by the internal eye monitor under the control of the co-efficient scanning engine [see Fig. 2.21(b)]. The optimal coefficient configuration is then selected by a maximum-eye-opening searching algorithm. This method can produce visualized eye-diagram with distinct eye width and eye height, thus providing an intuitional window to observe the equalization effect. Nonetheless, there exist two drawbacks in the eye monitor-based equalization adaptation. One is the high power consumption of the eye monitor (including full-rate slicer, clock PI, driving buffer, scanning engine, and searching algorithm) can significantly degrade the power effi-ciency of the serial link. The other is the contradiction of the design complexity, scan-ning speed, and measuring accuracy. Precise eye measurement needs high-resolution DAC and PI for slicing level adjustment and sampling position moving, which not on-ly complicates the design but also significantly prolongs the eye-scanning time. The eye monitor presented in [141] shows that the combination of a 3-bit DAC and a 4-bit PI contributes a total of 210 different masks, and it is a good balance for a 10 Gb/s design. In addition, the eye-scanning accuracy is also limited by the slicer sensitivity, slicer offset, and PI nonlinearity.

Spectrum Matching-Based Adaptation- Fig. 2.21(c) presents the spectrum matching-based adaptation, which is applicable to the RX-CTLE and one tap RX-FFE as it only provides one control voltage [134, 142, 143]. The control voltage is optimized by forc-ing the imbalance of the spectrum split by the frequency f_m to zero [see Fig. 2.21(c)], where f_m equals $0.28/T_b$ and T_b is the bit period [134]. This f_m is selected based on the fact that it equally splits the power energy of the spectrum for ideal random bina-ry sequences. Note that the setup of f_m as $0.28/T_b$ is valid only for purely-random or pseudo-random data streams [134]. There are several difficulties in this adaptation method. Firstly, the LPF and HPF are directly connected to the critical path [Fig. 2.21(c)], which could degrade the maximum bandwidth. Secondly, the splitting band-width is difficult to control since the passive components utilized in the LPF and HFP are sensitive to PVT variations. Thirdly, the effective power detection is challenging,

especially for the high-frequency power detection. Finally, the accuracy is limited by various system uncertainties . For example, the unbalanced power detection between the low-frequency and high-frequency rectifiers could lead to underestimate or overestimate of the boosting factors, thus resulting in a suboptimal solution [142].

Chapter 3

Design of the Ring-Based Injection-Locked Clock Multiplier (RILCM)

Clock multipliers continue to play important roles in modern wireline communication systems. The rapid growth of per-lane data rate paired with the high-volume lane integration has posed more stringent requirements on the clock multipliers, including high-frequency ability, low-jitter generation, small-area occupation, and low-power consumption. Over the past decades, plenty of efforts have been made to develop such clock multipliers. Phase locked loop (PLL) is attractive because of its compact implementation, robust operation, and convenient configuration. Nonetheless, the infeasibility of combining the preferred properties of small area (within ring-oscillator) and low jitter (within LC-oscillator) is prone to degrade its competitiveness. DLL-based clock multiplier is an alternative solution that can offer superior jitter performance, while obviating large-area inductors [144, 79]. However, the duty cycle error and fixed pattern jitter caused by mismatches could hinder its widespread uses in practical applications. Recently, injection locking has attracted increasing attentions since it exhibits obvious advantages over the above methods, including simple structure, high power efficiency, and low phase noise [81, 83, 82, 145]. It has shown a great potential on a variety of applications such as clock multiplication [85, 146], frequency division [147, 148], clock distribution [149], and clock data recovery [150].

This chapter presents a ring-oscillator-based injection-locked clock multiplier (RIL-CM) that seeks to achieve the good properties of low jitter generation, small area occupation, and high power efficiency. To adaptively adjust the frequency offset, we have developed a hybrid FTL. Meanwhile, a lock-loss detection and lock recovery (LLD-LR) is devised to endow the RILCM with a similar lock-acquisition ability as conventional PLL, thus excluding the initial frequency setup aid and preventing potential lock loss. To satisfy the requirements of high operation speed, high detection accuracy, and low output disturbance, a compact timing-adjusted phase detector (T-PD) tightly combined with a well-matched charge pump (CP) is designed. To further reduce the output jitter, a full-swing pseudo-differential delay cell (FS-PDDC)-based injection-locked ring-VCO (IL-RVCO) is developed as well.

The remainder of this chapter is organized as follows. Section 3.1 summarizes the challenges in the RILCM design and previous solutions. Section 3.2 describes the RIL-CM architecture. The proposed IL-RVCO, the devised phase shift detection, and the designed LLD-LR are presented in Section 3.3, 3.4, and 3.5, respectively. Section 3.6 details the experimental results and Section 3.7 summarizes the implemented RILCM.

3.1 Challenges in RILCM and Previous Solutions

3.1.1 Challenges in RILCM

It is a nontrivial task to design a robust RILCM for practical applications and the challenges mainly focus on the following aspects. Firstly, the jitter suppression is sensitive to the frequency offset between the target frequency and the free-running frequency of the oscillator. Specifically, the phase noise tracking ability will decline rapidly as the frequency offset increases [81]. Moreover, it is quite challenging to detect the frequency offset since the accumulated phase error can always be reset by the injection pulse. Therefore, the free-running frequency of the voltage-controlled oscillator (VCO) should be tuned as close as possible to the center of the locking range to obtain an optimum jitter suppression. Secondly, the injection locking technique cannot suppress the $1/f^3$ noise of the VCO. This is because the injection locking is actually e-
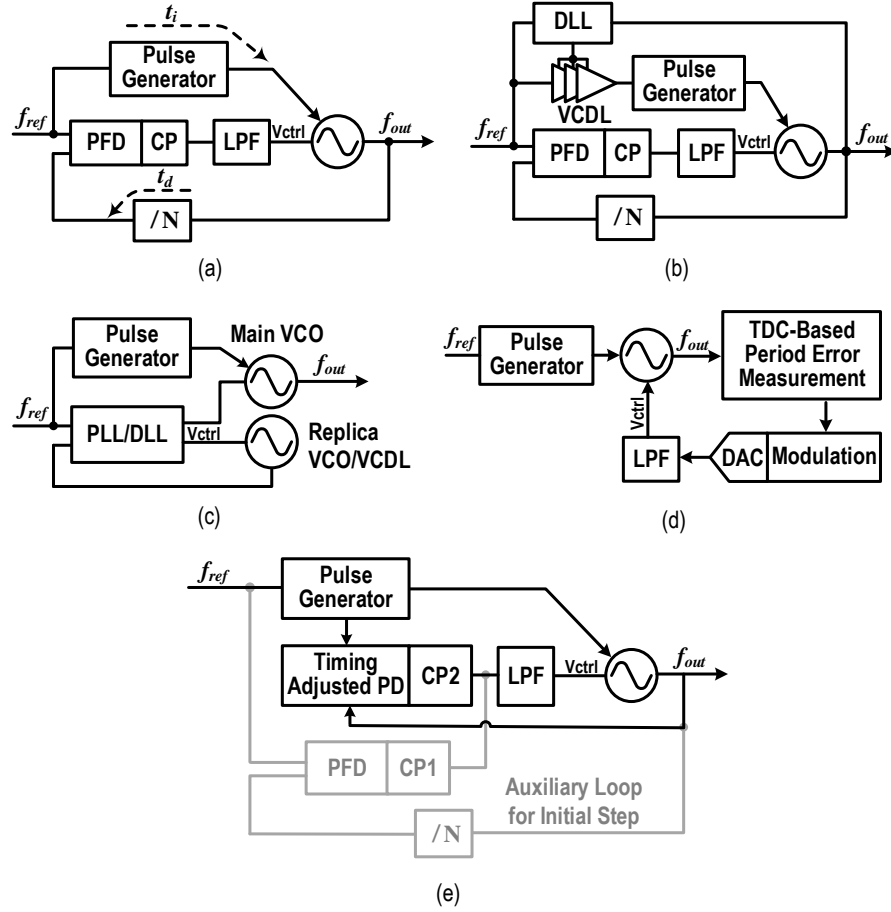
Figure 3.1: Previous frequency tracking techniques. (a)Traditional IL-PLL, (b) IL-PLL with DLL-based injection position adjustment, (c) dual-loop architecture with replica-VCO/VCDL, (d) TDC-based FTL, and (e) TPD-based FTL.

quivalent to a single-pole feedback system that can only achieve 20 dB/dec of in-band noise shaping [82, 89]. It means that the injection locking technique suppresses the $1/f^2$ noise (converted from white noise) of the VCO but not its $1/f^3$ noise (converted from flick noise). Thirdly, the injected VCO is possibly locked to some harmonic frequency of the injection signal [151]. This can be traditionally solved by introducing a beginning-calibration procedure [152, 145, 153] to initially adjust the control voltage close to the desired value. However, it cannot prevent the hidden risk of possibly losing lock due to its limited lock-in range and weak lock-acquisition ability [86, 87]. As a consequence, robust frequency tracking techniques with low-frequency noise suppression abilities are highly demanded to overcome these difficulties.

3.1.2 Prior Arts

Fig. 3.1 summarizes the previous frequency tracking techniques that are utilized to address the aforementioned issues. According to the frequency offset detection mechanism, they are categorized into two different classes. One is based on traditional PLL/DLL [see Fig. 3.1(a), (b), and (c)] and the other is based on injection caused phase shift detection (PSD) [see Fig. 3.1(d) and (e)].

Fig. 3.1(a) shows the most general injection-locked (IL)-PLL, where the PLL system keeps the natural frequency of the VCO located at the desired frequency harmonic [88]. The main problem of this scheme is the mutual-pulling between the PLL locking force and the injection locking force, which could degrade the jitter performance or even result in a stability problem. The mutual-pulling is usually caused by the delay mismatch between t_i (the intrinsic delay of the pulse generator) and t_d (the delay of the asynchronous divider) [see Fig. 3.1(a)], and their delay fluctuations over different PVT corners make it even more difficult to handle. This problem was solved in [82] by adding a voltage-controlled delay line (VCDL) preceding the pulse generator [see Fig. 3.1(b)]. Driven by the DLL loop, the delay of the VCDL is adaptively adjusted to maintain an optimal injection position. This method removes the timing issue with the penalty of an additional DLL loop. Fig. 3.1(c) describes the dual-loop architecture, where the frequency deviation is monitored by a separate PLL utilizing a replica-VCO [83] or an independent DLL using the same delay cell as the main V-CO [84]. The physical separation of the FTL and the injection-locked oscillator (ILO) can effectively prevent the mutual-pulling problem between the two locking forces. However, there are still several drawbacks within this architecture. Firstly, the auxiliary PLL/DLL consumes substantial extra power which lowers the power efficiency. Secondly, the fabrication mismatch constrains the calibration precision. Thirdly, the separate FTL cannot suppress the $1/f^3$ noise of the VCO, since the flick noise tracked by the PLL/DLL is independent of that in the main VCO. Generally, the common feature of the above mentioned architectures is employing an additional PLL/DLL loop to correct the frequency offset. Hence, they can be classified as PLL/DLL-based FTLs. The main drawback of these FTLs is the low efficiencies in power consumption and

area occupation.

Meanwhile, the PSD-based FTLs are attracting more attentions because of their low power consumption and high jitter performance. By merging the frequency offset detection and the injection error detection into one single PSD, the always-on PLL/DLL in the aforementioned FTLs is only required to work during the frequency initialization, thus saving substantial power consumption. Considering the fact that the phase disturbance induced by the device noise is equally detected by the PSD without distinction, thus the FTL is capable of attenuating the VCO in-band noise like traditional IL-PLL. Combining with the 20 dB/dec noise shaping introduced by the injection locking, the $1/f^3$ noise of the VCO can be completely suppressed. Fig. 3.1(d) and (e) respectively presents the digital and analogical PSD-based FTLs [85, 146]. The former adopts a time-to-digital converter (TDC) to measure the periodic phase errors caused by frequency offset [85], while the latter utilizes a TPD to detect the phase shift between the injection-pulse center and the zero-crossing point of the IL-VCO [146]. For the TDC-based FTL, its performance is restricted by the TDC resolution and control voltage granularity. The complex logic operation associated with the complicated circuit implementation also reduces its power efficiency. In contrast, the TPD-based FTL shows superior power efficiency since its operation only involves the TPD, CP, and LPF. As an example, the IL-PLL designed in [146] with the TPD-based FTL achieves a figure-of-merit (FOM) of -247 dB at 3.2 GHz. However, there still exist several challenges within the TPD-based FTL. Firstly, it is quite challenging to design a high-speed TPD since it needs to process the most high speed injection pulse. Secondly, the TPD must have high detection accuracy to distinguish the small phase shift caused by the frequency offset. Thirdly, the hidden risk of possibly losing lock along with its limited locking range and weak lock-acquisition ability reduces its robustness and reliability [86, 87]. This work is aimed to address these issues in the TPD-based FTL.
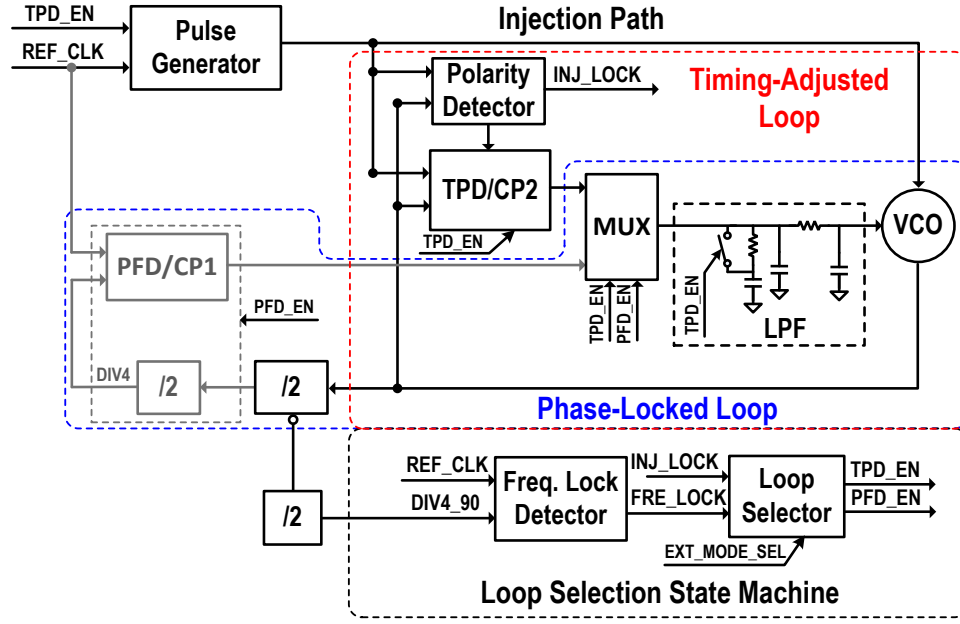
Figure 3.2: The architecture of the proposed RILCM.

3.2 Proposed RILCM Architecture

3.2.1 Overall Architecture

Fig. 3.2 shows the block diagram of the proposed RILCM. It contains a pulse generator (PG) and a hybrid FTL consisting of a traditional PLL, a timing-adjusted loop (TAL), and a loop-selection state machine (LSSM). Driven by the LSSM, the LPF/VCO alternately connects to PFD/CP1 and TPD/CP2 to accomplish lock acquisition. When the FTL switches from PLL to TAL, the resistor in series with the capacitor is shorted to remove the stabilizing zero in the loop gain. This is because the injection locking gives rise to the inclusion of a high pass filter within the TAL, thus making it a first-order system.

This design has two main features. One is the newly developed TPD, which utilizes limited transistors to achieve both high detection accuracy and high operation speed. Meanwhile, a polarity detection mechanism is introduced to avoid positive feedback. The other is the introduced LLD-LR in the hybrid FTL, which automatically switches the FTL to traditional PLL mode for a specific duration to undertake lock recovery in case that an injection-lock loss is detected. In doing so, the pull-in range of the RILCM is effectively extended, which not only solves the problem of initial lock acquisition but also prevents the hidden risk of losing lock in normal operation mode. Owing to these

68
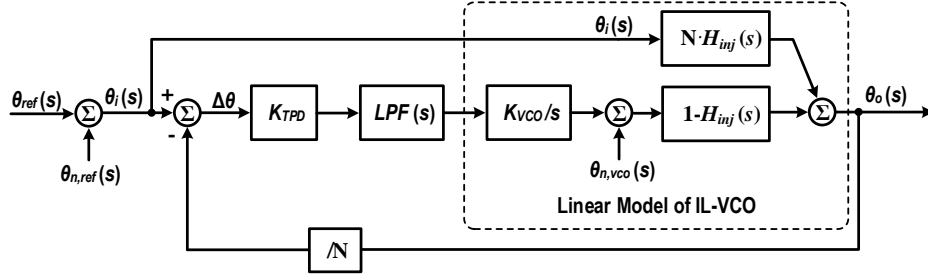
Figure 3.3: Linear model of the RILCM in case of the injection-locked condition, where $\theta_{ref}(s)$, $\theta_i(s)$, $\theta_o(s)$, $\theta_{n,ref}(s)$, $\theta_{n,vco}(s)$ represent the reference input phase, total input phase, output phase, reference input noise, and VCO noise, respectively.

two techniques, the proposed RILCM effectively prevents the mutual-pulling issue in conventional IL-PLLs while keeping their good properties of enhanced in-band noise suppression and high operation robustness, thus making it a competitive option for commercial applications.

3.2.2 Architecture Modeling

Fig. 3.3 displays the detailed linear model of the RILCM with the TAL, where the two main noise sources [i.e., the reference noise $\theta_{n,ref}(s)$ and the RVCO noise $\theta_{n,vco}(s)$] are included. In contrast to traditional PLL, the injection locking gives rise to the inclusion of $[1 - H_{inj}(s)]$ within the TAL loop [85, 89], where $H_{inj}(s)$ denotes the normalized phase transfer function of the injection locking. It can be approximated by an LFP with a left-plane pole around the tracking bandwidth of the IL-VCO [89, 80, 154]. The presence of such an HPF accounts for the in-band phase noise attenuation in terms of resetting the phase errors at the arrival of each injection pulse. To explore the system stability and phase transfer characteristics, the closed-loop characteristic equation is formulated as below,

$$[(\theta_i(s) - \theta_o(s)/N) \cdot K_{TPD} \cdot LPF(s) \cdot K_{VCO}/s + \theta_{n,vco}(s)]$$

$$\cdot [1 - H_{inj}(s)] + \theta_i(s) \cdot N \cdot H_{inj}(s) = \theta_o(s), \quad (3.1)$$

where $\theta_i(s)$ is the summation of the reference input $\theta_{ref}(s)$ and the reference noise $\theta_{n,ref}(s)$. Rearranging Eq. (3.1), the closed-loop transfer function can be obtained by

$$
\begin{aligned}
\theta_o(s) &= \theta_i(s) \cdot \frac{N \cdot LG(s)}{1 + LG(s)} + \theta_i(s) \cdot \frac{N}{1 + LG(s)} \cdot H_{inj}(s) \\
&\quad + \theta_{n,vco}(s) \cdot \frac{1}{1 + LG(s)} \cdot [1 - H_{inj}(s)], \\
&= \theta_{ref}(s) \cdot \frac{N \cdot LG(s)}{1 + LG(s)} \cdot [1 - H_{inj}(s)] + N \cdot \theta_{ref}(s) \cdot H_{inj}(s) \\
&\quad + \theta_{n,ref}(s) \cdot \frac{N \cdot LG(s)}{1 + LG(s)} \cdot [1 - H_{inj}(s)] + N \cdot \theta_{n,ref}(s) \cdot H_{inj}(s) \\
&\quad + \theta_{n,vco}(s) \cdot \frac{1}{1 + LG(s)} \cdot [1 - H_{inj}(s)],
\end{aligned}
\tag{3.2}
$$

where the first line represents the phase transfer of $\theta_{ref}(s)$, the second line stands for the noise transfer of $\theta_{n,ref}(s)$, the third line denotes the noise transfer of $\theta_{n,VCO}(s)$, and $LG(s)$ is the loop gain, written as

$$
LG(s) = \frac{1}{N} \cdot K_{TPD} \cdot LPF(s) \cdot \frac{K_{VCO}}{s} \cdot [1 - H_{inj}(s)].
\tag{3.3}
$$

***Stability Consideration*-** The lock acquisition in this RILCM is achieved by alternatively enabling the PLL and TAL under the control of the LSSM. Hence, its stability problem involves two aspects. One is that the transition process between the two loops must be smooth so as to avoid large voltage ripples on the control line of the IL-VCO. The other is that the PLL and TAL must be separately stabilized regardless of whichever loop is activated. To guarantee smooth switching transitions, the MUX is placed before the LPF (see Fig. 3.2) such that the sudden charge injection/extration caused by the loop switching can be effectively neutralized by the large capacitor in the shared LPF. To provide sufficient phase margin for the PLL, a resistor in series with the loop filter capacitor is added in the LPF to create a stabilizing zero in the loop gain. However, this stabilizing zero is not needed in the TAL since a pole located at the origin can be eliminated by the $[1 - H_{inj}(s)]$ in Eq. (3.3). Accordingly, the serial resister that aids to stabilize the PLL should be shorted to maintain an adequate phase margin when the TAL is selected (see Fig. 3.2). The elimination of the serial resistor also helps to reduce the ripples on the control voltage, hence improving the spur
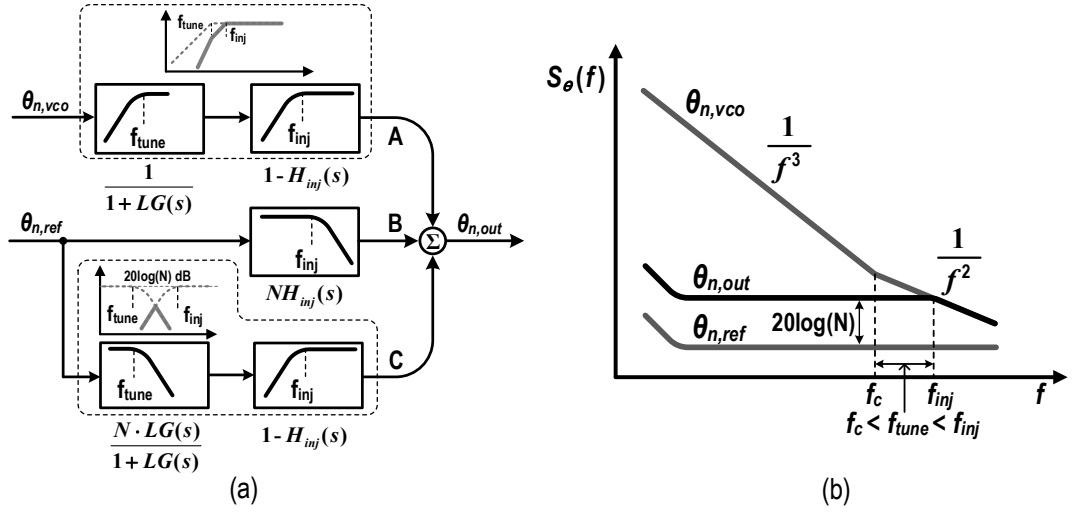
Figure 3.4: NTF characteristics of the RILCM. (a) NTF behaviors and (b) simplified noise shaping characteristics. Here, f_c is the corner frequency of the oscillator, f_{inj} stands for the bandwidth of the injection locking, f_{tune} denotes the tunable bandwidth of the TAL, $1/f^2$ represents the white noise of the oscillator, and $1/f^3$ is the flick noise of the oscillator.

performance. Referring to Eq. (3.3), we can find that the secondary pole within the TAL is subject to the dominant pole of $H_{inj}(s)$. Therefore, the unity-gain bandwidth of the loop gain should be designed smaller than the -3 dB bandwidth of $H_{inj}(s)$ so as to guarantee sufficient phase margin. Meanwhile, to suppress the $1/f^3$ noise of the VCO, the TAL bandwidth f_{tune} is expected to be larger than the corner frequency f_c of the VCO. In this design, the bandwidth of the injection locking is designed to be 40 MHz while the TAL bandwidth can be adjusted by changing the CP current.

Noise Shaping Characteristics- Following the closed-loop transfer function in Eq. (3.2), Fig. 3.4(a) describes the noise transfer function (NTF) behaviors of the two main noise sources $\theta_{n,ref}$ and $\theta_{n,vco}$. The three NTFs in Eq. (3.2) are generalized into three noise transfer paths: A, B, and C. Path A stands for the NTF from the VCO, path B refers to the main NTF of the reference, and path C represents the secondary NTF path from the reference. The TAL leads to the inclusion of an extra $[1/(1 + LG(s))]$ within the NTF of the IL-VCO [see path A in Fig. 3.4(a)] and introduces an additional path [see path C in Fig. 3.4(a)] from the reference noise to the VCO output. The equivalent NTFs for these two paths are plotted in gray solid line [see Fig. 3.4(a)]. For path A, the presence of the $[1/(1 + LG(s))]$ provides 20 dB/dec noise suppression. Combining with the 20 dB/dec attenuation contributed by the $[1 - H_{inj}(s)]$, the

$1/f^3$ noise of the VCO can be significantly suppressed as long as the bandwidths of f_{tune} and f_{inj} are larger than the VCO corner frequency f_c. This requirement can be easily satisfied by adjusting the TAL loop parameters and injection strength. Path B denotes the main noise transfer mechanism of the RILCM, which can be considered as the reference NTF of the IL-VCO without the TAL. As for path C, the reference noise transferred to the VCO output is negligible. Because the equivalent NTF of the cascaded $[LG(s)/(1 + LG(s))]$ and $[1 - H_{inj}(s)]$ shows significant attenuations over all frequencies as long as their bandwidths satisfy $f_{tune} < f_{inj}$ [see Fig. 3.4(a)]. This requirement can be naturally met as it coincides with the loop stability request. Fig. 3.4(b) presents the simplified noise-shaping characteristics of the proposed RILCM with the TAL. The injection locking along with the TAL can completely suppress the in-band noise of the VCO, hence making its in-band noise tightly track the reference noise.

3.3 Injection-Locked Ring Voltage-Controlled Oscillator (IL-RVCO)

The LC oscillator has demonstrated excellent performance on phase noise and power efficiency. However, its large area occupation, narrow tuning range, and inductor-caused cross-coupling make it less suitable for multi-lane applications [153, 151]. In contrast, the ring oscillator shows more potential in such applications because of its wide operation range, multi-phase generation, and compact layout implementation. Moreover, the recently developed injection locking technique makes it possible to achieve a comparable jitter performance to its LC counterpart [82, 145]. This section will firstly describe the IL-RVCO based on a new FS-PDDC, and then explore the relative phase difference (i.e., the crossing point of the IL-RVCO output relative to the injection center) with respect to the frequency offset.

(a)

(b)   (c)
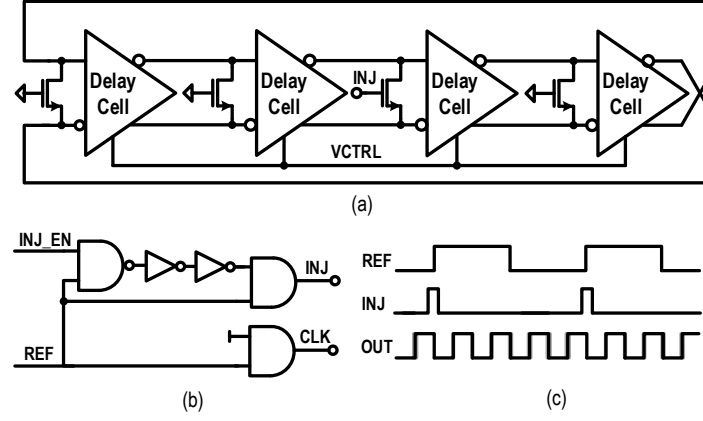
Figure 3.5: IL-RVCO. (a) Four-stage RVCO implementation, (b) pulse generator, and (c) injection locking behavior.

(a)   (b)

(c)   (d)
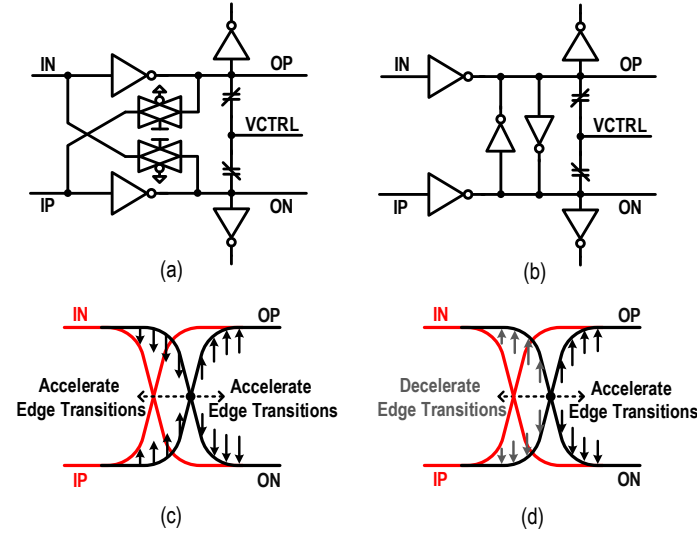
Figure 3.6: (a) FTG-based FS-PDDC, (b) CCI-based FS-PDDC, (c) effect of the FTGs, and (d) effect of the CCIs. Here, the arrows stand for the effort directions that are offered by the FTGs or CCIs.

3.3.1 Implementation of the IL-RVCO

Fig. 3.5(a) shows the adopted IL-RVCO, which consists of four identical delay cells and its frequency is adjusted by the control voltage (VCTRL). The injection pulse is applied to one of the four stages, while other injection transistors are connected to the ground to avoid disrupting injection. By injecting the narrow pulses produced by the pulse generator in Fig. 3.5(b) into the IL-RVCO, the accumulated jitter can be periodically corrected by the injection pulse at every reference cycle [see Fig. 3.5(c)]. Fig. 3.6(a) presents the proposed FS-PDDC, where the pseudo differential output is

ensured by a pair of forward transmission gates (FTGs). To illustrate the unique features of this FS-PDDC, another representative implementation is also described in Fig. 3.6(b), whose pseudo differential output is guaranteed by two cross-coupled inverters (CCIs) [155].

The common feature of these two FS-PDDCs is that they both employ a pair of back-to-back varactors to tune the free-running frequency of the VCO, where the VCTRL is fed to the common body of the two varactors. In principle, when the VCTRL goes down, the equivalent voltage applied to the varactors increases, implying that the delay cells need to drive higher load capacitances. Hence, the free-running frequency of the VCO becomes low. Conversely, as the VCTRL goes high, the VCO frequency will rise. Compared to conventional supply-regulated delay cells [156, 155], the main advantages of these FS-PDDCs are their high output swing and fixed common-mode voltage (around half of the power supply), which preclude the demands of level shift correction [123, 157], and thereby facilitate their applications. Fig. 3.6(c) and (d) describes the effects on edge transitions that are contributed by the FTGs and CCIs [see Fig. 3.6(a) and (b)], where the arrows stand for the effort directions that are offered by the FTGs or CCIs. Obviously, the arrows in Fig. 3.6(c) always coincide with the edge transitions, thus accelerating them. The reason is that the transmission delay from IP to OP (IN to ON) through the FTG is similar to that from IN to OP (IP to ON) via the inverter. In contrast, the CCIs decelerate the edge transitions in the portion preceding the crossing point, while accelerating the edge transitions succeeding the crossing point [see Fig. 3.6(d)]. This can be understood by realizing that the state changes of the CCIs happen at the crossing point. Before that, they provide negative feedback to preserve previous states [see the gray arrows in Fig. 3.6(d)]. After that, they contribute positive feedback to speed up the state changes [see the black arrows in Fig. 3.6(d)]. Compared to the half-negative and half-positive feedback associated with the CCIs in Fig. 3.6(b), the FTGs in Fig 3.6(a) contribute persist positive feedback, which makes the FTG-based FS-PDDC a more promising solution for high-frequency applications.
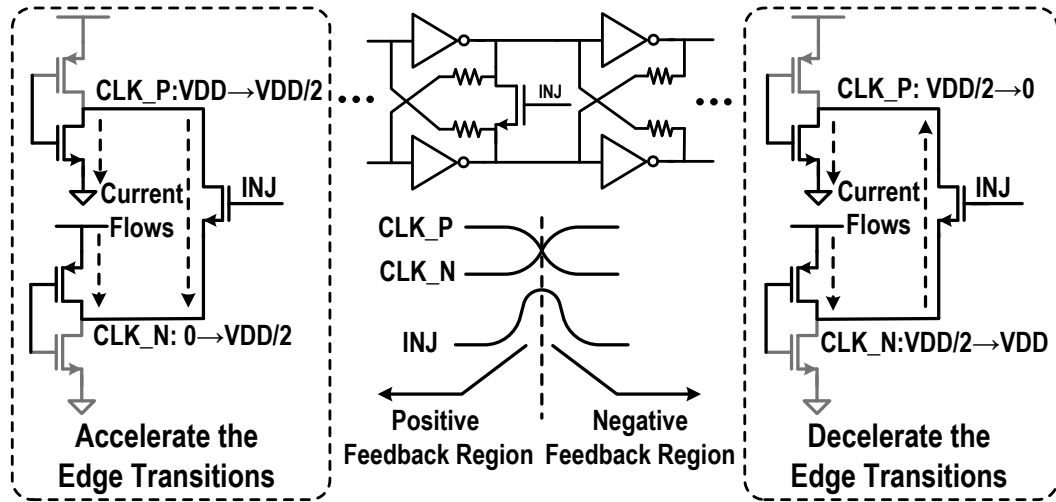
Figure 3.7: Effect of the injection pulse on the speed of edge transitions, where the proceeding portion of the injection pulse contributes positive feedback while the following portion provides negative feedback.

3.3.2 Relationship Between the Relative Phase Difference and the Frequency Offset

Previous work has demonstrated that the most challenging task in the TAL is how to detect the difference between the free-running frequency of the VCO and the target frequency, since the VCO output frequency is not changed with the control voltage in locked conditions [82, 158]. Inspired by the design in [82], the relative phase difference of the VCO output with respect to the center of the injection pulse is used to estimate the frequency offset in this design. To explore the relationship between the relative phase difference and the frequency offset, Fig. 3.7 summarizes the effect of the injection pulse on the speed of edge transitions. An ideal injection is depicted at the center of the diagram when the crossing point of the differential output clock occurs at the center of the injection pulse. The left subfigure describes the current flow through the injection transistor for the preceding part of the injection pulse. During this period, CLK_P falls to VDD/2 from VDD while CLK_N rises to VDD/2 from 0. The current flows from CLK_P to CLK_N through the injection transistor, providing an additional current path for both pulling down CLK_P and pulling up CLK_N. Therefore, the preceding part of the injection pulse contributes a positive feedback that accelerates both the rising and falling edges. On the contrary, the following part of
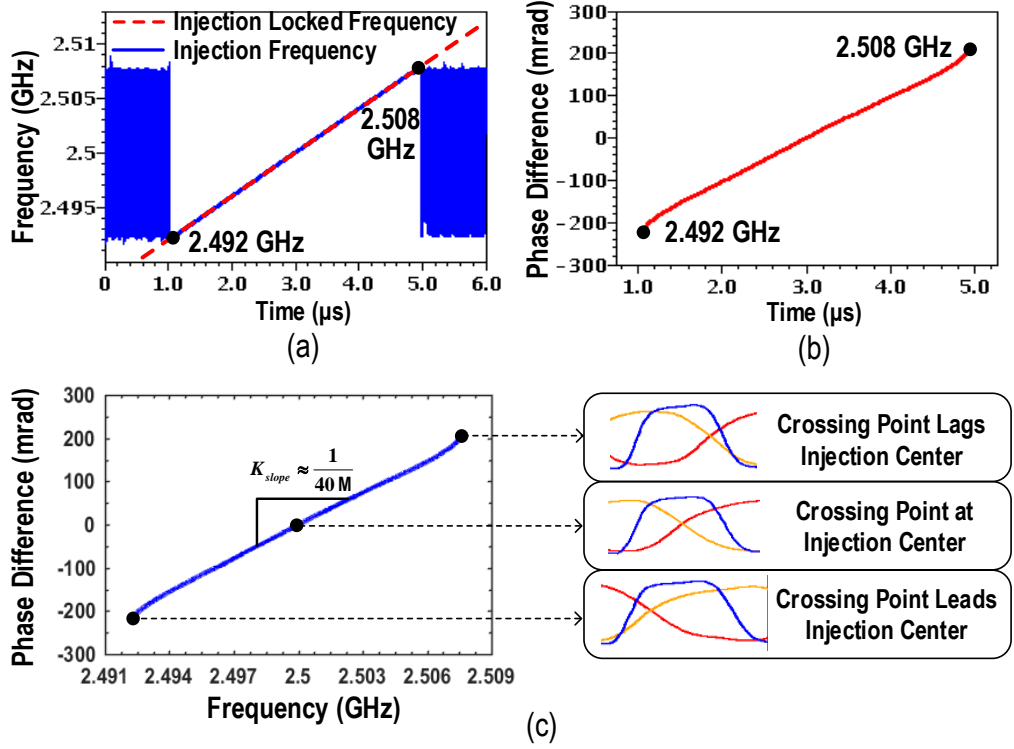
Figure 3.8: Transient simulation results of the IL-RVCO. (a) Injection locking range, (b) the relative phase difference with respect to the transient time, and (c) the relative phase difference versus the frequency offset.

the injection pulse results in negative feedback. As illustrated in the right subfigure, CLK_P falls from VDD/2 to 0 while CLK_N rises from VDD/2 to VDD. The current flows from CLK_N to CLK_P, which slows down the edge transitions. Based on the above analysis, when the free running frequency is lower than the target frequency, the output clock period needs to be decreased to catch up the injection signal and hence the crossing point should be located succeeding the injection center to make sure that the positive feedback is stronger than the negative feedback to speed up the VCO. Conversely, the crossing point should be located proceeding the injection center to slow down the VCO. When the free running frequency equals the target frequency, the injection center should be located at the crossing point, where the phase-noise reduction contributed by the injection locking reaches its maximum [151].

Fig. 3.8 displays the transient simulation results of the IL-RVCO, where an injection pulse with a slow ramping frequency is applied to the RVCO, while the control voltage is set to a fixed value that makes the center frequency of the IL-RVCO locate

around 10 GHz. The simulated frequencies of the RVCO's quarter-rate output and the injection pulse are plotted in Fig. 3.8(a). Obviously, the IL-RVCO can track the injection pulse in a locking range of 2.491-2.509 GHz. Fig. 3.8(b) depicts the relative phase difference (i.e., the crossing point of the IL-RVCO output to the center of the injection pulse) with respect to the transient time. Replacing the transient time with the frequency offset in the horizontal axis, the relationship between the relative phase difference and the frequency offset can be obtained [see Fig. 3.8(c)], where the visual locking positions are also given in the right waveforms. Clearly, the relative phase difference can be regarded as linear with respect to the frequency offset in the vicinity of the locking center. According to the analysis in Appendix A, the reciprocal of the slope K_{slope} is actually equal to the tracking bandwidth of the phase transfer function $H_{inj}(s)$ in Fig. 3.3. The linear relationship of the relative phase difference versus the frequency offset and the explicit tracking bandwidth lay a solid foundation for the FTL design, including the TPD implementation, stability analysis, and bandwidth optimization.

3.4 The Proposed Phase Difference Detection

The main function of the TPD in the FTL is to detect the phase difference from the crossing point of the differential output clock to the injection-pulse center to indicate the frequency deviation between the free-running frequency of the VCO and the target output frequency. Many attempts have been made to obtain an accurate phase difference. In [153], a sub-sampling TPD (SSTPD), which embeds the sample-and-hold (S/H) circuits into one of the stages, is adopted to monitor the injection timing. However, the heavy load of the S/H along with the subsequent voltage-to-current can dramatically prolong the delay of the SSTPD embedded stage, which not only slows down the maximum operation speed of the VCO but also leads to an I, Q matching problem. Additionally, its output polarity is unpredictable since the sampled output is subject to the injection positions (falling edge or rising edge). This could lead to a probability of 50% to form an undesired positive feedback at the initial state. Another TPD consisting of four AND gates, six D-flip-flops (DFFs), and several logic gates is developed to convert the phase differences to voltage pulses [146]. Nevertheless, its
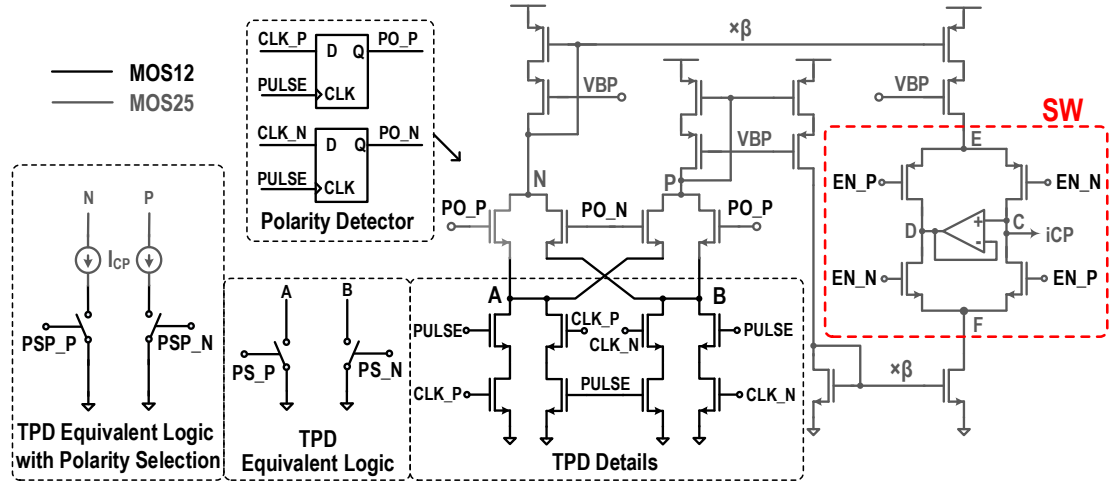
Figure 3.9: Circuit implementation of the combined TPD and CP.

complicated circuit implementation increases power consumption and area occupation. Meanwhile, the logic operation involving with the narrow injection pulse constrains its maximum operation frequency, thus making it less suitable for high-speed applications.

To address these issues, a tightly combined TPD and CP with a polarity detector (POD) is proposed (see Fig. 3.9), where both fast 1.2 V transistors and large-size 2.5 V transistors are employed to provide the capabilities of high operation speed and high matching accuracy. The phase detection is carried out by comparing the differential paths that are connected to the injection pulse and the VCO's complementary outputs. Each path adopts two symmetrically connected branches to performs the NAND function. Owing to the compact symmetrical implementation that solely utilizes fast NMOS transistors, this TPD can achieve a high operation speed with a low power consumption. For the output of the CP, a differential structure with the enabling signals EN_P and EN_N along with a voltage follower AMP is applied to realize smooth mode transitions between the PLL and TAL. The voltage follower is used to make the voltage V(D) always follow V(C) to avoid obvious charge extraction when the output is activated. Similarly, the CP in the PLL loop also utilizes these techniques to make the two charge pumps (CP1 and CP2) compatible with each other. It is worth noting that the CP works in 2.5 V power domain, which is capable of producing high-swing control voltages to help to extend the operation range of the RVCO.
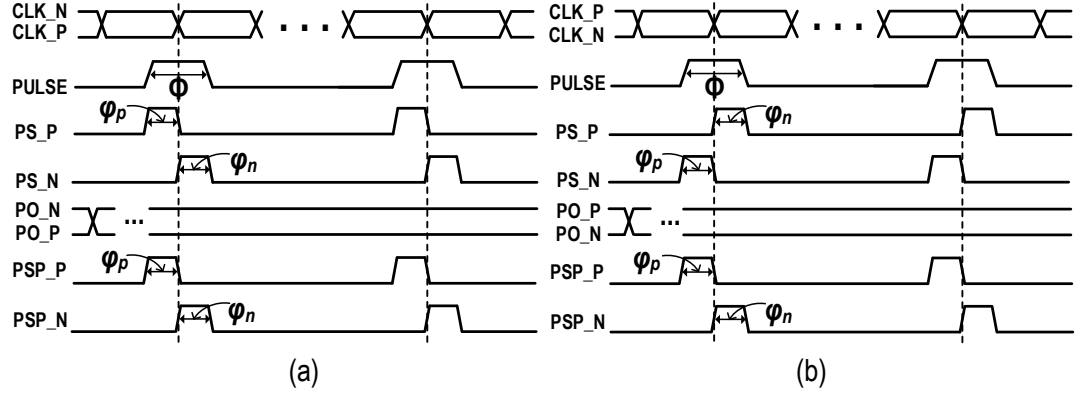
Figure 3.10: Locking behaviour of the proposed TPD. (a) Waveforms when injection occurs at the falling edge of CLK_P, and (b) waveforms when injection occurs at the rising edge of CLK_P.

3.4.1 Principle of the Proposed Timing-Adjusted Phase Detector

Fig 3.10 shows the locking behaviour of the proposed TPD, where the operation of the TPD logic can be considered as a pair of on/off switches that are controlled by the equivalent signals of PS_P and PS_N. Obviously, the injection pulse is partitioned into two sections φ_p and φ_n by the crossing point of the high-speed complementary clocks. When the injection center is leading the crossing point, the pulse width φ_p is larger than φ_n, and vice versa. This width difference is then converted to current by the following CP in Fig. 3.9, where the instant current is determined by the threshold voltage of the common-gate high voltage transistor and its source-equivalent turning-on resistor of the phase detecting transistors.

When the TAL is stable, the average output current of the CP should be zero, thus the crossing point of the VCO's output should be located at the center of the injection pulse. It is under such an exact condition that the frequency of the free-running VCO becomes close to the target frequency, according to the analysis of the relationship between the phase difference and frequency offset in Section 3.3.2. This means that the alignment of the injection pulse center and VCO's output crossing point is a common target for both the injection locking and frequency tracking. Therefore, the race condition between the two pulling forces is eliminated.

3.4.2 Polarity Selection

One common problem in the existing TPD-based TALs is that an improper injection position may lead to an undesired positive feedback [82, 153]. To be more specific, Fig. 3.10 illustrates the functional waveform of the TPD logic when injection occurs at different transition edges. For the condition that the injection happens at the rising edge of CLK_P as shown in Fig. 3.10(a), the equivalent pulses of PS_P and PS_N can be given by

$$PS\_P = CLK\_N \cdot PULSE, \tag{3.4}$$

$$PS\_N = CLK\_P \cdot PULSE. \tag{3.5}$$

When the injection occurs at the falling edge of CLK_P as depicted in Fig. 3.10(b), they can be induced by

$$PS\_P = CLK\_P \cdot PULSE, \tag{3.6}$$

$$PS\_N = CLK\_N \cdot PULSE. \tag{3.7}$$

Clearly, if no measure is taken, the value of the detected phase difference will change to the opposite sign as the injection position switches between the two possible locking conditions depicted in Fig 3.10. This will make the TAL have a 50% chance to operate in positive feedback in the initial state, which may cause a false lock or even a fail lock since the injection locking range is small. To solve this problem, a POD shown in Fig. 3.9 is introduced to produce the polarity signals PO_P and PO_N by distinguishing the edge types at the injection instant. The equivalent function of the TPD with the polarity selection is also depicted in Fig. 3.9, where the waveforms for the final equivalent inputs of PSP_P and PSP_N are described in Fig. 3.10. It can be seen that the connection of the detected pulses of PS_P and PS_N are exchanged by the polarity selection signals of PO_P and PO_N. Therefore, the same equivalent pulses of PSP_P and PSP_N for both conditions shown in Fig. 3.10 can be acquired. Consequently, the possible positive feedback is avoided.
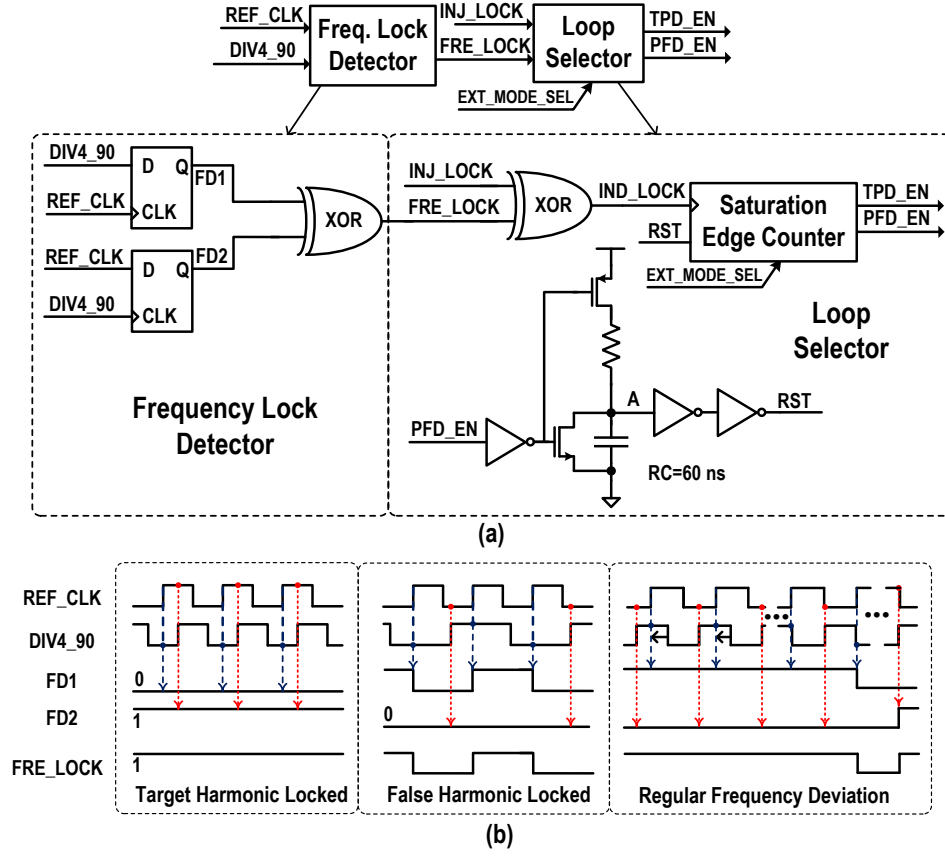
Figure 3.11: Implementation of the introduced LSSM. (a) Circuit details and (b) behavior of the FLD.

3.5 Mechanism of the Lock-Loss Detection and Lock Recovery (LLD-LR)

3.5.1 Operation Process of the LLD-LR

There exist initial lock acquisition problem and losing lock risk in previous TPD-based TALs due to their limited locking range and weak lock-acquisition ability [146, 153]. To overcome these difficulties, a complete LLD-LR mechanism is embedded into the hybrid FTL under the control of the LSSM. Fig. 3.11(a) gives the details of the LSSM. It consists of a frequency lock detector (FLD) and a loop selector (LS). Applying the injection-lock indicator INJ_LOCK and frequency-lock indicator FRE_LOCK to the LS, the total edge transitions on INJ_LOCK and FRE_ LOCK are recorded by a saturated counter. Once the number reaches a specific value (4 in this design), the LS will switch the FTL from TAL to PLL to start a lock-acquisition process. Simultaneously, the RC timer with a time constant of 60 ns is launched to charge node A.

When its voltage climbs to the inverter threshold, the LS is reset and the FTL switches back to TAL to engage injection locking. If the VCO successfully locks to the injection pulse at the target frequency, both the INJ_LOCK and FRE_LOCK will stay static, and so does the LS. Otherwise, this process will be repeated until injection locking is achieved. During the initial period, the injection lock can be obtained by repeating this LLD-LR process. During the normal operation period, lock loss can be detected in time to activate this LLD-LR process. Additionally, it is worth noting that almost no extra power is dissipated in the normal loss detecting mode since there is no signal transition in the LSSM.

3.5.2 Principles of the Lock Loss and False Lock Detection

Fig. 3.11(b) describes the functional behavior of the FLD. When the feedback frequency is exactly equal to the reference frequency under the locked condition [left subset in Fig. 3.11(b)], the outputs FD1 and FD2 of the mutual sampling D-flip-flops (DFFs) stay unchanged and thus the frequency-lock indicating signal FRE_LOCK remains static. For the case when the frequency of the feedback clock equals the sub-harmonic or multiple-harmonic of the reference frequency [middle subset in Fig. 3.11(b)], the FRE_LOCK must be the delayed version of the low-frequency clock since the mutual sampling can reserve all the timing information of the low-frequency clock. For the regular condition when there is a frequency deviation between the feedback clock and reference clock [right subset in Fig. 3.11(b)], the FLD can also produce transitions on FRE_LOCK. Generally, only when the VCO is running at the target frequency, the frequency-lock indicating signal FRE_LOCK stays static. Hence, the presence of transitions on FRE_LOCK can be considered as a frequency-lock failure.

Although the FLD can detect any frequency deviation [see Fig. 3.11(b)], it takes a long time to bring in a cycle slip to generate the frequency-loss edge transitions when the frequency of the VCO is close to the target frequency. Due to the small locking range, there is a high likelihood of such an occurrence during the injection locking process. To speed up the lock-loss detection, the INJ_LOCK (buffered version of PO_P) is also applied to the LS. Recalling the cases when VCO is locked to the

injected pulse as shown in Fig. 3.10, the DFFs in the POD triggered by the rising edge of the injected pulse will always sample the same logic level. Therefore, the polarity signal INJ_LOCK stays unchanged either in logic high or logic low. Conversely, if the injected pulse fails to lock to the VCO, the injection position will change with phase error accumulation, which will finally bring in a cycle slip. It is at this specific moment the polarity signal INJ_LOCK will present an edge transition, which can be considered as an effective indicator of injection-lock failure. By monitoring the edge transitions on both INJ_LOCK and FRE_LOCK, any injection failure including injection-lock loss and false harmonic lock can be quickly detected.

3.6 Experimental Results

3.6.1 Tools and Fabrication Process

The RILCM is designed using a Dell R730 server with two E5-2609V4 CUPs, 128 G memory and 8 T hard disk. The schematic, layout, and simulation are respectively finished by Schematic Composor, Virtuoso Layout, and Spectre/aps that are developed by Cadence. The software version is IC5141. The layout verification and parasitic extraction are carried out by layout versus schematics (LVS)/design rule check (DRC) and parasitic extraction (PEX) using Caliber2013 that is developed by Mentor Graphics. To characterize the jitter performance of the fabricated prototype, a very clean reference clock is generated by a KEYSIGHT N5191A. For a 2.5 GHz output, it presents phase noises of -146 dBc/Hz and -150 dBc/Hz at 1 MHz and 10 MHz offset, respectively. The rms-jitter integrated from 10 kHz to 40 MHz is 38.7 fs. Without special explanation, the rms-jitter in the following description is designated to be integrated over the same frequency range.

The prototype chip is designed and fabricated utilizing a 65 nm process. Under a typical corner, the cut-off frequency (f_T) of the NMOS transistor and the inverter delay with a fan-out-of-4 in this process achieve 200 GHz and 13 ps, respectively. These two metrics indicate that the utilized 65 nm process is able to provide enough bandwidth and timing margin for the targeted 10 GHz RILCM design. Although an advanced
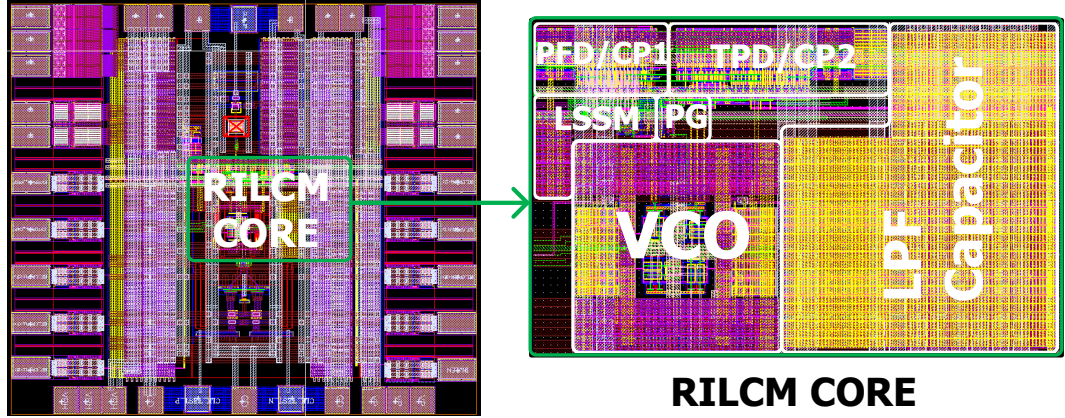
Figure 3.12: Layout view of the whole RILCM chip, where the block placement of the core circuits is illustrated in the left view.
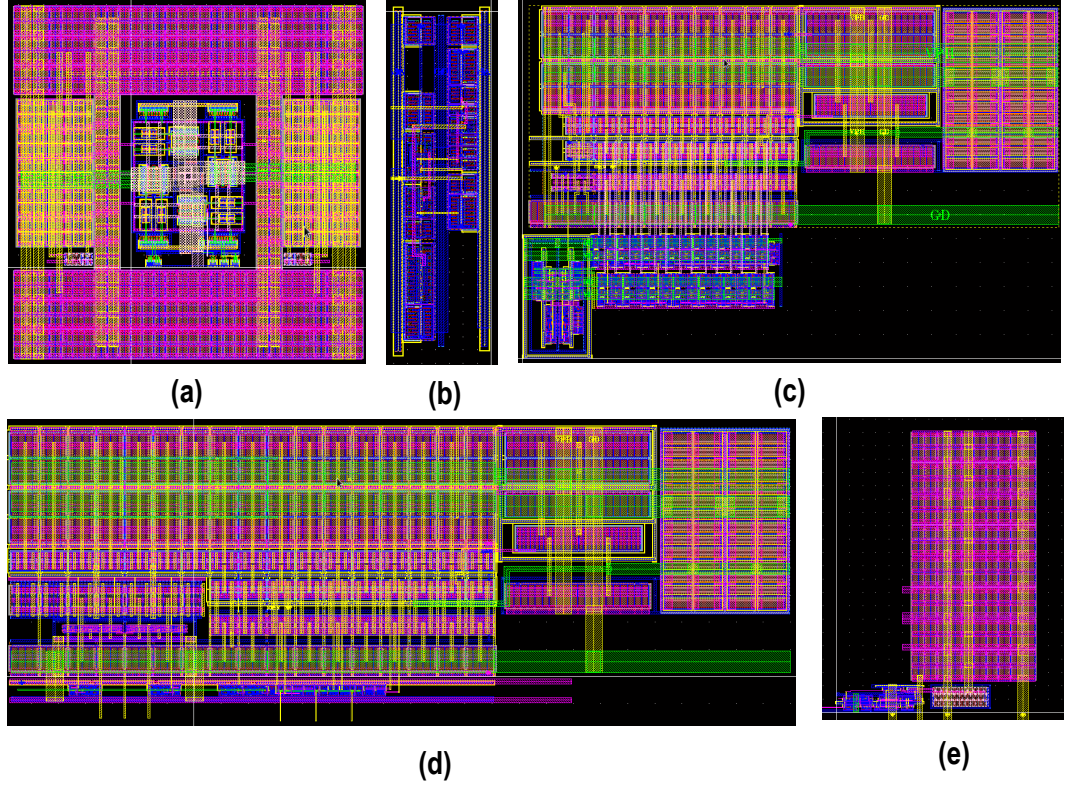
Figure 3.13: Layout views of the crucial blocks. (a) VCO, (b) PG, (c) PFD/CP1, (d) TPD/CP2, and (e) LSSM.

process with a smaller minimum channel length such as 45 nm, 32 nm, 22 nm and 16 nm can offer higher f_T and shorter inverter delay, their high prices make them not available for us. Fortunately, our RILCM mainly focuses on the hybrid-loop frequency tacking architecture, improved FS-PDDC-based RVCO, TPD circuit implementation and LLD-LR mechanism. These techniques can still be verified by the economical and practical 65 nm CMOS process.

3.6.2 Layout and Simulation Results

3.6.2.1 Layout Designs

Fig. 3.12 displays the layout view of the whole RILCM chip, where the block placement of the core circuits is illustrated in the left view. The PG is placed very close to the VCO to reduce the parasitic capacitance of the pulse output, and hence provides an injection pulse with sharp edges. The PFD/CP1, TPD/CP2, and LSSM are placed together to facilitate the connections among the mode selection signals. The LFP is put close to the VCO to reduce the effect caused by supply fluctuations. Fig. 3.13 further presents the layout views of the crucial blocks. As shown in Fig. 3.13(a), the VCO layout is implemented in a ring, which assists to make each of the delay cell share the same parasitic capacitance, and hence optimize the noise performance of the VCO. The main design point of the PG is to optimize the parasitic capacitance on the pulse output node [see Fig. 3.13(b)]. As for the PFD/CP1 and TPD/CP2 shown in Fig. 3.13(c) and (d), we have paid special attentions to guarantee the two comparison branches are symmetrical, and thereby reduce the mismatch between the two comparing phases. The main consideration for the LSSM is the convenience to route the connection signals.
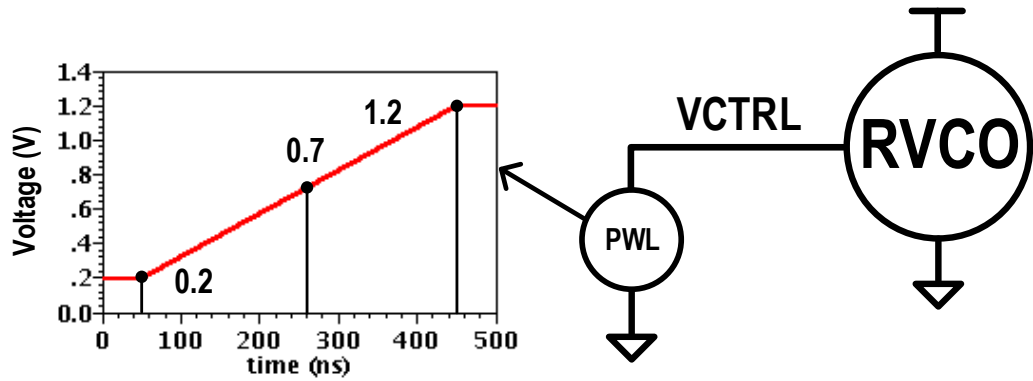
Figure 3.14: Simulation setup of the RVCO, where the left curve depicts the VCTRL of the RVCO.
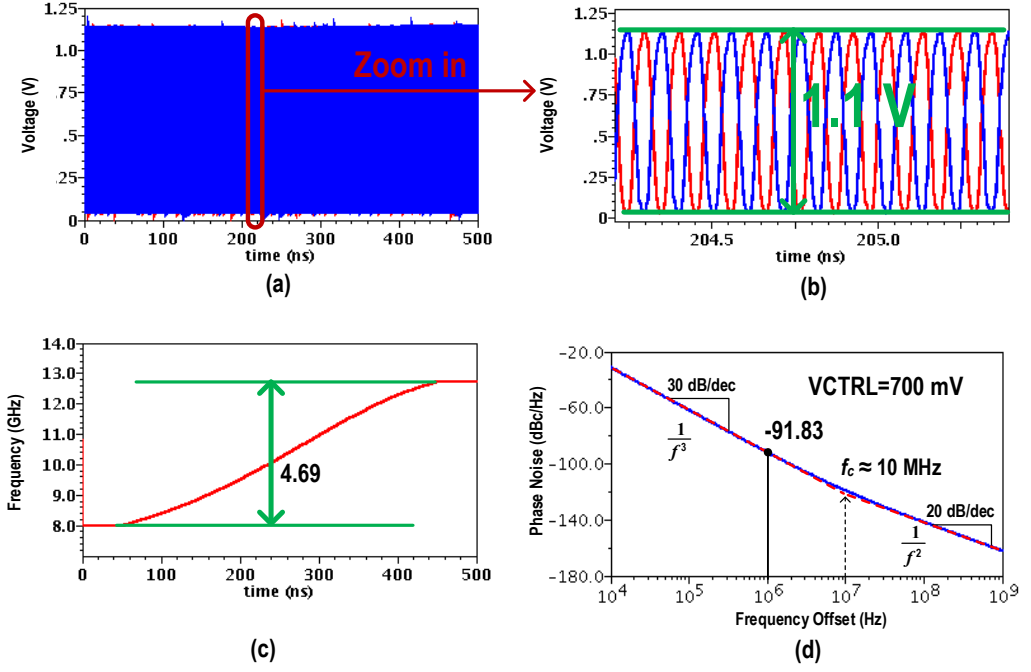
Figure 3.15: Simulation results of the RVCO. (a) Differential output clock, (b) swing reduction, (c) frequency range, and (d) phase noise.
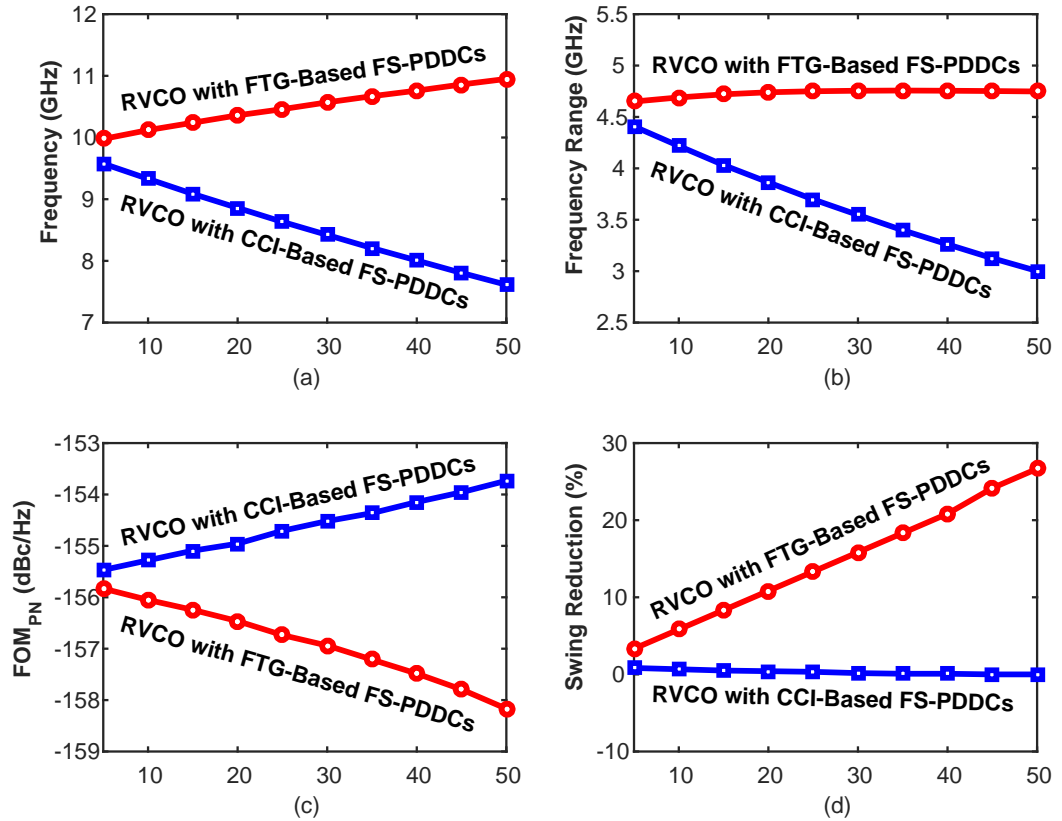
Figure 3.16: Simulated performance comparison of the RVCOs with FTG-based and CCI-based FS-PDDCs in terms of (a) operation frequency, (b) frequency range, (c) FOM_{PN}, and (d) swing reduction. Here, the horizontal axes denote the percentage of the FTG/CCI to the main inverter in dimension.

3.6.2.2 Simulated Performance of the RVCO

Fig. 3.14 describes the simulation setup of the RVCO, where the VCTRL rises from 0.2 V to 1.2 V in a liner mode to continuously adjust the operation frequency of the RVCO. Fig. 3.15 (a) demonstrates the transient output waveforms of the RVCO. Fig. 3.15 (b) shows the zooming waveforms, which clearly show that the swing of the RVCO outputs is shrunk to 1.1 V. Fig. 3.15 (c) displays the operation frequency of the RVCO, which shows that the frequency range of the RVCO is 4.69 GHz when the VCTRL changes from 0.2 V to 1.2 V. Fig. 3.15 (d) gives the simulated phase noise of the RVCO when the VCTRL is set to 0.7 V. The corner frequency of the $1/f^3$ noise is around 10 MHz and the phase noise at 1 MHz offset is -91.83 dBc/Hz.

To compare the performance of the RVCOs with the FTG-based and CCI-based FS-PDDCs that are described in Fig. 3.6(a) and (b), we repeated the simulations in Fig. 3.15 using the setup in Fig. 3.14 while changing the ratio of the the FTG/CCI to the main inverter. Fig. 3.16 summarizes the simulated comparison results, where the horizontal axis is the percentage of the FTG/CCI to the main inverter in dimension. As depicted in Fig. 3.16(a), (b), and (c), the RVCO integrated with the FTG-based FS-PDDCs holds the advantages of higher operation frequencies, wide tunable ranges, and lower $\mathrm{FOM_{PN}}$s over that with the CCI-based FS-PDDCs. Here, the $\mathrm{FOM_{PN}}$ refers to the the phase noise FOM of the VCO, which is defined by

$$FOM_{PN} = L\left(f_0, \Delta f\right) + 10log\left(\frac{\Delta f^2}{f_0^2} \cdot \frac{P_{DC}}{1mW}\right), \qquad (3.8)$$

where $L(f_0, \Delta f)$ is the single-side band phase noise at a frequency offset Δf from a carrier frequency at f_0, and P_{DC} denotes the power consumption. A lower $\mathrm{FOM_{PN}}$ indicates a better VCO [147]. When the percentage of the FTG/CCI to the main inverter increases from 5% to 50%, the metrics of the RVCO with the FTG-based FS-PDDCs show a trend of optimization [see the red curves with circle markers in Fig. 3.16(a), (b), and (c)], while those associated with the RVCO using the CCI-based FS-PDDCs exhibit a deterioration trend [see the blue curves with square markers in Fig. 3.16(a), (b), and (c)]. Particularly, for the RVCO with the FTG-based FS-PDDCs, the opera-

tion frequency rises from 9.98 to 10.95 GHz, the tunable range slightly increases from 4.65 to 4.75 GHz, and the FOM_{PN} upgrades from -155.8 to -158.2 dBc/Hz. As for the RVCO with the CCI-based FS-PDDCs, the operation frequency drops from 9.6 to 7.6 GHz, the tunable range declines from 4.4 to 3.0 GHz, and the FOM_{PN} degrades from -155.5 to -153.7 dBc/Hz. These are because the increased FTGs provide a higher pre-driving ability and thus enhance the positive feedback, while the enlarged CCIs offers a superior reinforcement on the negative feedback over that on the positive feedback. On the other hand, the increased pre-driving ability gives rise to a prominent swing reduction on the RVCO with the FTG-based FS-PDDCs [see the red curve with circle markers in Fig. 3.16(d)], which is not desired in some applications. In this design, the percentage of the FTG to the main inverter is chosen to be 15% to ensure that the swing reduction is controlled under 10%.
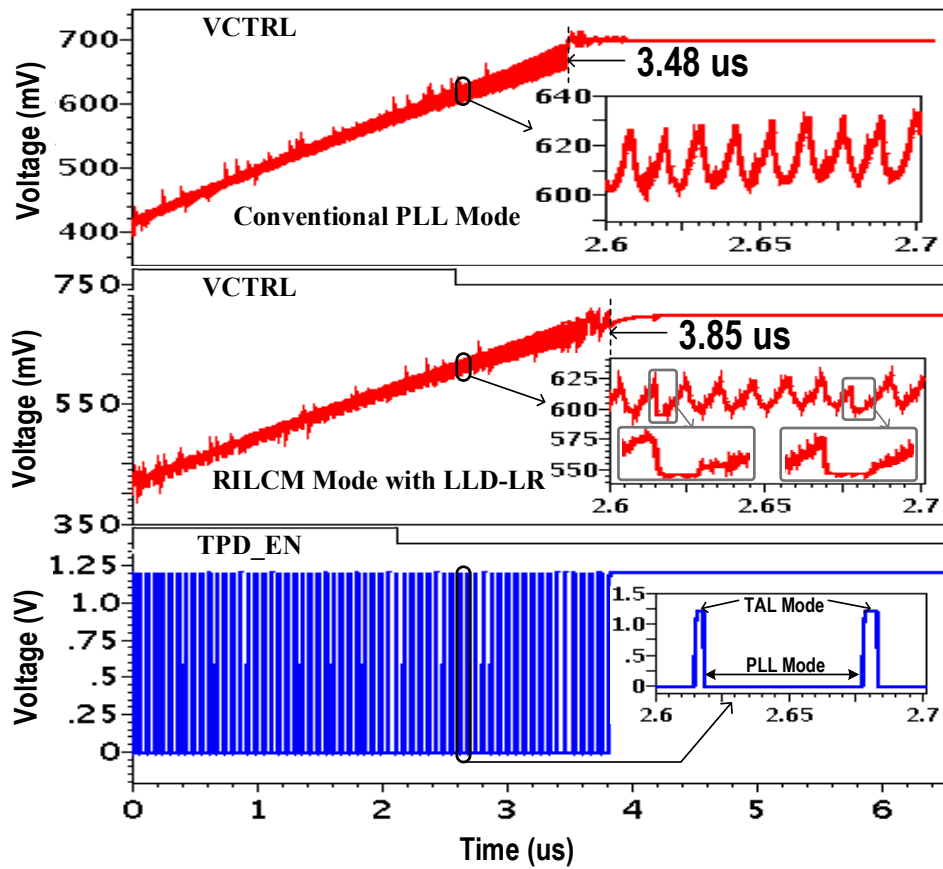
Figure 3.17: Comparison of the transient procedure when operating in conventional PLL mode and RILCM mode with LLD-LR.
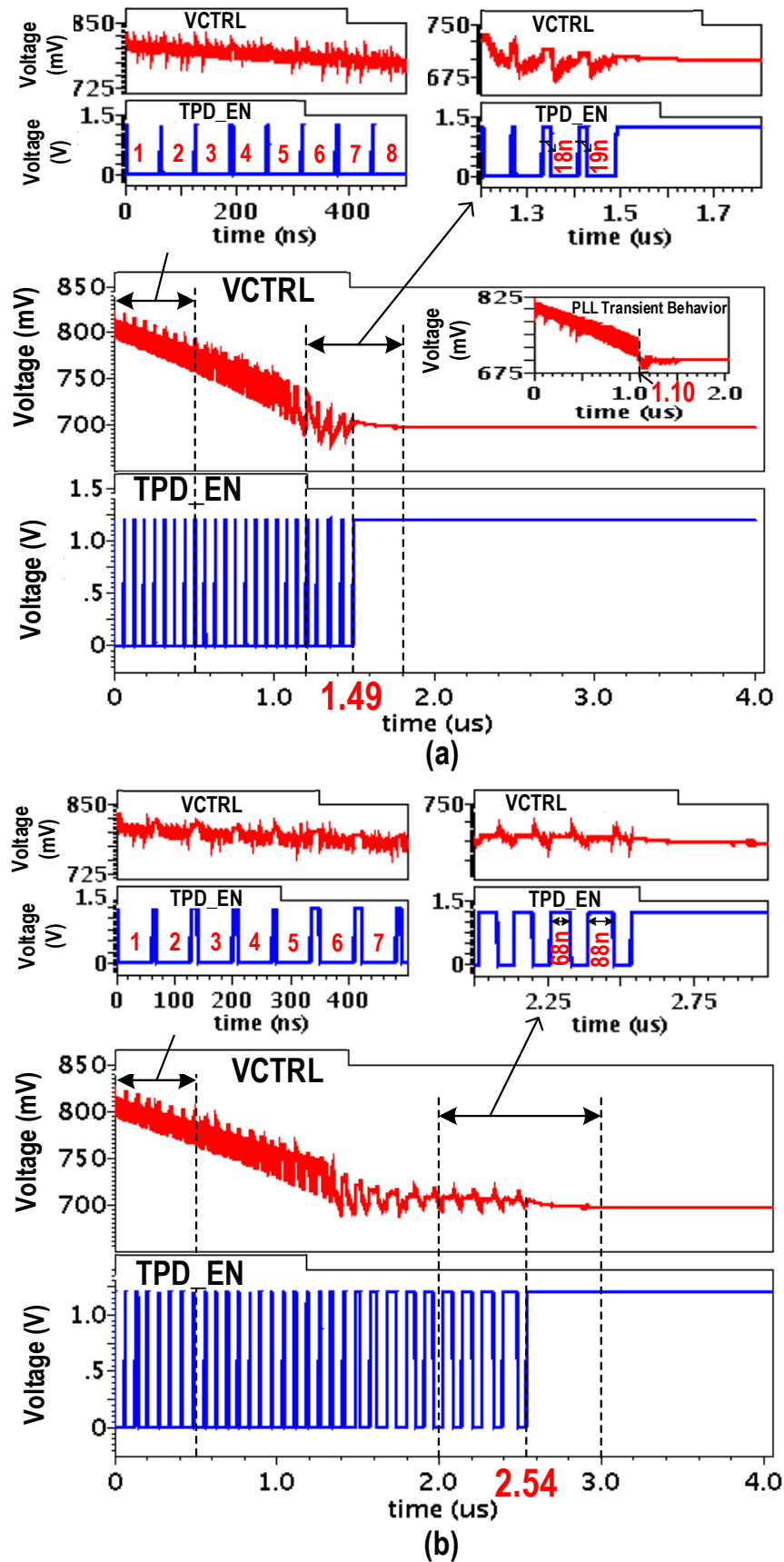
Figure 3.18: Transient behavior comparison. (a) With injection-lock indicator INJ_LOCK and (b) without injection lock indicator INJ_LOCK.

3.6.2.3 Settling Behavior of the Hybrid Frequency Tracking Loop

The simulated settling behavior of the proposed RILCM with the LLD-LR is plotted in Fig. 3.17, where the PLL and the TAL work alternately under the control of TPD_EN and PFD_EN. As shown in the zooming subfigure, although the settling process is periodically interrupted by frequent TAL engagement, it still exhibits a similar lock-acquisition process to the traditional PLL loop. This is because the lock loss can always be quickly detected by the designed LSSM, thus making the FTL operate in PLL mode occupy a high time proportion. Benefiting from the improved lock-acquisition ability, the issues mentioned previously such as possible harmonic locking and weak robustness are completely resolved.

Fig. 3.18 shows the transient behavior for the cases with and without the injection-lock indicator INJ_LOCK. Obviously, they share similar acquisition behavior when the VCTRL is far away from its target value, since the large frequency differences make the frequency-loss detection close to the combined injection-loss and frequency-loss detection. For instance, the details for the first 500 ns are depicted in the top-left subsets in Fig. 3.18(a) and (b). However, when the VCO frequency is close to the target frequency, namely the control voltage VCTLR approaches its target value as detailed in the top-right subsets in Fig. 3.18(a) and (b), the detecting method only using the frequency-lock loss indicator REF_LOCK requires a long time (e.g., 68 ns, 88 ns) to trigger the PLL loop. On the other hand, the strategy monitoring both the frequency-lock loss signal FRE_LOCK and injection-lock loss signal INJ_LOCK can greatly shorten the detecting time (e.g., 18 ns, 19 ns). Consequently, the detection method involving both frequency-lock loss and injection-lock loss makes the transient behavior of the proposed RILCM more similar to the traditional PLL, which brings in significant convenience and facility for fast start-up applications.

3.6.3 Chip Micrograph and Measurement results

3.6.3.1 Chip Micrograph and Power Breakdown

Fig. 3.19 shows the die micrograph of the fabricated prototype. The chip size including pads is 0.8×0.9 mm^2, where the active area of the RILCM only occupies
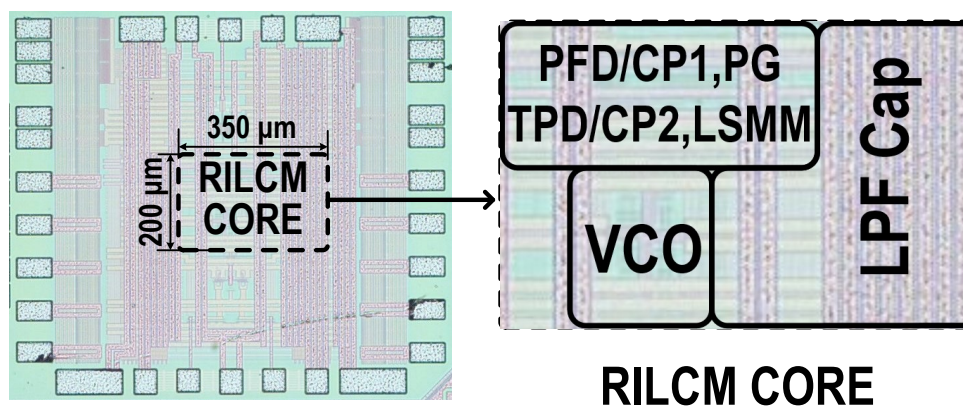
Figure 3.19: Die micrograph of the RILCM.
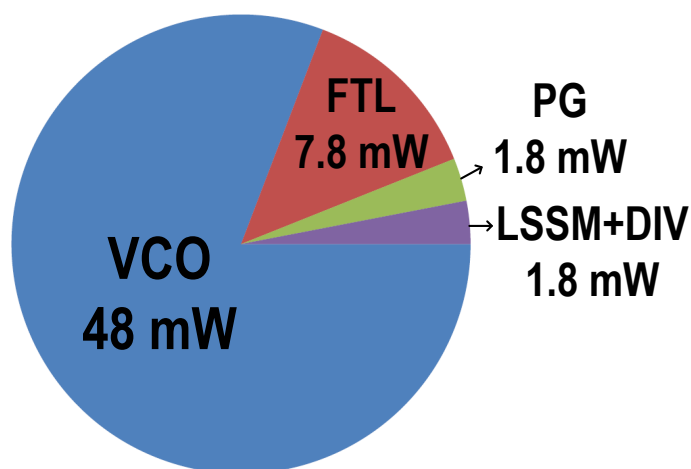
Figure 3.20: Power breakdown of the RILCM.
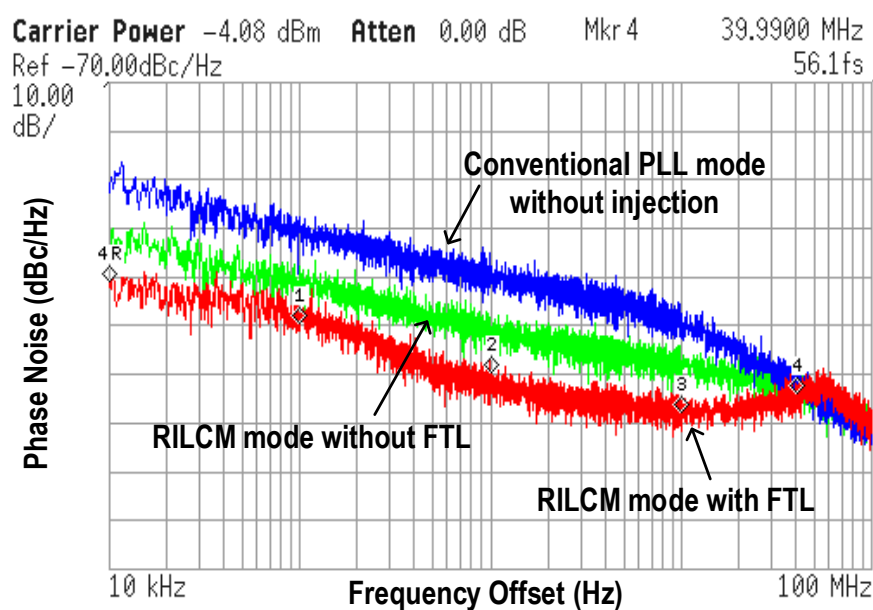
Figure 3.21: Measured phase noise with half-rate output at 5GHz.
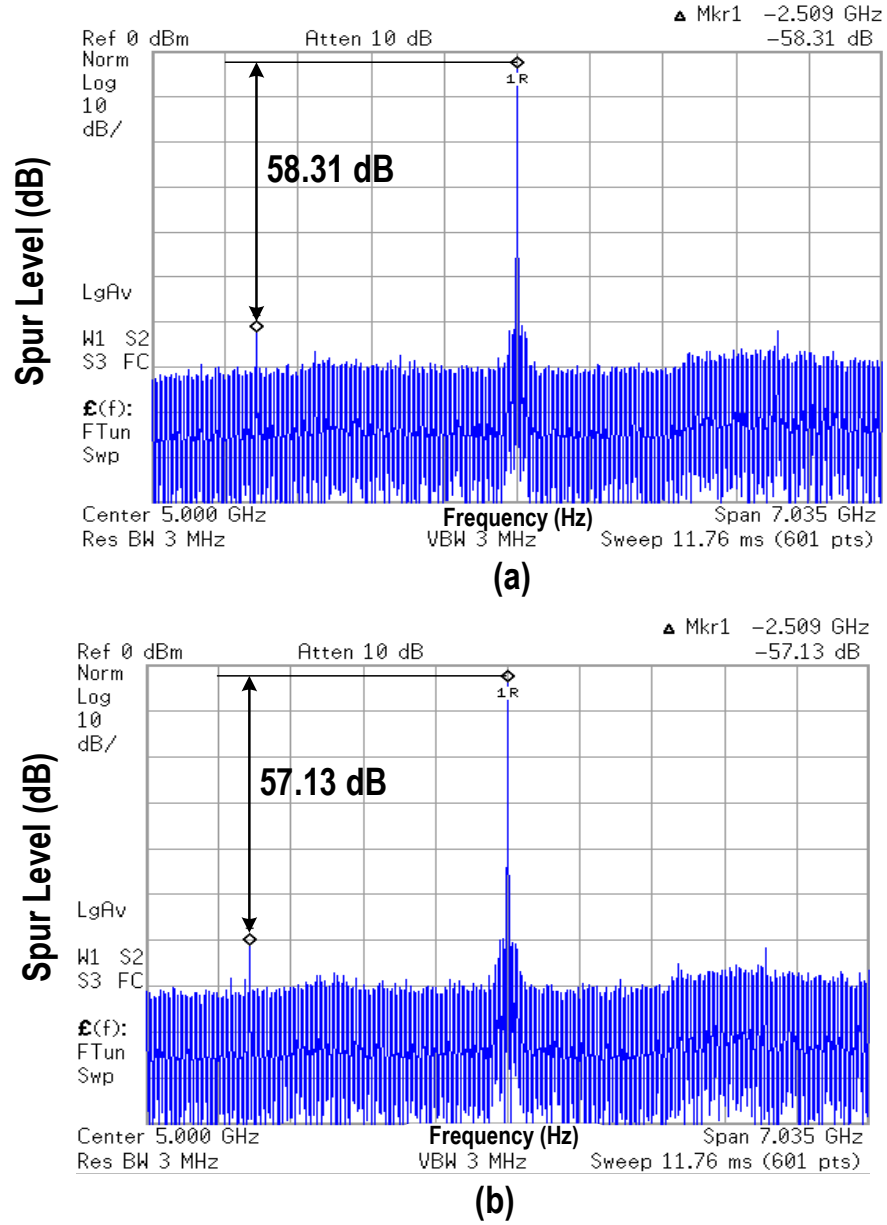
Figure 3.22: Measured reference spur with half-rate output at 5GHz. (a) RILCM without FTL and (b) RILCM with FTL.

0.07 mm^2. The power consumption is 59.4 mW, where 44.5 mA is drawn from a 1.2 V supply and 2.4 mA is provided by a 2.5 V supply. The power breakdown is given in Fig. 3.20. The introduced LSSM along with the two dividers only costs 3.0% (1.8 mW). The fabricated chip is mounted on a printed circuit board by wire-bonding. The output clock of the RILCM is firstly divided by 2, and then applied to an output buffer for measurement.
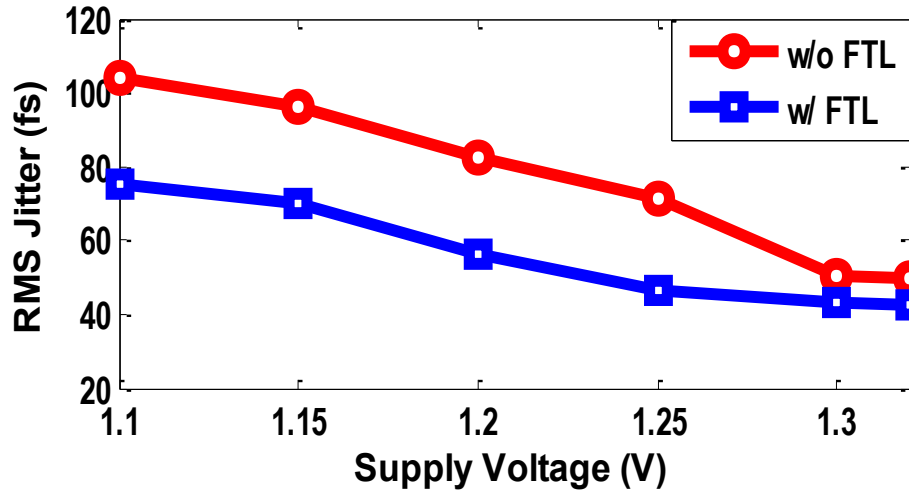
Figure 3.23: Integrated rms-jitter versus supply voltage.
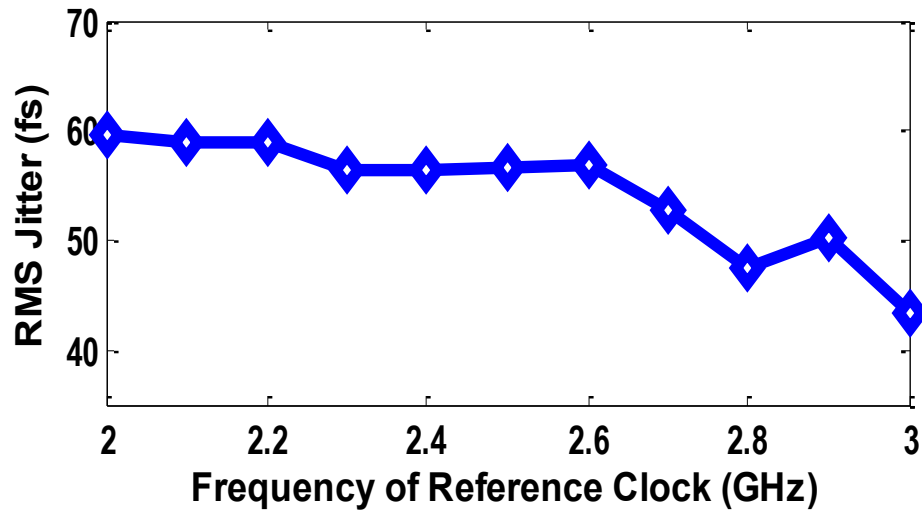
Figure 3.24: Integrated rms-jitter versus reference frequency.

3.6.3.2 Phase Noise and Spur Level Performance

Fig. 3.21 describes the measured phase noise (using half-rate output at 5 GHz) in three operation modes: conventional PLL without injection, RILCM with and without FTL. The measured phase noises are -120 dBc/Hz, -128 dBc/Hz, and -138 dBc/Hz, respectively, at an offset frequency of 10 MHz for the above three operation modes. Correspondingly, the measured rms-jitters are 390.2 fs, 130.0 fs, and 56.1 fs. Obviously, the implemented RILCM demonstrates significant improvement on noise performance due to the noise shaping contributed by the pulse injection and the continuous FTL. As illustrated in Fig. 3.22 (a) and (b), the measured reference spur levels without and with the FTL are 58.31 dB and 57.13 dB, respectively. Note that Fig. 3.22 (a) is measured

under an ideal condition with a nearly zero frequency deviation that is initially set, the slight spur degradation (1.2 dB) indicates that the FTL can adjust the injection window to an optimal position without introducing destructive disturbance.

3.6.3.3   Integrated-Jitter Performance

By repeating the phase noise measurement and jitter integration shown in 3.21, the rms-jitter under different testing conditions can be obtained. Fig. 3.23 depicts the rms-jitter versus the supply voltage for modes with and without the FTL, where the rms-jitter decreases as the supply voltage varies from 1.1 V to 1.32 V. This is because the improved supply voltage makes the swing of the proposed VCO increase, which helps sharpen the transition edges to reduce device noise to jitter conversion. To evaluate the operation range of the RILCM, we recorded the rms-jitter while continuously adjusting the reference frequency. The measurement results (see Fig. 3.24) demonstrate that the RILCM can produce high performance clocks (i.e., rms-jitter keeps lower than 60 fs) over a wide range of 8-12 GHz.

Table 3.1: PERFORMANCE SUMMARY OF THE RILCM

	JSSC09 [85]	ISSCC13 [146]	ISSCC15 [158]	ISSCC14 [82]	ISSCC16 [81]	JSSC14 [151]	This work
Architecture	LC-ILCM	LC-ILCM	LC-ILCM	PPM Ring-ILCM	Ring-ILCM	Ring-ILCM	Ring-ILCM
Freq. Tracking Method	FTL w/ TDC	FTL w/ Timing Adjusted PD	FTL w/ Pulse Gating	None	FTL w/ Replica-Delay Cell	Dual Loop w/ Replica-VCO	FTL w/ TPD
Lock-Acquisition Auxiliary	Manually-Tuned Control Voltage	PLL Initialization	Coarse Freq. Selection	Manually-Tuned Control Voltage	Coarse Freq. Selection	None	None
Loss Detection, Lock Recovery	Not Available	Not Available	Not Available	Not Available	Not Available	Available	Available
Output Freq.	3.2 GHz	2.4 GHz	6.75-8.25 GHz	2-16 GHz	0.96-1.44 GHz	0.5-1.6 GHz	8.0-12.0 GHz
Reference Freq.	50 MHz	150 MHz	105-129 MHz	0.25-2.0 GHz	120 MHz	40-300 MHz	2.0-3.0 GHz
Phase Noise at 1 MHz Offset	-127.4 dBc/Hz	-126.4 dBc/Hz	-113.5dBc/Hz	-115 dBc/Hz	-134.4 dBc/Hz	-124 dBc/Hz	-133.8 dBc/Hz
Jitter$_{rms}$ (δ_t) (Integ. Range)	130 fs (100k-40MHz)	188 fs (1k-40MHz)	190 fs (10k-100MHz)	268 fs (100k-1GHz)	185 fs (10k-40MHz)	700 fs (10k-40MHz)	56.1 fs (10k-40MHz)
Power Diss. (P_{DC})	28.6 mW	5.2 mW	2.25 mW	46.2 mW	9.5 mW	0.97 mW	59.4 mW
Reference Spur	-64 dBc	-49 dBc	-40 dBc	-48 dBc	-53 dBc	-57 dBc	-57.13 dBc
FOM	-243.2 dB	-247.0 dB	-251.0 dB	-235 dB	-244.9 dB	-243 dB	-247.3 dB
Active Area	0.4 mm^2	0.25 mm^2	0.25 mm^2	0.044 mm^2	0.06 mm^2	0.022 mm^2	0.07 mm^2
Technology	130 nm CMOS	65 nm CMOS	65 nm CMOS	20 nm CMOS	65 nm CMOS	65 nm CMOS	65 nm CMOS

3.6.4 Performance Comparison

Table 3.1 compares the performance of our RILCM with state-of-the-art ILCMs that have the capability of frequency tracking. Obviously, the phase noise at 1 MHz offset and integrated jitter of our RILCM outperforms other RILCMs and even comparable to the LC-ILCMs. This is mainly owing to the well combination of the injection locking and frequency tracking, both of which could provide significate noise suppression. Additionally, the high-swing RVCO also helps to reduce the phase noise. The good spur level indicates that the FTL can tune the RVCO to the target free-running frequency and hence make the injection happens around the optimal position. Meanwhile, it has a much smaller area occupation in contrast to those LC-ILCMs [85, 146, 158]. Additionally, the designed LLD-LR enables our RILCM with similar lock acquisition ability to conventional PLLs, thus making it a robust solution for commercial productions.

It is worthy to note that some parameters of the proposed RILCM are inferior. The tuning range of the proposed RILCM is less than that developed in [82] due to the limited tuning range of the back-to-back connected varactors. Fortunately, the 4 GHz tuning range is still relatively wide, which can satisfy most of the applications. The power consumption of our RILCM is higher than previous studies. However, the power consumption alone cannot be considered as the performance criterion since it is mainly determined by the utilized transistor sizes rather than the developed techniques. To estimate the power efficiency of the proposed RILCM, the FOM of the ILCMs are calculated, which is defined as,

$$FOM = 10 \cdot log \left[\left(\frac{\delta_t}{1s} \right)^2 \cdot \frac{P_{DC}}{1mW} \right], \tag{3.9}$$

where δ_t is the rms-jitter of the output signal and P_{DC} is the power consumption. It is usually considered as the performance-evaluation parameter of the clock multipliers. Clearly, The proposed RILCM achieves the best FOM (-247.3 dB) among the RILCMs [82, 81, 151], which indicates that the proposed RILCM (mainly referring to the architecture and circuit topologies) has the potential to achieve a better FOM (i.e., power efficiency) than previously developed clock multipliers. As for the area occupation, it is subject to the process, transistor sizes, and decoupling capacitance values. If an

Figure 3.25: Performance-area-speed graph.

advanced process with a smaller minimum channel length such as 45 nm, 32 nm, 22 nm and 16 nm is utilized, the area occupation can be significantly optimized.

Fig. 3.25 gives a comparison between the proposed RILCM and previous work in terms of performance-area-speed trade-off. It can be easily seen that our RILCM achieves a good balance among jitter performance, area occupation, operation speed, and power efficiency.

3.7 Chapter Summary

This chapter presents a RILCM using a newly developed TPD-based hybrid FTL capable of producing a low-jitter, high-speed output at a low power consumption and a small active area occupation. The RILCM occupies 0.07 mm^2, while producing a 56.1 fs rms-jitter at 10 GHz oscillation frequency and consuming a power of 59.4 mW.

The utilization of the newly developed FS-PDDC-based RVCO leads to a low device noise to phase noise conversion and a high convenience for subsequent applications. A compact TPD associated with a well-matched CP is designed to accomplish high phase-difference-detection accuracy and low charge-pumping disturbance. By timely starting a traditional PLL under the control of the LSSM, the essential frequency initialization in prior FTL-based-ILCMs is eliminated. The LLD-LR mechanism benefits the developed RILCM with the comparable lock-acquisition ability to conventional PLL, thus making it a robust solution for commercial productions. Moreover, the designed LSSM only consumes little additional power since most of the logics stay static when target harmonic locking is obtained. Overall, the proposed system achieves a good balance of performance-area-speed-efficiency trade-off when compared to other work.

Chapter 4

The Transmitter Design

As one of the most important components in serial links, the transmitter (TX) needs to produce full-rate data stream with precise timing for correct data transmission and provide sufficient voltage swing and appropriate equalization such that the received signal can maintain an adequate swing to make the receiver capable of distinguishing the transmitted data bits without errors. This chapter presents a 5-50 Gb/s transmitter with a 4-tap forward-feed equalizer (FFE), where the unit interval (UI)-spaced serial data are produced by four parallel 4:1 multiplexers (MUXs). This scheme brings in several benefits, including compact layout implementation, accurate 1UI-delay generation, and wide operating range. To mitigate the inherent large self-drain capacitance of the 4:1 MUX, an enhanced 4:1 pulling-down unit cell is proposed, which not only improves the maximum operation speed, but also effectively reduces the charge-sharing effect. A compact latch-array with an interleaved-retiming technique is adopted to produce the required 16 paths of quarter-rate data streams, where the retiming clocks for both the latch array and the 4:1 MUXs are generated by a clock bundle that is implemented in power-efficiency CMOS style.

In the rest of this chapter, we will firstly illustrate the design challenges in the high-speed transmitter, and then present the designed transmitter architecture. Following that, the enhanced 4:1 MUX and clocking techniques for the transmitter will be described. Finally, the experimental results of the transmitter will be discussed.
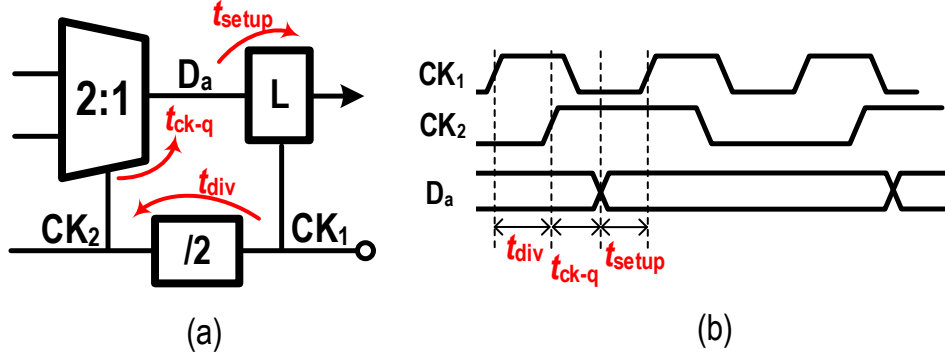
Figure 4.1: (a) Critical path and (b) timing diagram for the 2:1 MUX. Here, t_{div} is the delay of the divider, t_{ck-q} is the ck-to-q delay of the 2:1 MUX, and t_{setup} is the setup time of the sampling latch.

4.1 Design Challenges in High-Speed Transmitter

The difficulties in the high-speed transmitter design mainly focus on two aspects. The first one is the timing constrains for the final-stage serialization, the second one is the bandwidth limitations for high-speed blocks such as latches, MUXs, and clock/data driving buffers, which usually involve a tradeoff between the bandwidth extension and power consumption.

4.1.1 Timing Constraints

Fig. 4.1 re-draws the critical path and timing diagram in the 2:1 MUX. Note that the latch needs to sample D_a with CK_1, hence sufficient setup time and hold time for the sampling latch must be satisfied to guarantee the correct functionality. As shown in Fig. 4.1(b), the hold time can be easily met as the data always hold an adequate time after the arrival of CK_1. To satisfy the setup time constrain, the following equation must be held.

$$t_{div} + t_{ck-q} + t_{setup} < 1UI, \tag{4.1}$$

where t_{div} is the delay of the divider with a division factor of 2, t_{ck-q} is the ck-to-q delay of the 2:1 MUX, and t_{setup} is the setup time of the sampling latch. The other possible critical path is the located at the final data selection stage, where the margin

for the sampling is 1 UI. It can be expressed as

$$t_{setup}^{MUX} + t_{hold}^{MUX} < 1UI, \tag{4.2}$$

where t_{setup}^{MUX} and t_{hold}^{MUX} separately stand for the setup time and hold time of the final 2:1 MUX. As the data rate increases, the reduced bit period will lower these timing margins and hence limit the maximum operation rate. Moreover, the delay changes associated with the process, voltage, and temperature (PVT) variations make this problem even more challenging. To overcome this difficulty, traditional half-rate transmitters often insert extra delay-matching buffers [27, 24] or phase calibration loops [100, 33, 26] between CK_1 and the latch [see Fig. 4.1(a)]. For the former method, the delay fluctuation between the multiplexing path and the delay-matching path may excess 1 UI and thereby causes bit errors. For the latter approach, the timing margin is subject to the accuracy of phase detection, which could reduce the stability, reliability, and robustness of the serializer. Meanwhile, both of these two techniques involves substantial power and area overhead. An alternative solution is to replace the last three 2:1 MUXs with a single 4:1 MUX [159, 32, 24, 99]. The resulting quarter-rate serialization relaxes the critical path timing margin to 3 UI, halves the maximum clock speed, and saves considerable power, thus making it a promising solution for the high-speed serialization. It is worthy to note that these benefits come with the penalty of a doubled self-drain capacitance, which dramatically degrades the bandwidth of the 4:1 MUX and hence limits its maximum operation speed.

4.1.2 Bandwidth Limitations

The transmitter contains a large number of latches, MUXs, and data/clock driving buffers that operate at high speeds. As the data rate increases, the bandwidth requirements for these blocks rise accordingly. An insufficient bandwidth could make the signal difficult to reach the top or return to bottom, thus resulting in an attenuated amplitude. This could bring in significant detriments to the high-speed transmitter. Firstly, the insufficient bandwidth can make the ck-to-q delay of the MUX occupy a prominent portion of the bit period and hence restricts the maximum operation rate.
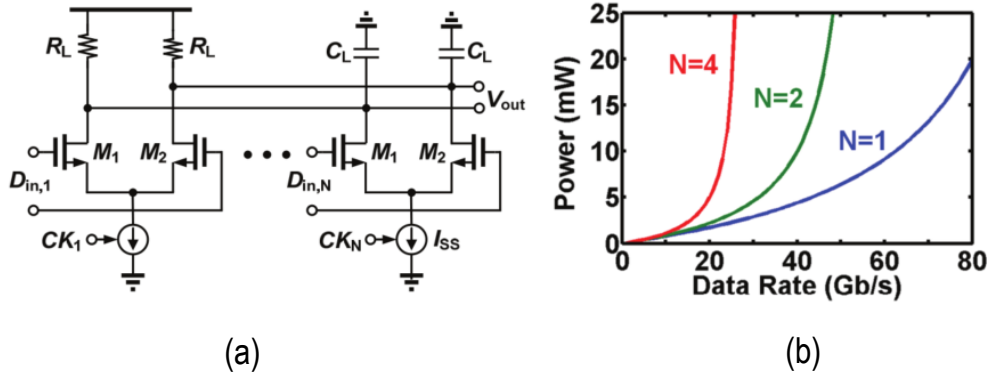
Figure 4.2: (a) Traditional CML-based MUX implementation and (b) power consumption with different multiplexing ratio [16]. Here, N refers to the the multiplexing branch number.

Secondly, the limited bandwidth could slow down the transition edges of the transmitting clocks, which will deteriorate the jitter performance of the clock. Thirdly, the insufficient bandwidth could lead to prominent inter-symbol interface (ISI). Specifically, the limited bandwidth makes the bit pulses cannot reach the top or return to bottom and thereby results in long tail over the succeeding bits.

As a general method, the bandwidth can be extended by burning more power. Fig. 4.2 describes the power consumption versus data rates with different multiplexing ratios (i.e., 1, 2, and 4), where the 1:1 MUX actually refers to the clock/data buffer and the performance of the latch can be estimated by the 2:1 MUX. At low data rates, the power consumption is linear to the data rate, where the self-drain capacitance can be neglected. As the data rate rises, the power consumption grows exponentially. This can be understood by noting that the self-drain capacitance gradually becomes the dominant load and thereby the resulting bandwidth of the MUXs cannot be extended by solely increasing the transistor sizes and power consumption. Referring to the curves in Fig. 4.2(b), it seems that the half-rate serialization with the 2:1 MUX is much more efficient than the quarter-rate serialization with the 4:1 MUX. However, the quarter-rate serialization scheme eliminates the three half-rate latches, two half-rate 2:1 MUXs, and a large number of quarter-rate latches as well as a few half-rate clock/data driving buffers. These significant power savings can effectively compensate for the power increase in the 4:1 MUX. The other advantage of this multiplexing scheme is that it can significantly relax the timing constrains for the final stage data se-
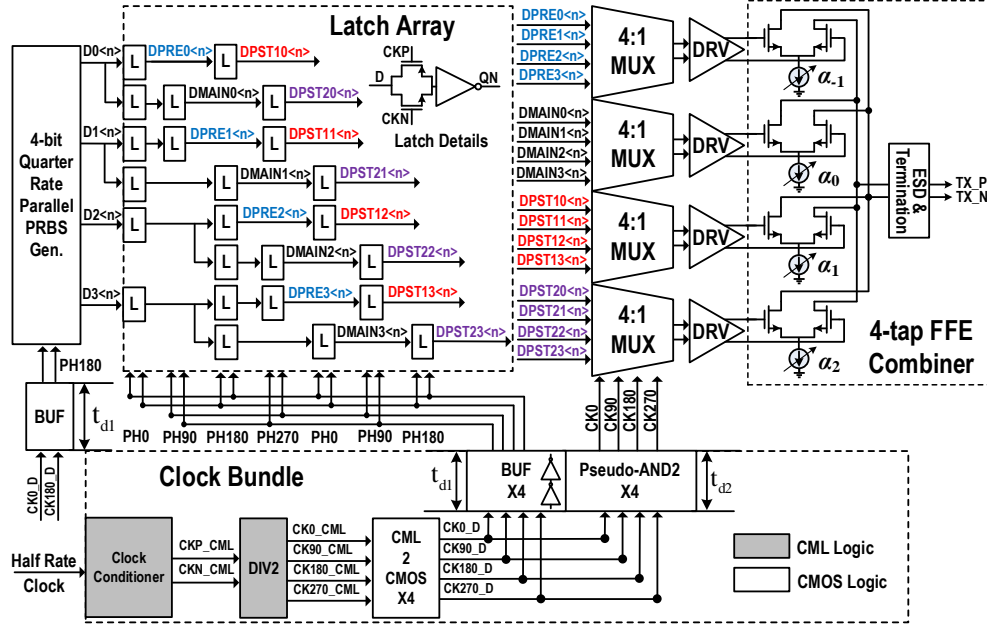
Figure 4.3: Block diagram of the transmitter chip.

rialization since the data to be multiplexed operate at quarter rate rather than half rate. The input data width is doubled and hence provides a doubled timing margin, which makes it possible to produce the full-rate data stream across PVT variations without additional matching buffers and phase tuning mechanism. Owing to these good properties, the quarter-rate architecture has become one of the most promising solutions in the 20+ Gb/s transmitter designs. One of the main task in this work is to optimize the operation speed and energy efficiency of the 4:1 MUX, including topology consideration, unit cell enhancement, and clocking optimization.

4.2 Transmitter Architecture

4.2.1 Overall Architecture

The block diagram of the transmitter chip is illustrated in Fig. 4.3. It consists of a multi-MUX-based 4-tap FFE combiner, a latch array, an on-chip PRBS generator, and a clock bundle. In principle, the on-chip PRBS is utilized to generate the parallel quarter-rate data streams D0<n>, D1<n>, D2<n>, and D3<n>. These four data streams are then interleavedly latched by the compact latch array to produce the 16-path quarter-rate data for the following four 4:1 MUXs. The desired timing rela-

tionship (see the signal positions in the latch array), which enables each MUX to share the same timing margin, is satisfied by 90°-spaced quarter-rate clock relatching. After the four 4:1 MUXs, the four full-rate UI-spaced serial sequences are firstly buffered by the pre-drivers and then sent to the 4-tap FFE combiner to finally pre-distort the output waveform and launch to the transmission channel. In the clock bundle, a clock conditioner is employed to convert the incoming single-end half-rate clock into differential outputs, which are then fed into a divider (DIV2) to generate the quart-rate I, Q clocks. Applying these quadrature clocks to four CML2CMOS converters, they are transformed into full swing clocks, which are further applied to four driving buffers and four pseudo-AND2s to produce 50% and 25% duty cycle clocks for the latch array and the 4:1 MUXs, respectively.

4.2.2 Features of the Transmitter

The main feature of the transmitter chip is the compact implementation of the multiple 4:1 MUX-based 4-tap FFE, which not only relaxes the stringent timing requirement of the final serialization stage, but also provides a robust approach to support a wide operation range. The quarter-rate multiplexing scheme implemented by the 4:1 MUXs significantly relaxes the stringent timing requirement. The interleaved-latching method is able to guarantee the 16 quarter-rate data streams always maintain the sufficient timing margins for the 4:1 MUXs. To improve the performance of the 4:1 MUX, we propose a new unit cell to cancel the charge-sharing effect, which not only reduces its output jitter, but also helps to optimize the self-drain capacitance and hence improves its maximum operation speed. For the clocking, the shared 25% duty cycle UI-spaced clocks are produced by pseudo-NANDs. This clocking scheme not only possesses the good property of the high power efficiency, but also provides full swing outputs and hence optimize the sizes of the gating transistors in the 4:1 MUX.
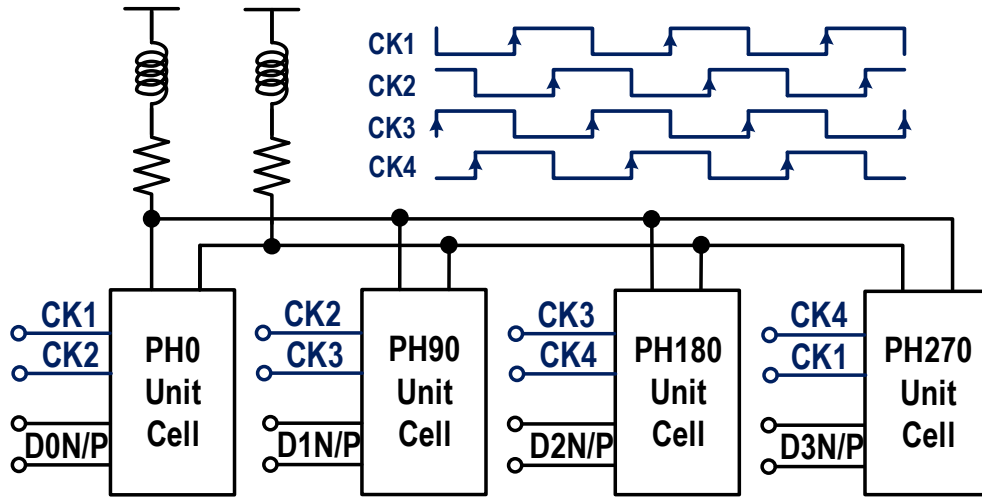
Figure 4.4: Conceptional circuit schematic of the traditional 4:1 MUX.
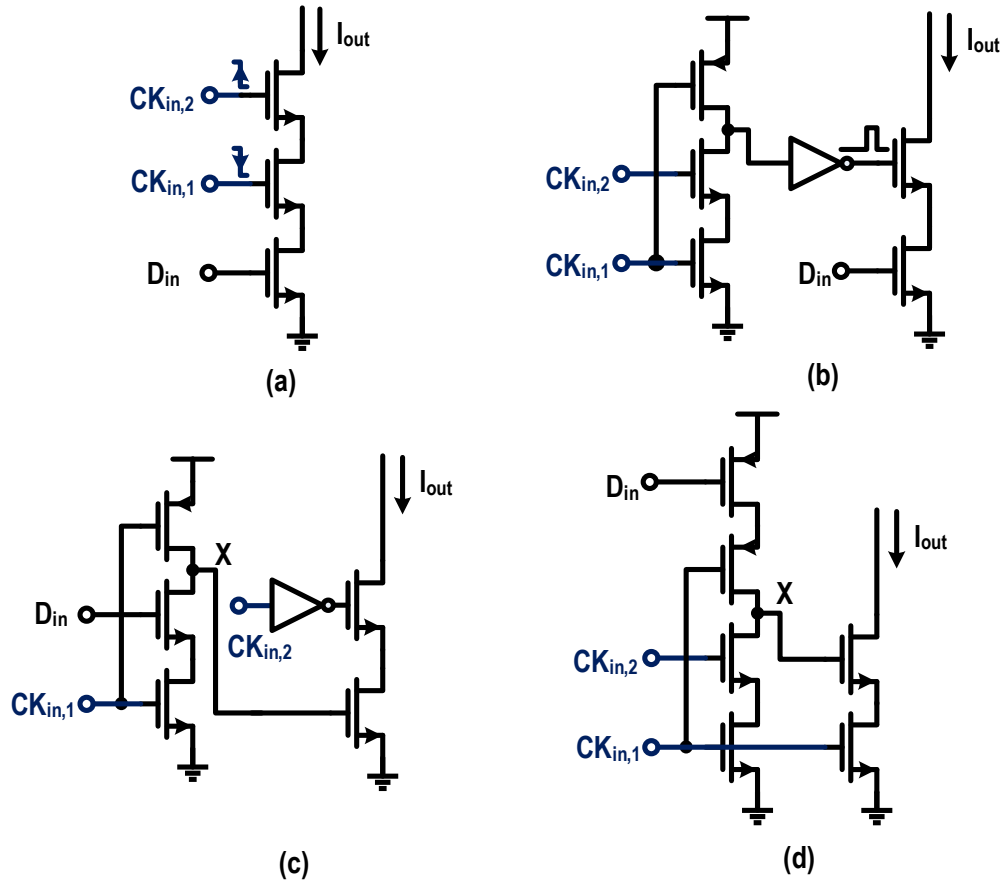
Figure 4.5: Four possible unit cell implementations of the 4:1 MUX.

4.3 Enhanced 4:1 Multiplexer (MUX)

4.3.1 Previous 4:1 MUXs

Fig. 4.4 displays the conceptional schematic implementation of the traditional 4:1

MUX, which consists of four pulling-down unit cells and a pair of shunt-peaked loads.

Each unit cell performs two tasks, i.e., clock ANDing and data sampling, where the former refers to ANDing the two adjacent clock phases to determine the edge positions of the output pulse and the latter represents the input data sampling and hence decides the logic of the output pulse.

Fig. 4.5 shows four possible implementations of the unit cell within the 4:1 MUX. One common feature in these unit cells is that the current source is eliminated to reduce the number of the stacked devices. In the first implementation [see Fig. 4.5(a)], the ANDing and sampling operations are combined into one stage and hence the number of the internal nodes can be reduced to the minimum. Nonetheless, these stacked devices in the output stage need large sizes to provide sufficient driving current. The increased device size shows a large capacitance load for the preceding stage and manifests a increased self-drain capacitance, which in return limits the maximum operation speed and/or the achievable power efficiency. To mitigate these issues, a second realization shown in Fig. 4.5(b) is developed, where a separate sampling stage is introduced to AND the two adjacent clock phases $CK_{in,1}$ and $CK_{in,2}$ to produce the 25% duty-cycle pulse. This pulse is then applied to the output stage to gate the enabling transistor to transmit the input data D_{in} to the output. By separating the ANDing and sampling operations into two stages, the stacked devices in the output stage are reduced to two, which could significantly improve the operation speed and power efficiency of the 4:1 MUX. However, the involvement of processing the 25% duty cycle pulse along with the sharp edge requirement has posed a high requirement on the 1-UI pulse generation. To avoid the involvement of the 25% duty cycle pulse, a third possible implementation of the unit cell is developed in [24]. As shown in Fig. 4.5(c), the leading clock $CK_{in,1}$ is firstly sampled by the input data D_{in} to remove the high pulses whenever D_{in} is low (corresponding to no discharging current in the output stage). After that, this data-selected clock together with the $CK_{in,2}$ will generate the pulse current to transmit the input data onto the output with an accurate UI spacing. This technique possesses three advantages. Firstly, the involvement of 25% duty cycle is precluded and hence the stringent speed requirement on the inter nodes is relaxed. Secondly, the switching activity of the preceding sampling sate is actually determined by the input data D_{in}.

For a random input data with equal polarities, the switching activity is 50%, which is lower than that of the design in Fig. 4.5(b). Finally, the sampling stage actually performs the function of a latch and thereby a latch in the preceding stage can be saved. Fig. 4.5(d) shows a variant of the design in Fig. 4.5(c) [32]. Instead of using a NMOS for the first latch, a PMOS latch is utilized to keep node X pre-discharged rather than pre-charged. This allows to remove the intermediate inverter, which reduces the operation devices and hence leads a significant power saving. This unit cell also naturally implements the latching function and therefore saves a latch in the preceding data path. The main disadvantage of this topology is the stacked devices in the latch, which could slow down the edge transitions of node X, thus limiting its maximum operation speed. Another common drawback within the unit cells in Fig. 4.5(c) and (d) is that both the sampling and ANDing operations are integrated together in the unit cell, hence ruling out the possibility of the ANDing stage sharing.

4.3.2 Topology Consideration

Fig. 4.6(a) describes the schematic of the developed 4:1 MUX. Like the traditional 4:1 MUX shown in Fig. 4.5, it is composed of a pair of shunt-peaked loads and four identical pull-down unit cells. Unlike the conventional 4:1 MUX that are directly driven by the quadrature 50% duty cycle clocks, these unit cells are activated sequentially by four 25% duty cycle UI-spaced phases (CK0-90-180-270) to combine the four quarter-rate data streams (D0-1-2-3) into one serial sequence (SDATA) [see Fig. 4.6(b)]. Compared to the 4:1 MUXs presented in [24, 32] that combine both the ANDing operation and sampling operation into the pulling-down unit cell, the unit cell in this design only performs the sampling operation while the ANDing operation is carried out by the pseudo-AND2s in the clock bundle (see Fig. 4.3). This splitting arrangement allows the four 4:1 MUXs in Fig. 4.3 to share one common ANDing stage, thus exhibiting more potentials on power efficiency.

(a)

(b)
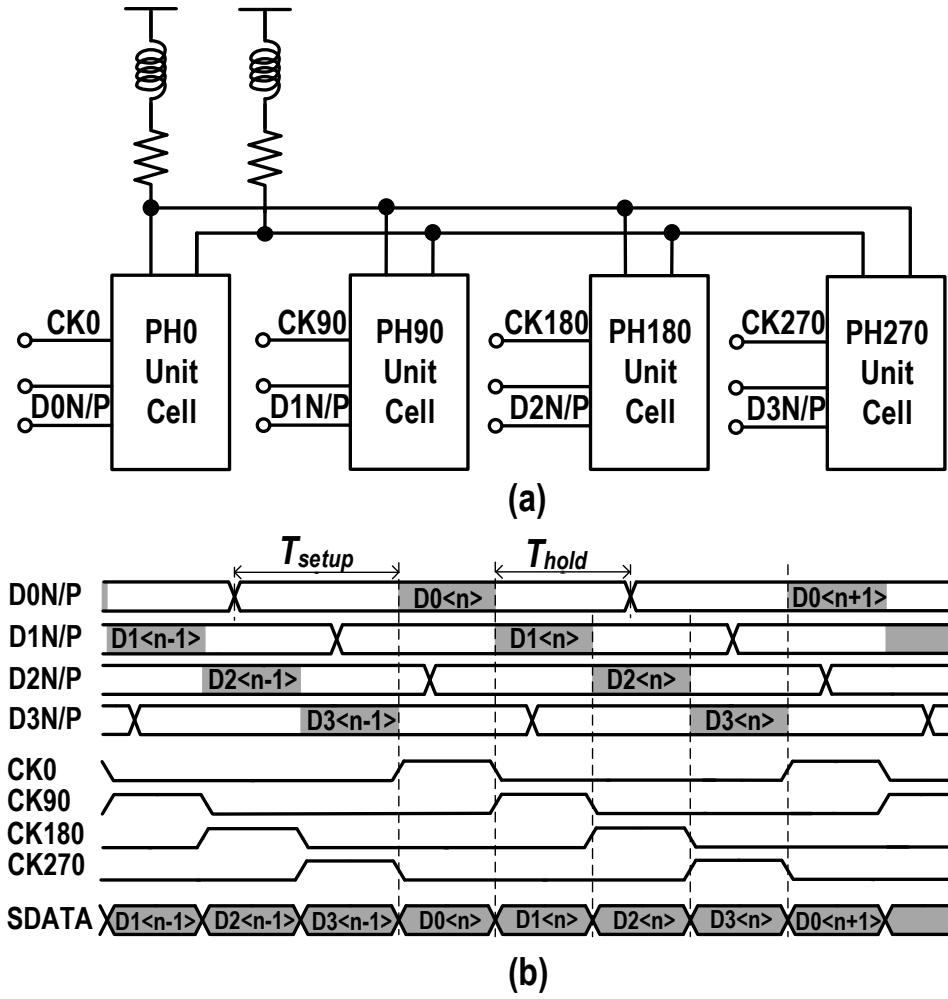
Figure 4.6: Topology of the 4:1 MUX. (a) Conceptual schematic and (b) timing diagram.

4.3.3 Enhancement on the Unit Cell of the 4:1 MUX

The main drawback of the quarter-rate serialization is the doubled self-drain capacitances of the 4:1 MUX, which significantly constrain the maximum operation speed. Consequently, bandwidth extending techniques for the 4:1 MUX are highly desired. This part will firstly discuss the drawbacks in traditional unit cells and then presents our optimization techniques. Fig. 4.7 depicts the two widely used traditional unit cells that support the splitting placement of ANDing and sampling operations. To optimize the operation speed, the current source transistors are eliminated to avoid stacked devices. In the data-up structure [101, 32] depicted in Fig. 4.7(a), the output can be corrupted by the data transitions on other branches through the forward-coupling path from the data input to the output when the MUX is performing data selection on one branch [37]. Fig. 4.7(b) describes the clock-up structure [21, 103], which addresses
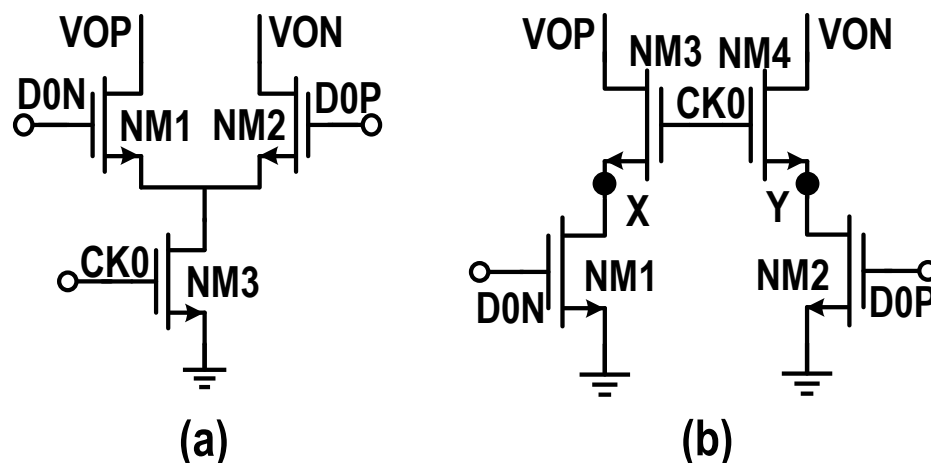
Figure 4.7: Traditional unit cell implementations for high-speed 4:1 MUX. (a) Data-up structure and (b) clock-up structure.
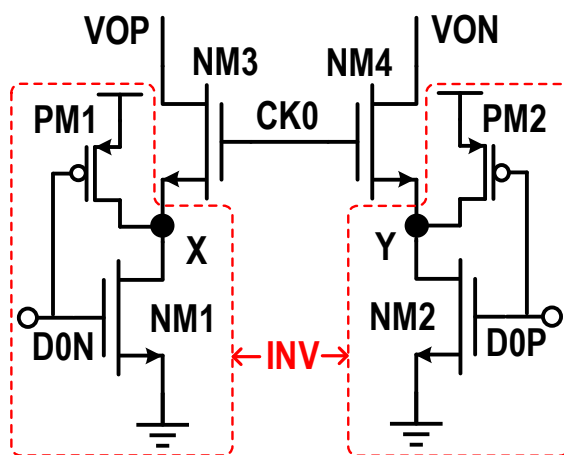
Figure 4.8: Improved unit cell implementation.

the forward-coupling problem by moving the clocking pairs to the top to eliminate the feed-through path. However, it suffers from severe charge-sharing effect between the outputs VOP/VON and junction nodes X/Y in the form of causing glitches on two consecutive bits at high level or slowing down the rising edges for low-to-high transitions. Inspired by the voltage mode source-series terminated (SST) driver discussed in [98], we introduce a pair of pre-charging transistors PM1/PM2 connecting to nodes X/Y to mitigate this effect. As shown in Fig. 4.8, the pre-charging PM1/PM2 and the data-gating NM1/NM2 actually constitute two inverters, which make nodes X/Y be always pre-driven to desired states, thus eliminating the charge-sharing effect. Compared to the SST implementation in [98], the improved 4:1 MUX exhibits more potentials on high-speed applications. The reason is that it can fully exploit the process potentials as
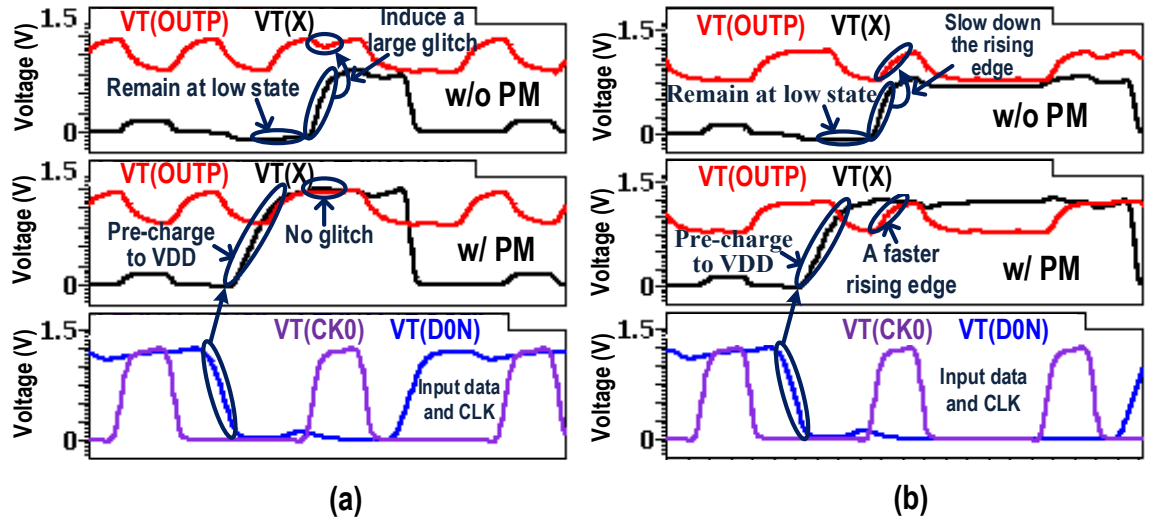
Figure 4.9: Effect of the introduced PM on (a) high-level glitches and (b) edge transitions.

its compact NMOS driving topology naturally features fast current switching speed and small parasitic capacitance. Additionally, the speed-constraining output capacitances including self-drain load, routing wire, and far-end driving load can be neutralized by adopting on-chip peaking inductors. In the rest of this part, we will discuss the adverse effect of the charge-sharing in conventional clock-up structure and the favorable effect of the introduced pre-charging transistors.

(1) *Charge-sharing effect in conventional clock-up structure*

The top row of the simulated waveforms in Fig. 4.9(a) and (b) demonstrates the two adverse effects of the charge-sharing in the conventional clock-up structure [see Fig. 4.7(b)]. Assuming the upcoming data D0P/D0N are logic high/low, node Y is pre-discharged to the ground through NM2, which helps to speed up the falling edge. The voltage of node X depends on previous transmitted data. In case that the previous D0N is logic low, node X should have been charged to an allowed maximum value $(VDD - V_{THN})$ during the selection-enabled period (high pulse duration of CK0), which should maintain to the present instant since NM1 has always been in cut-off state. This will not cause prominent charge-extraction effect, as node X has already been charged to the allowed maximum value by the previous transmitted bit. If the previous D0N is logic high, node X should keep the ground voltage that is pulled down during the hold time in previous bit period [i.e., T_{hold} in Fig. 4.6(b)]. When

109

the high pulse of CK0 arrives, the capacitance at node X will extract charge from the output, thus causing a remarkable glitch for two consecutive output bits at high level or slowing down the rising edge for a low-to-high transition [see the waveform details in the top row of Fig. 4.9(a) and (b)]

(2) *The effect of the introduced pre-charging transistors*

To demonstrate the effect of the introduced pre-charging transistors PM1/PM2 shown in Fig. 4.8, we take PH0 branch as an example to illustrate the operation process of the proposed pull-down unit cell. When input data arrive, depending on D0N/D0P, nodes X/Y are either pre-charged to VDD or pre-discharged to VSS by the two inverters consisting of PM1/PM2 and NM1/NM2. This makes nodes X/Y always pre-driven to the desired states that are coincident with the output signal levels. As the high level of CK0 comes, NM3/NM4 are turned on to send D0N/D0P to the MUX's outputs. After a period of 1 UI, the pull-down path is switched off by the falling edge of CK0 and the voltage level of nodes X/Y stays unchanged until the next input data come. The main feature of this 4:1 MUX is its ability of eliminating the charge-sharing effect caused by parasitic capacitances at nodes X/Y, which brings in several benefits. Firstly, the deterministic jitter and glitches caused by charge-sharing extraction can be remarkably mitigated [see the middle row in Fig. 4.9(a) and (b)]. Moreover, the glitch elimination effectively improves the noise margin that allows a lower output swing to save power. Secondly, the elimination of the charge-sharing effect makes the capacitances at nodes X/Y less significant. Thus, large-size NM1/NM2 can be used to enhance the discharging capabilities. Note that the output swing is determined by the proportion of resistive load and equivalent resistance of stacked NM1/NM3 (NM2/NM4). For a fixed minimum output swing, the big size of NM1/NM2 implies that NM3/NM4's size can be reduced. The smaller size of NM3/NM4 helps to decrease the self-drain capacitances of the unit cells. Consequently, the bandwidth of the overall 4:1 MUX can be expanded. Thirdly, the added transistors PM1/PM2 provide another path through NM3/NM4 to help to pull up the output, which can accelerate the rising transitions.
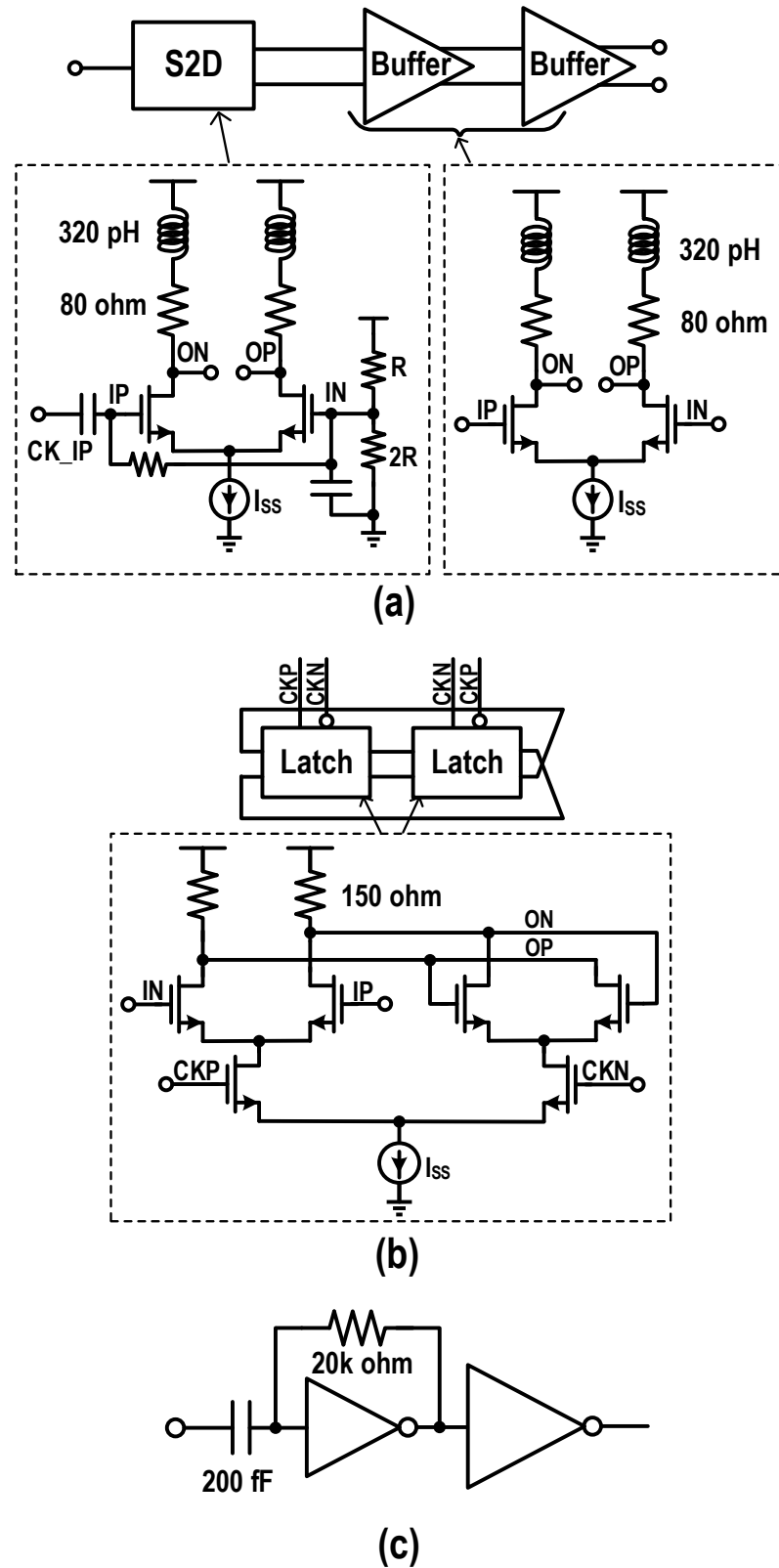
Figure 4.10: Circuit details of the clocking blocks. (a) Clock conditioner, (b) DIV2, and (c) CML2CMOS.

4.4 Clocking for the Transmitter

4.4.1 Topology of the Clock Bundle

As depicted at the bottom of Fig. 4.3, the desired full swing clocks for the latch array and the 4:1 MUXs are produced by a clock bundle, where current-mode logic (CML)-style circuits are employed in the clock conditioner and DIV2 to support the most high-speed (half-rate) operation while the CML2CMOS and pseudo-AND2 that operate at quarter rate are implemented in a more power efficient CMOS style.

4.4.2 Clocking Blocks

Fig. 4.10 presents the implementation details of these clocking blocks. In the clock conditioner [see Fig. 4.10(a)], an AC-coupled CML with one input connected to the fixed common voltage (2VDD/3) is adopted to perform the single-end input to differential output conversion. This differential clock is further rectified by two CML buffers. To reduce the power consumption, multi-layer on-chip inductors are employed to neutralize the output capacitances. For the DIV2, a traditional inductorless CML latch shown in Fig. 4.10(b) is used to balance the operation speed and layout compactness. Fig. 4.10(c) gives the schematic details of the CML2CMOS, where an AC-coupled inverter with a feedback resistor is utilized to convert the CML voltage level to full swing CMOS logic. This compact CML2CMOS possesses the good properties of small area occupation and high power efficiency. To some extent, it is also capable of performing the function of duty cycle correction since the DC voltage of the converted full-swing clock is feedback to bias the common voltage of the inverter.

For the pseudo-AND2, its function is to AND the two 50% duty cycle half-rate clocks with a 90° phase shift to generate the 25% duty cycle clocks (CK0-90-180-270 in Fig. 4.3) for the 4:1 MUX. As the final retiming stage, the transmitter performance largely relies on these clocks since any timing deviation will be converted into final output jitter directly. This necessitates the following two desirable properties: i) the high pulse width for each phase should be an accurate UI period, and ii) the spacing between any two adjacent phases should be the same, which equals 1 UI. Generally
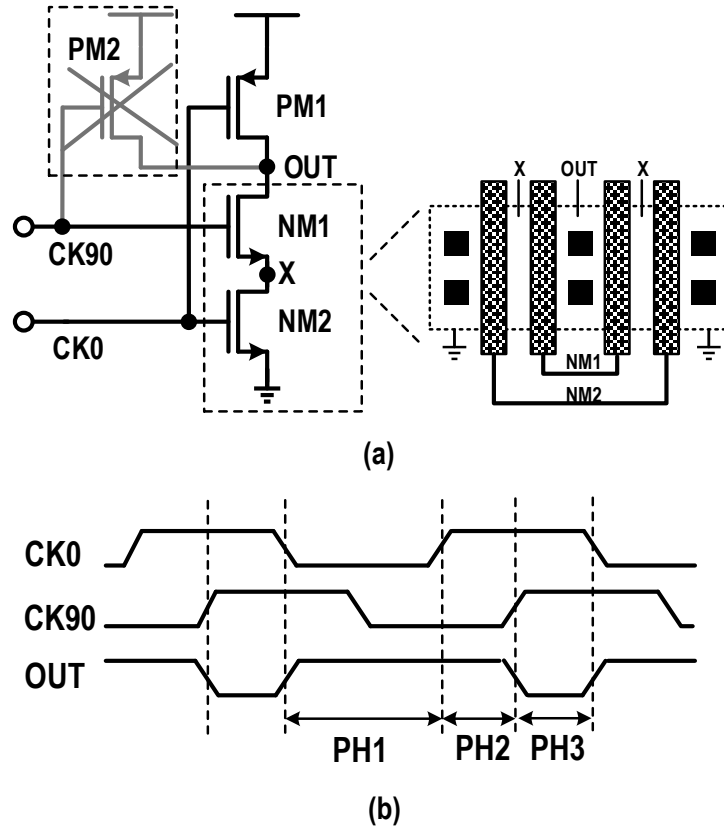
Figure 4.11: Pesudo-NAND2. (a) Circuit details and (b) operation waveform.

speaking, these pulses can be created by NOR/AND of two 50% duty-cycle half-rate clocks with 90° phase shifts. Considering the fact that serial NMOS transistors are much faster than serial PMOS transistors, NAND2 associated with a driving inverter could be a better choice. Fig. 4.11 presents the designed pseudo NAND2 and its operation waveforms. In contrast to conventional NAND2, this pseudo-NAND2 eliminates the pulling-up transistor PM1 [see Fig. 4.11(a)]. In doing so, the output capacitance can be reduced, thus leading to a higher operation speed. The similar circuit realizations of the pseudo-AND2 and the BUF (consisting of two cascaded inverters) also mitigate the delay mismatch between t_{d1} and t_{d2} (see Fig. 4.3), which helps to meet the stringent timing constraints against PVT variations. Fig. 4.11(b) presents the operation waveforms of the pseudo NAND2. At the beginning of PH1, node OUT is pulled up to VDD by PM1, which can be held during PH2 since NM1 is still in closed state. In PH3, both NM1 and NM2 are turned on to generate the UI-spaced pulse. It is worth noting that there does exist charge-sharing effect between the capacitance at node X
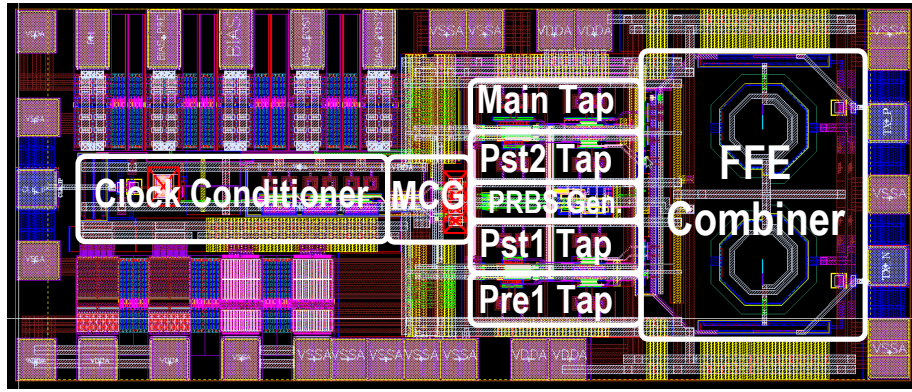
Figure 4.12: Layout view of the whole transmitter chip.

and the output. Particularly, at the beginning of PH1, CK0 goes down to trigger PM1 to charge the output node, while node X extracts charge through NM1 since CK90 is still remaining at high state. To alleviate this effect, an abutment layout approach with minimum gate spacing [see Fig. 4.11(a)] is exploited to reduce the parasitic capacitance at node X. The big serial transistors are divided into several small serial transistors, and every two small ones are connected in parallel, sharing a common drain region to reduce the junction area.

4.5 Experimental Results

4.5.1 Tools and Fabrication Process

The transmitter is designed using a Dell R730 server with two E5-2609V4 CUPs, 128 G memory and 8 T hard disk. The schematic, layout, and simulation are respectively finished by Schematic Composor, Virtuoso Layout, and Spectre/aps that are developed by Cadence and the Cadence version is IC5141. The layout verification and parasitic extraction are carried out by layout versus schematics (LVS)/design rule check (DRC) and parasitic extraction (PEX) using Caliber2013 that is developed by Mentor Graphics. To perform the measurements of the fabricated prototype, a KEYSIGHT N5191A is used to generate the input clock and a KEYSIGHT DSA-X 93204A with a 80 GS/s and 32 GHz bandwidth is utilized to characterize the jitter performance of the transmitter.
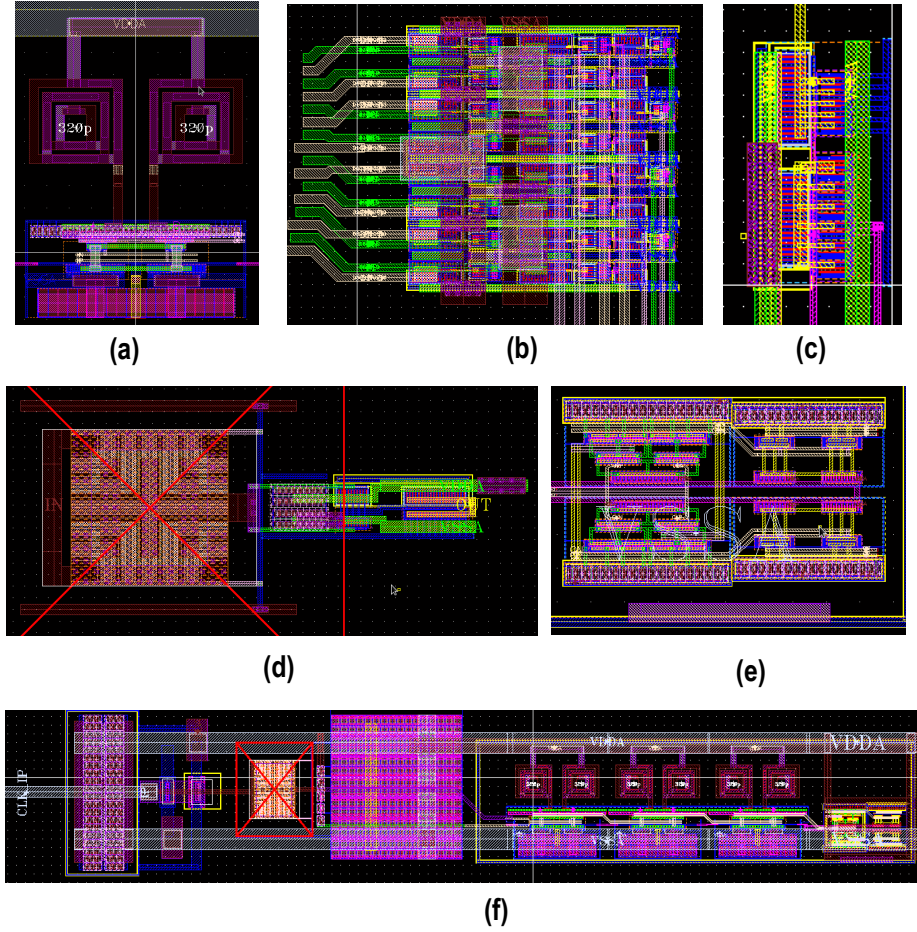
Figure 4.13: Layout views of the crucial blocks. (a) 4:1 MUX, (b) interleaved-retiming latch array, (c) pesudo-NAND2 with an inverter, (d) CML2CMOS converter, (e) DIV2, and (f) clock conditioner.

The prototype chip is designed and fabricated utilizing a 65 nm process. Under a typical corner, the cut-off frequency (f_T) of the NMOS transistor and the inverter delay with a fan-out-of-4 in this process achieve 200 GHz and 13 ps, respectively. This implies that the utilized 65 nm process is able to provide enough bandwidth and timing margin for the targeted 40 Gb/s transmitter design. Although an advanced process with smaller minimum channel length such 45 nm, 32 nm, 22 nm and 16 nm can offer higher f_T and shorter inverter delay, their high prices make them not available for us. Fortunately, our transmitter mainly focuses on the interleaved latching-based sequence generation, multi-MUX-based 4-tap FFE implementation, and 4:1 MUX enhancement, which can still be verified by the economical and practical 65 nm CMOS process.

4.5.2 Layout and Simulation Results

4.5.2.1 Layout Designs

Fig. 4.12 displays the layout view of the whole transmitter chip. The FFE combiner is located at the right edge of the chip to directly drive the output pads. The four paths consisting of 4:1 MUXs and drivers (i.e., main tap, pst2 tap, pst1 tap, and pre tap in Fig. 4.12) are placed next to the FFE combiner to reduce the driving length of the connection wires. The PRBS generator and the latch array are dispersed at the blank places among these four multiplexing paths to generate the quarter-rate data with appropriate delays. The clock conditioner and the MCG is put at the left side of the chip to provide proper clocks for the PRBS generator, latch array, and 4:1 MUXs.

Fig. 4.13 further presents the layout views of the crucial blocks. For the 4:1 MUX shown in Fig. 4.13(a), the parasitic capacitances on the output nodes are optimized to support a maximum operation speed. For the latch array displayed in Fig. 4.13(b), special attentions are paid to the latch placement to facilitate the signal connections. For the pesudo NAND2 shown in Fig. 4.13(c), an abutment layout approach with a minimum poly spacing is adopted to optimize the parasitic capacitance on node X as shown in Fig. 4.11. For the CML2CMOS converter, DIV2, and clock conditioner [see Fig. 4.13(d), (e), and (f)], special attentions are paid to the parasitic capacitance optimization, hence making the received clock can be well amplified, rectified, and divided.

4.5.2.2 Simulation Results

Fig. 4.14 illustrates the simulation setup of the transmitter chip. The inputs of bias_main, bias_pre, bias_pst1, and bias_pst2 are corresponding to the four tap weights of the FFE combiner. The input clock operates at 25 GHz. The muxed data are the direct outputs of the 4:1 MUX on the main-tap path. The output data are DC coupled to a pair of far-end 50 ohm resistors through a channel with a 12 dB attenuation at 20 GHz.

To evaluate the effect of the introduced PMs in the 4:1 MUX, the transient output and overlapped eye-diagrams using the traditional unit cell [see Fig. 4.7(b)] and the
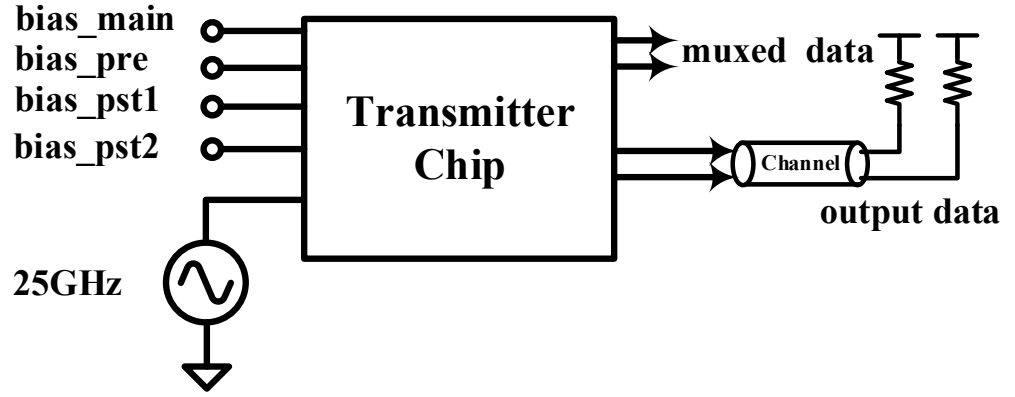
Figure 4.14: Simulation setup of the transmitter chip.
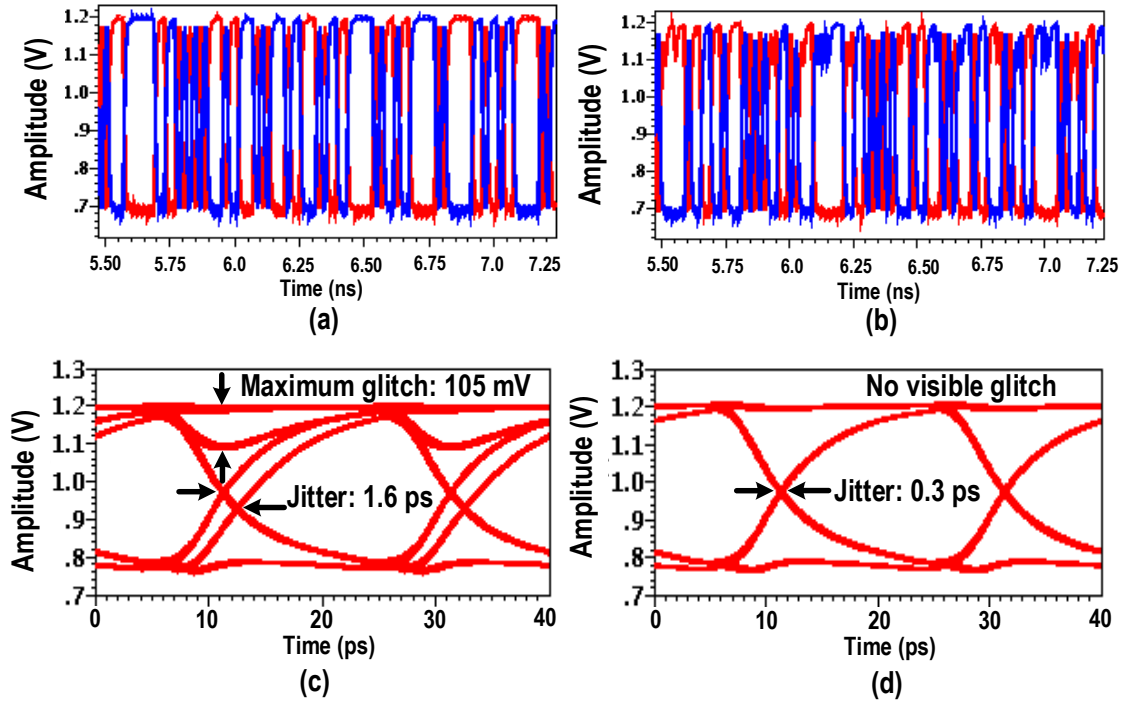
Figure 4.15: (a) Transient waveform of the traditional unit cell, (b) transient waveform of the enhanced unit cell, (c) eye-diagram of the the traditional unit cell, and (d) eye-diagram of the the enhanced unit cell.

enhanced unit cell (see Fig. 4.8) are separately displayed in Fig. 4.15. The simulated eye-diagrams indicate that the ISI induced by the charge-sharing is reduced from 1.6 ps to 0.3 ps and the voltage glitches are mostly removed. It worthy to note that there exists an drawback within this proposed 4:1 MUX. Its output swing is sensitive to PVT variations. The reason is that the equivalent resistance of the two stacked transistors
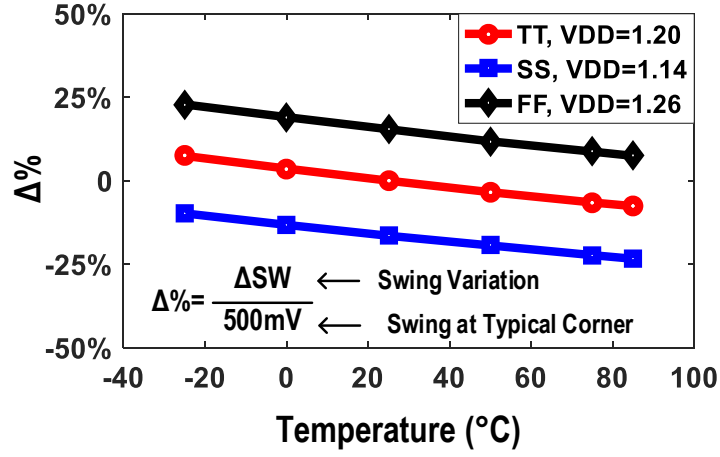
Figure 4.16: Swing variations of the improved unit cell under different PVT corners.
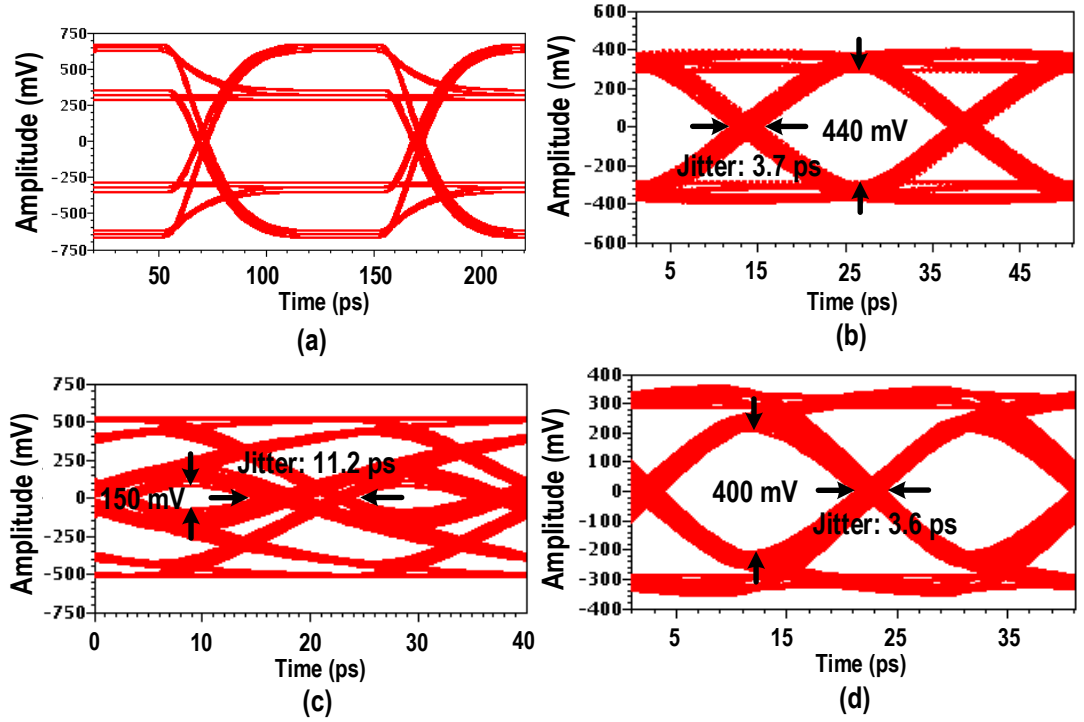
Figure 4.17: Simulation eye-diagrams of the transmitter at (a) 10 Gb/s with over equalization, (b) 40 Gb/s with proper equalization, (c) 50 Gb/s without equalization, and (d) 50 Gb/s with proper equalization.

could change a lot under different PVT corners. Fig. 4.16 gives the swing variations for different PVT corners, where the swing variation can be controlled under 25% and it can be further reduced by adopting a tunable resistor described in [24].

The performance of a transmitter is usually characterized by its output eye-diagram, which folds a time-domain waveform into one or several bit periods. The two critical parameters of the eye-diagram refer to the voltage swing and inner eye opening, where
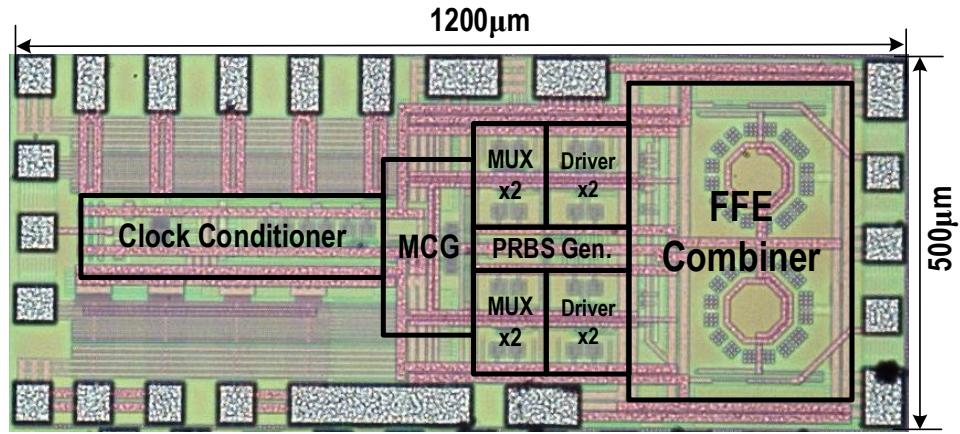
Figure 4.18: Chip micrograph of the transmitter.
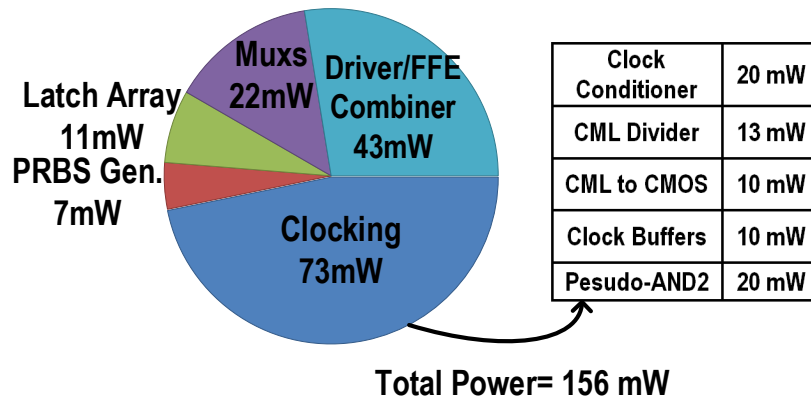
Figure 4.19: Power breakdown of the transmitter when operating at 50 Gb/s.

the former determines the transmitter output power and sets a requirement for the receiver sensitivity, while the latter indicates the overall performance of the jitter, noise, and effective bandwidth. Fig. 4.17 shows the simulated eye-diagrams. Fig. 4.17(a) displays the simulated eye-diagram at 10 Gb/s with an over equalization, where the sub-levels are contributed by the FFE taps. Fig. 4.17(b) presents the simulated eye-diagram at 40 Gb/s with a proper equalization, where the horizontal jitter and the vertical eye opening are 3.7 ps and 440 mV, respectively. Fig. 4.17(c) and (d) gives the eye-diagram comparison before and after applying an appropriate equalization at 50 Gb/s. Clearly, the FFE can significantly optimize the eye opening, where the horizontal jitter is reduced from 11.2 ps to 3.6 ps and the vertical swing is increased from 150 mV to 400 mV.
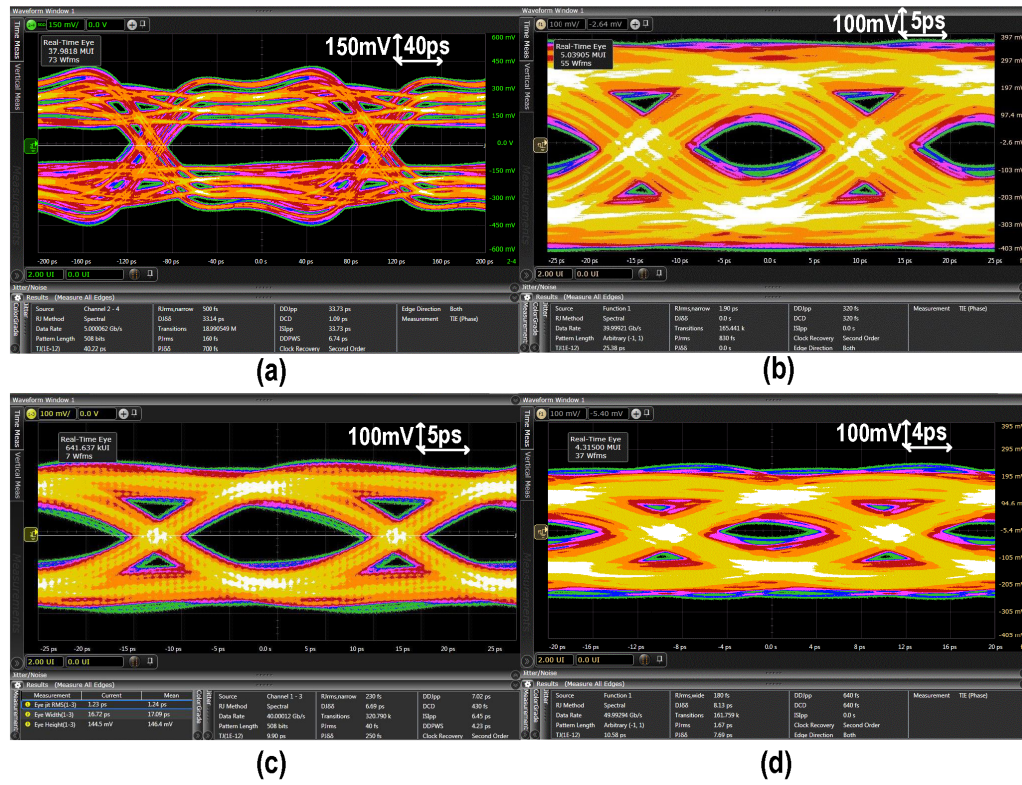
Figure 4.20: Measured output eye-diagrams of the transmitter at (a) 5 Gb/s with over equalization, (b) 40 Gb/s without equalization, (c) 40 Gb/s with proper equalization, and (d) 50 Gb/s with proper equalization.

4.5.3 Chip Fabrication and Measurement Results

4.5.3.1 Chip Fabrication and Power Consumption

Fig. 4.18 presents the chip micrograph, which occupies an area of 0.6 mm^2. Fig. 4.19 shows the power breakdown of the transmitter chip. It consumes 156 mW from a 1.2 V supply when operating at 50 Gb/s, where the four enhanced 4:1 MUXs only consume 22 mW. The fabricated chip is mounted on a printed circuit board (PCB) through wire-bonding. The transmitter output is measured after a compound channel consisting of doubled bonding wire, PCB trace, and connection cable.

4.5.3.2 Measurement Results

Fig. 4.20 gives the measured eye-diagrams under different conditions. Fig. 4.20(a) depicts the over-equalized eye-diagram when operating at 5 Gb/s, where the four sub-levels are contributed by the four FFE taps. Fig. 4.20(b) and (c) presents the output eye-diagrams at 40 Gb/s before and after applying the 4-tap FFE. The comparison
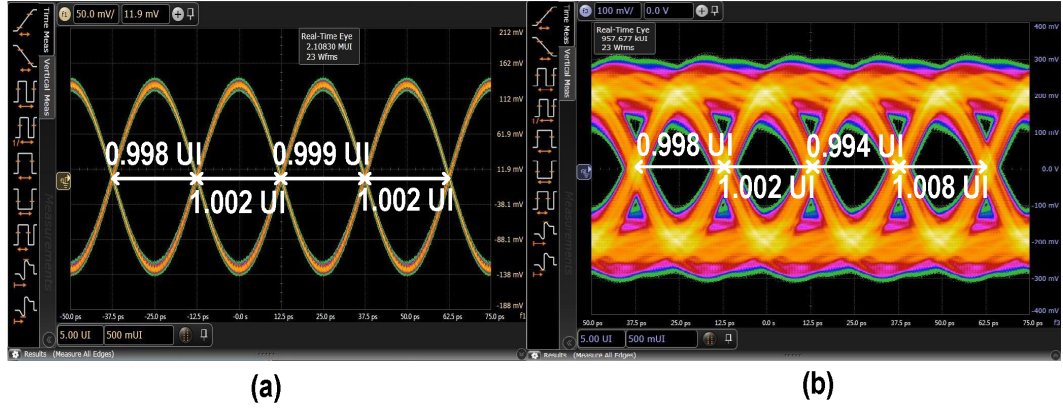
Figure 4.21: Measured output eye-diagrams with four separate eyes. (a) Clock pattern and (b) PRBS pattern.

shows that the FFE can significantly improve the inner eye opening. Specifically, the eye height and eye width are optimized from 140 mV and 0.45 UI to 180 mV and 0.68 UI, respectively. Meanwhile, the thickness of the eyelid is dramatically reduced from around 330 mV to 140 mV. Fig. 4.20(d) displays the properly-compensated eye-diagram at the maximum operation speed of 50 Gb/s. Its eye height and eye width are 50 mV and 0.38 UI. Clearly, a wide operation range from 5 Gb/s to 50 Gb/s is achieved, which is mainly attributed to the multi-MUX-based FFE implementation. Fig. 4.21 further illustrates the transmitter output with four separate eyes. It can be seen that the horizontal eye widths for both fixed clock and PRBS patterns are almost identical, thus proving that the four sampling phases are properly aligned.

4.5.4 Performance Comparison

Table 4.1 compares the measurement results of our transmitter chip with other transmitters operating at similar data rates. The results indicate that this transmitter chip achieves wider operation range, lower jitter performance, and better power efficiency than others. These are mainly owing to the proposed high-speed 4:1 MUX and the compact interleaved-latching scheme. The comparison also shows the area of our transmitter is much larger than that developed in [99], this is mainly due to the following two reasons. Firstly, the area of our transmitter refers to the whole chip including the core circuits, decoupling transistors, and input/output PADs, while the area in [99] only includes the core circuits. Secondly, the transmitter in [99] is designed based on

Table 4.1: PERFORMANCE SUMMARY OF THE TRANSMITTER

Reference	[26]	[99]	[24]	This work
Technology (nm)	65	14	65	65
Supply (V)	1.2	N/A	1.2	1.2
Data Rate (Gb/s)	60	16-40	50-64	5-50
Chip Area(mm^2)	2.1×1.0	0.215×0.13	1.2×1.0	1.2×0.5
FFE	N/A	4-tap	4-tap	4-tap
1UI-delay Gen.	N/A	Multi-MUX	LC-delay	Multi-MUX
MUX Type	2:1	4:1	4:1	4:1
Data Jitter RJ (ps_{rms})	1.08@30Gb/s	0.33@28Gb/s 0.51@40Gb/s	N/A	0.23@40Gb/s 0.18@50Gb/s
Data Jitter (ps) TJ (BER=10^{-12})	N/A	10.72@28Gb/s 12.89@40Gb/s	N/A	9.90@40Gb/s 10.58@50Gb/s
Power (mW)	450	518	199	156
Energy Efficiency (pJ/bit)	7.5	12.9	3.1	3.1

a 14 nm process, which is much smaller than the 65 nm process.

4.6   Chapter Summary

The quarter-rate transmitter with 4-tap FFE is implemented in 65 nm CMOS process. The integration of a bandwidth enhanced 4:1 MUX and an interleaved-retiming latch array makes the transmitter possess good properties of both low power consumption (3.1 pJ/bit) and small area occupation ($1.2 \times 0.5 mm^2$). The measurement results show that the developed transmitter can achieve a maximum operation speed of 50 Gb/s with a total jitter of 10.58 ps after a 12 dB loss channel. Owing to the multi-MUX-based FFE implementation, the transmitter can operate as low as 5 Gb/s and thus a wide operation range can be obtained.

Chapter 5

The Receiver Design

The main task of the receiver (RX) is to extract the originally transmitted data from the received signal using appropriate equalization and clock data recovery (CDR) techniques [69, 61, 70, 10]. This chapter presents a quarter-rate receiver operating at 40 Gb/s. It employs a two-stage continuous-time linear equalizer (CTLE) as the analog front-end and integrates an improved CDR to extract the sampling clocks and retime the incoming data. To automatically balance the jitter tracking and jitter suppression, passive low-pass filters (LPFs) with adaptively adjusted bandwidth are introduced into the data-sampling path, where the controlling code of the bandwidth is truncated from the frequency code generated by the integral path of the digital LPF within the C-DR loop. To optimize the linearity of the phase interpolation, a time-averaging-based compensating phase interpolator (PI) is proposed, which significantly optimizes the differential nonlinearity (DNL) and integral nonlinearity (INL) of the phase interpolation, thus improving the phase-step and phase-spacing uniformities of the sampling clocks.

In the remainder of this chapter, we firstly discuss the design considerations of the receiver, and then present the overall receiver chip and illustrate its main features. After that, the architecture-level improvement on the CDR loop and the linearity-optimized compensating PI are elaborately discussed in the following two sections. Finally, the experimental results are presented and discussed.

5.1 Design Considerations of the Receiver

5.1.1 Receiver Sensitivity

Receiver sensitivity is the minimum differential voltage level that the receiver can correctly differentiate between a "0" and a "1". It is a function of the input referred noise, offset, minimum latch resolution, and bit error rate (BER) requirement. It can be calculated by

$$V_s^{pp} = 2V_n^{rms}\sqrt{SNR} + V_{min} + V_{offset},$$ (5.1)

where V_s^{pp} is the receiver sensitivity, V_n^{rms} denotes the equivalent input random noise, SNR represents the signal-to-noise ratio, V_{min} stands for the minimum latch resolution, and V_{offset} refers to the equivalent input offset. V_n^{rms} usually comes from matching impedances, input amplifiers, and data slicers. The SNR is determined by the BER requirement, e.g. $\sqrt{SNR}$=7 for a $BER = 10^{-12}$. V_{min} stems from the hysteresis, finite regeneration gain, and bounded noise sources. Typically, its value is smaller than 5 mV. V_{offset} is subject to circuit mismatches, which primarily exhibits a strong function of the V_{th} mismatch and a weak function of electron mobility mismatch. Although a large area (4×) can reduce the input offset [1/(2×)], it is not feasible in practical designs due to the excessive area occupation and power consumption. In practical designs, offset correction circuitry is usually employed to reduce the input offset from a potentially large uncorrected value (>50 mV) to near 1 mV.

5.1.2 CDR Bandwidth

The CDR bandwidth is one of the most important parameters in the CDR design, which involves a tradeoff of jitter tracking, jitter suppression, and jitter tolerance. A narrow bandwidth can provide prominent input-jitter suppression and help to reduce the jitter peaking, while a wide bandwidth can enhance the capability of jitter tracking and jitter tolerance. To suppress jitter amplification and accumulation in long-haul telecommunication systems, a narrow bandwidth is usually specified (e.g., 120 kHz

for optical carrier (OC)-192 in synchronous optical network (SONET) [5]). To improve the jitter tacking ability in chip-to-chip connections, a relatively wide bandwidth is frequently utilized (e.g., 10 MHz for 32G fiber channel (FC) [160]). A wide CDR bandwidth also helps to suppress the VCO phase noise, thus reducing the jitter of the sampling clocks (i.e., optimizing the jitter generation), which finally helps to lower the link BER. Historically, the CDR bandwidth in many SerDes protocols such as peripheral component interconnect express (PCIE), Infiniband, FC, and common electrical interface (CEI) grows linearly with the data rate, which is usually defined as 1/1667 or 1/2500 of the data rate.

5.1.3 Challenges within High-Speed CDR

As the data-rate approaches to the process limit, the short unit interval (UI) significantly compresses the jitter budget for the CDR at the RX-side. This means there is a even smaller margin left for sampling position deviation, clock dithering, random and/or deterministic jitter, duty cycle distortion, and spacing errors among different phases [23], thus setting higher standards on low-frequency jitter tracking, high-frequency jitter suppression, recovered clock jitter generation, sampling clock duty cycle precision and phase-spacing accuracy. These requirements bring in significant challenges in designing a high performance CDR [25, 23, 123], mainly because of the following reasons. Firstly, the tightly coupled jitter tolerance (JTOL) and jitter transfer (JTRAN) parameters make it difficult to design a low bandwidth for JTRAN to suppress the incoming jitter. Secondly, the cycle-limited dithering caused by steady-state oscillation contributes a substantial amount of deterministic jitter. Thirdly, the inevitable loop latency along with the data-rate proportional CDR bandwidth may degrade the system phase margin.
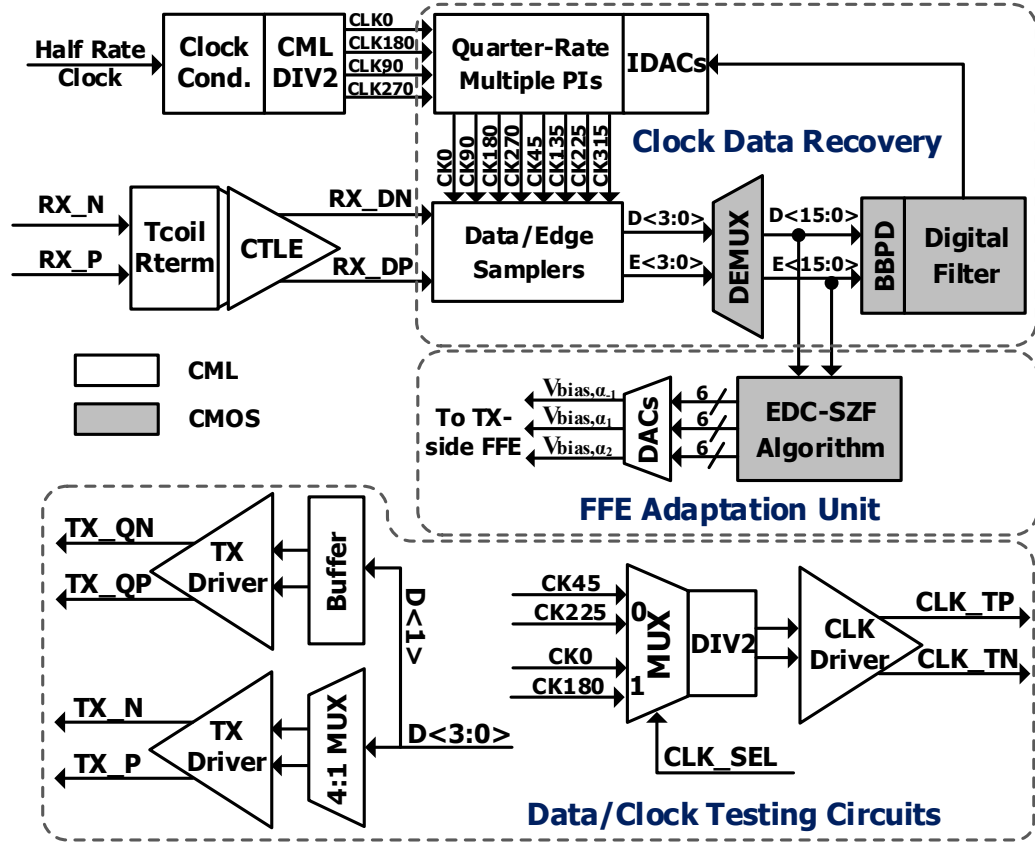
Figure 5.1: Block diagram of the receiver chip.

5.2 Receiver Architecture

5.2.1 Overall Architecture

Fig. 5.1 describes the block diagram of the receiver chip. It consists of a two-stage CTLE, a quarter-rate CDR, an feed-forward equalizer (FFE) adaptation unit, and some testing circuits for the recovered data and clock measurements. The received signal is firstly equalized by the CTLE and then sliced by eight quarter-rate data and edge samplers, where the sampling clocks are generated by two quarter-rate compensating PIs and the sampling positions are adjusted by a digital CDR using bang-bang phase detectors (BBPDs). To support the high operation speed, the samplers, PIs and clock/data buffers are implemented in current-mode logic (CML) type [10]. To alleviate the timing problem, a quarter-rate sampling scheme using multiple PIs is used to extend the slicer regeneration time. The channel loss is compensated for by the TX-FFE and RX-CTLE, where the TX-FFE is adaptively adjusted by the proposed edge-data correlation based sign zero-forcing algorithm (EDC-SZF) (refer to Section 6.1) while the
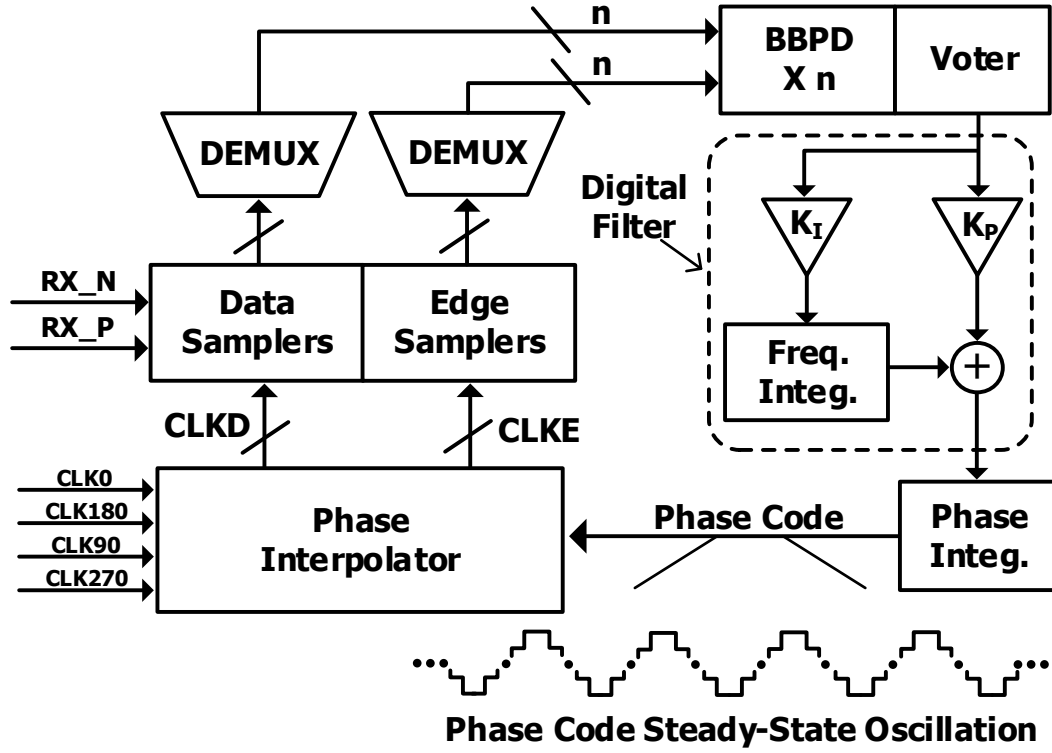
Figure 5.2: Conventional BBPD-based CDR.

RX-CTLE is manually calibrated.

5.2.2 Features of the Receiver

There are two main features in this receiver chip. One is the improved CDR architecture, where passive LPFs with adaptively adjusted bandwidth are introduced into the data-sampling path to automatically balance jitter tracking and jitter suppression for data decisions. In doing so, the JTRAN bandwidth can be adjusted separately without affecting the bandwidth of the JTOL. The other is the proposed compensating PI, which not only improves the phase-step uniformity but also reduces the phase-spacing drifting between edge and data sampling clocks.

5.3 Improved Digital CDR

5.3.1 Dithering Behavior in Digital CDR

Fig. 5.2 displays the conventional architecture of the BBPD-based CDR. Due to the nonlinear behaviour and inevitable loop delay, the phase code applied to the PI usually
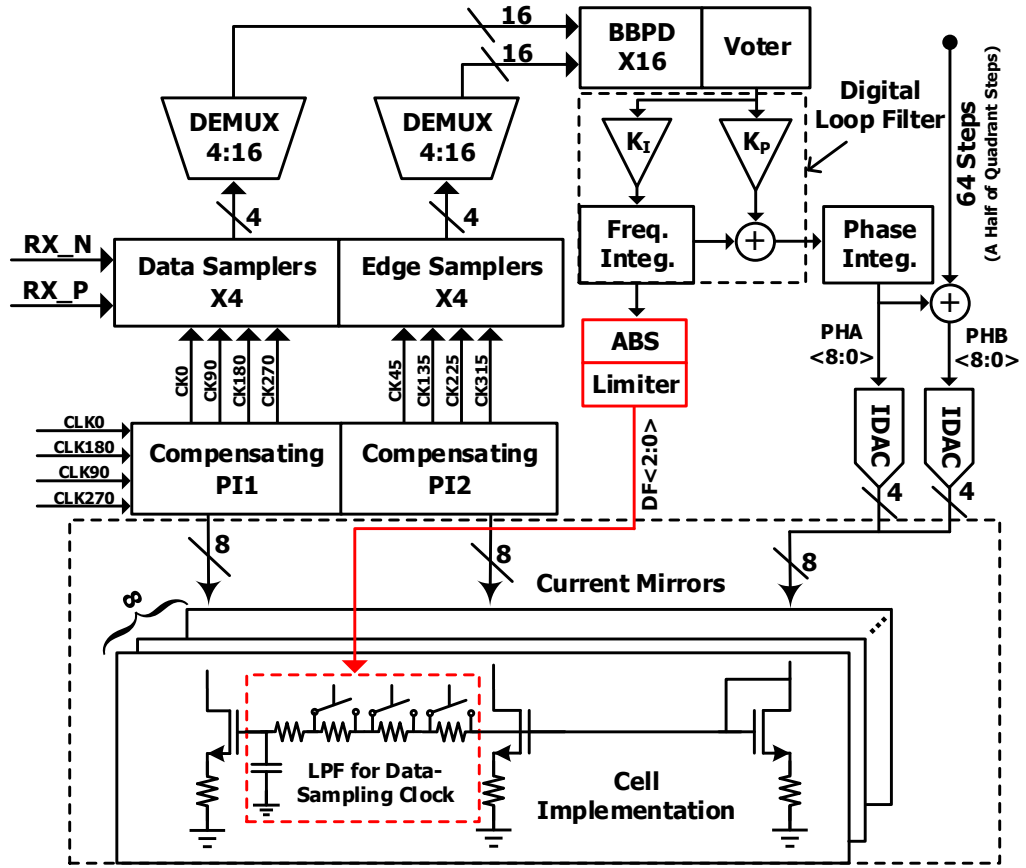
Figure 5.3: Block diagram of the modified CDR architecture.

exhibits steady-state oscillation, which brings in substantial deterministic jitter through rotating the PIs. This effect can become more severe as the data rate increases, the reason is that the increased loop gain and the not-well-scaled loop latency are prone to causing a larger limit-cycle oscillation amplitude. To attenuate this amplitude, a split-path CDR/DFE architecture is proposed in [161], which employs a digital averaging technique to filter the phase code for the separate data-sampling clocks. This approach can effectively improve the JTOL amplitude at high frequencies, but the inevitable delay added by the digital averaging block may make the sampling clocks drift away from the optimal positions, thus degrading the maximum tolerable amplitude at low frequencies.

5.3.2 Architecture Improvement

Fig. 5.3 shows the block diagram of the improved CDR. It employs separate PI1 and PI2 to produce the two sets of 45°-spaced clocks for the data sampling and edge

sampling, where passive LPFs are introduced into the clock branch for the data sampling to provide extra jitter suppression on the data-sampling clocks. The bandwidth of these introduced LPFs is adaptively adjusted by the same DF<2:0>, which is the absolute value of the truncated frequency code generated from the integral path of the digital loop filter. In this design, the minimum bandwidth of the LPFs is about 4 MHz while the maximum one is around 50 MHz. Particularly, a limiter is utilized to set the DF<2:0> to its maximum value when the frequency code goes too large. In principle, a large frequency code indicates a continuous phase slewing to accommodate to the accumulative jitter tracking. Thus, a wide bandwidth is chosen to improve the jitter tracking ability. On the contrary, a small frequency code implies that there is little trackable jitter. Accordingly, a narrow bandwidth is selected to suppress the high-frequency jitter.

For the implementation, 16 BBPDs associated with a majority voter are adopted to generate a 5-bit signed phase error, which is filtered by a digital loop filter consisting of a proportional path and an integral path to produce a 14-bit output. Here, the top 9 bits are applied to a 12-bit phase integrator whose output is then truncated to form the phase code PHA<8:0>, which is further circularly added by 64 steps (a half of quadrant phase steps) to obtain PHB<8:0>. These phase codes are applied to two current digital-to-analog converters (IDACs) to produce 8 paths of weighted currents that are fed into a current mirror array consisting of 8 identical slots. As shown in Fig. 5.3, each slot generates two branches of currents, one is directly mirrored for the edge-sampling PI2, while the other is mirrored through a LPF for the data-sampling PI1.

5.3.3 Behavior of the Improved CDR

The working principle of the BBPD is illustrated in Fig. 5.4(a). Considering the fact that the data sampling occurring at the center of the eye-diagram serves as a reference to judge whether the edge sampling is leading or lagging the input data transitions, there should be sufficient margin for the data sampling. Accordingly, the outputs of the data samplers show a fairly low sensitivity to phase errors in normal operating
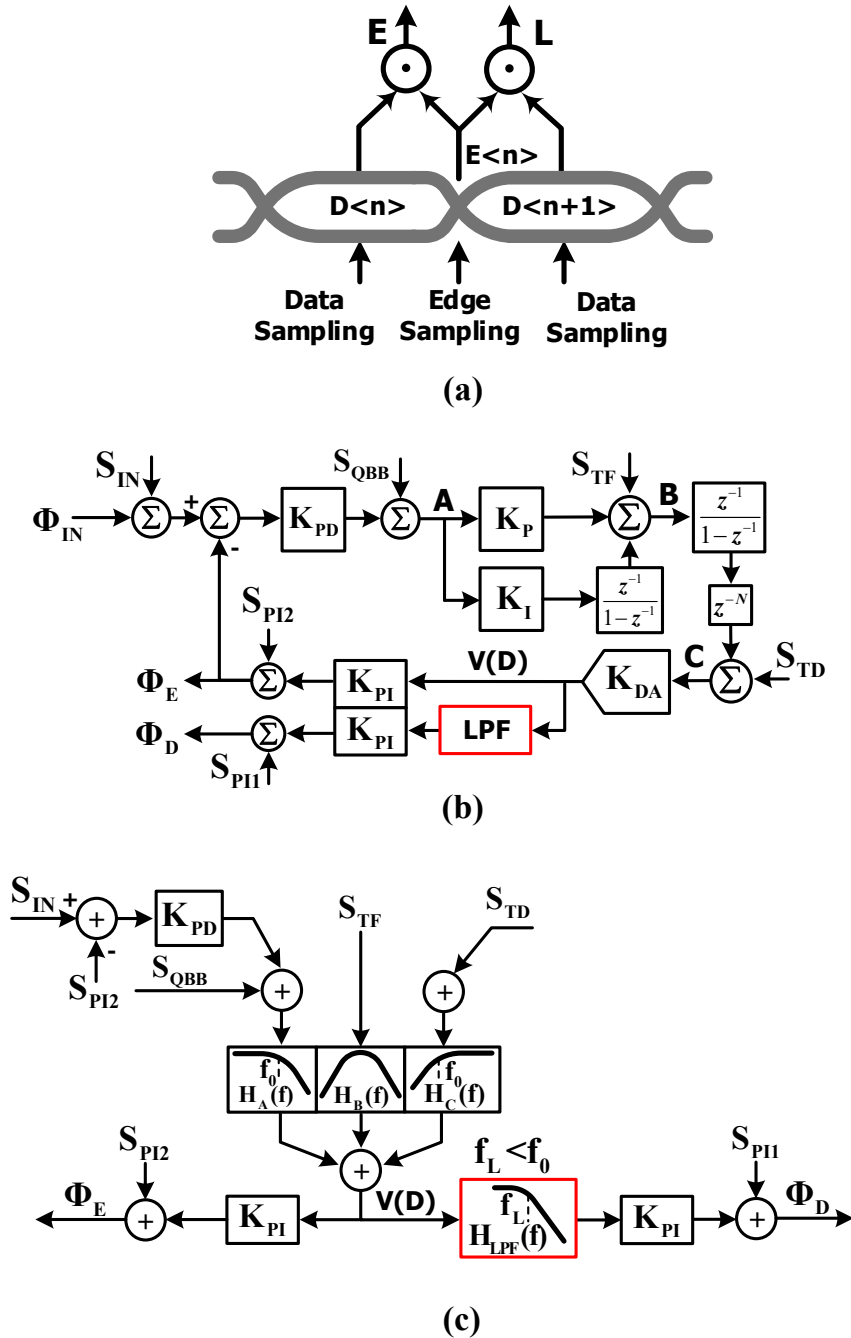
Figure 5.4: Functional view of the introduced LPFs. (a) Principle of the BBPD, (b) linearized CDR model, and (c) jitter transfer functions.

CDRs, which means that further jitter suppression on data-sampling clocks exhibits little effect on the loop parameters for jitter tracking. Leveraging this characteristic of the BBPD, we introduce LPFs into the data-sampling path to further filter the output jitter while keeping the loop parameters unchanged to satisfy the jitter tolerance specification. Fig. 5.4(b) presents the small-signal model of the modified CDR, where

the LPF located outside of the feedback loop is able to provide additional jitter suppression for the data-sampling clocks [see Fig. 5.4(c)]. Therefore, the dithering jitter caused by the limit-cycle oscillation can be effectively attenuated. The noise sources are also depicted in Fig. 5.4(b), including the input noise (S_{IN}), quantization noise (S_{QBB}) of the BBPD, truncation noise I (S_{TF}) due to finite resolution of the integral path, truncation noise II (S_{TD}) due to limited resolution of the IDAC, and nonlinearity noise (S_{PI1}, S_{PI2}) of the PIs. Fig. 5.4(c) displays the transfer function characteristics for these noise sources. It can be seen that the introduced LPFs can dramatically attenuate the remaining band-frequency and high-frequency components from S_{TF} and S_{TD}. The low-frequency components of S_{IN}, S_{PI2}, and S_{QBB} can be further reduced by these LPFs when lower bandwidths are employed. Simultaneously, the potential jitter peak can be suppressed to alleviate the jitter amplification problem.

5.4 Compensating Phase Interpolator

The nonlinearity of phase interpolation can result in serious adverse effects on the overall performance of the CDR. Specifically, the differential nonlinearity (DNL) introduces a much larger phase jump than the ideal one, which can be directly converted into recovered clock jitter. The integral nonlinearity (INL) can make the data-sampling clocks drift away from their optimal decision points in quarter-rate architectures using multiple PIs [23]. To optimize the PI nonlinearity, fine weight current sources have been adopted in [115]. Unfortunately, the non-uniformity of the tail current sources gives rise to fluctuant common-mode output, which may distort the phase-interpolated clocks through common-mode to differential-mode conversion. Moreover, its performance is also subject to input waveform shape and fabrication mismatches. Another approach that is also usually adopted to optimize the PI linearity is the octagonal PI [122], which needs eight 45°-spaced clock phases to perform the phase interpolation. Correspondingly, it requires a complex phase rotator and phase controlling circuits to generate the octagonal phase constellation. Note that even in the octagonal PI, there does exist nonlinearity in theory. As a consequence, new techniques that can improve the linearity of the phase interpolation are still highly demanded.
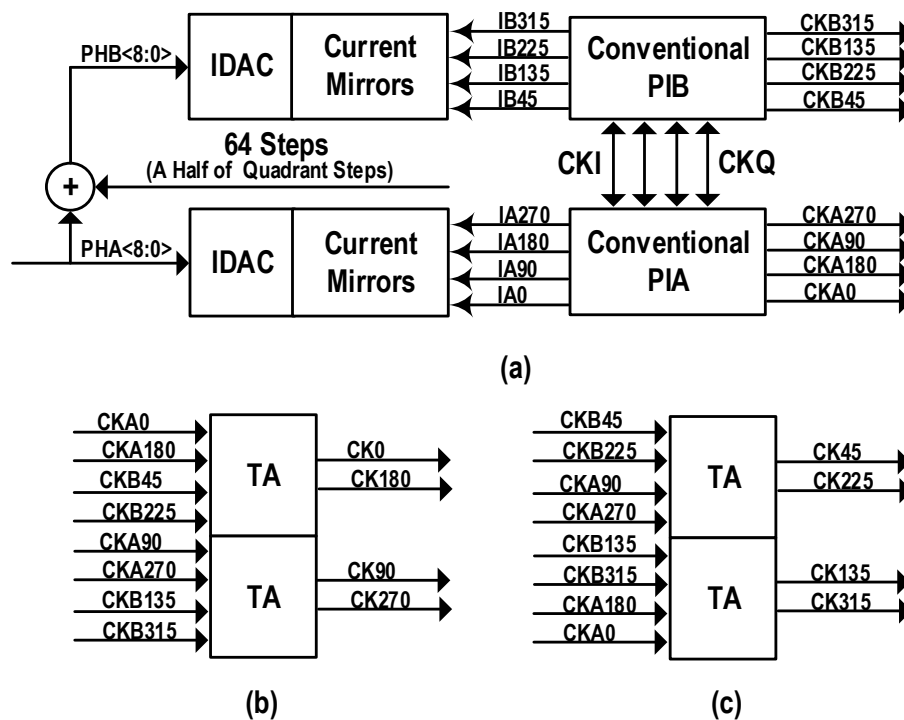
Figure 5.5: Proposed compensating PI. (a) Quarter-rate 45°-spaced clock generation, (b) in-phase I, Q clock generation for the data sampling, and (c) 45° phase-shifted I, Q clock generation for the edge sampling.
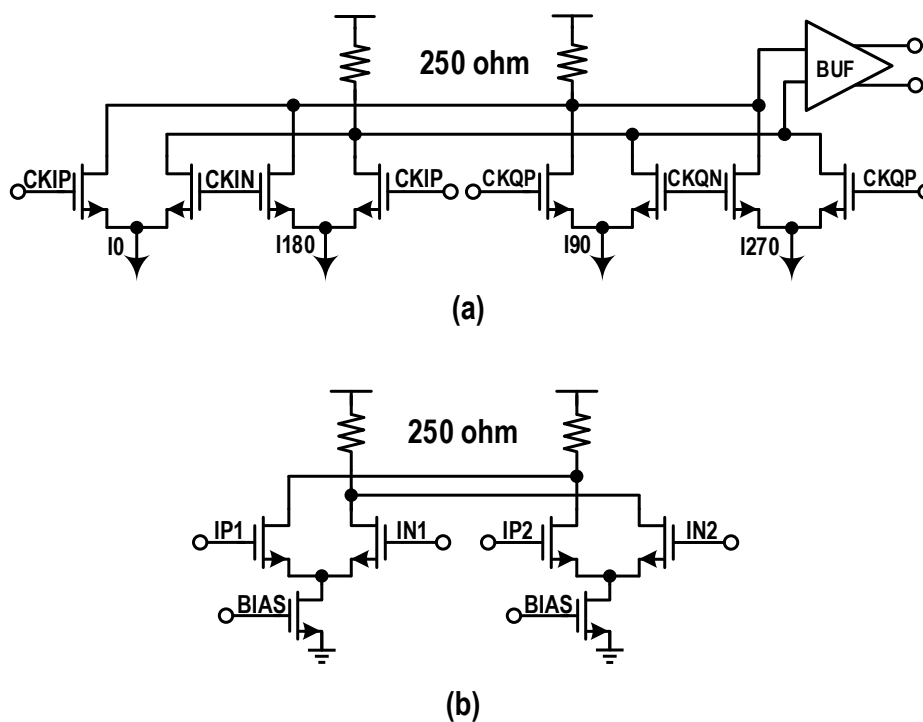
Figure 5.6: Details of (a) quadrature PI and (b) TA.

5.4.1 Implementation Details

Fig. 5.5 shows the conceptional block diagram of the compensating PI. It employs two conventional PIs (PIA and PIB) with 1/2-quadrant-step spaced phase codes (PHA<8:0> and PHB<8:0>) to produce the two sets of 45°-spaced clocks (CKA0-90-180-270 and CKB45-135-225-315) [see Fig. 5.5(a)]. The two sets of 45°-spaced clocks are then applied to four time averaging (TA) [see Fig. 5.5(b) and (c)] to generate the final data and edge sampling clocks. Specifically, the data-sampling clocks (CK0-90-180-270) are obtained by averaging CKA0-90-180-270 and CKB45-135-225-315, while the edge-sampling clocks (CK45-135-225-315) are attained by averaging CKA90-180-270-0 and CKB45-135-225-315. Fig. 5.6 further displays the schematic details of the quadrature PI and TA, which are implemented in CML style. The simulation also shows that the additional PI and TAs in each compensating PI consume around 10 mW, which occupies 50% of the compensating PI.

5.4.2 Linearity Analysis

Taking the sinusoidal waveform to approximate the input-clock wave shape, the quadrature input clocks can be expressed by

$$
\begin{aligned}
CK_I &= A sin(2\pi ft), \\
CK_Q &= A cos(2\pi ft),
\end{aligned}
\tag{5.2}
$$

where A and f are the amplitude and frequency of the input clock. Then the output of the traditional PIA can be calculated by

$$
\begin{aligned}
CK_{PIA} &= (1-\alpha) A sin(2\pi ft) + \alpha A cos(2\pi ft) \\
&= A_{PIA} sin(2\pi ft + \theta_{PIA}),
\end{aligned}
\tag{5.3}
$$

$$
\theta_{PIA} = arctan(\frac{\alpha}{1-\alpha}),
\tag{5.4}
$$

$$
A_{PIA} = \sqrt{\alpha^2 + (1-\alpha)^2} A,
\tag{5.5}
$$
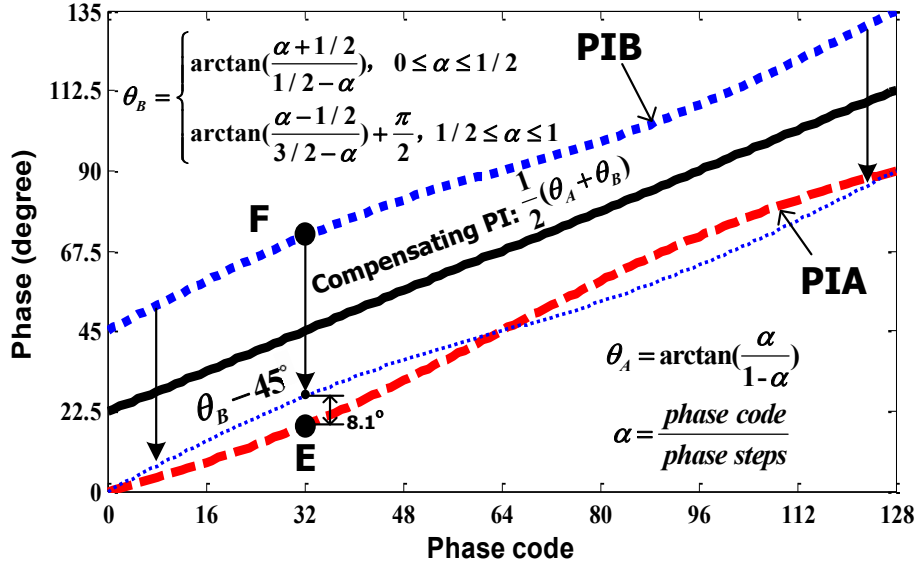
Figure 5.7: Phase transfer characteristics based on trigonometric-function approximation.

where α is the ratio of the current phase code to the total phase steps and its range always meets $0 \leq \alpha \leq 1$. Similarly, the equations for PIB can also be obtained, written as

$$CK_{PIB} = A_{PIB}sin(2\pi ft + \theta_{PIB}),\qquad(5.6)$$

where

$$\theta_{PIB} = \begin{cases} arctan(\frac{\alpha+1/2}{1/2-\alpha}), 0 \leq \alpha \leq 1/2, \\ arctan(\frac{\alpha-1/2}{3/2-\alpha}), 1/2 \leq \alpha \leq 1. \end{cases}\qquad(5.7)$$

$$A_{PIB} = \begin{cases} \sqrt{(\alpha+1/2)^2 + (1/2-\alpha)^2}A, 0 \leq \alpha \leq 1/2, \\ \sqrt{(\alpha-1/2)^2 + (3/2-\alpha)^2}A, 1/2 \leq \alpha \leq 1. \end{cases}\qquad(5.8)$$

Previous studies [23, 103] have demonstrated that this 45°-spaced clock generation can be directly used in CDR designs. However, the nonlinearity of the traditional PI could significantly degrade the performance of the CDR. To gain more insight into this issue, the red dashed and blue dotted lines in Fig. 5.7 respectively present the phase transfer curves according to Eq. 5.4 and 5.7. Clearly, the phase transfer curves of
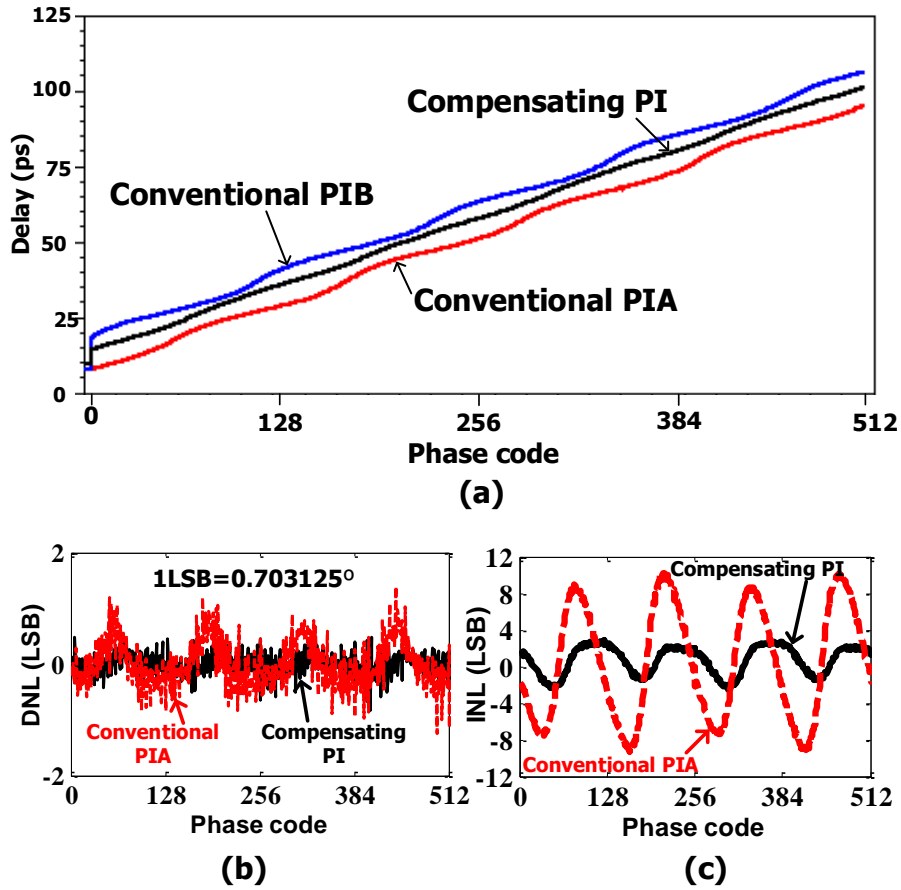
Figure 5.8: Simulation results of the phase compensating PI. (a) Simulated phase transfer characteristics, (b) DNL performance, and (c) INL performance.

the traditional PIA and PIB present an S-shape phase transfer characteristic. When PIA rotates to point E and PIB rotates to point F, the phase shift between them can reach a maximum of 8.1° (or 0.09 UI). For the designs directly using these phases as the sampling clocks [23, 103], since the edge-sampling clocks tightly track the edge transitions in the received data stream, any phase-spacing variation between the edge-sampling and data-sampling clocks could make the data-sampling clocks drift away from the expected decision point. As a result, the data decision margin is reduced, which directly degrades the CDR performance. Moreover, improving the PI resolution cannot optimize this effect since fine step weights cannot change the shape of the phase transfer characteristics.

Referring to the time-averaging effect of the TA, the output phase of the compen-

sating PI can be expressed as

$$\theta_{CPI} = \frac{1}{2} \begin{cases} arctan(\frac{\alpha}{1-\alpha}) + arctan(\frac{\alpha+1/2}{1/2-\alpha}), 0 \le \alpha \le 1/2, \\ arctan(\frac{\alpha}{1-\alpha}) + arctan(\frac{\alpha-1/2}{3/2-\alpha}), 1/2 \le \alpha \le 1. \end{cases} \tag{5.9}$$

The black solid line in Fig. 5.7 displays the phase transfer curve of the compensating PI according to Eq. 5.9, which indicates that a more linear phase transfer curve with negligible phase deviations smaller than $0.17°$ can be achieved. This is mainly because of the compensating characteristics of the phase transfer curves of PIA and PIB. In contrast to the theoretical analysis, the practical linearity could be degraded by the transistors' inherent nonlinearity and the nonideal input clock waveform. Fig. 5.8 shows the transistor-level simulation results of the compensating PI. It can be seen that the maximum DNL and INL of the compensating PI can be significantly improved over the traditional PI, where the INL can be controlled below 2.5 LSB (or $1.8°$), which is only a quarter of that of the conventional PI.

5.5 Experimental Results

5.5.1 Tools and Fabrication Process

The receiver is designed using a Dell R730 server with two E5-2609V4 CUPs, 128 G memory and 8 T hard disk. The schematic, layout, and simulation are respectively finished by Schematic Composor, Virtuoso Layout, and Spectre/aps that are developed by Cadence and the Cadence version is IC5141. The layout verification and parasitic extraction are carried out by layout versus schematics (LVS)/design rule check (DRC) and parasitic extraction (PEX) using Caliber2013 that is developed by Mentor Graphics. To perform the measurements of the fabricated prototype, an Anritsu MP1812A is used to generate the 40 Gb/s input data through combining four 10 Gb/s PRBS7 sequences, a Tektronix BSA286C is used to characterize the CDR performance, and a KEYSIGHT DSA-X 93204A with an 80 GS/s and 32 GHz bandwidth is utilized to characterize the jitter performance of the output waveforms.

The prototype chip is designed and fabricated utilizing a 65 nm process. Under
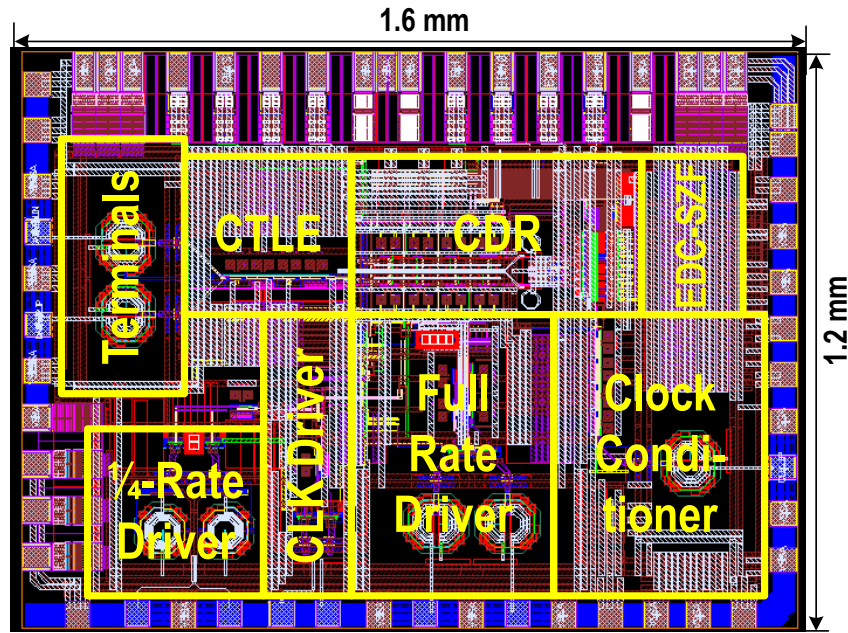
Figure 5.9: Layout view of the whole transmitter chip.

a typical corner, the cut-off frequency (f_T) of the NMOS transistor and the inverter delay with a fan-out-of-4 in this process achieve 200 GHz and 13 ps, respectively. This implies that the utilized 65 nm process is able to provide enough bandwidth and timing margin for the targeted 40 Gb/s receiver design. Although an advanced process with smaller minimum channel length such 45 nm, 32 nm, 22 nm and 16 nm can offer higher f_T and shorter inverter delay, their high prices make them not available for us. Fortunately, our receiver mainly focuses on the CDR architecture improvement and high-linearity compensating PI implementation, which can still be verified by the economical and practical 65 nm CMOS process.

5.5.2 Layout and Simulation Results

5.5.2.1 Layout Designs

Fig. 5.9 displays the layout view of the whole receiver chip. The Terminals, CTLE, and CDR located at the top side of the chip are the core blocks of the receiver. They are placed in a line to guarantee the layout symmetry and reduce the parasitic effect on the high-speed signals. The clock conditioner is placed close to the PI to facilitate the high-speed clock connection. The full-rate driver, clock driver, and quarter-rate driver are placed at the bottom side to output the measurement signals.

(a)

(b)
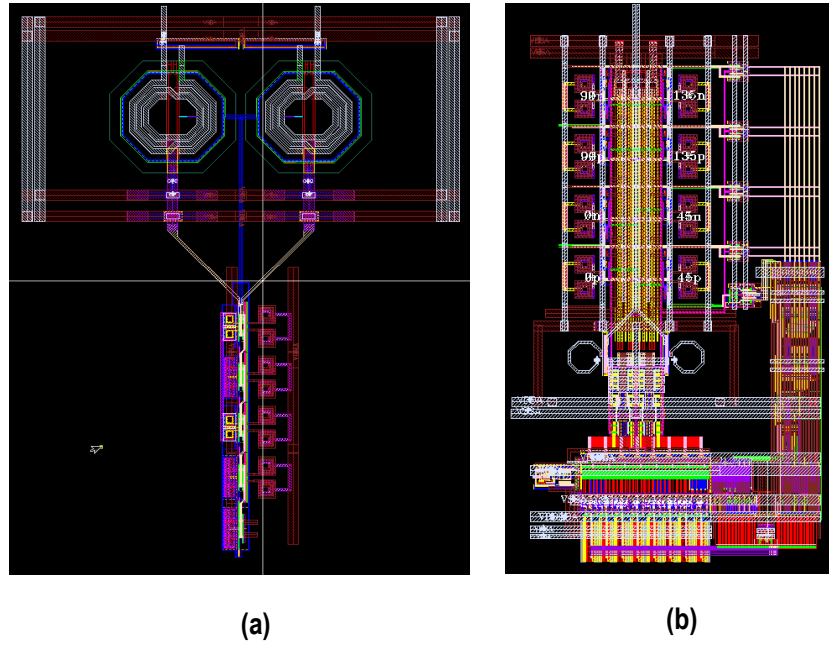
Figure 5.10: Layout views of the (a) Terminals+CTLE and (b) CDR.

(a)

(b)

(c)
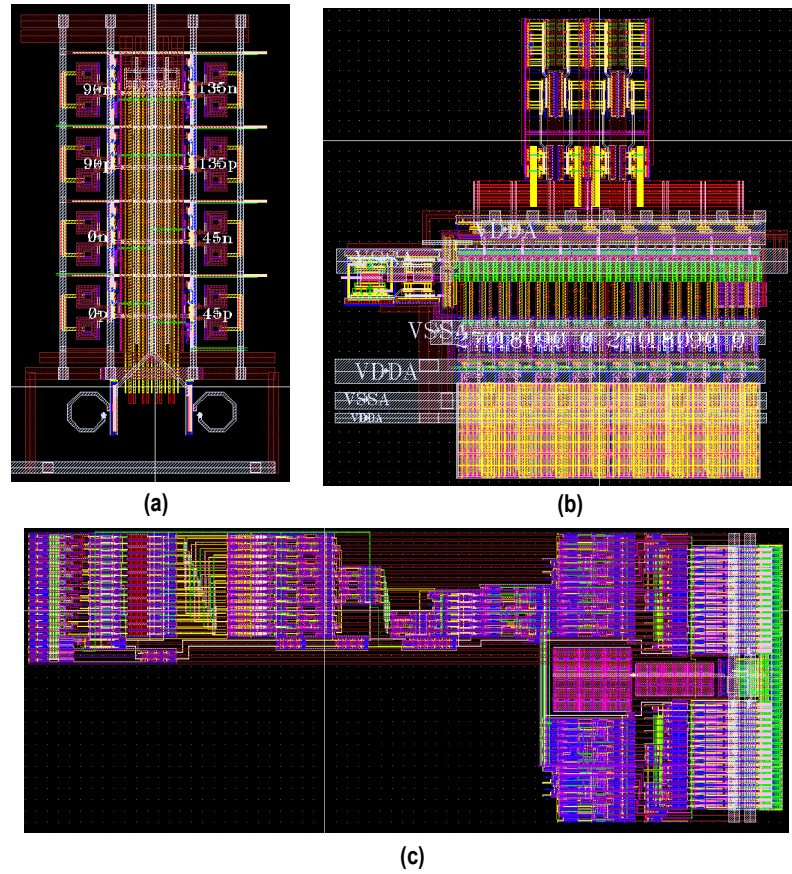
Figure 5.11: Layout views of the crucial blocks within the CDR. (a) Samplers, (b) compensating PI, and (c) digital loop filter.
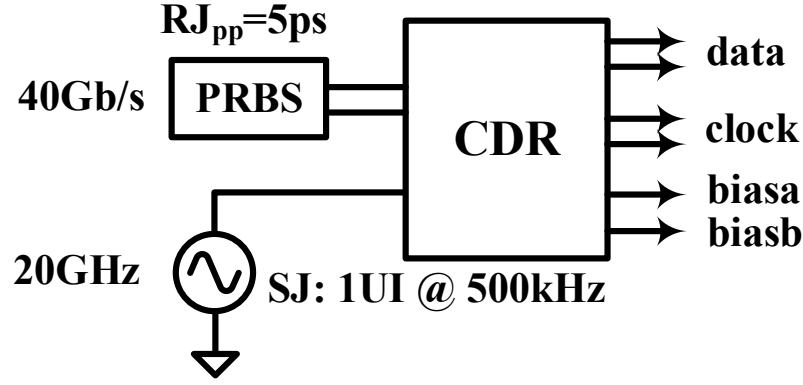
Figure 5.12: Simulation setup of the CDR. A PRBS generator is used to produce the 40 Gb/s input data with 5 ps peak-to-peak jitter, a clock generator is utilized to produce the 20 GHz input clock with a 1 UI amplitude sinusoidal jitter at 500 kHz, the output data refers to the input data at the samplers, the output clock is the recovered data-sampling clock, the output biasa represents the current mirror bias for $0°$-phase before the LFP, and the biasb stands for the current mirror bias for $0°$-phase after the LFP.

Fig. 5.11 gives the layout views of the blocks in the CDR. For the samplers [see Fig. 5.11(a)], multi-layer inductors are used in the first latch to extend its bandwidth. For the compensating PI [see Fig. 5.11(b)], the inductors are removed to reduce the area occupation. For the digital loop filter [see Fig. 5.11(c)], it is designed based on the standard cells provided by the foundry.

5.5.2.2 Effect of the Adaptively-Adjusted Bandwidth

To validate the effect of the adaptively-adjusted bandwidth, simulations are performed based on the simulation setup in Fig. 5.12. Fig. 5.13 displays the filtering effect on the current mirror bias for $0°$-phase and the jitter performance of the data-sampling clock with different LPF bandwidths, where the eye-diagrams are overlapped from 0.9 μs to 2.1 μs. For the simulated diagrams with the bandwidth of 4 MHz in Fig. 5.13(a), the high-frequency ripples on the bias can be significantly suppressed by the LPF. However, the dithering jitter of the data-sampling clock reaches 7.54 ps, which is much larger than that of the edge-sampling clock without the LPF (3.04 ps). It means that the CDR performance is actually deteriorated. This is mainly because of the prominent phase shift caused by the LPF delay. As the bandwidth increases, the delay-caused phase shift becomes smaller, thus indicating a descending trend in dither-
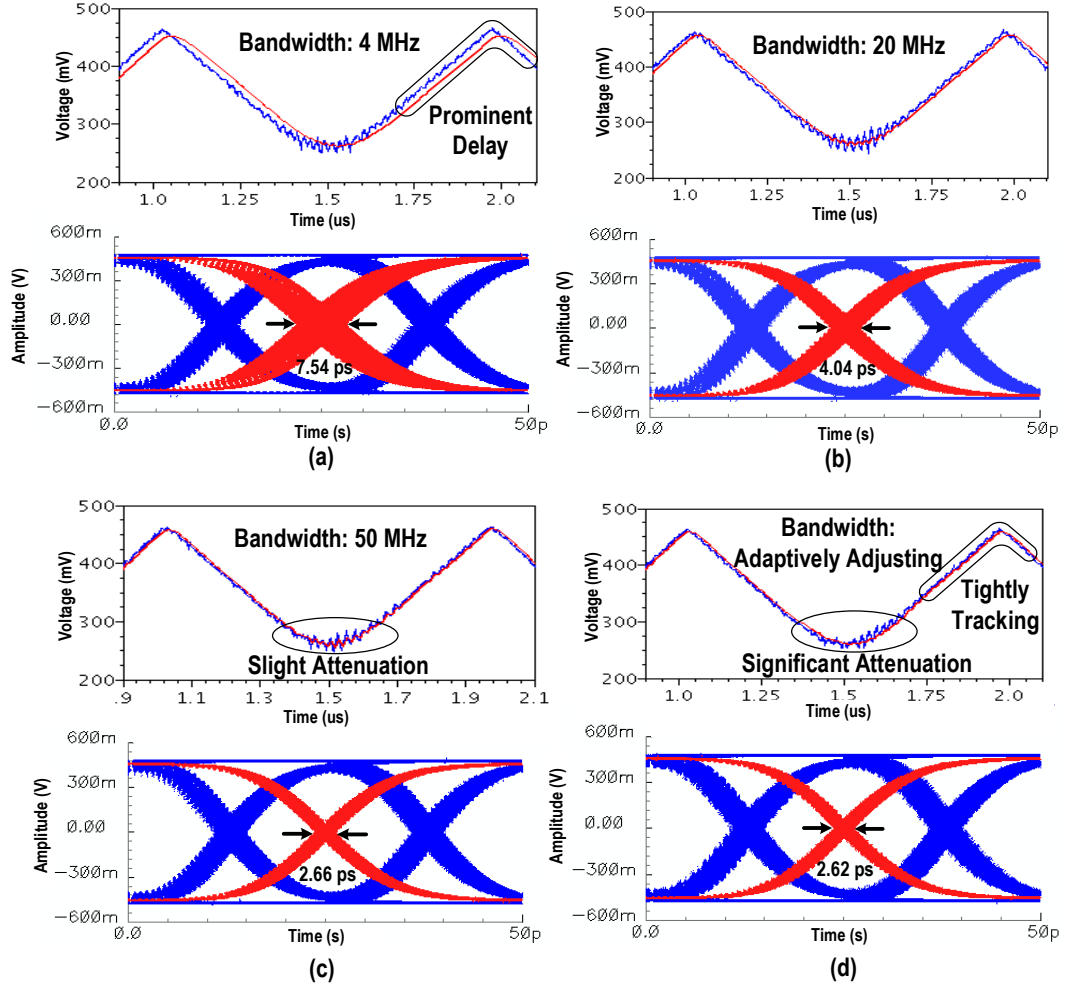
Figure 5.13: Effect of the LPFs with a bandwidth of (a) 4 MHz, (b) 20 MHz, (c) 50 MHz, and (d) adaptively-adjusting.

ing jitter of the sampling clock [see Fig. 5.13(b) and (c)]. For the bandwidth fixed at 50 MHz, the dithering jitter of the data-sampling clock (2.66 ps) becomes smaller than that of the edge-sampling clock (3.04 ps). This implies that the jitter optimization contributed by the bias-ripple suppression overwhelms the delay-caused phase shift. Based on the above discussion, it can be found that adopting a fixed bandwidth is inadvisable since the low bandwidth suffers from delay-caused phase shift while the high bandwidth exhibits limited jitter suppression. Fig. 5.13(d) presents the simulation results when utilizing the proposed bandwidth-adaptively-adjusting technique, where the low dithering jitter is achieved by balancing the bias tracking and ripple suppression. The high-frequency ripple at the slow input-jitter changing region [circled region in Fig. 5.13(d)] can be effectively attenuated while the phase variations at fast input-jitter changing region [surround region in Fig. 5.13(d)] can be tightly tracked.
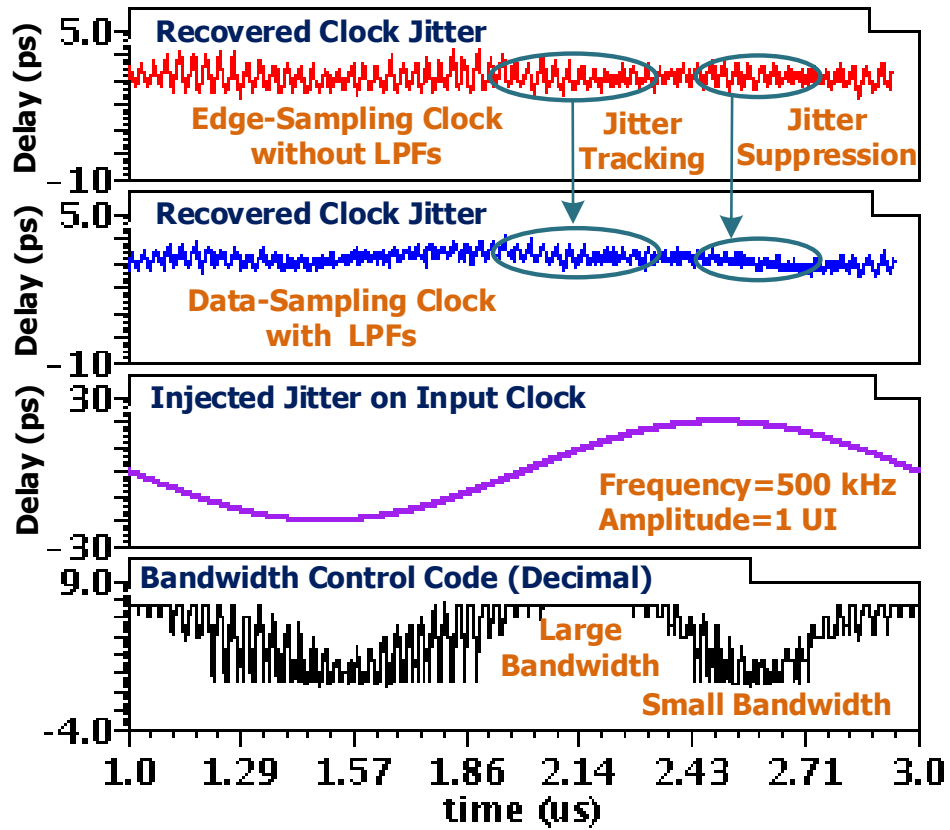
Figure 5.14: Properties of the adaptive-bandwidth jitter suppression.

To further explore the bandwidth-adaptively-adjusting process, Fig. 5.14 gives the transient simulation waveforms. For the fast input jitter changing region (jitter tracking region), a large frequency code is accumulated in the frequency integrator (see Fig. 5.3), thus a high bandwidth control code DF<2:0> for the LPFs can be obtained (see the bottom waveform in Fig. 5.14). As a result, the data-sampling clocks can tightly track the edge-sampling clocks to avoid data-sampling lagging. For the slow input jitter changing region (jitter suppression region), the frequency code becomes small and so does the bandwidth control code DF<2:0>. Correspondingly, the bandwidth of the LPFs decreases, thus exhibiting prominent jitter suppression effect. Owing to the proposed adaptive bandwidth-adjusting scheme, the jitter suppression and jitter tracking can be automatically balanced in this CDR. Overall, this automatic bandwidth selection technique makes it possible to use a low bandwidth to significantly suppress the high-frequency jitter while exhibiting little effect on the low-frequency jitter tracking ability.
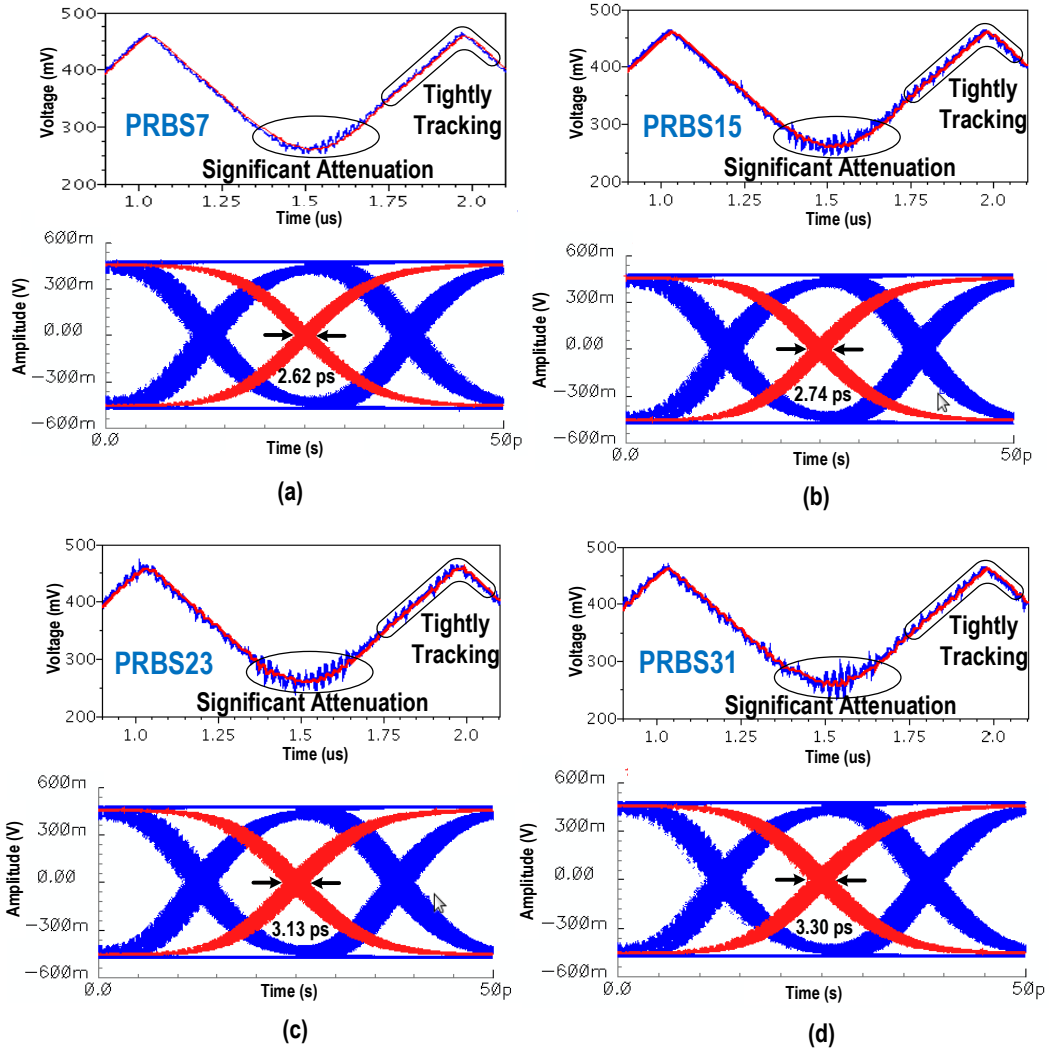
Figure 5.15: Effect of different input patterns on jitter attenuation. (a) PRBS7, (b) PRBS15, (c) PRBS23, and (d) PRBS31.

5.5.2.3 Effect of Different Input Patterns

To demonstrate the jitter suppression effect with different patterns, we have repeated the simulations with the adaptively-adjusted bandwidth using the setup shown in Fig. 5.12. As depicted in Fig. 5.15, when the input pattern ranges from PRBS7 to PRBS15, PRBS23, and PRBS31, the jitter performance of the recovered clock becomes slightly worse. This is because the increased run-length of "1s" or "0s" extends the wandering time of the CDR loop, thus causing a larger amplitude of steady-state oscillation and hence increase the deterministic jitter. Additionally, the high-frequency jitter suppression effect becomes more prominent as the max run-length of the input pattern increases (see the voltage ripple attenuation in Fig. 5.15).

(a)

Total Power=225mW
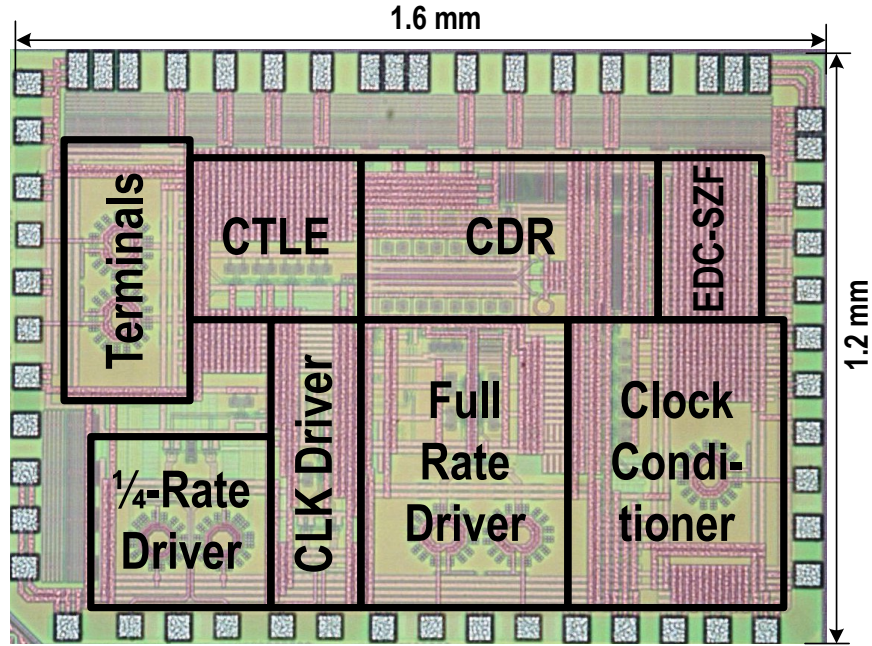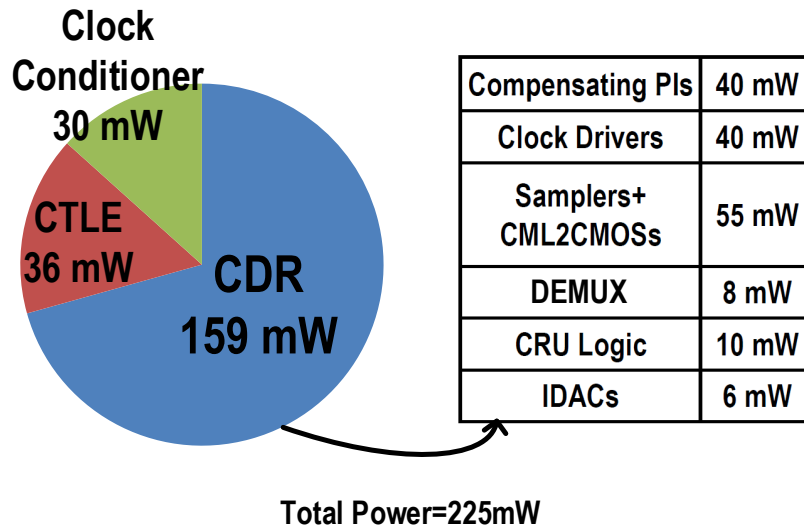
(b)

Figure 5.16: (a) Chip micrograph and (b) power breakdown of the receiver.

5.5.3 Chip Fabrication and Measurement Results

5.5.3.1 Chip Fabrication and Power Consumption

The prototype receiver chip is fabricated in 65-nm CMOS process. Fig. 5.16 illustrates its micrograph and power breakdown when applying a 1.2 V supply and operating at 40 Gb/s. The receiver chip occupies 1.92 mm^2 (including the testing circuits) and dissipates 225 mW power (excluding the testing circuits). The fabricated chip is
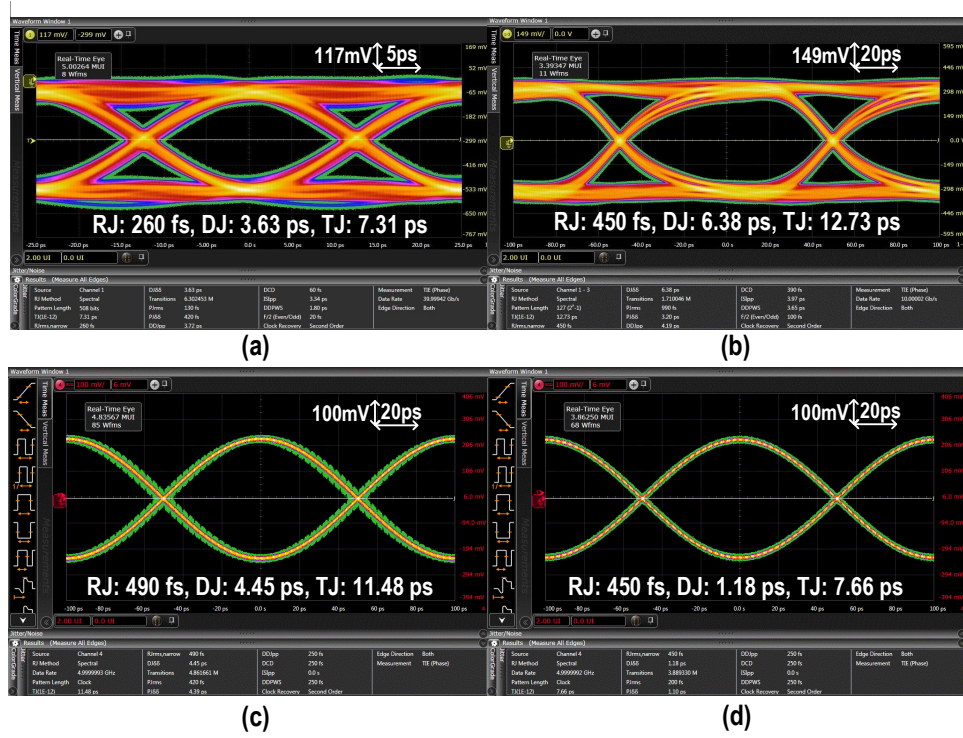
Figure 5.17: Measured eye-diagrams for (a) input data at 40 Gb/s, (b) recovered data at 10 Gb/s, (c) recovered edge-sampling clock without LPFs at 5 GHz, and (d) recovered data-sampling clock with LPFs at 5 GHz.

mounted on a printed circuit board (PCB) through wire-bonding. The receiver inputs and outputs are connected to the instruments through double-bonding wires, PCB traces, and connection cables.

5.5.3.2 Measurement Results

The receiver standalone measurement results are presented in this part. Fig. 5.17(a) shows the eye-diagram of the 40 Gb/s input data, where the single-end eye height and eye width are around 410 mV and 0.71 UI. Fig. 5.17(b) presents the eye-diagram of the 10 Gb/s recovered data with a total jitter of 12.73 ps. The eye-diagrams of the recovered clocks (divided by 2) for the data sampling and edge sampling are shown in Fig. 5.17(c) and (d), which reveal that the introduced LPFs can optimize the total jitter from 11.48 ps to 7.66 ps. To demonstrate the effect of the LPFs with adaptively-adjusting bandwidth, the JTRAN and JTOL curves are measured using a Tektronix BSA286C with a CDR block. The input peak-to-peak swing is tuned to 800 mV and the control voltage of the CTLE is manually set to 710 mV. The JTRAN curves in Fig.
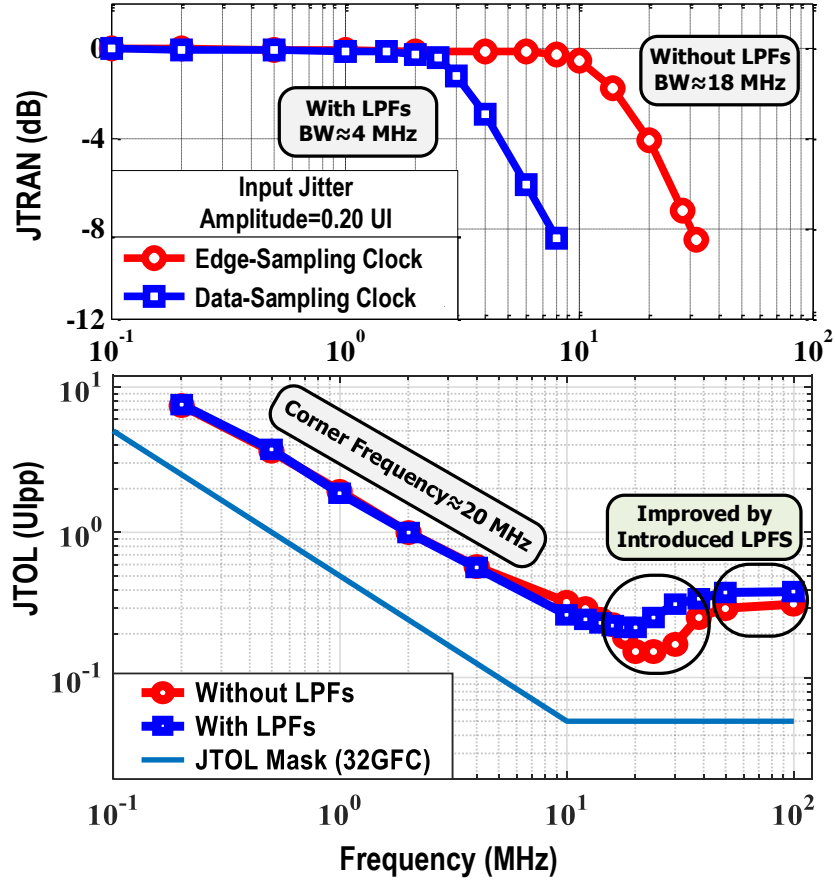
Figure 5.18: Measured JTRAN and JTOL with PRBS7 at 28 Gb/s.

5.18 illustrate that the bandwidth of the data-sampling path depending on the LPFs is 4 MHz, which is much smaller than 18 MHz for the edge-sampling path determined by the loop parameters. The measured JTOL in Fig. 5.18 indicates that the embedded LPFs result in a significant dip attenuation around the corner frequency and improve the JTOL amplitudes apparently at high jitter frequencies. Meanwhile, the adaptively-adjusting bandwidth of the LPFs makes them exhibit little effect on the phase-tracking slew rate at low jitter frequencies. Additionally, the corner frequency of the JTOL is about 20 MHz, which is much larger than the JTRAN bandwidth of 4 MHz.

5.5.4 Performance Comparison

Table 5.1 compares the performance of our receiver with previous studies. It can be seen that the maximum tolerable amplitude of sinusoidal jitter at high frequency (0.41 UI@100 MHz) outperforms the other two, which is mainly because of the introduced LPFs and the developed compensating PI. As for the reason why this parameter is so

Table 5.1: PERFORMANCE SUMMARY OF THE RECEIVER

	[23]	[123]	This work
Technology (nm)	28	22	65
Supply (V)	1.1/0.85	1.07	1.2
Data Rate (Gb/s)	40	4-32	40
Multi-phase Clock Gen.	DLL+PIs	MCDLL+PIs	DIV2+PIs
Jitter Suppression	Split-path CDR	N/A	Adaptive-BW LPFs
JTOL Amplitude (UI)	0.2@80MHz	0.2@40MHz	0.41@100MHz
JTOL Bandwidth (MHz)	10	20*	20
Chip Area (mm^2)	0.81/lane**	0.079/lane	1.92
Power (mW)	630*†	79.64††	225

*Estimated from jitter tolerance results, **Area of whole transceiver
*†Including FFE+DFE equalization, ††Including RX-FFE

important is because it directly indicates that our receiver has the ability of relaxing the timing budget of the link and hence optimizes the communication BER. Meanwhile, it is worthy to note that the area occupation and power consumption of our receiver are larger than the design presented in [123]. This is mainly because of the following two reasons. One is that the area occupation and the power consumption in [123] are measured based on the the core circuits, while these two parameters in our design are measured based on the whole chip, including the core circuits, testing circuits, decoupling transistors, and connection pads. The other is that the receiver in [123] is implemented in a 22 nm process, which naturally possesses the good properties of smaller area and lower power consumption. If this receiver is also implemented in such an advanced processes, the receiver should have the ability to operate at a higher data rate with a smaller area occupation and a lower power consumption than the one implemented in the 65 nm process.

5.6   Chapter Summary

This chapter presents a 40 Gb/s receiver with excellent performance on both jitter suppression and jitter tracking, where a compensating PI is designed to alleviate the issues of non-uniform phase steps and I, Q phase-spacing drifting. Moreover, the introduced bandwidth-adaptively adjusted LPFs can provide additional high-frequency

jitter attenuation for data-sampling clocks, while leaving the edge-sampling clocks un-filtered to maintain a high jitter tracking capacity.

Chapter 6

Overall Serial Link and Adaptive Equalization

To overcome the channel loss and satisfy the stringent power and area budgets, sophisticated equalization design is demanded to compensate for the channel loss while balancing the cost of power and area overheads. Based on the transmitter (TX) and receiver (RX) chips designed in the previous two chapters, this chapter constructs a chip-to-chip connection where the output of the transmitter chip and the input of the receiver chip are DC connected over a 12-cm printed circuit board (PCB) trace. A combined TX-side feed-forward equalizer (FFE) and RX-side continuous-time linear equalizer (CTLE) is adopted to compensate for the channel loss. The control voltage of the RX-CTLE is manually calibrated while the tap weights of the TX-FFE are automatically adjusted by a newly developed edge-data correlation-based sign zero-forcing (EDC-SZF) adaptation engine located at the RX-side.

In the rest of this chapter, Section 6.1 illustrates the equalization scheme employed in the serial link. The proposed EDC-SZF adaptation is presented in section 6.2. It begins by summarizing the drawbacks in previous adaptation techniques and then presents the update iteration and the derivation of the proposed EDC-SZF algorithm. Section 6.3 finally gives the link setup and experimental results.
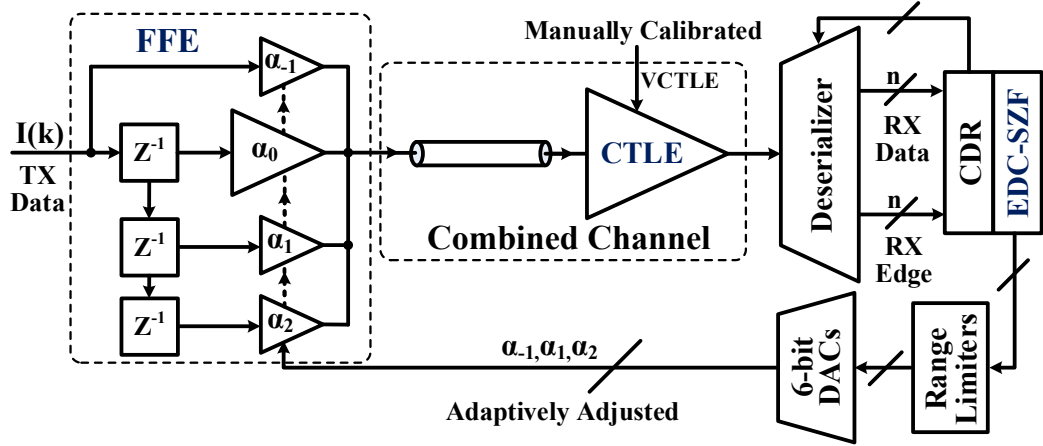
Figure 6.1: Implemented equalization scheme with the proposed EDC-SZF algorithm. Here, TX-FFE and RX-CTLE are employed to compensate for the channel loss, the control voltage of the RX-CTLE (VCTLE) is manually calibrated while the tap weights $(\alpha_{-1}, \alpha_1, \alpha_2)$ of the TX-FFE are adaptively adjusted by the proposed EDC-SZF.

6.1 Serial Link and Channel Equalization

6.1.1 Link Connection and Equalization Scheme

Fig. 6.1 describes the block diagram of the serial link along with the equalization scheme, where the output of the transmitter chip is directly connected to the receiver chip through a channel. It employs a TX-FFE and a RX-CTLE to compensate for the channel loss. The decision feedback equalizer (DFE) is ruled out here, mainly because of its operation speed limitation, complicated implementation, and significant power consumption [162, 101]. These overheads generally result from the increased number of data samplers within the DFE [34, 25]. The RX-CTLE is manually calibrated while the tap weights of the TX-FFE are adaptively adjusted by an EDC-SZF algorithm at the RX-side. The digital tap weights generated by the EDC-SZF engine are firstly constrained by three range limiters and then applied to three 6-bit digital-to-analog converters (DACs) to produce the bias voltages for the TX-FFE taps. These bias voltages are transferred to the transmitter through PCB traces. To save the output pins, the DACs in practical implementations are located at the TX-side and the controlling tap-weight codes are sent through the communication channel under the control of the status state machine in the media access control (MAC) layer [163]. In our prototype,
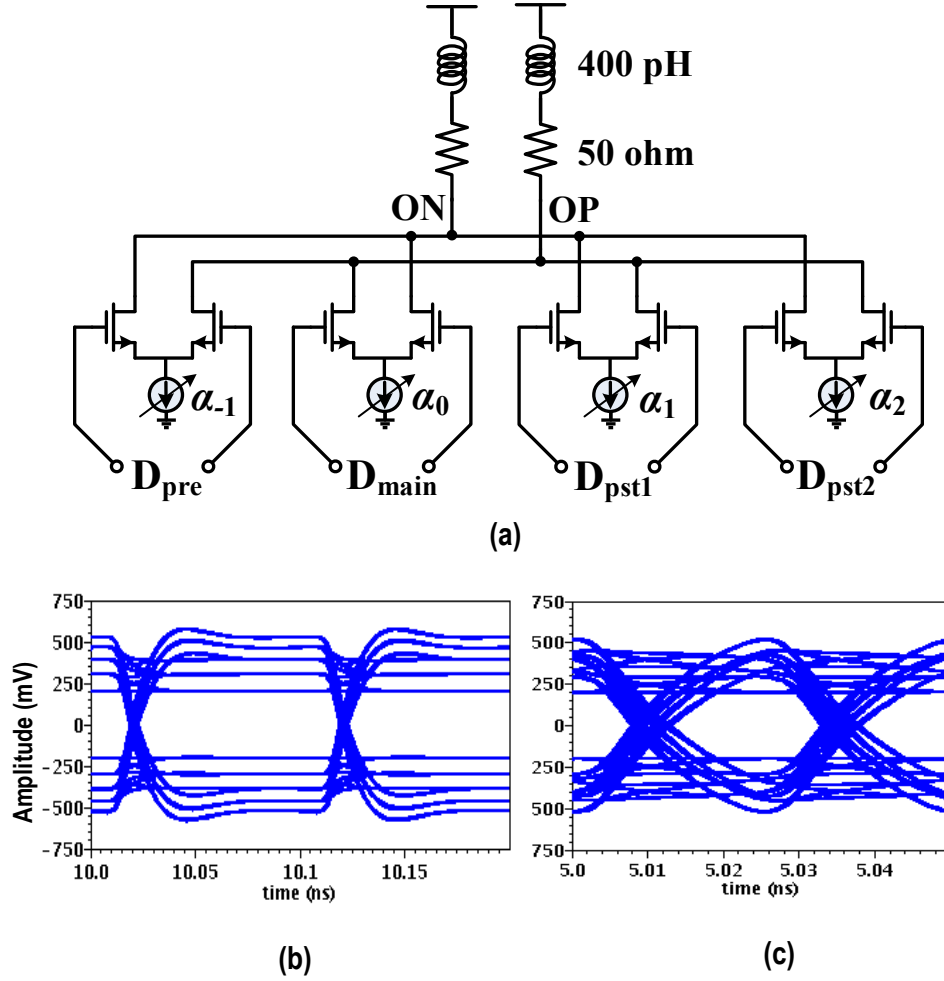
Figure 6.2: TX-FFE. (a) Schematic details, (b) simulated output eye-diagram at 10 Gb/s, and (c) simulated output eye-diagram at 40 Gb/s.

due to the lack of the MAC layer, the DACs are located at the RX-side and the bias voltages are transferred to the transmitter through PCB traces.

6.1.2 Equalizer Implementation Details

Fig. 6.2(a) shows the schematic details of the TX-FFE. It is realized by a 4-tap current-mode logic (CML) combiner, where the tap weights are adjusted by changing the bias voltages of the current sources. Fig. 6.2(b) and (c) display the simulated near-end eye-diagrams at 10 Gb/s and 40 Gb/s when applying -3 dB, -6 dB, and -3 dB equalization coefficients to the pre, post1, and post2 cursors in the FFE. The circuit implementation of the RX-CTLE and its frequency responses with different control voltages are presented in Fig. 6.3. To optimize the equalization configuration,

(a)

(b)
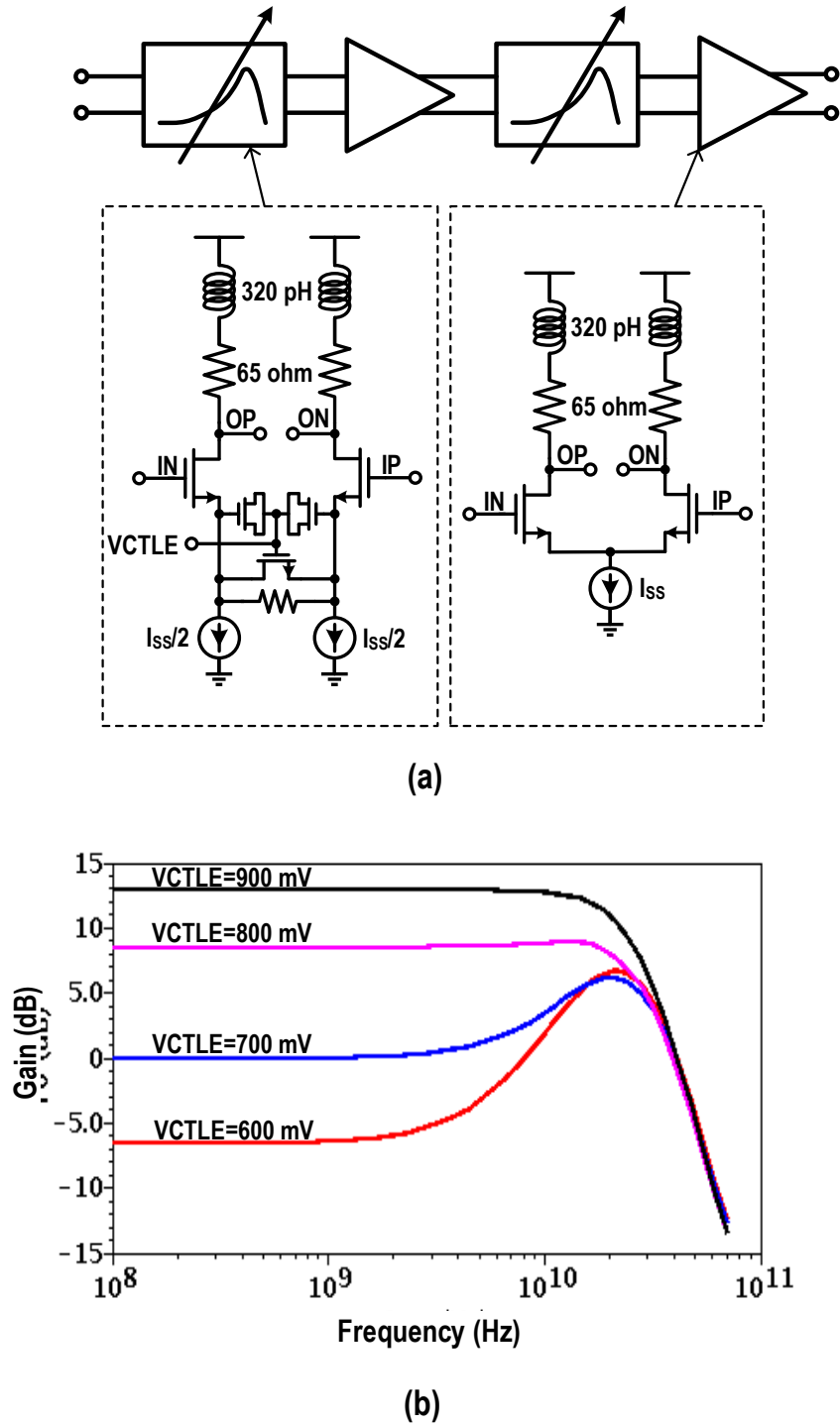
Figure 6.3: RX-CTLE. (a) Schematic details and (b) frequency responses for different control voltages.

the control voltage of the RX-CTLE is manually adjusted while the tap weights of the TX-FFE are adaptively adjusted by a low-cost EDC-SZF adaptation engine. In the remainder of this section, we will focus on the design of the proposed EDC-SZF algorithm.

6.2 Edge-Data Correlation-Based Sign Zero-Forcing (EDC-SZF)

6.2.1 Drawbacks of Previous Adaptation Algorithms

Previous adaptation algorithms for wireline communications can be mainly categorized into sign-sign least mean square (SS-LMS), zero-forcing (ZF), and maximum eye opening (MEO)[129, 130, 131, 105, 132, 133]. The SS-LMS algorithm, which aims to minimize the mean square error between the specific eye height and the measured eye height, is widely used to adjust the equalization coefficients for its simplicity and robustness [129, 34, 130, 131]. However, it needs auxiliary samplers to extract the sign error between the equalized and expected eye heights. This makes it less competitive for applications operating at tens of Gb/s because of the following reasons. Firstly, the additional high-speed samplers consume considerable power. Secondly, these auxiliary samplers degrade the bottleneck bandwidth because their input capacitances are directly connected to the maximum-speed signal path. Thirdly, more samplers mean more input and output signals, which make the layout routing more complicated. The traditional ZF solution is achieved by forcing the cross-correlation between error sequence $\varepsilon_k = I_k - \hat{I}_k$ and desired information sequence I_k to be zero. Its main drawback is the requirement of an auxiliary $\hat{I}_k$ measuring analog-to-digital converter (ADC) [105, 132], which also dramatically reduces the bandwidth of the full-rate driver, thus limiting the maximum operating speed. Additionally, it also needs a large amount of logic to perform matrix multiplication [132]. For the MEO method, the evaluation of the received signal eye opening is fulfilled by gradually adjusting the sampling thresholds and the sampling positions. Instead of producing error information, this approach can provide the visual received eye-diagram at a cost of a complete eye monitor, which usually incorporates threshold-adjusting samplers, phase-adjusting PIs, micro-controller, and measurement softwares [133].

6.2.2 Iteration of the EDC-SZF

To preclude the auxiliary circuits in previous adaptation algorithms [129, 130, 131, 34, 105, 132, 133], a low-cost EDC-SZF algorithm utilizing edge-data cross-correlation is developed. The target is to force the cross-correlation between the sign of the edge-sampling errors and received data to zero. The iterative procedure of the TX-FFE tap weights is given by,

$$\alpha_l(k+1) = \alpha_l(k) - \lambda \cdot sign[e(k)] \cdot D(k-l), (l = -1, 0, 1, 2), \qquad (6.1)$$

where $\alpha_l(k)$ is the instant l-tap weight, $sign[e(k)]$ represents the sign of the edge sampling error, $D(k)$ denotes the recovered data, and λ stands for the scale factor controlling the adjustment rate and its value is usually much smaller than 1. The sign of the edge sampling error $sign[e(k)]$ caused by the inter-symbol interface (ISI) is directly mapped from the quantized edge sequence $E(k)$, and it is correlated with the data bit $D(k-l)$ to produce the product $sign[e(k)] \cdot D(k-l)$. The result is then integrated to update the FFE tap weight $\alpha_l(k)$.

The main feature of this approach is that it only involves the existing quantized edge sequence $E(k)$ and recovered data sequence $D(k)$. As a result, the essential auxiliary circuits such as samplers, ADCs, and PIs in previous adaptive equalizations [129, 130, 131, 105, 132, 133] are removed, thus exhibiting more potentials on operation speed and cost effectiveness.

6.2.3 Correlation between Edge Information and Recovered Data

When dealing with band-limited channels that result in ISI, it is convenient to develop an equivalent discrete-time model for the continuous-time system. The reason is that the transmitter sends discrete-time symbols with a period of T and the output at the receiver side is also a discrete-time signal with samples of the same period. Fig. 6.4 presents the UI-width pulse response of a typical dispersion channel, where h_k and $h_{k+0.5}$ denote the ISI tail values at data-sampling and edge-sampling points, respectively. According to the signal processing principles, the received discrete-time signal
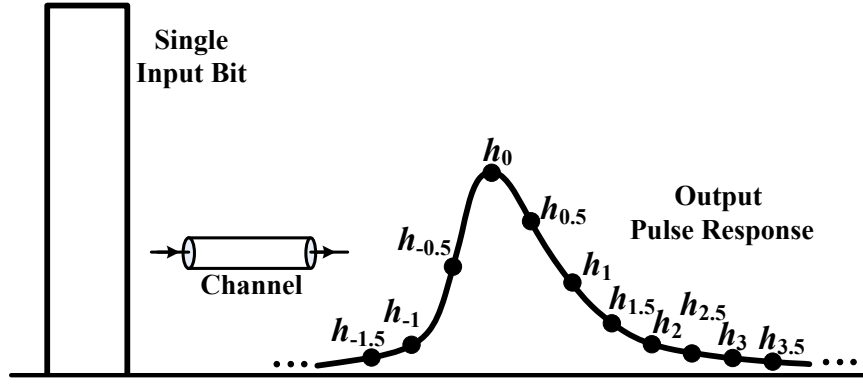
Figure 6.4: Pulse response of a typical dispersion channel.

q_k can be computed by the convolution of the input data sequence I_k and channel pulse response h_k,

$$q_k = \sum_i I_i h_{k-i}. \tag{6.2}$$

For a normal operating serial link where the data-sampling clock always locates at the center of the eye-diagram, q_k and $q_{k+0.5}$ can be considered as the sampled analog values before binary quantization. After the decision latches, q_k is quantized to the data sequence D_k, while $q_{k+0.5}$ is quantized to the edge sequence E_k. Applying the cross-correlation function to the edge-sampled sequence $q_{k+0.5}$ and the recovered data sequence D_k, we can get,

$$
\begin{aligned}
R_{e,d}(n) &= \sum_j q_{j+0.5} D_{j-n} = \sum_j q_{j+0.5} I_{j-n} \\
&= \sum_j \left(\sum_i I_i I_{j-n} h_{j+0.5-i} \right) \\
&= \sum_j \left(I_{j-n} I_{j-n} h_{j+0.5-(j-n)} + \sum_{i \neq j-n} I_i I_{j-n} h_{j+0.5-i} \right) \\
&= \sum_j h_{n+0.5} + \sum_j \left(\sum_{i \neq j-n} I_i I_{j-n} h_{j+0.5-i} \right).
\end{aligned}
\tag{6.3}
$$

Here, D_k is replaced by the input sequence I_k because the bit-error-rate (BER) is usually quite low ($< 1e^{-12}$) for proper operating serial links. Assuming $m = j - i$, we

have,

$$\sum_j \left(\sum_{i \neq j-n} I_i I_{j-n} h_{j+0.5-i} \right) = \sum_j \left(\sum_{m \neq n} I_{j-m} I_{j-n} h_{m+0.5} \right)$$
$$= \sum_{m \neq n} \left(\sum_j I_{j-m} I_{j-n} h_{m+0.5} \right) = 0. \tag{6.4}$$

Note that the sum indexes of i and j traverse over all the integers except for $i = j - n$, thus m should also round over all integers except for $m = n$. The final derivation of Eq. (6.4) is obtained based on the fact that the time-shifted data sequences I_{j-m} and I_{j-n} $(m \neq n)$ are actually independent with each other, since the transmitted data streams in wireline systems are usually random sequences. Substituting Eq. (6.4) into Eq. (6.3) , the cross-correlation function is simplified to,

$$R_{e,d}(n) = \sum_j h_{n+0.5}. \tag{6.5}$$

By normalizing the cross-correlation function, we obtain,

$$\rho_{e,d}(n) = h_{n+0.5}. \tag{6.6}$$

Clearly, the normalized cross-correlation coefficient $\rho_{e,d}(n)$ between the sequence $q_{k+0.5}$ and the recovered data sequence D_k exactly equals the residual ISI value with a time shift of $(n + 0.5)T$, as shown in Fig. 6.4.

6.2.4 Derivation of the EDC-SZF

For a transmitter with an l-tap UI-spaced FFE, the pre-distorted output can be represented by,

$$t(k) = \sum_l \alpha_l I(k - l), \tag{6.7}$$

where $I(k)$ is the transmitting sequence, α_l denotes the tap weight, and l is the tap index [133]. To make the analysis more compact, the cascaded passive channel and RX-CTLE is treated as a combined channel with a new pulse response of c_k. By

calculating the convolution of pre-distorted output $t(k)$ and the channel pulse response c_k, the received discrete-time sequence before binary quantization can be given by

$$r(k) = \sum_l \alpha_l \left(\sum_i I(i) c_{k-l-i} \right).$$ (6.8)

Following the steps of the cross-correlation analysis in 6.2.3 and using the derived results, we attain the cross-correlation coefficient between the edge-sampling error sequence $r(k + 0.5)$ and the recovered data sequence $D(k)$,

$$\hat{\rho}_{e,d}(n) = \sum_l \alpha_l c_{n-l+0.5}.$$ (6.9)

For an ideally equalized serial link, the edge-sampling error sequence is supposed to be a 0-sequence. Hence, all the cross-correlation coefficients should be zero. However, this needs infinite taps to cancel all the residual ISI. Considering the fact that the ISI tail decreases exponentially as the time goes on, it is reasonable to assume that the ISI affects a finite number of symbols and previous research has demonstrated that equalizers with a specific number of taps can effectively compensate for legacy channels [130, 131, 164, 133, 123]. In principle, when the tap weights are adjusted close to the targeted values, the resulting cross-correlation coefficient $\hat{\rho}_{e,d}(n)$ should be forced towards zero. Taking the implemented 4-tap FFE in this design as an example, for a group of proper tap weights, we have,

$$\hat{\boldsymbol{\rho}}_{e,d} = \boldsymbol{C}\boldsymbol{\alpha} = \mathbf{0},$$ (6.10)

where,

$$\hat{\boldsymbol{\rho}}_{e,d} = (\hat{\rho}_{e,d}(-1), \hat{\rho}_{e,d}(0), \hat{\rho}_{e,d}(1), \hat{\rho}_{e,d}(2))^T,$$

$$\boldsymbol{\alpha} = (\alpha_{-1}, \alpha_0, \alpha_1, \alpha_2)^T,$$

$$C = \begin{pmatrix} c_{0.5} & c_{-0.5} & c_{-1.5} & c_{-2.5} \\ c_{1.5} & c_{0.5} & c_{-0.5} & c_{-1.5} \\ c_{2.5} & c_{1.5} & c_{0.5} & c_{-0.5} \\ c_{3.5} & c_{2.5} & c_{1.5} & c_{0.5} \end{pmatrix}.$$

To find the optimal TX-FFE tap weights, a recursive equation is constructed as,

$$\boldsymbol{\alpha}(k+1) \;\; = \boldsymbol{\alpha}(k) - \lambda C \boldsymbol{\alpha}(k) = \boldsymbol{\alpha}(k) - \lambda \hat{\rho}_{e,d}(k). \tag{6.11}$$

In each iteration, a small portion of the instant cross-correlation coefficient vector $\lambda \hat{\rho}_{e,d}(k)$ is subtracted from the tap weight vector $\boldsymbol{\alpha}(k)$ to make it closer to the targeted value. For the convergence, mathematic analysis (see Appendix B) indicates that a sufficient condition is to keep the 1-norm of matrix $\boldsymbol{I} - \boldsymbol{\lambda C}$ smaller than 1 (i.e., (i.e., the maximum absolute column sum is smaller than 1). For any bandwidth-limited channel, the transmitted symbol will spread over multiple symbols at the RX-side, thus making the above conditions held. Consequently, a set of optimal tap weights of the TX-FFE can be obtained by the iterative Eq. (6.11). It is worthy to note that when the transmission channel is beyond the scope of the equalization ability or over-equalized by improperly setting the control voltage of the RX-CTLE, the tap-weight coefficients will go too high (or low). To manage this contingency, the rang limiters depicted in Fig. 6.1 are inserted between the EDC-SZF and DACs, which are used to keep the control codes received by the DACs not larger (or smaller) than the specific maximum (or minimum) values.

Taking $sign[e(k)]$ as the binary quantization of the edge-sampling error, the cross-correlation between the sign of the edge-sampling error and received data: $sign[e(k)] \cdot D(k-l)$ can be considered as an instant estimation of the $\hat{\rho}_{e,d}(l)$. Hence, the final iterative equation presented in previous part can be obtained [refer to Eq. (6.1)].

6.2.5 Implementation of the EDC-SZF

Fig. 6.5 depicts the implementation of the EDC-SZF adaptation algorithm, which contains three identical paths to process the quantized data and edge sequences to pro-
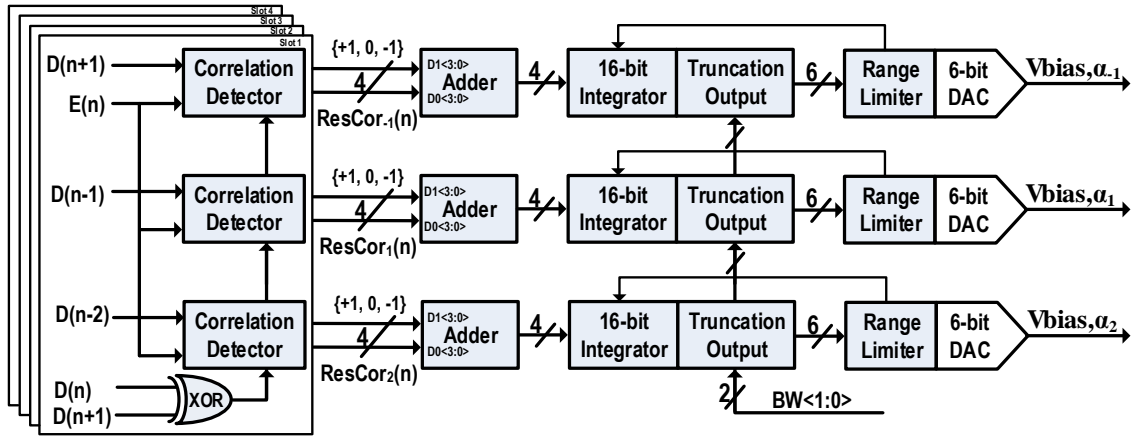
Figure 6.5: Block diagram of the EDC-SZF adaptation algorithm.
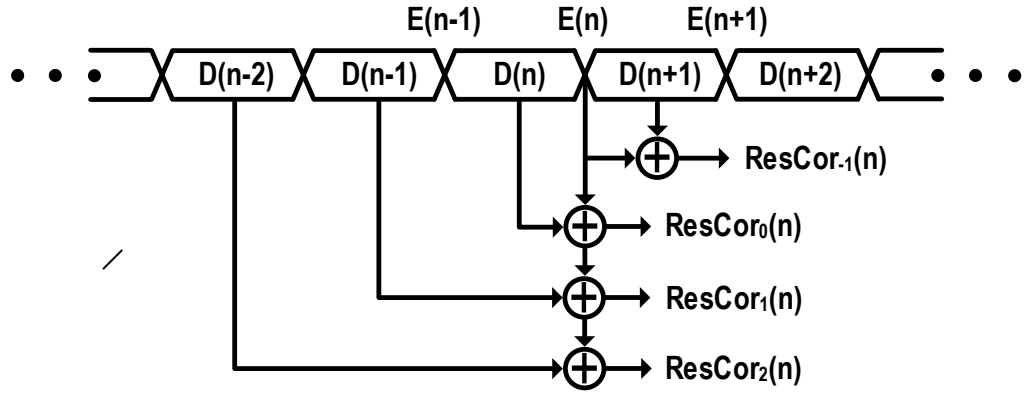
(a)

D(n-l) $\oplus$ E(n)	D(n) $\oplus$ D(n+1)	ResCor$_l$1(n)	ResCor$_l$0(n)
0	0	0	0
1	0	0	0
0	1	0	1
1	1	1	1

Note: The signed ResCor$_l$(n) is represented by two bits: ResCor$_l$1(n) and ResCor$_l$0(n).

(b)

Figure 6.6: Correlation detector. (a) Operation principle illustration and (b) function table.

duce the desired bias voltages for TX-FFE taps. Here, the main tap weight is pre-fixed to accelerate the convergence speed. In each path, the edge and data streams with a proper time shift are applied to a correlation detector (CD) to generate the residual correlation $ResCor_l(n)$, which is used to represent the $sign[e(n)] \cdot D(n - l)$ in Eq. (6.1). These parallel correlation coefficients are firstly summed and then fed into a

16-bit integrator to execute the iteration of Eq. (6.1), where λ is determined by the subsequent truncation operation. In this design, a set of consecutive 4-bit data/edge of the 1/16-rate demultiplexed data/edge are employed, which ensures that the data/edge information used for equalization adaptation comes from different samplers. This de-centralized error collection method reduces the possibility of non-optimal adaptation caused by imperfections such as fabrication mismatch, duty cycle distortion, and I, Q quadrature error. Fig. 6.6 further details the operation principle and function table of the CD. Clearly, if there is no transition ($D(n) \oplus D(n+1) = 0$), $ResCor_l(n)$ is assigned 0. In case of a data transition ($D(n) \oplus D(n+1) = 1$), $ResCor_l(n)$ is assigned +1 or -1 when the polarities of $D(n-l)$ and $E(n)$ are identical ($D(n-l) \oplus E(n) = 0$) or opposite ($D(n-l) \oplus E(n) = 1$).

(a)   (b)

(d)
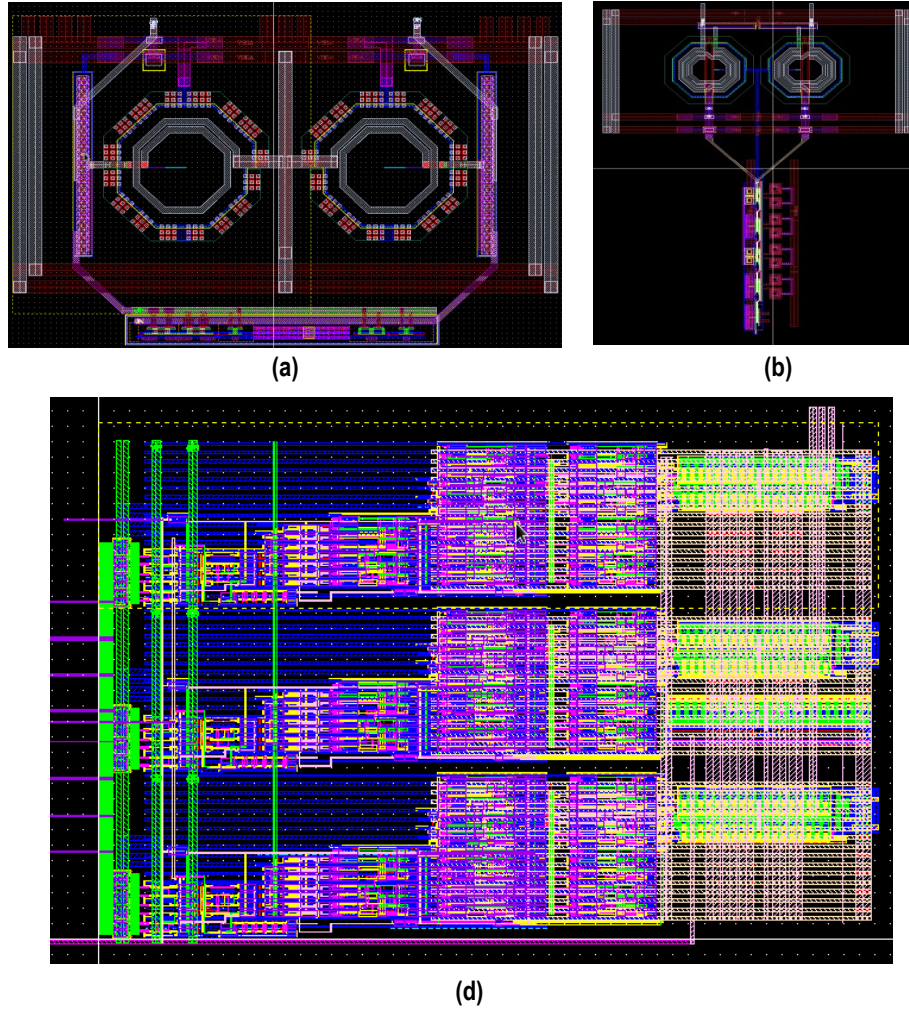
Figure 6.7: Layout views of the equalization blocks. (a) TX-FFE, (b) RX-CTLE, and (c) EDC-SZF.

6.3 Experimental Results

6.3.1 Layout and Simulation Results

6.3.1.1 Layout Designs

Fig. 6.7 displays the layout views of the equalization blocks. For the TX-FFE [see Fig. 6.7(a)], a pair of standard inductors is utilized to neutralize the capacitances on the output nodes. For the RX-CTLE [see Fig. 6.7(b)], two T-coil inductors are used in the Terminals to support the high current ability, while multi-layer inductors are adopted in the CTLE stages to save the area occupation. For the EDC-SZF [see Fig. 6.7(c)], it is implemented based on the standard cells provided by the foundry.
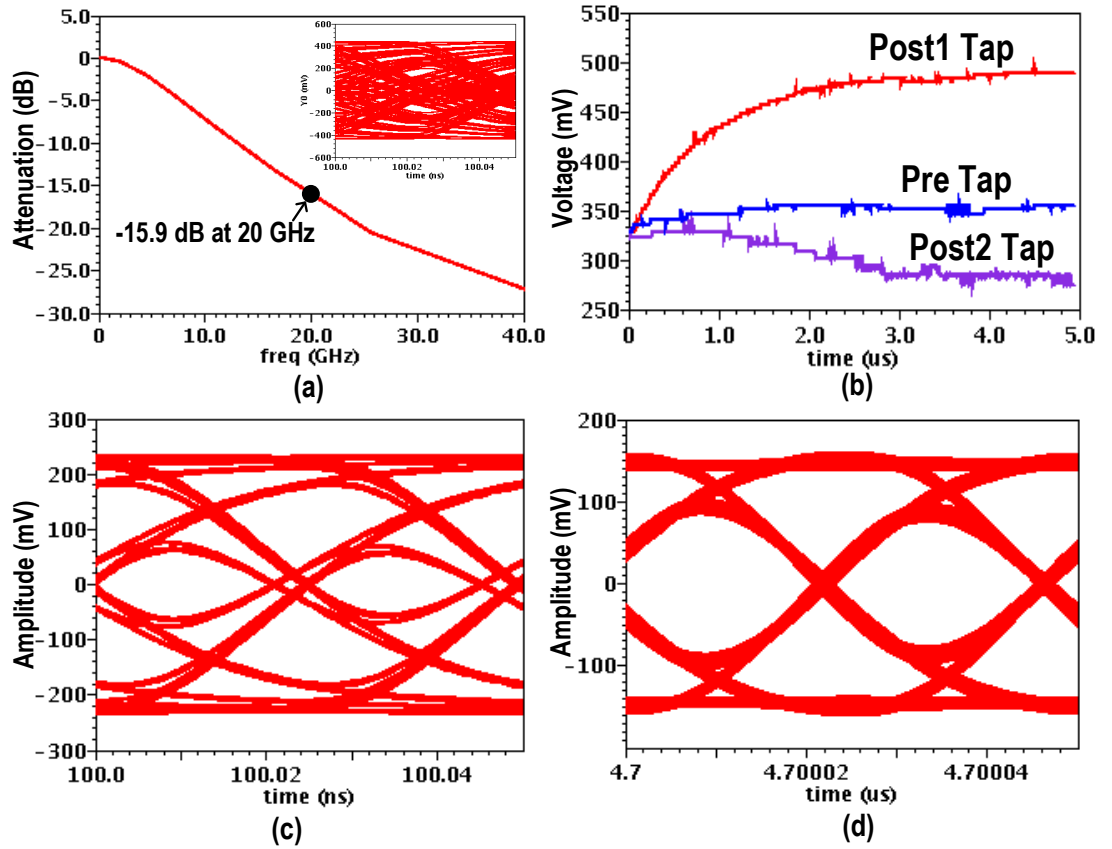
Figure 6.8: Transistor-level simulation of the EDC-SZF adaptation. (a) Channel frequency response, (b) convergence process of the TX-FFE tap weights, (c) eye-diagram with zero TX-FFE tap weights, and (d) eye-diagram with adaptively-adjusted TX-FFE tap weights.

(a)

(b)

-4.64 dB @ 5.0 GHz
-11.26 dB @ 10.0 GHz
-16.34 dB @ 20.0 GHz
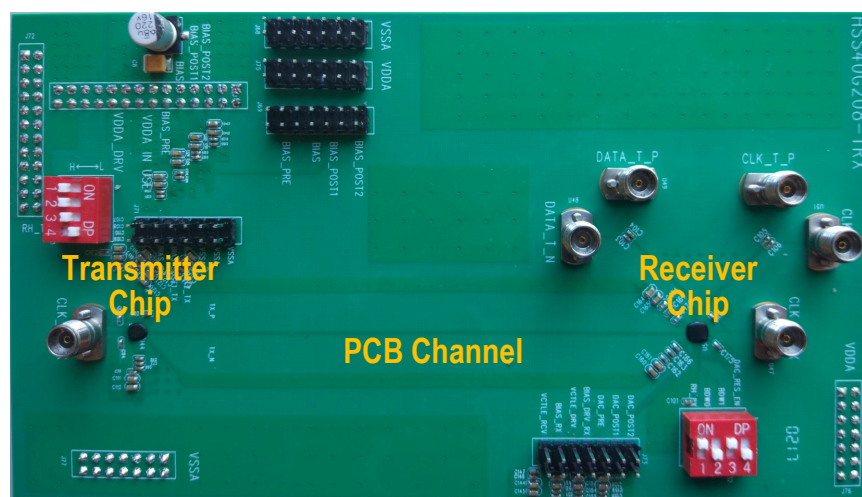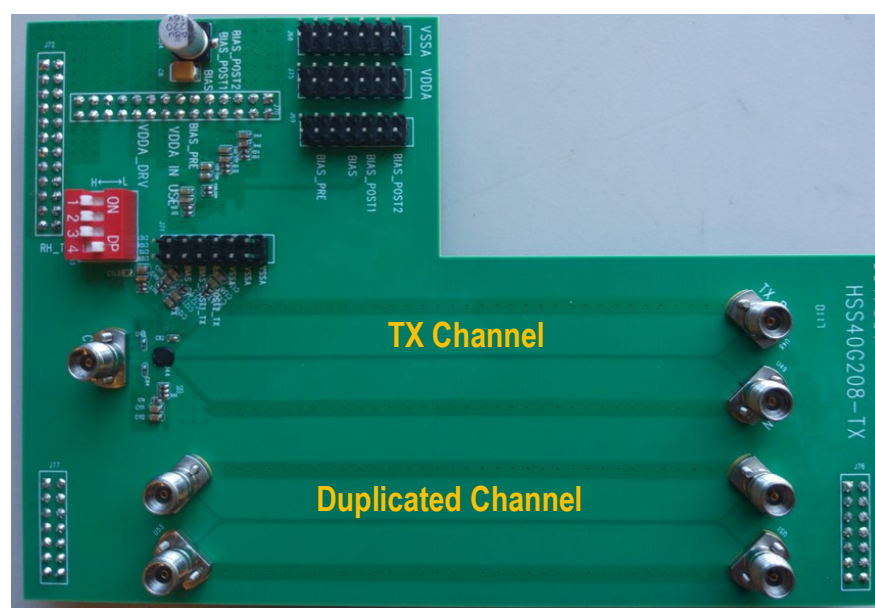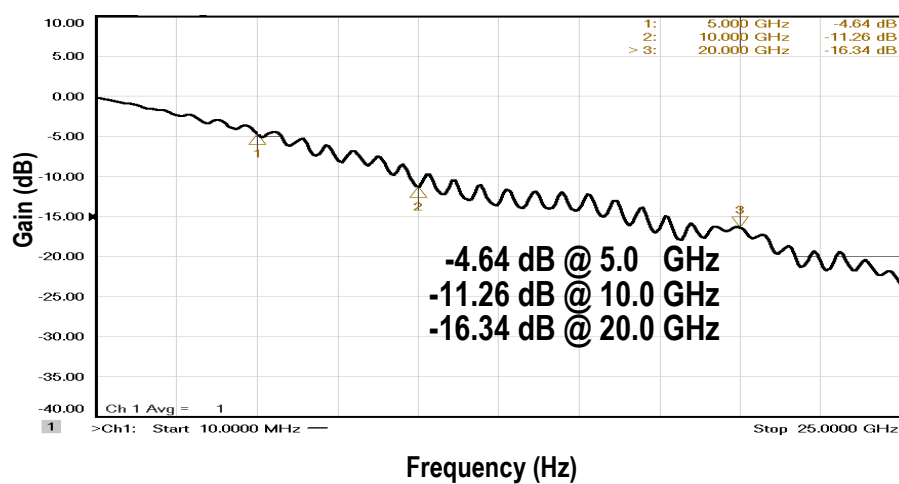
(c)

Figure 6.9: Constructed chip-to-chip interconnect. (a) Testing PCB, (b) auxiliary PCB, and (c) duplicated channel frequency response.

161
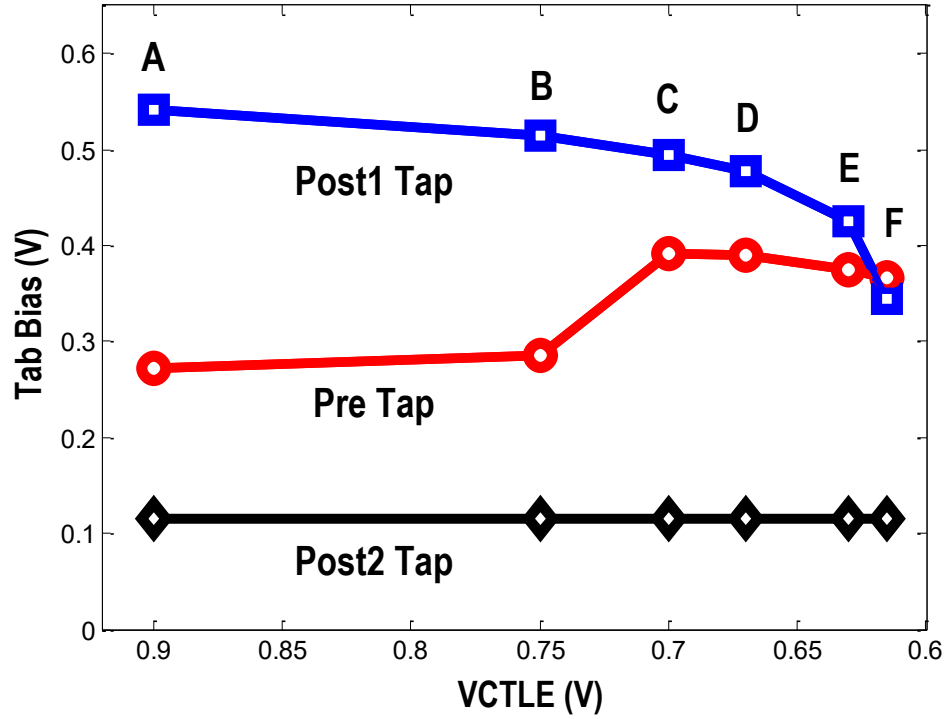
Figure 6.10: Adaptively-adjusted bias voltages of the TX-FFE with different RX-CTLE control voltages.
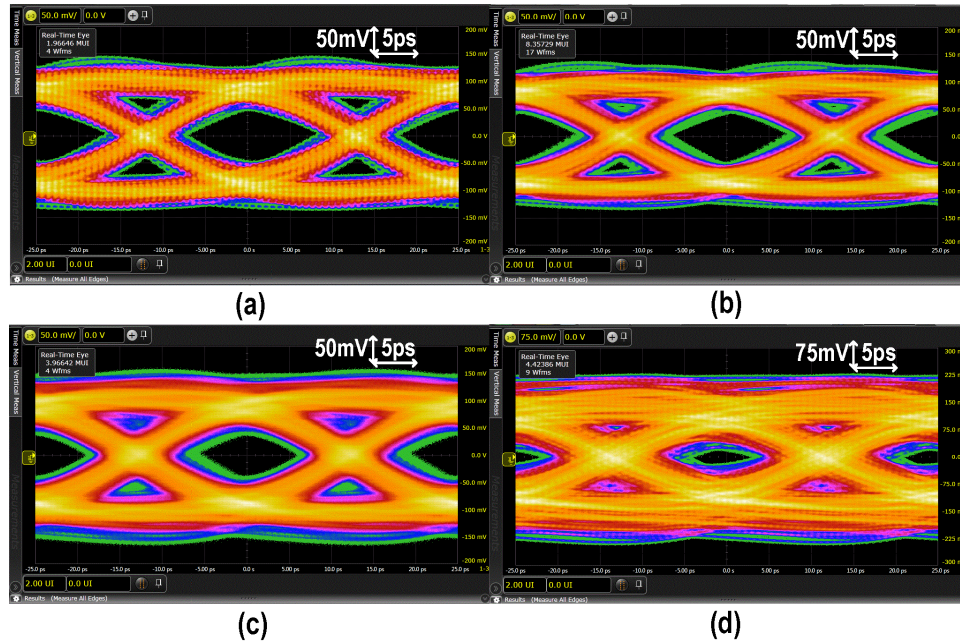
Figure 6.11: Measured far-end eye-diagrams for (a) bias condition A, (b) bias condition B, (c) bias condition D, and (d) bias condition F depicted in Fig. 6.10.

6.3.1.2 Simulation Results

Fig. 6.8 gives the transistor-level simulation results of the serial link with the EDC-SZF adaptation, where the control voltage of the RX-CTLE is pre-set to 700 mV, and
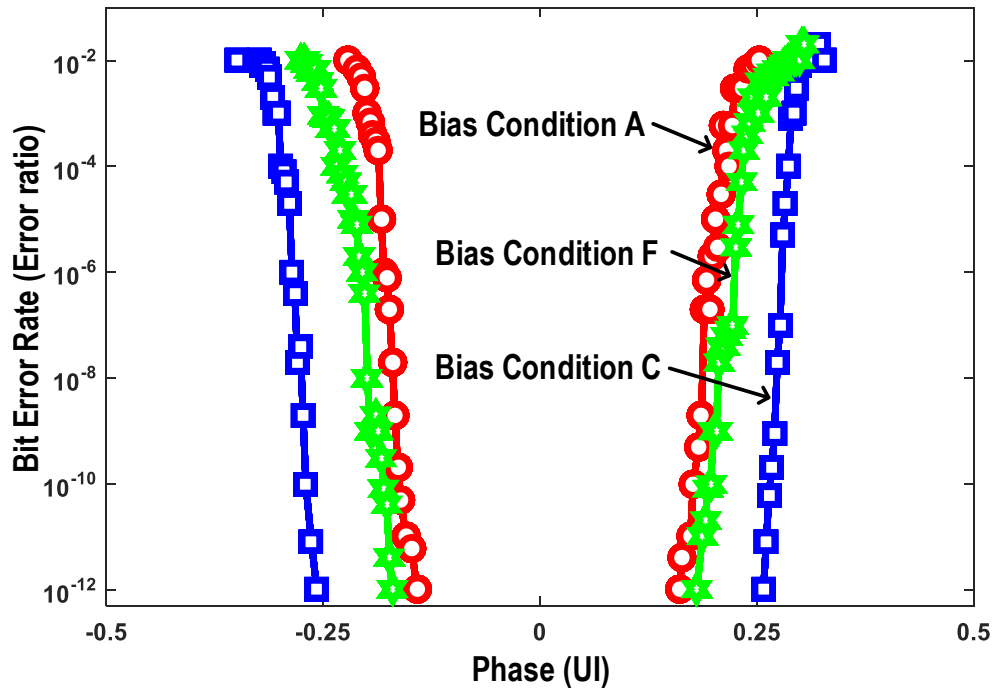
Figure 6.12: Measured bathtub curves under different bias conditions depicted in Fig. 6.10.

the dispersive channel is imitated by an LPF with a -15.9 dB loss at 20 GHz. The channel frequency response and the eye-diagram after the channel are shown in Fig. 6.8(a). Fig. 6.8(b) describes the convergence process of the TX-FFE tap weights. Fig. 6.8(c) and (d) displays the eye-diagrams (measured at the output of the RX-CTLE) with zero and adaptively-adjusted tap weights, respectively. It can be easily seen that the developed EDC-SZF adaptation algorithm can gradually tune the TX-FFE tap weights to optimal values, which can effectively optimize the eye opening and eyelid thickness.

6.3.2 Measurement Results

Fig. 6.9 shows the measurement setup of the serial link. As shown in Fig. 6.9(a), a chip-to-chip interconnect is constructed. The outputs of the transmitter chip and the inputs of the receiver chip are separately wire-bonded to the two terminals of a 12 cm PCB channel. Meanwhile, an auxiliary PCB with a transmitter chip bonding to a replica channel and a pair of duplicated PCB traces are also manufactured to measure the far-end eye-diagrams and evaluate the channel characteristics [see Fig. 6.9(a)]. Fig.

6.9(c) depicts the frequency response of the PCB channel, where the channel loss at the half-baud frequency is over 16 dB.

Fig. 6.10 shows the adaptively-adjusted bias voltages of the TX-FFE taps as the control voltage of the RX-CTLE changes from 900 mV to 615 mV [see the corresponding equalization abilities in Fig. 6.3(b)]. Fig. 6.11 describes the far-end eye-diagrams under the bias conditions of A, B, D, and F depicted in Fig. 6.10. As the control voltage of the RX-CTLE is decreased (i.e., improving the high-frequency peaking ability of the RX-CTLE), the TX-FFE bias voltages are adjusted accordingly to decrease the equalization capability of the TX-FFE, thus maintaining the frequency response of the combined TX-FFE, RX-CTLE, and transmission channel close to a flat profile. By detecting the BER while adjusting the sampling positions, the bathtub diagram can be obtained. Fig. 6.12 displays the measured bathtub curves under the bias conditions of A, C, and F described in Fig. 6.10. For the balanced equalization coefficient allocation under bias condition C, the horizontal eye opening at BER=10^{-12} achieves 0.51 UI, which is much better than those measured under bias condition A (0.30 UI) and bias condition F (0.35 UI). This proves that a combination scheme of the TX-FFE and RX-CTLE is a good choice for the equalization of the 40 Gb/s link.

6.4   Chapter Summary

This chapter constructs a serial link over a > 16 dB loss PCB channel using the chips designed in Chapter 4 and 5. A combined TX-FFE and RX-CTLE is employed to compensate for the channel loss. To obtain the optimal equalization coefficients and track the channel-loss variations with respect to operation environment, a low-cost EDC-SZF adaptation algorithm is proposed to automatically adjust the TX-FFE's tap weights. Unlike previous adaptation techniques that need auxiliary circuits to extract the error information, the proposed EDC-SZF adaptation performs the tap-weight adjustment through processing the existing data and edge sequences, hence introducing little overheads to the link.

Chapter 7

Conclusions and Future Work

7.1 Conclusions

The rapid growth of the computing power and storage volume has led to an explosive bandwidth demand on data communication in both telecommunication equipments and inter/intra data centers. To accommodate to this requirement, the data rate of the wireline SerDes transceiver has been continuously increased. Currently, 25-28 Gb/s serial links have stepped into the period of industrial deployment. The 38-64 Gb/s transceivers, which will play a key role in the next-generation data rate have attracted increasing attentions in both the industry and the academia. This thesis addresses some of the architecture-level and circuit-level challenges associated with such cutting-edge wireline transceiver designs. Several advanced techniques are developed to optimize the operation speed, power efficiency, performance margin, and area occupation. The prototype chips of a 10 GHz clock multiplier, a 40 Gb/s transmitter, and a 40 Gb/s receiver are separately designed and fabricated in a 65 nm CMOS process. The main features of these designed chips are summarized as below.

- The main features of the implemented ring-oscillator-based injection-locked clock multiplier (RILCM) focus on three aspects. Firstly, a hybrid frequency tracking loop is proposed to automatically adjust the control voltage of the injection-locked voltage-controlled oscillator (VCO). By introducing a lock-loss detection and lock recovery mechanism, the hybrid loop endows the RILCM with a similar lock-acquisition ability as conventional PLLs, thus excluding the ini-

tial frequency setup aid and preventing the potential lock-loss risk. Secondly, a full-swing pseudo-differential delay cell is developed to optimize the phase noise performance of the VCO. Thirdly, a compact timing-adjusted phase detector tightly combined with a well-matched charge pump is designed to satisfy the requirements of high operation speed, high detection accuracy, and low output disturbance. The measurement results show that the implemented 10 GHz RIL-CM chip achieves a good balance among jitter performance, area occupation, operation speed, and power efficiency.

- The main features of the implemented transmitter focus on three aspects. Firstly, a 4-tap feed-forward equalizer (FFE) based on multiple multiplexers (MUXs) is designed. Thanks to the retiming-based symbol-spaced sequence generation, it can support a wide operation range of 5-50 Gb/s. Secondly, an enhanced 4:1 MUX is developed. By introducing a pair of pre-charging PMOS transistors in the pulling-down unit cell, it completely eliminates the charge-sharing effect, which not only improves the jitter performance of the 4:1 MUX but also helps to extend its maximum bandwidth. Thirdly, a compact latch array associated with an interleaved-retiming technique is designed. By interleaved-retiming the parallel data, the 16 paths quarter-rate data streams with appropriate delays can be obtained. The measurement results indicate that the fabricated 40 Gb/s transmitter chip achieves excellent jitter performance and power efficiency.

- The main features of the implemented receiver focus on two aspects. One is the architecture-level improvement on the clock data recovery (CDR). By introducing passive low-pass filters with an adaptively adjusted bandwidth into the data-sampling path, the jitter tracking and jitter suppression for data decisions can be automatically balanced, thus improving the jitter tolerance of the CDR. The other is the time-averaging-based compensating phase interpolator, which not only improves the phase-step uniformity but also reduces the phase-spacing errors between the edge and data sampling clocks. The measurement results show that the maximum tolerable amplitude of implemented 40 Gb/s receiver chip outperforms previous receivers at high frequencies.

- Using the designed transmitter and receiver chips, a chip-to-chip communication link over a 12-cm printed circuit board (PCB) channel is constructed. It employs a combination of TX-FFE and RX-CTLE to compensate for the channel loss. A low-cost edge-data correlation-based sign zero-forcing (EDC-SZF) adaptation algorithm is proposed to automatically adjust the TX-FFE's tap weights. The measurement results indicate that the equalization scheme of the combination of TX-FFE and RX-CTLE is a good choice for the equalization of the 16 dB loss channel at 40 Gb/s, and the proposed EDC-SZF adaptation can effectively tune the TX-FFE to its optimal tap weights for a given control voltage applied to the RX-CTLE.

7.2 Future Work

The factors to consider when designing a serial communication link mainly include data transmission rate, power efficiency, and channel characteristics. The first factor is usually set by particular operation standards, the other two factors largely depend on the network infrastructure, operation medium, and link spaces. As the requirement for the data rates goes beyond 40 Gb/s, efforts in channel optimization, on-chip transmission line, and modulation scheme should also be made to further optimize the factors of the serial link. As a consequence, the following items could be the future tasks to further optimize the link performance.

- Enhancing the chip-package co-design. The chips presented in this dissertation are measured through mounting them directly on the PCB using gold-bonding wires. The inductive parasitics of the bonding wires will inevitably cause discontinuities. These discontinuities will degrade the signal integrity in terms of reinforcing the undesired signal inflections. One can extract the models of the bonding wires through high frequency electromagnetic field simulations and treat them as electrical components during the chip design. This chip-package co-design method provides a possible way to reduce the effect of the bonding wires and hance improves the continuity of the transmission channel.

- Developing on-chip transmission lines. The wavelength for a 20 GHz (Nyquist frequency of 40 Gb/s) signal is around 1.5 cm, which makes a 150 μm (one tenth of the wavelength) connection wire should be considered as a transmission line. Moreover, the highest frequency of interest is actually determined by the rise/fall time of the transmission signal, which means even shorter connection wires should be modeled as transmission lines. Instead of the lump parasitic capacitors and inductors, the parasitic effect of the transmission line is characterized by the characteristic impedance. By placing a resistive matching termination at the far-end, the parasitic effect can be theoretically neutralized, thus saving substantial driving power. Meanwhile, the serial parasitic resistance can degrade the performance of the transmission line, especially for long connection wires. Additionally, the requirement of physical uniformity for transmission lines has also posed significant challenges for the layout routing.

- Exploring advanced techniques on the four-level pulse amplitude modulation (PAM4) chipset design. PAM4 has been considered as one of the most promising multi-level modulation schemes for next-generation data rates, due to its doubled channel capacity, moderate signal-to-noise ratio (SNR), and applicability to the existing infrastructure. It uses four distinct amplitude levels to convey two bits in one symbol, thus halving the Nyquist frequency to refine the system loss budget and/or increase the link speed. However, it suffers from a 9.5 dB SNR attenuation since the eye height is reduced to one third of the non-return-to-zero (NRZ) modulation. To mitigate this effect, the transmitter is demanded to output a large swing with a high linearity, while the receiver is required to automatically adjust the threshold levels to correctly extract the most significant bit and the least significant bit. Additionally, the inherent inter-symbol interface associated with the edge transitions among different symbol levels makes the clock data recovery design in the PAM4 mode much more challenging than that in the NRZ mode. Moreover, the three-eye-opening requirement has posed new challenges in the equalization design.

Bibliography

[1] C. V. N. Index, "The zettabyte era-trends and analysis." Cisco white paper, http://www.cisco.com/c/en/us/solutions/collateral/service-provider/visual-networking-index-vni/vni-hyperconnectivity-wp.html, Jun. 2016. [Online]. Accessed 26-Feb.-2017.

[2] T. P. Morgan, "Driving the Ethernet roadmap at 100x speeds." Thenextplatform, https://www.nextplatform.com/2015/03/31/driving-the-ethernet-roadmap-at-100x-speeds/, Mar. 2015.

[3] S. Voinigescu *et al.*, "SiGe BiCMOS for analog, high-speed digital and millimetre-wave applications beyond 50 GHz," in *Proc. IEEE Bipolar/BiCMOS Circuits and Technology Meeting*, pp. 1–8, Oct. 2006.

[4] Optical Internetworking Forum, "OIF CEI-56G application note-Common electrical interface at 56Gb/s." OIF application note, http://www.oiforum.com/wp-content/uploads/OIF-CEI-white-paper-final-Mar-23-2016.pdf, 2016. [Online]. Accessed 26-Feb.-2017.

[5] Telecordia Technologies, *Synchronous Optical Network (SONET) Transport Sys-tems: Common Generic Criteria*, Sep. 2000. GR-253-CORE.

[6] T. Toif *et al.*, "A 22-Gb/s PAM-4 receiver in 90-nm CMOS SOI technology," *IEEE J. Solid-State Circuits*, vol. 41, pp. 954–965, Apr. 2006.

[7] T. Toifl, *Low-Power High-Speed CMOS I/Os: Design Challenges and Solutions*. IBM Research GmbH Zurich Research Laboratory, 2012.

[8] C. Kromer *et al.*, "A 25-Gb/s CDR in 90-nm CMOS for high-density interconnects," *IEEE J. Solid-State Circuits*, vol. 41, pp. 2921–2929, Dec. 2006.

[9] J. F. Bulzacchelli *et al.*, "A 10-Gb/s 5-tap DFE/4-tap FFE transceiver in 90-nm CMOS technology," *IEEE J. Solid-State Circuits*, vol. 41, pp. 2885–2900, Dec. 2006.

[10] L. Rodoni *et al.*, "A 5.75 to 44 Gb/s quarter rate CDR with data rate selection in 90 nm bulk CMOS," *IEEE J. Solid-State Circuits*, vol. 44, pp. 1927–1941, Jul. 2009.

[11] S. Sidiropoulos *et al.*, "A semidigital dual delay-locked loop," *IEEE J. Solid-State Circuits*, vol. 32, pp. 1683–1692, Nov. 1997.

[12] G.-Y. Wei *et al.*, "A variable-frequency parallel I/O interface with adaptive power-supply regulation," *IEEE J. Solid-State Circuits*, vol. 35, pp. 1600–1610, Nov. 2000.

[13] A. Agrawal *et al.*, "A 19-Gb/s serial link receiver with both 4-tap FFE and 5-tap DFE functions in 45-nm SOI CMOS," *IEEE J. Solid-State Circuits*, vol. 47, pp. 3220–3231, Dec. 2012.

[14] R. Kreienkamp *et al.*, "A 10-Gb/s CMOS clock and data recovery circuit with an analog phase interpolator," *IEEE J. Solid-State Circuits*, vol. 40, pp. 736–743, Mar. 2005.

[15] H. Pan *et al.*, "A digital wideband CDR with 15.6kppm frequency tracking at 8Gb/s in 40nm CMOS," in *Proc. IEEE Int. Solid-State Circuits Conf. Dig. Tech. Papers*, pp. 442–443, Feb. 2011.

[16] M.-S. Chen, *Design of 60+Gb/s Serial-Link Transmitters Using Filter Techniques*. PhD thesis, Electrical Engineering, University of California, Los Angeles, 2015.

[17] B. Welch, "400G optics-technologies, timing, and transceivers." IEEE P802. 3bs, http://www.ieee802.org/3/bs/public/14_05/welch_3bs_01_0514.pdf, May. 2014. [Online]. Accessed 22-Oct.-2016.

[18] InfiniBand Trade Association, "InfiniBand roadmap." Mellanox Technologies, http://www.infinibandta.org/content/pages.php?pg=technology_overview. [Online]. Accessed 22-Oct.-2016.

[19] M. Cvijetic and I. B. Djordjevic, *Advanced Optical Communication Systems and Networks*, ch. 1, pp. 1–38. Artech House, 2013.

[20] P. C. Chiang *et al.*, "4 × 25 Gb/s transceiver with optical front-end for 100 GbE system in 65 nm CMOS technology," *IEEE J. Solid-State Circuits*, vol. 50, pp. 573–582, Feb. 2015.

[21] U. Singh *et al.*, "A 780 mW 4 × 28 Gb/s transceiver for 100 GbE gearbox PHY in 40 nm CMOS," *IEEE J. Solid-State Circuits*, vol. 49, pp. 3116–3129, Dec. 2014.

[22] T. Takemoto *et al.*, "A 25-Gb/s 2.2-W 65-nm CMOS optical transceiver using a power-supply-variation-tolerant analog front end and data-format conversion," *IEEE J. Solid-State Circuits*, vol. 49, pp. 1903–1916, Feb. 2014.

[23] R. Navid *et al.*, "A 40 Gb/s serial link transceiver in 28 nm CMOS technology," *IEEE J. Solid-State Circuits*, vol. 50, pp. 814–827, Dec. 2015.

[24] M. S. Chen and C. K. K. Yang, "A 50-64 Gb/s serializing transmitter with a 4-tap, LC-ladder-filter-based FFE in 65 nm CMOS technology," *IEEE J. Solid-State Circuits*, vol. 50, pp. 1903–1916, Apr. 2015.

[25] J. Lee *et al.*, "Design of 56 Gb/s NRZ and PAM4 SerDes transceivers in CMOS technologies," *IEEE J. Solid-State Circuits*, vol. 50, pp. 2061–2073, Sep. 2015.

[26] P. C. Chiang *et al.*, "60Gb/s NRZ and PAM4 transmitters for 400GbE in 65nm CMOS link," in *Proc. IEEE Int. Solid-State Circuits Conf. Dig. Tech. Papers*, pp. 42–43, Feb. 2014.

[27] H. Tao *et al.*, "40-43-Gb/s OC-768 16:1 MUX/CMU chipset with SFI-5 compliance," *IEEE J. Solid-State Circuits*, vol. 38, pp. 2169–2180, Dec. 2003.

[28] Inphi, "CMOS paves the road to 100 GbE mainstream markets." https://www.inphi.com/products/whitepapers/inphi_whitepaper_iphy_final.pdf, 2011. [Online]. Accessed 28-Jul.-2017.

[29] T. H. Lee, *The Design of CMOS Radio-Frequency Integrated Circuits*. Cambridge: Cambridge University Press, 1998.

[30] Altera, *Altera's 28-nm, Power-Efficient Transceivers*, Jan. 2013.

[31] IEEE 802.3, *50 Gb/s Ethernet Over a Single Lane and Next Generation 100 Gb/s & 200 Gb/s Ethernet Call For Interest Consensus Presentation*, Nov. 2015.

[32] A. A. Hafez, M.-S. Chen, and C.-K. K. Yang, "A 32-48 Gb/s serializing transmitter using multiphase serialization in 65 nm CMOS technology," *IEEE J. Solid-State Circuits*, vol. 50, pp. 763–775, Mar. 2015.

[33] S. Kaeriyama *et al.*, "A 40 Gb/s multi-data-rate CMOS transmitter and receiver chipset with SFI-5 interface for optical transmission systems," *IEEE J. Solid-State Circuits*, vol. 44, pp. 3568–3579, Dec. 2009.

[34] M. S. Chen *et al.*, "A fully-integrated 40-Gb/s transceiver in 65-nm CMOS technology," *IEEE J. Solid-State Circuits*, vol. 47, pp. 627–640, Mar. 2012.

[35] T. Shibasaki *et al.*, "A 56Gb/s NRZ-electrical 247mW/lane serial-link transceiver in 28nm CMOS," in *Proc. IEEE Int. Solid-State Circuits Conf. Dig. Tech. Papers*, pp. 64–65, Feb. 2016.

[36] J. Han *et al.*, "A 60Gb/s 288mW NRZ transceiver with adaptive equalization and baud-rate clock and data recovery in 65nm CMOS technology," in *Proc. IEEE Int. Solid-State Circuits Conf. Dig. Tech. Papers*, pp. 112–113, Feb. 2017.

[37] D. Cui *et al.*, "A dual-channel 23-Gbps CMOS transmitter/receiver chipset for 40-Gbps RZ-DQPSK and CS-RZ-DQPSK optical transmission," *IEEE J. Solid-State Circuits*, vol. 47, pp. 3249–3260, Dec. 2012.

[38] M. Harwood *et al.*, "A 225mW 28Gb/s SerDes in 40nm CMOS with 13dB of analog equalization for 100GBASE-LR4 and optical transport lane 4.4 applications," in *Proc. IEEE Int. Solid-State Circuits Conf. Dig. Tech. Papers*, pp. 326–327, Feb. 2012.

[39] K. Kaviani *et al.*, "A tri-modal 20-Gbps/link differential/DDR3/GDDR5 memory interface," *IEEE J. Solid-State Circuits*, vol. 47, pp. 926–937, Apr. 2012.

[40] ISSCC, *ISSCC 2016 trends*, Feb. 20016.

[41] T. Toifl *et al.*, "A 72mW 0.03mm^2 inductorless 40 Gb/s CDR in 65 nm SOI CMOS," in *Proc. IEEE Int. Solid-State Circuits Conf. Dig. Tech. Papers*, pp. 226–227, Feb. 2007.

[42] J. Savoj *et al.*, "Design of high-speed wireline transceivers for backplane communications in 28nm CMOS," in *Proc. IEEE Custom Integrated Circuits Conf.*, pp. 1–4, Sep. 2012.

[43] T. T. Vu, *Compound Semiconductor Integrated Circuits*, vol. 29. World Scientific, 2003.

[44] C.-K. K. Yang, *Design of High-Speed Serial Links in CMOS*. PhD thesis, Stanford University, Dec. 1998.

[45] H. Bakoglu, ed., *Circuits, Interconnections and Packaging for Very Large Scale Integration*. Addison Wesley Longman Publishing Co., 1990.

[46] H. Johnson and M. Graham, *High-Speed Digital Design*. Prentice-Hall, 1993.

[47] H. Johnson and M. Graham, *High-Speed Signal Propagation: Advanced Black Magic*. Prentice-Hall, 2003.

[48] W.-K. Chen, ed., *The VLSI Handbook*. Taylor & Francis Group, 2 ed., 2007.

[49] C. R. Paul, *Analysis of Multiconductor Transmission Lines*. John Wiley & Sons, 2 ed., 2008.

[50] T. Dhaene and D. D. Zutter, "Selection of lumped element models for coupled lossy transmission lines," *IEEE Trans. Comput. Aided Des. Integr. Circuits Syst.*, vol. 11, pp. 805–815, Jul. 1992.

[51] K. Fukuda *et al.*, "A 12.3-mW 12.5-Gb/s complete transceiver in 65-nm CMOS process," *IEEE J. Solid-State Circuits*, vol. 45, pp. 2838–2849, Dec. 2010.

[52] K.-L. J. Wong *et al.*, "A 27-mW 3.6-Gb/s I/O transceiver," *IEEE J. Solid-State Circuits*, vol. 39, pp. 602–612, Apr. 2004.

[53] H. Hatamkhani and C.-K. K. Yang, "Power analysis for high-speed I/O transmitters," in *Proc. Symp. VLSI Circuits*, pp. 142–145, Jun. 2004.

[54] A. Agrawal, *Design of High Speed I/O Interfaces for High Performance Microprocessors*. PhD thesis, The School of Engineering and Applied Sciences, Harvard University, Oct. 2010.

[55] B. Kim *et al.*, "A 10-Gb/s compact low-power serial I/O with DFE-IIR equalization in 65-nm CMOS," *IEEE J. Solid-State Circuits*, vol. 44, pp. 3526–3538, Dec. 2009.

[56] G. Balamurugan *et al.*, "A scalable 5-15 Gbps, 14-75 mW low-power I/O transceiver in 65 nm CMOS," *IEEE J. Solid-State Circuits*, vol. 43, pp. 1010–1019, Apr. 2008.

[57] J. Lee *et al.*, "56Gb/s PAM4 and NRZ SerDes transceivers in 40nm CMOS," in *Proc. IEEE Symp. VLSI Circ. Dig. Tech. Papers*, pp. 118–119, Jun. 2015.

[58] Tektronix, *Understanding and Characterizing Timing Jitter*, Feb. 2011.

[59] F. Rao and S. Hindi, "Frequency domain analysis of jitter amplification in clock channels," in *Proc. IEEE 21st Conference on Electrical Performance of Electronic Packaging and Systems*, pp. 51–54, Oct. 2012.

[60] S. Chaudhuri *et al.*, "Jitter amplification characterization of passive clock channels at 6.4 and 9.6 Gb/s," in *Proc. IEEE Electrical Performance of Electronic Packaging*, pp. 23–25, Feb. 2006.

[61] B. Casper and F. OMahony, "Clocking analysis, implementation and measurement techniques for high-speed data links-A tutorial," *IEEE Trans. Circuits Syst. I, Reg. Papers*, vol. 56, pp. 17–39, Jan. 2009.

[62] Maxim Integrated, *Converting between RMS and Peak-to-Peak Jitter at a Specified BER*, Apr. 2008.

[63] Y. Moon *et al.*, "A 0.6-2.5 GBaud CMOS tracked 3× oversampling transceiver with dead-zone phase detection for robust clock/data recovery," in *Proc. IEEE Int. Solid-State Circuits Conf. Dig. Tech. Papers*, pp. 212–213, Feb. 2001.

[64] J. L. Sonntag and J. Stonick, "A digital clock and data recovery architecture for multi-Gigabit/s binary links," *IEEE J. Solid-State Circuits*, vol. 41, pp. 1867–1875, Jul. 2006.

[65] P. K. Hanumolu *et al.*, "Digitally-enhanced phase-locking circuits," in *Proc. IEEE Custom Integrated Circuits Conf.*, pp. 361–368, Sep. 2007.

[66] A. Ghatak and K. Thyagarajan, *An Introduction to Fiber Optics*. Cambridge: Cambridge University Press, 1998.

[67] B. Razavi, *Design of Integrated Circuits for Optical Communications*. John Wiley & Sons. Inc, 2 ed., 2012.

[68] K. Kundert, *Verification of Bit-Error Rate in Bang-Bang Clock and Data Recovery Circuits*. The Designers Guide Community, May 2010.

[69] R. Reutemann *et al.*, "A 4.5 mW/Gb/s 6.4 Gb/s 22+1-lane source synchronous receiver core with optional cleanup PLL in 65 nm CMOS," *IEEE J. Solid-State Circuits*, vol. 45, pp. 2850–2860, Dec. 2010.

[70] N. Kalantari and J. F. Buckwalter, "A multichannel serial link receiver with dual-loop clock-and-data recovery and channel equalization," *IEEE Trans. Circuits Syst. I, Reg. Papers*, vol. 60, pp. 2920–2931, Nov. 2013.

[71] V. F. Kroupa, *Phase Lock Loops and Frequency Synthesis*. John Wiley & Sons Ltd, 2003.

[72] B. Razavi, ed., *Phase-Locking in High-Performance Systemss: From Devices to Architectures*. Wiley-IEEE Press, 2003.

[73] M. Mansuri and C.-K. K. Yang, "Jitter optimization based on phase-locked loop design parameters," *IEEE J. Solid-State Circuits*, vol. 37, pp. 1375–1382, Nov. 2002.

[74] J. G. Maneatis, "Low-jitter process-independent DLL and PLL based on self-biased techniques," *IEEE J. Solid-State Circuits*, vol. 31, pp. 1723–1732, Nov. 1996.

[75] M.-J. E. Lee, "Jitter transfer characteristics of delay-locked loops-theories and design techniques," *IEEE J. Solid-State Circuits*, vol. 38, pp. 614–615, Apr. 2003.

[76] C.-N. Chuang and S. luan Liu, "A 40GHz DLL-based clock generator in 90nm CMOS technology," in *Proc. IEEE Int. Solid-State Circuits Conf. Dig. Tech. Papers*, pp. 178–179, Feb. 2007.

[77] X. Gao et al., "Jitter analysis and a benchmarking figure-of-merit for phase-locked loops," *IEEE Trans. Circuits Syst. II, Exp. Briefs*, vol. 56, pp. 117–121, Feb. 2009.

[78] C. K. et al., "A low-power small-area 7.28-ps-jitter 1-GHz DLL-based clock generator," *IEEE Trans. Circuits Syst. II, Exp. Briefs*, vol. 37, pp. 1414–1420, Nov. 2002.

Bibliography

[79] R. Farjad-Rad *et al.*, "A low-power multiplying DLL for low-jitter multigigahertz clock generation in highly integrated digital chips," *IEEE J. Solid-State Circuits*, vol. 37, pp. 1804–1812, Dec. 2002.

[80] H.-Y. Chang, "A low-jitter low-phase-noise 10-Ghz sub-harmonically injection-locked PLL with self-aligned DLL in 65-nm CMOS technology," *IEEE Trans. Microwave Theory Tech.*, vol. 62, pp. 543–555, Mar. 2014.

[81] S. Choi *et al.*, "A 185 fs$_{rms}$-integrated-jitter and -245dB FOM PVT-robust ring-VCO-based injection-locked clock multiplier with a continuous frequency-tracking loop using a replica-delay cell and a dual-edge phase detector," in *IEEE Int. Solid-State Circuits Conf. Dig. Tech. Papers*, pp. 194–195, Feb. 2016.

[82] J.-C. Chien *et al.*, "A pulse-position-modulation phase-noise-reduction technique for a 2-to-16GHz injection-locked ring oscillator in 20nm CMOS," in *IEEE Int. Solid-State Circuits Conf. Dig. Tech. Papers*, pp. 52–53, Feb. 2014.

[83] W. Deng *et al.*, "A 0.022mm^2 970μW dual-loop injection-locked PLL with -243 dB FOM using synthesizable all-digital PVT calibration circuits," in *IEEE Int. Solid-State Circuits Conf. Dig. Tech. Papers*, pp. 248–249, Feb. 2013.

[84] M. Kim *et al.*, "A 450-fs jitter PVT-robust fractional-resolution injection-locked clock multiplier using a DLL-based calibrator with replica-delay-cells," in *Proc. IEEE Symp. VLSI Circ. Dig. Tech. Papers*, pp. C142–C143, Jun. 2015.

[85] B. M. Helal *et al.*, "A low jitter programmable clock multiplier based on a pulse injection-locked oscillator with a highly-digital tuning loop," *IEEE J. Solid-State Circuits*, vol. 44, pp. 1391–1400, May 2009.

[86] M. Raj *et al.*, "A 4-to-11GHz injection-locked quarter-rate clocking for an adaptive 153fJ/b optical receiver in 28nm FDSOI CMOS," in *IEEE Int. Solid-State Circuits Conf. Dig. Tech. Papers*, pp. 404–405, Feb. 2015.

[87] K. Hu *et al.*, "A 0.6 mW/Gb/s, 6.4-7.2 Gb/s serial link receiver using local injection-locked ring oscillators in 90 nm CMOS," *IEEE J. Solid-State Circuits*, vol. 45, pp. 899–908, Apr. 2010.

[88] J. Lee and H. Wang, "Study of subharmonically injection-locked PLLs," *IEEE J. Solid-State Circuits*, vol. 44, pp. 1539–1553, May 2009.

[89] S. Ye *et al.*, "A multiple-crystal interface PLL with VCO realignment to reduce phase noise," *IEEE J. Solid-State Circuits*, vol. 37, pp. 1795–1803, Dec. 2002.

[90] X. Qi *et al.*, "Compact on-chip wire models for the clock distribution of high-speed i/o interfaces," in *Proc. IEEE Electrical Performance of Electronic Packaging*, pp. 235–238, Oct. 2008.

[91] K. Hu *et al.*, "Comparison of on-die global clock distribution methods for parallel serial links," in *Proc. IEEE International Symposium on Circuits and Systems*, pp. 1843–1846, May 2009.

[92] F. OMahony *et al.*, "A low-jitter PLL and repeaterless clock distribution network for a 20Gb/s link," in *Proc. IEEE Symp. VLSI Circ. Dig. Tech. Papers*, pp. 29–30, Jun. 2006.

[93] L. Xiu, "Clock technology: The next frontier," *IEEE Circuits and Systems Magazine*, vol. 17, pp. 27–46, May. 2017.

[94] J. Poulton *et al.*, "A 14-mW 6.25-Gb/s transceiver in 90-nm CMOS," *IEEE J. Solid-State Circuits*, vol. 42, pp. 2745–2757, Dec. 2007.

[95] S. Chan *et al.*, "A resonant global clock distribution for the cell broadband-engine processor," in *Proc. IEEE Int. Solid-State Circuits Conf. Dig. Tech. Papers*, pp. 512–513, Feb. 2008.

[96] N. Holland, *Interfacing Between LVPECL, VML, CML, and LVDS Levels*. Texas Instruments, 2002.

[97] Cypress Semiconductor, *A Comparison of CML and LVDS for High-Speed Serial Links*, 2002.

[98] C. Menolfi *et al.*, "A 28Gb/s source-series terminated tx in 32nm CMOS SOI," in *Proc. IEEE Int. Solid-State Circuits Conf. Dig. Tech. Papers*, pp. 334–335, Feb. 2012.

[99] J. Kim *et al.*, "A 16-to-40Gb/s quarter-rate NRZ/PAM4 dual-mode transmitter in 14nm CMOS," in *Proc. IEEE Int. Solid-State Circuits Conf. Dig. Tech. Papers*, pp. 60–61, Feb. 2015.

[100] K. Kanda *et al.*, "A single-40 Gb/s dual-20 Gb/s serializer IC with SFI-5.2 interface in 65 nm CMOS," *IEEE J. Solid-State Circuits*, vol. 44, pp. 3580–3589, Dec. 2009.

[101] H. Wang and J. Lee, "A 21-Gb/s 87-mW transceiver with FFE/DFE/Analog equalizer in 65-nm CMOS technology," *IEEE J. Solid-State Circuits*, vol. 45, pp. 909–919, Apr. 2010.

[102] L. Henrickson *et al.*, "Low power fully integrated 10-Gb/s SONET/SDH transceiver in 0.13-μm CMOS," *IEEE J. Solid-State Circuits*, vol. 38, pp. 1595–1601, Oct. 2003.

[103] B. Raghavan *et al.*, "A sub-2 W 39.8-44.6 Gb/s transmitter and receiver chipset with SFI-5.2 interface in 40 nm CMOS," *IEEE J. Solid-State Circuits*, vol. 48, pp. 3219–3228, Dec. 2013.

[104] X. Zheng, C. Zhang, and S. Yuan *et al.*, "An improved 40 Gb/s CDR with jitter-suppression filters and phase-compensating interpolators," in *Proc. IEEE Asian Solid-State Circuits Conf. (ASSCC)*, pp. 85–88, Nov. 2016.

[105] J. W. Bergmans, *Digital Baseband Transmission and Recording*, ch. 8, pp. 400–412. Springer Science & Business Media, 1996.

[106] F.-T. Chen *et al.*, "A 10-Gb/s low jitter single-loop clock and data recovery circuit with rotational phase frequency detector," *IEEE Trans. Circuits Syst. I, Reg. Papers*, vol. 61, pp. 3278–3287, Nov. 2014.

[107] N. Kocaman *et al.*, "An 8.5-11.5-Gbps SONET transceiver with referenceless frequency acquisition," *IEEE J. Solid-State Circuits*, vol. 48, pp. 1975–1884, Aug. 2013.

[108] M. S. Jalali *et al.*, "A reference-less single-loop half-rate binary CDR," *IEEE J. Solid-State Circuits*, vol. 50, pp. 2037–2047, Sep. 2015.

[109] A. Pottbacker *et al.*, "A Si bipolar phase and frequency detector IC for clock extraction up to 8 Gb/s," *IEEE J. Solid-State Circuits*, vol. 27, pp. 1747–1751, Dec. 1992.

[110] M. ta Hsieh and G. E. Sobelman, "Architectures for multi-gigabit wire-linked clock and data recovery," *IEEE Circuits and Systems Magazine*, vol. 8, no. 4, pp. 45–57, 2008.

[111] B. Razavi, "Challenges in the design of high-speed clock and data recovery circuits," *IEEE Communications Magazine*, pp. 94–101, Aug. 2002.

[112] M. H. Perrott *et al.*, "A 2.5-Gb/s multi-rate 0.25-μm CMOS clock and data recovery circuit utilizing a hybrid analog/digital loop filter and all-digital referenceless frequency acquisition," *IEEE J. Solid-State Circuits*, vol. 41, pp. 2930–2944, Dec. 2006.

[113] J. C. Scheytt *et al.*, "A 0.155-, 0.622-, and 2.488-Gb/s automatic bit-rate selecting clock and data recovery IC for bit-rate transparent SDH systems," *IEEE J. Solid-State Circuits*, vol. 34, pp. 1935–1943, Dec. 1999.

[114] H. S. Muthali *et al.*, "A CMOS 10-Gb/s SONET transceiver," *IEEE J. Solid-State Circuits*, vol. 39, pp. 1026–1033, Jul. 2004.

[115] M. Y. He and J. Poulton, "A CMOS mixed-signal clock and data recovery circuit for OIF CEI-6G+ backplane transceiver," *IEEE J. Solid-State Circuits*, vol. 41, pp. 597–606, Mar. 2006.

[116] H.-H. Chang *et al.*, "Low jitter and multirate clock and data recovery circuit using a MSADLL for chip-to-chip interconnection," *IEEE Trans. Circuits Syst. I, Reg. Papers*, vol. 51, pp. 2356–2364, Dec. 2004.

[117] B. Razavi, *Monolithic Phase-Locked Loops and Clock Recovery Circuits: Theory and Design*. Wiley-IEEE Press, 1996.

[118] Y. Sun and H. Wang, "Analysis of digital bang-bang clock and data recovery for multi-gigabits serial transceivers," in *Proc. IEEE Custom Integrated Circuits Conf.*, pp. 13–16, Sep. 2009.

[119] S. Tertinek *et al.*, "Binary phase detector gain in bang-bang phase-locked loops with DCO jitter," *IEEE Trans. Circuits Syst. II, Exp. Briefs*, vol. 57, pp. 941–945, Dec. 2010.

[120] N. D. Dalt, "Markov chains-based derivation of the phase detector gain in bang-bang PLLs," *IEEE Trans. Circuits Syst. II, Exp. Briefs*, vol. 53, pp. 1195–1199, Nov. 2006.

[121] J. Kim *et al.*, "Simulation and analysis of random decision errors in clocked comparators," *IEEE Trans. Circuits Syst. I, Reg. Papers*, vol. 56, pp. 1844–1857, Aug. 2009.

[122] G. R. Gangasani *et al.*, "A 16-Gb/s backplane transceiver with 12-tap current integrating DFE and dynamic adaptation of voltage offset and timing drifts in 45-nm SOI CMOS technology," *IEEE J. Solid-State Circuits*, vol. 47, pp. 1828–1841, Aug. 2012.

[123] T. Musah *et al.*, "A 4-32 Gb/s bidirectional link with 3-tap FFE/6-tap DFE and collaborative CDR in 22 nm CMOS," *IEEE J. Solid-State Circuits*, vol. 49, pp. 3079–3090, Dec. 2014.

[124] P. K. Hanumolu *et al.*, "Equalizer for high-speed links," *International Joruanl of High Speed Electronics and Systems*, vol. 15, pp. 429–458, Jul. 2005.

[125] J. F. Bulzacchelli *et al.*, "A 28-Gb/s 4-tap FFE/15-tap DFE serial link transceiver in 32-nm SOI CMOS technology," *IEEE J. Solid-State Circuits*, vol. 47, pp. 3232–3248, Dec. 2012.

[126] M. Altmann and F. Spagna, *Adaptive Tx Equalization*. IEEE 802.3ap, Nov. 2004.

[127] S. S. Mohan *et al.*, "Bandwidth extension in CMOS with optimized on-chip inductors," *IEEE J. Solid-State Circuits*, vol. 35, pp. 346–355, Mar. 2000.

[128] S. Ibrahim and B. Razavi, "Low-power CMOS equalizer design for 20-Gb/s systems," *IEEE J. Solid-State Circuits*, vol. 46, pp. 1321–1336, Jun. 2011.

[129] C. Thakkar *et al.*, "A 10 Gb/s 45 mW adaptive 60 GHz baseband in 65 nm CMOS," *IEEE J. Solid-State Circuits*, vol. 47, pp. 952–968, Apr. 2012.

[130] J. Jaussi *et al.*, "A 205mW 32Gb/s 3-tap FFE/6-tap DFE bidirectional serial link in 22nm CMOS," in *Proc. IEEE Int. Solid-State Circuits Conf. Dig. Tech. Papers*, pp. 440–441, Feb. 2014.

[131] M. Pozzoni *et al.*, "A multi-standard 1.5 to 10 Gb/s latch-based 3-tap DFE receiver with a SSC tolerant CDR for serial backplane communication," *IEEE J. Solid-State Circuits*, vol. 44, pp. 1306–1315, Apr. 2009.

[132] H. Higashi *et al.*, "A 5-6.4-Gb/s 12-channel transceiver with pre-emphasis and equalization," *IEEE J. Solid-State Circuits*, vol. 40, pp. 978–985, Apr. 2005.

[133] K. Krishna *et al.*, "A multigigabit backplane transceiver core in 0.13-μm CMOS with a power-efficient equalization architecture," *IEEE J. Solid-State Circuits*, vol. 40, pp. 2658–2666, Dec. 2005.

[134] J. Lee, "A 20-Gb/s adaptive equalizer in 0.13-μm CMOS technology," *IEEE J. Solid-State Circuits*, vol. 41, pp. 2058–2066, Sep. 2006.

[135] Wong and Lok, "Theory of digtial communications: Chapter 4 intersymbol interference and equalization." http://wireless.ece.ufl.edu/twong/Notes/Comm/ch4.pdf. [Online]. Accessed 16-Set.-2017.

[136] schober, "Signal detection and estimation: Equalization of channels with ISI." http://courses.ece.ubc.ca/564/chapter6.pdf. [Online]. Accessed 16-Set.-2017.

[137] Communication Capstone Design, "Channel equalization." Electrical Engineering, http://courses.washington.edu/ee417/handouts/handout2.pdf. [Online]. Accessed 16-Set.-2017.

[138] J. Savoj *et al.*, "A low-power 0.5-6.6 Gb/s wireline transceiver embedded in low-cost 28 nm FPGAs," *IEEE J. Solid-State Circuits*, vol. 48, pp. 2582–2594, Nov. 2013.

[139] J. Savoj *et al.*, "A wide common-mode fully-adaptive multi-standard 12.5 Gb/s backplane transceiver in 28 nm CMOS," in *Proc. IEEE Symp. VLSI Circ. Dig. Tech. Papers*, pp. 104–105, Jun. 2012.

[140] B. Analui *et al.*, "A 10Gb/s eye-opening monitor in 0.13 μm CMOS." http://researcher.watson.ibm.com/researcher/files/us-sasha/10Gbps_Eye_Monitor_18_3_Behnam_Analui_ISSCC.pdf. [Online]. Accessed 26-Feb.-2017.

[141] B. Analui *et al.*, "A 10-Gb/s two-dimensional eye-opening monitor in 0.13-μm standard CMOS," *IEEE J. Solid-State Circuits*, vol. 40, pp. 2689–2699, Dec. 2005.

[142] J.-S. Choi *et al.*, "A 0.18-μm CMOS 3.5-Gb/s continuous-time adaptive cable equalizer using enhanced low-frequency gain control method," *IEEE J. Solid-State Circuits*, vol. 39, pp. 419–425, Mar. 2004.

[143] S. Gondi *et al.*, "A 10Gb/s CMOS adaptive equalizer for backplane applications," in *Proc. IEEE Int. Solid-State Circuits Conf. Dig. Tech. Papers*, pp. 328–329, Feb. 2005.

[144] P. C. Maulik and D. A. Mercer, "A DLL-based programmable clock multiplier in 0.18-μm CMOS with 70 dBc reference spur," *IEEE J. Solid-State Circuits*, vol. 42, pp. 1642–1648, Aug. 2007.

[145] Y.-C. Huang and S.-I. Liu, "A 2.4-GHz subharmonically injection-locked PLL with self-calibrated injection timing," *IEEE J. Solid-State Circuits*, vol. 48, pp. 417–428, Feb. 2013.

[146] I.-T. Lee *et al.*, "A divider-less sub-harmonically injection-locked PLL with self-adjusted injection timing," in *IEEE Int. Solid-State Circuits Conf. Dig. Tech. Papers*, pp. 414–415, Feb. 2013.

[147] H. M. Cheema *et al.*, *60-GHz CMOS Phase-Locked Loops*. Springer Sciencet & Business Media, 2010.

[148] V. Manassewitsch, ed., *Frequency Synthesizers*. New York: Wiley, 1987.

[149] L. Zhang *et al.*, "Injection-locked clocking: A low-power clock distribution scheme for high-performance microprocessors," *IEEE Trans. VLSI. syst*, vol. 16, pp. 1251–1256, Sep. 2008.

[150] J. Lee and M. Liu, "A 20-Gb/s burst-mode clock and data recovery circuit using injection-locking technique," *IEEE J. Solid-State Circuits*, vol. 43, pp. 619–630, Mar. 2008.

[151] A. Musa *et al.*, "A compact, low-power and low-jitter dual-loop injection locked PLL using all-digital PVT calibration," *IEEE J. Solid-State Circuits*, vol. 49, pp. 50–60, Jan. 2014.

[152] P. Park, J. Park, H. Park, and S. Cho, "An all-digital clock generator using a fractionally injection-locked oscillator in 65nm CMOS," in *IEEE Int. Solid-State Circuits Conf. Dig. Tech. Papers*, pp. 336–337, Feb. 2012.

[153] C.-F. Liang and K.-J. Hsiao, "An injection-locked ring PLL with self-aligned injection window," in *IEEE Int. Solid-State Circuits Conf. Dig. Tech. Papers*, pp. 90–91, Feb. 2011.

[154] D. Dunwell and A. C. Carusone, "Modeling oscillator injection locking using the phase domain response," *IEEE Trans. Circuits Syst. I, Reg. Papers*, vol. 60, pp. 2823–2833, Nov. 2013.

[155] Y.-H. Kwak *et al.*, "A 20 Gb/s clock and data recovery with a ping-pong delay line for unlimited phase shifting in 65 nm CMOS process," *IEEE Trans. Circuits Syst. I, Reg. Papers*, vol. 60, pp. 303–313, Feb. 2013.

[156] E. Alon *et al.*, "Replica compensated linear regulators for supply-regulated phase-locked loops," *IEEE J. Solid-State Circuits*, vol. 41, pp. 413–424, Feb. 2006.

[157] L. Kull *et al.*, "Implementation of low-power 6-8 b 30-90 GS/s time-interleaved ADCs with optimized input bandwidth in 32 nm CMOS," *IEEE J. Solid-State Circuits*, vol. 51, pp. 636–648, Mar. 2016.

[158] A. Elkholy *et al.*, "A 6.75-to-8.25GHz 2.25mW 190fs$_{rms}$ integrated-jitter PVT-insensitive injection-locked clock multiplier using all-digital continuous frequency-tracking loop in 65nm CMOS," in *IEEE Int. Solid-State Circuits Conf. Dig. Tech. Papers*, pp. 188–189, Feb. 2015.

[159] P. Chiang *et al.*, "A 20-Gb/s 0.13-μm CMOS serial link transmitter using an LC-PLL to directly drive the output multiplexer," *IEEE J. Solid-State Circuits*, vol. 40, pp. 1004–1011, Apr. 2005.

[160] INCITS, *Fiber Channel Physical Interface-6*, Oct. 2013.

[161] M. Hossain *et al.*, "A 4x40 Gb/s quad-lane CDR with shared frequency tracking and data dependent jitter filtering," in *IEEE Symp. VLSI Circuits Dig. Tech. Papers*, pp. 1–2, Jun. 2014.

[162] T. O. Dickson, J. F. Bulzacchelli, and D. J. Friedman, "A 12-Gb/s 11-mW half-rate sampled 5-tap decision feedback equalizer with current-integrating summers in 45-nm SOI CMOS technology," *IEEE J. Solid-State Circuits*, vol. 44, pp. 1298–1305, Apr. 2009.

[163] D. Vijayaraghavan *et al.*, "Highly configurable FPGA-integrated PCI Express 3.0 digital IP architecture," in *DesignCon*, pp. 1274–1288, Jan.-Feb. 2011.

[164] H. Kimura *et al.*, "A 28 Gb/s 560 mW multi-standard SerDes with single-stage analog front-end and 14-tap decision feedback equalizer in 28 nm CMOS," *IEEE J. Solid-State Circuits*, vol. 49, pp. 3091–3103, Dec. 2014.

[165] R. A. Horn and C. R. Johnson, *Matrix analysis*. Cambridge university press, 2012.

Appendices

Appendix A   Modeling of the Injection-Locked Oscillator (ILO)

A.1   Behavior Model of the ILO

The discussions in [89, 154] show that it is reasonable to assume the injection event shifts the ILO output phase instantaneously and the phase shift is linear with respect to the instantaneous phase difference relative to the injection signal. These assumptions are also supported by the circuit simulations and measurement results. This means each injection phase shift can be modeled as an additional phase step that is applied to the oscillator output. Fig. A1(a) shows the ILO waveform within the nth injection period. The total $2N\pi$ is divided into two portions of $\varphi_{osc}(n)$ and $\varphi_{inj}(n)$, which are separately contributed by the self-oscillation of the oscillator and the pulling of the injection pulling. Under such a locking condition, the relationship of $\varphi_{osc}(n)$ and $\varphi_{inj}(n)$ should satisfy,

$$\varphi_{osc}(n) + \varphi_{inj}(n) = 2N\pi, \tag{A1}$$

where N is the factor of harmonic injection. The phase accumulation produced by the oscillator self-oscillation can be calculated by,

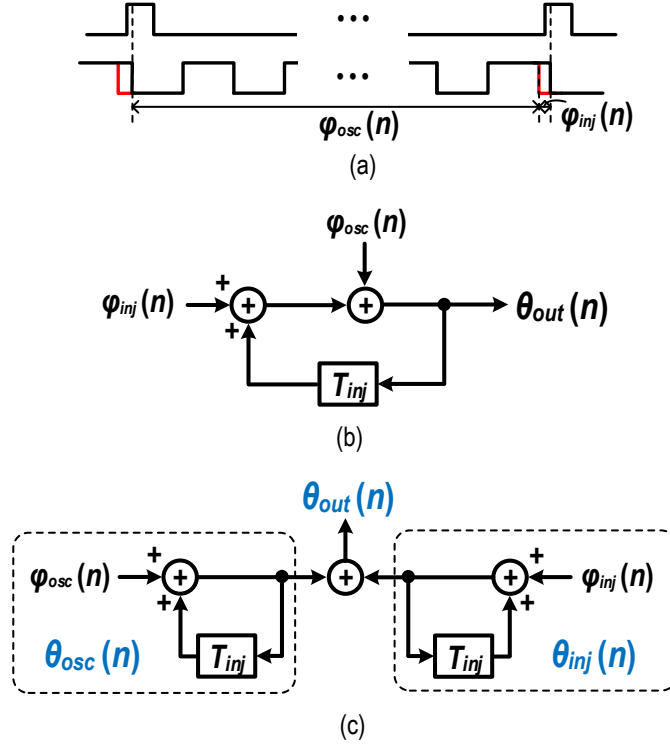$$\varphi_{osc}(n) = \frac{2N\pi\omega_0}{\omega_{lock}}, \tag{A2}$$

Figure A1: Phase accumulation behavior of the ILO. (a) Output waveform of the ILO in one injection period, (b) flow-chart diagram of the phase accumulation, and (c) intuitive diagram of the phase accumulation.

where ω_0 stands for the free-running frequency of the oscillator and ω_{lock} represents the target frequency of the ILO when it is locked to the injection signal. Accordingly, the phase shift contributed by the injection pulling should be,

$$\varphi_{inj}(n) = \frac{2N\pi(\omega_{lock} - \omega_0)}{\omega_{lock}}. \tag{A3}$$

Considering the fact that the ILO output phase can be calculated by summing all the discrete phases in different injection periods, the ILO can be modeled as a discrete phase integrator with an updating period of T_{inj}. The phase accumulation behavior of the ILO is described in Fig. A1(b), which can be transformed into Fig. A1(c) to give a more instructive view. Corresponding to the phase contribution in each injection period, the total output phase $\theta_{out}(n)$ of the ILO is also divided into $\theta_{osc}(n)$ and $\theta_{inj}(n)$, where the former denotes the accumulated phase upon the oscillator self-oscillation and the latter represents the summation of the phase shift produced by the injection
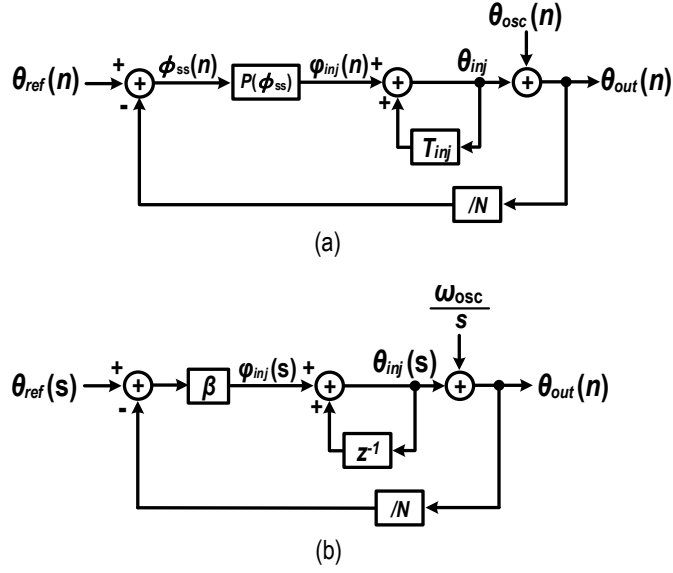
Figure A2: Model of the ILO. (a) Signal flow chart and (b) linear model.

event.

A.2 Linear Model of the ILO

According to the discussion in [154], the phase shift φ_{inj} is a function of the instantaneous phase difference between the injection reference signal and oscillator output, $\phi_{ss} = \theta_{ref} - \theta_{out}/N$, which is usually defined as $\varphi_{inj} = P(\phi_{ss})$. Here, the phase difference is defined as the horizontal coordinate of the oscillator output crossing point that locates inside the injection pulse relative to the center of the injection pulse. Embedding this phase shift function into Fig. A1(c), the complete signal flow chart of the ILO can be obtained [see Fig. A2(a)]. Since the integration of the $\varphi_{osc}(n)$ actually equals the output phase of the free-running oscillator, we replace the right chart surrounded by the dashed line with the the θ_{osc}. When the ILO reaches steady-state with a relative phase difference of ϕ_{ss}, the ILO can be modeled as a linear phase transfer system for small signal analysis. The phase shift φ_{inj} can be treated as a linear function with respect to the phase difference ϕ_{ss} by a factor of β, which can be approximated by the instantaneous slope of $P(\phi_{ss})$ at $\phi_{ss,lock}$,

$$\beta = \frac{dP(\phi_{ss})}{d\phi_{ss}}\bigg|_{\phi_{ss}=\phi_{ss,lock}}. \tag{A4}$$

Then the linear model of the ILO is constructed as shown in Fig. A2(b). To explore the phase transfer characteristics, the closed-loop characteristic equation is formulated as,

$$[\theta_{ref}(s) - \theta_{out}(s)/N] \cdot \beta \cdot \frac{1}{1 - z^{-1}} + \frac{\omega_{osc}}{s} = \theta_{out}(s), \qquad (A5)$$

where ω_{osc} is the angular frequency of the the oscillator. According to the digital signal processing theorem, the discrete transfer function $1/(1 - z^{-1})$ can be approximated by the continuous transfer function of $1/(sT_{inj})$, where T_{inj} is the period of the injection signal (i.e. sampling period). Substituting this approximation into Eq. (A5) and rearranging it, we can get the ILO closed-loop transfer function,

$$\theta_{out}(s) = \theta_{ref}(s) \cdot \frac{N\beta}{sNT_{inj} + \beta} + \frac{\omega_{osc}}{s} \cdot \frac{sNT_{inj}}{sNT_{inj} + \beta}. \qquad (A6)$$

From Eq. (A6), the phase transfer function of the input reference is,

$$H_{ref}(s) = \frac{N\beta}{sNT_{inj} + \beta} = \frac{N}{1 + \dfrac{s}{\frac{\beta}{NT_{inj}}}} = \frac{N}{1 + \dfrac{s}{\omega_{TB}}} = NH_{inj}(s),$$

$$(A7)$$

where $H_{inj}(s)$ is the normalized $H_{ref}(s)$. Obviously, the phase transfer function $H_{ref}(s)$ is actually a first-order LPF with a left-plane pole located at $\omega_{TB} = \beta/(NT_{inj})$ and its DC-gain is $20log(N)$ dB. Hence the ILO shows a low-frequency noise tracking ability of the input reference.

Reviewing Eq. (A6), the phase transfer function of the oscillator can be written as,

$$H_{osc}(s) = \frac{sNT_{inj}}{sNT_{inj} + \beta} = 1 - H_{inj}(s). \qquad (A8)$$

Clearly, the $H_{osc}(s)$ is a first-order HPF with the same pole as the $H_{ref}(s)$ and its high-frequency gain is 0 dB. Thereby, the ILO exhibits a low-frequency noise suppression for the oscillator in 20 dB/dec.

A.3 Tracking Bandwidth of the ILO

According to the discussion in [154], the relative phase difference will settle to a steady state, ϕ_{ss}, where each injection event causes a phase shift $P(\phi_{ss})$ that is just sufficient to cancel the phase drift resulting from the frequency offset. This condition can be expressed by,

$$P(\phi_{ss}) = \frac{2N\pi(f_{lock} - f_0)}{f_{lock}}, \tag{A9}$$

where N is the multiplication factor, f_{lock} denotes the locked frequency, and f_0 represents the free-running frequency of the oscillator. For a different frequency offset, there exists a different steady state ϕ_{ss}. Assume there is a small phase perturbation $\Delta\theta_{inj}$ in the injection signal, then the output phase perturbation $\Delta\theta_{out}$ can be predicted by $\beta\Delta\theta_{inj}$, where β is the instantaneous slope of the $P(\phi_{ss})$. It can be obtained by taking the derivative of Eq. (A9). resulting in,

$$\beta = \frac{dP(\phi_{ss})}{d\phi_{ss}}\bigg|_{\phi_{ss}=\phi_{ss,lock}}. \tag{A10}$$

Note that the small perturbations in the injection signal intends to cause an instantaneous output frequency change, hence the output frequency f_{lock} can be considered as the intermediate variable of $P(\phi_{ss})$. Substituting Eq. (A9) into Eq. (A10) and simplifying it using $f_{lock} \approx f_0$, we can get,

$$\beta = \frac{2N\pi}{f_{lock}} \cdot \frac{df_{lock}}{d\phi_{ss}}\bigg|_{\phi_{ss}=\phi_{ss,lock}}. \tag{A11}$$

Substituting Eq. (A11) into $\omega_{TB} = \beta/(NT_{inj})$ and combining with $\omega_{TB} = 2\pi f_{TB}$, we can get the tracing bandwidth,

$$f_{TB} = \frac{1}{N} \cdot \frac{df_{lock}}{d\phi_{ss}}\bigg|_{\phi_{ss}=\phi_{ss,lock}}. \tag{A12}$$

The tracking bandwidth can also be obtained by the intuitive transient analysis. Based on the deduced slope β of the phase shift $P(\phi_{ss})$ with respect to ϕ_{ss}, the output

phase perturbation can be written as,

$$\Delta\theta_{out} = \frac{2N\pi}{f_{lock}} \cdot \left.\frac{df_{lock}}{d\phi_{ss}}\right|_{\phi_{ss}=\phi_{ss,lock}} \cdot \Delta\theta_{inj}, \tag{A13}$$

If we assume the the first-order phase transfer function of the IL-RVCO is,

$$H_{inj}(s) = \frac{N}{1 + \frac{s}{\omega_{TB}}}, \tag{A14}$$

where N is the harmonic factor of the IL-RVCO and ω_{TB} is the angular frequency of the tracing bandwidth. Then its transient response for a small step input $\Delta\theta_{inj}$ should be

$$\Delta\theta_{out} = N\Delta\theta_{inj}(1 - e^{-\omega_{TB}t}). \tag{A15}$$

For an injection period, $\omega_{TB}T_{inj}$ can be considered as much smaller than 1, then $(1 - e^{-\omega_{TB}T_{inj}})$ can be approximated by $\omega_{TB}T_{inj}$. Correspondingly, Eq. (A15) can be simplified as

$$\Delta\theta_{out} = N\omega_{TB}T_{inj} \cdot \Delta\theta_{inj}. \tag{A16}$$

Compare Eq. (A13) with Eq. (A16), we can get the equation

$$\frac{2N\pi}{f_{lock}} \cdot \left.\frac{df_{lock}}{d\phi_{ss}}\right|_{\phi_{ss}=\phi_{ss,lock}} = N\omega_{TB}T_{inj}. \tag{A17}$$

Rearrange Eq. (A17), we attain

$$\omega_{TB} = \frac{2\pi}{f_{lock}T_{inj}} \cdot \left.\frac{df_{lock}}{d\phi_{ss}}\right|_{\phi_{ss}=\phi_{ss,lock}}. \tag{A18}$$

Considering $\omega_{TB} = 2\pi f_{TB}$ and $f_{lock} = N/T_{inj}$, Eq. (A18) can be simplified as

$$f_{TB} = \frac{1}{N} \cdot \left.\frac{df_{lock}}{d\phi_{ss}}\right|_{\phi_{ss}=\phi_{ss,lock}}, \tag{A19}$$

which is the same as Eq. (A12).

Appendix B   Convergence Proof of the Proposed EDC-SZF Iteration

The iterative equation in Section 6.2.2 can be rewritten as,

$$x^{k+1} = (I - \lambda B)x^k + f, \tag{A20}$$

where $x^k \in \mathbb{R}^\ell$ with $\ell \in \mathbb{N}^+$, $\lambda \in (0, 1)$, I denotes the identity matrix, and $f \in \mathbb{R}^\ell$ is a fixed constant vector. It is well known that when discussing the convergence issue, the norm (distance) defined on $\mathbb{R}^\ell$ should be specified to make it a normed space. With respect to the properties of matrix B, we choose the 1-norm and denote the normed space as $(\mathbb{R}^\ell, \| \cdot \|_1)$. For a vector $x \in \mathbb{R}^\ell$, the 1-norm could be defined as,

$$\| x \|_1 = \sum_{i=1}^{\ell} | x_i | . \tag{A21}$$

In addition, the 1-norm for matrix $A = (a_{ij})_{i,j=1,2,\cdots \ell}$ has the following two equivalent definitions [165],

$$\| A \|_1 = \sup_{x \in \mathbb{R}^\ell} \frac{\| Ax \|_1}{\| x \|_1}, \tag{A22}$$

$$\| A \|_1 = \max_{1 \leq j \leq \ell} \sum_{i=1}^{\ell} |a_{ij}|. \tag{A23}$$

Because $(\mathbb{R}^\ell, \| \cdot \|_1)$ is a compact space, the convergence of $\{x^k\}_{k=1}^\infty$ is equivalent to that the sequence $\{x^k\}_{k=1}^\infty$ is a Cauchy sequence in $(\mathbb{R}^\ell, \| \cdot \|_1)$.

For convenience, we denote $T := I - \lambda B$. In the following, we prove that $\| T \|_1 < 1$ is a sufficient condition to ensure the sequence $\{x^k\}_{k=1}^\infty$ is a Cauchy sequence. Let

$n, m \in \mathbb{N}^+$, without loss of generality, assuming $n > m$, we then obtain,

$$
\begin{aligned}
\parallel x^n - x^m \parallel_1 &\leq \parallel x^n - x^{n-1} \parallel_1 + \cdots + \parallel x^{m+1} - x^m \parallel_1 \\
&\leq \parallel T \parallel_1^{n-1} \parallel x^1 - x^0 \parallel_1 + \cdots \\
&\qquad\qquad + \parallel T \parallel_1^m \parallel x^1 - x^0 \parallel_1 \\
&\leq \parallel T \parallel_1^m \sum_{k=0}^{\infty} \parallel T \parallel_1^k \parallel x^1 - x^0 \parallel_1 \\
&\leq \parallel T \parallel_1^m \left(\frac{1}{1- \parallel T \parallel_1} \right) \parallel x^1 - x^0 \parallel_1,
\end{aligned}
\tag{A24}
$$

where Eq. (A22) and a simple iteration are used for deducing the second inequality. When the condition $\parallel T \parallel_1 < 1$ is satisfied, we have $\lim_{m \to \infty} \parallel T \parallel_1^m = 0$. Hence, for all $\epsilon > 0$, there exists a constant $M > 0$ such that for any $n, m \geq M$, the following inequality holds,

$$
\parallel x^n - x^m \parallel_1 \leq \epsilon.
\tag{A25}
$$

This means $\{x^k\}_{k=1}^{\infty}$ is a Cauchy sequence. Therefore,

$$
\parallel I - \lambda B \parallel_1 < 1,
$$

is a sufficient condition to make the iterative Eq. (A20) convergent.